Experimental and numerical investigation of equivalent stress intensity factor models for fatigue life predictions

A Thesis

Submitted in Partial Fulfillment of the

Requirements for the Degree of

DOCTOR OF PHILOSOPHY

by

SAJITH S

(Roll No: 11610333)

Department of Mechanical Engineering

Indian Institute of Technology Guwahati

Guwahati – 781039, India

March 2020

Department of Mechanical Engineering
Indian Institute of Technology Guwahati
Guwahati – 781039, India

CERTIFICTE

It is certified that the work contained in the Thesis titled **"Experimental and numerical investigation of equivalent stress intensity factor models for fatigue life predictions"** submitted by **Sajith S** to the Indian Institute of Technology Guwahati for the award of the degree of Doctor of Philosophy has been carried out under our supervision in the Department of Mechanical Engineering, Indian Institute of Technology Guwahati. This work has not been submitted elsewhere for the award of any other degree.

11th March, 2020

(K.S.R.K. Murthy)
Professor
Department of Mechanical Engineering
Indian Institute of Technology Guwahati
Guwahati – 781039

(P.S. Robi)
Professor
Department of Mechanical Engineering
Indian Institute of Technology Guwahati
Guwahati – 781039

Dedicated to my parents and family

ACKNOWLEDGEMENTS

This thesis is the outcome of seven years of research work done in this IIT Guwahati. The exercise was by no means an easy task and during this long period, I have been guided and supported by many people. My grateful thanks are due to all of them for their valuable help at various stages during this tenure. I now have the opportunity to acknowledge my indebtedness to all of them.

At the very first, I would like to express my gratefulness particularly to my supervisors Prof. K.S.R.K. Murthy and Prof. P.S. Robi, Department of Mechanical Engineering, IIT Guwahati, for their guidance, valuable advice and useful suggestions. I sincerely believe that without their able support, the research work would not have been possible. I would like to offer my heartfelt thanks to my doctoral committee members, Prof. D. Chakraborty, Prof. P. Biswas and Prof. A.K. Singh for their valuable suggestions and recommendations.

My particular appreciations are expressed to all the faculty members of Mechanical Engineering Department, IIT Guwahati in general and the Head, Mechanical Engineering Department in particular for providing me a conducive environment for pursuing my research work. I am grateful to the entire technical staff of Central Workshop, IIT Guwahati for their help in preparing some of the experimental specimens. I would like to express my special thanks to Mr. Shiv Shukla for helping me while conducting the experiments. I acknowledge Mr. Venkata Reddy (Service Engineer, BiSS, Bangalore, India) for the help in understanding the fatigue crack growth experiments. I am thankful to Central Instrumentation Facility and Centre for Nano Technology for providing UTM and FESEM facility for this work. I would also like offer my thanks to colleagues Mr. Sanjib Sarma, Mirzaul, Dr. Debabrata, Pranjol, Uttam, Abhay, Sandipan, Manjeet and other research scholars with whom I helped me at various stages of the work. I would like to extend my heartfelt thanks to Dr. H.N. Bar and Dr. S. Sivaprasad, scientists NML, Jamshedpur for providing assistance on fatigue crack growth experimetns, without which the experimental work would not have been possible. Also I extent my thanks to my friends Mr. Anoop. Vishnu, Dr. Jiss, Vasu, Dileep, Thomas, Dr. Vivek, Arjun and all others who helped me

I wish to express my warm gratitude to all members of my family and my wife who have been pivotal in helping me keep a calm state of mind at all times and to my wife in particular for her constant encouragement and unique capacity of confidence building. Last but

not the least I would like to express my sincere thankfulness to Ministry of Human Resource Development, Govt. of India for providing financial assistance during the doctoral program.

11th March 2020

IIT Guwahati Sajith S

TABLE OF CONTENTS

भारतीय प्रौद्योगिकी संस्थान गुवाहाटी
Indian Institute of Technology Guwahati

ABSTRACT

Fracture of engineering components due to the fatigue is an important research area of fracture mechanics. Prediction of crack length versus number of loading cycles (fatigue life) or crack growth curves of vital engineering components is paramount importance in the damage tolerance design and structural integrity analyses. Due to the complex geometry, boundary conditions and loading, such predictions are to be made using the numerical methods such as finite element method etc. The Paris law is a popular and an established fatigue crack growth law for the mode I loading conditions. This law and its variants are extensively used for the prediction of the mode I fatigue life of engineering components. However, due to the same reasons such as the complex geometry, boundary conditions and loading, often, the cracks are subjected to the mixed mode loading conditions. An important issue that made understanding of the mixed mode fatigue phenomena is due to the non-self-similar crack growth i.e., crack grows in a curvilinear manner than in the direction of its axis. In 1974, Tanaka extended the mode I Paris law to the mixed mode (I/II) loading conditions and is termed as the modified Paris law. This law relates the mixed mode fatigue crack growth rate to the equivalent stress intensity factor (ΔK_{eq}) which is a function of the mode I and mode II stress intensity factors. Subsequently, due to the widespread use of the modified Paris law, a large number of various ΔK_{eq} models are appeared in the literature for the last 40 decades. Using these models, a large number of mixed mode (I/II) fatigue experiments are conducted to correlate the crack growth rate with the selected ΔK_{eq} model. Furthermore, numerous studies appeared on the numerical prediction of the mixed mode fatigue life of engineering components using the selected ΔK_{eq} models. To the knowledge of the author, no serious attempt till date is available for an exhaustive study on comparison of their performances while using with the modified Paris law for the prediction of the mixed mode fatigue life. Clearly, the analyst will be perplexed in assessing which of these models provide numerical predictions of the mixed mode fatigue lives close to the experimental data or on the conservative side. The works which provide a meaningful and substantiated answer to the above question are very scare. In view of the importance of fatigue fractures of engineering components, and frequent occurrence of the mixed mode (I/II) fatigue loading, in the present investigation an extensive study has been made to understand the nature of predictability of various ΔK_{eq} models in

numerical estimation of the mixed mode (I/II) fatigue life of the engineering components while using the modified Paris law.

In the present work, predictability of the equivalent stress intensity factor models is assessed with the help of experimental and finite element simulation data. For this purpose, mixed mode fatigue crack growth experiments are carried out using the widely used Compact Tension Shear specimen using Al 6061-T6 alloy and SS 316 for three different loading angles and fatigue crack growth life are obtained. The fatigue crack growth data contains significant scattering and comparison of the crack growth lives obtained from numerical simulation is difficult. In order to overcome this, a three parameter double exponential model for fitting the fatigue life data is proposed in this work. During the numerical estimation of the fatigue life, the fatigue crack path needs to be estimated at each step. The available displacement based techniques for the stress intensity factor determination was unable to estimate the sign of the mode II stress intensity factor and thus unable to estimate the fatigue crack path. A novel displacement based technique based on the crack flank opening and sliding displacements is also proposed in this work.

Numerical fatigue crack growth simulations are performed and mixed mode fatigue life are estimated using the specimen geometry and loading conditions used in the experiment. The predictability of the equivalent stress intensity factor models are assessed by comparing the estimated fatigue life with the experimental fatigue life and important conclusions are made. For definitive conclusions, three different error estimates are formulated in this work. The numerical simulation is also repeated using the experimental results published in the literature to further verify the predictability of the selected models. The results of the present work show that, the models proposed by Irwin is identified to be providing accurate estimates of the mixed mode (I/II) fatigue life. One of the models proposed by Tanaka is found to be providing accurate fatigue life prediction for lower mode mixity angles and the model introduced by Demir is accurate at higher mode mixity angles. The models proposed by Richard and Yan are offering conservative estimates of the mixed mode fatigue life.

LIST OF FIGURES

LIST OF TABLES

NOMENCLATURE

Latin characters

a	Crack length
a_0	Initial crack length
A_0, A_1	Coefficients of the Generalized Westergaard for opening mode
b, c	CTS specimen geometry parameters
C	Paris' constant
C_0, C_1	Coefficients of the Generalized Westergaard for shear mode
E	Young's modulus
G	Energy release rate
k	Double exponential model constant
K_{IC}	Plane strain fracture toughness
$K_{I,\max}$	Mode I stress intensity factor corresponding to the maximum load
$K_{I,\min}$	Mode I stress intensity factor corresponding to the minimum load
$K_{II,\max}$	Mode II stress intensity factor corresponding to the maximum load
$K_{II,\min}$	Mode II stress intensity factor corresponding to the minimum load
$K_{I,th}$	Mode I threshold stress intensity factor
$K_{II,th}$	Mode II threshold stress intensity factor
L_2	Euclidean norm
m	Paris' exponent
N	Number of loading cycles
p	Double exponential model exponents
P	Applied load
$P_1, P_2,$ and P_3	Punctual loads
$P_{\max}$	Maximum applied load
$P_{\min}$	Minimum applied load

q	Double exponential model exponents
r^2	Goodness of fit
R	Load ratio
u, v	Displacement in x and y directions, respectively
$x-y$	Cartesian coordinate system
x_i, y_i	Crack tip coordinates in i-th step

Greek alphabets

α	Loading angle
β	The ratio of mode I and mode I fracture toughness
Δa	Crack increment
ΔK_{eq}	Equivalent stress intensity factor range
$\Delta K_{eq-\max}$	Maximum equivalent stress intensity factor range
ΔK_I	Mode I stress intensity factor range
ΔK_{II}	Mode II stress intensity factor range
Δv	Crack opening displacement
Δu	Crack sliding displacement
θ	Polar coordinate component
θ_c	Crack propagation angle
θ_r	Angle the crack makes with x axis
κ	Kolosov's constant
υ	Poisson’s ratio
σ_u	Ultimate stress
σ_y	Yield stress
$\sigma_{\theta,c}$	Critical tangential (circumferential) stress
$\sigma_{\theta,\max}$	Maximum tangential (circumferential) stress
μ	Shear modulus

Abbreviations

COD	Crack opening displacement
CSD	Crack sliding displacement

CT	Compact tension
CTS	Compact tension shear
DET	Displacement extrapolation technique
EDM	Electrical discharge machining
FCG	Fatigue crack growth
FESEM	Field emission scanning electron microscopy
MTS	Maximum tangential stress
Q8	Eight noded quadrilateral
QPE	Quarter point element
RMS	Root mean square
SED	Strain energy density
SIF	Stress intensity factor
UTM	Universal testing machine

Chapter 1

Introduction

1.1 Fatigue failures

Fatigue crack growth is arguably the most important topic in fracture mechanics. The term fatigue refers to the gradual degradation of the strength and eventual failure of the component in the presence of cracks over a period of time under the cyclic loads much lower than the static strength of the component. Materials and the component design affect the development of cracks, and these factors can be taken into consideration to reduce the probability of occurrence of the fatigue cracks to an extent, but this possibility of failures cannot be avoided completely. Findlay and Harrison (2002) provide valuable statistics about the percentage of causes of failure that occur in engineering and aircraft components (Fig. 1.1). Accordingly, metallurgical studies and post-failure indicate that more than 50 percent of the structural failures are preceded by some period of crack growth, i.e., fatigue failures (Findlay and Harrison, 2002) as illustrated in Fig. 1.1.

The inherence of cracks and metallurgical defects in structural components are ineluctable. These defects act as stress raisers and develop an intense local stress field around them. Under cyclic loading conditions, cracks can either nucleate from these defects, or the existing crack can grow further, both of which in turn degrade the strength and reduce the residual life of the structural components. Generally, three stages can be identified in the entire fatigue failure period viz. (a) crack initiation stage, (b) crack propagation stage, and (c) final fracture stage. Once a crack is nucleated, it grows to the macroscopic crack size and, after that, propagates deep into the component at higher rates in a subcritical manner under the external cyclic loads, even if the loads/stresses are much below the static strength of the component. When the crack length reaches a critical size, i.e., during the final stage, an unstable fracture of the components occurs in which most of the cases in an insidious manner. Thus, the majority of the fatigue failures of the structural and engineering components leads to catastrophic

accidents without giving warning and are the result of crack initiation at the stress concentration zones. Among the three stages of the fatigue failure, the steady-state fatigue crack propagation period is a significant component in the overall lifetime of the structure. The number of loading cycles requires for the initiation of the crack depends significantly on the material microstructure and often varies. Also, the initiation of the microcrack does not considerably alter the residual strength and integrity of the structure. Thus the primary focus of the crack growth studies are on the steady-state crack growth stage.

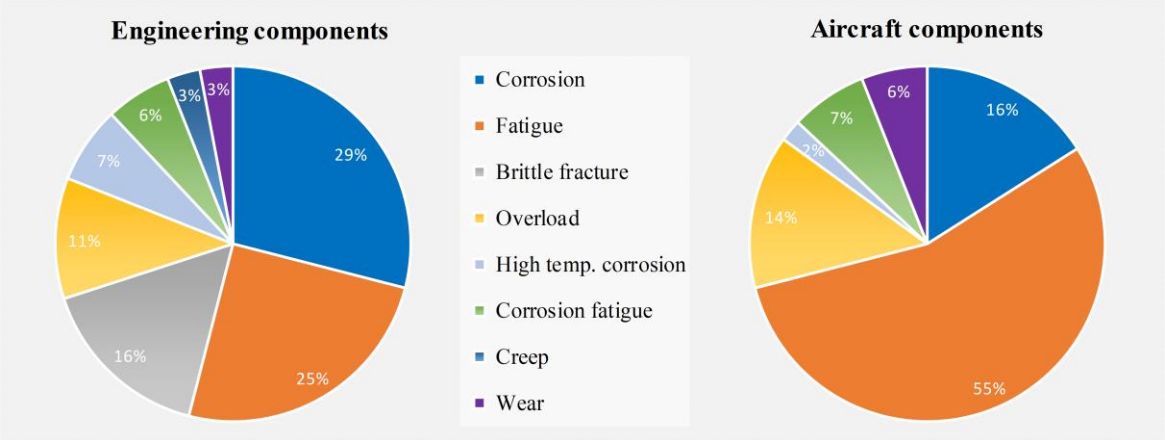

Figure 1.1 Summary of causes of failures of engineering and aircraft components (Findlay and Harrison, 2002)

Based on the number of load cycles at which a component fails, the fatigue failure can be broadly classified as (a) low cycle fatigue and (b) high cycle fatigue. In the engineering terms, if a component fails within 10^3 load cycles, then it is said to be failed under low cycle fatigue. On the other hand, if a component survives for a large number of cycles greater than 10^3 cycles, then it is said to be failed due to the high cycle fatigue. The majority of the engineering and structural components fail due to the high cycle fatigue, which involves elastic deformation during the subcritical crack growth. Consequently, fractures are brittle in the engineering sense, and the present work mainly pertains to the aspects of high cycle fatigue failures.

1.2 A brief historical background of fatigue

The first study on fatigue failure was believed to be in 1829 by Albert using mine-hoist chains made of cast iron (Albert, 1838). The increased use of ferrous metals expanded the interest in fatigue studies. The first detailed study of fatigue was carried out in 1843 following

a railway accident by Rankine (1843), who identified the characteristics of fatigue fracture and the dangerous effect of stress concentrations. Braithwaite first introduced the term fatigue in 1854 (Braithwaite, 1854) for cracking of the components under repeated loading. During the period 1852-1869, Wohler (1860) conducted systematic studies about the fatigue strength of railway axles using bending, torsion, and axial loads. He characterized the fatigue behavior of materials in terms of the stress-cycles $(S-N)$ curves and introduced the concept of endurance limit. Gerber in 1874 and Goodman in 1899 calculated the allowable maximum stress levels and developed methods for fatigue life calculations at different mean stress levels (Schütz, 1996).

Another noticeable contribution in this field is the Bauschinger effect (Bauschinger, 1886), which discussed the difference in the elastic limit of metals under cyclic loading as compared to the monotonic loading. This theory laid the foundation for understanding the low cycle fatigue behavior and the damage accumulation theories. At the beginning of the 20th century, the fatigue mechanisms are explained with the help of crystallization theory and introduced the slip bands by Ewing, Rosenhain, and Humfrey (Ewing and Rosenhain, 1900; Rosenhain and Humfrey, 1910). In their studies, the progression of slip band intrusions and extrusions lead to the formation of cracks.

Based on stress analysis by Inglis (1913) and the energy methods by Griffith (1921), the physical phenomena of crack growth were described, and a theoretical framework for the propagation of cracks in brittle solids was proposed. In 1957, George Irwin extended the work of Griffith (1921) to include ductile materials, such as metals, which have led to the development of the subject, linear elastic fracture mechanics (LEFM) (Irwin, 1957). Irwin represented the amplitude of the stress field ahead of the crack tip using the stress intensity factor (SIF) (Irwin, 1957). With the introduction of SIF and linear elastic fracture mechanics, many attempts have been made to characterize the fatigue crack propagation in terms of the SIFs. The pioneering work of Griffith and Irwin was fulfilled in 1961 when Paris (1961) developed the fatigue crack growth law, which bears his name for mode I loading conditions. They developed a correlation for the fatigue crack growth rate as a function of the stress intensity factor range (ΔK). This discovery revolutionized the field of fatigue research and analysis because it allowed engineers to analyze and predict the crack growth behaviour with the knowledge of material geometry and the far-field stresses. On the other hand, in 1974,

Tanaka (1974) proposed a modified form of the Paris law for components subjected to mixed mode (I/II) loading, which is now widely in use for fatigue life prediction.

1.3 Design against fatigue failure

Design against fatigue failure is one of the predominant research areas in solid mechanics, and there are various approaches in use for this. As mentioned previously, depending on the processes involved in fatigue crack growth, the whole period of crack growth until the final fracture can be divided into two: crack initiation period and crack growth or propagation period (Fig. 1.2). The stress concentration factor (K_t) is used for characterizing the crack initiation, whereas for characterizing the fatigue crack growth period, the stress intensity factor (K) is used under small scale yielding conditions.

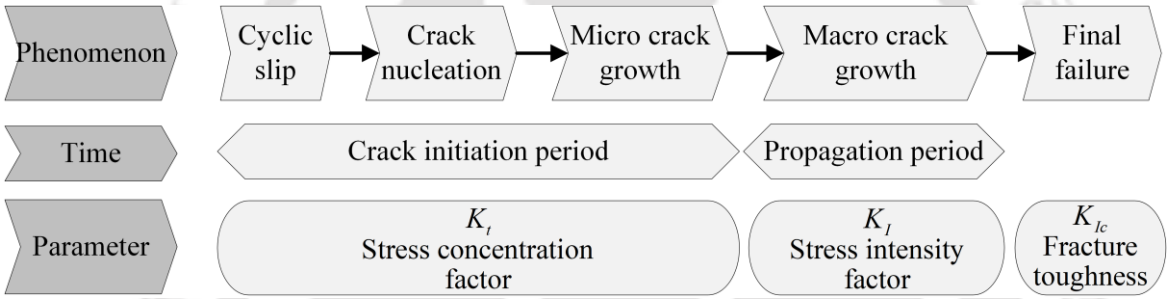

Figure 1.2 Different stages of the fatigue crack growth and relevant factors (Schijve, 2009)

1.3.1 Different approaches in design against fatigue failure

The fatigue design philosophies can be broadly divided into two approaches, the total life approach and the fracture mechanics approach. The main distinctions between design philosophies depend on the quantitative treatment of crack initiation and fatigue crack growth phases (Suresh, 1998). The different philosophies of fatigue design provide various guidelines for the design and maintenance of the components for improved fatigue resistance. The differences in guidelines are a result of the varying degrees to which the role of crack initiation and crack growth are incorporated in the calculation of the useful fatigue life (Suresh, 1998).

1.3.1.1 Total life approach to fatigue design

The total life fatigue design approach considers the total cyclic life to failure and characterizes in terms of cyclic stress range ($S-N$ curve approach) or strain range ($\varepsilon-N$ curve approach). In this classical approach, the total number of stress cycles, or strain cycles

required to generate a crack and to subsequent failure is estimated under controlled loads or displacements in the laboratory environment. Various methods are developed to include the effect of the mean stress, stress concentrations, environmental factors, variable multiaxial loads in conjunction with the stress-based and strain-based approaches. Classical approaches discussed above are widely used for the designing of engineering components where the crack initiation life constitutes a major portion of the total fatigue life. The classical approaches, in general, represent design against fatigue crack initiation (Suresh, 1998).

1.3.1.2 Fracture mechanics based approach to fatigue design

The fracture mechanics approach in fatigue design follows damage tolerant design philosophy. The basic underlying idea of this approach is that it assumes that all critical engineering components inherently contain defects/cracks before the service loads start acting on them. Further, this approach permits the use of components under service loads even if they contain sub-critical cracks. In such cases, the fatigue life or simply life of a component is defined as the number of loading cycles required for the crack growth from its initial size to the critical size as the number of load cycles consumed in the final fracture stage is negligible. In this approach, the fatigue life is predicted using the principles of fracture mechanics. For complex configurations and loading conditions, numerical methods are usually employed for the prediction of fatigue life. Life is predicted based on the linear-elastic fracture mechanics (LEFM) based analysis or the elastic-plastic fracture mechanics (EPFM) based analysis. The use of LEFM is valid under small scale yielding (SSY) conditions, i.e., long cracks subjected to relatively low stresses, which is generally the case under high cycle fatigue. Based on this approach, crack growth laws are generally formulated in terms of the SIF as it is the most important parameter in the LEFM. Thus, under SSY conditions, Paris' law (Paris et al., 1961) is widely employed for the fatigue life prediction of engineering components under opening mode or mode I loading conditions. For general in-plane loading, a modified form of the Paris' law proposed by Tanaka (1974) is widely used for the mixed-mode (I/II) fatigue life prediction. Various modifications of Paris' law are also available to incorporate the effects of stress ratio, mean stress, overload effect etc. (Chowdhury and Sehitoglu, 2016; Rozumek, 2014).

1.3.2 Damage tolerance and inspection interval

In damage tolerant design, as the name suggests, the critical structural and engineering components may be safely operated even in the presence of cracks, which may eventually grow

in service up to a permissible value before the withdrawal of the component from service. Thus, this design philosophy starts at the design level of the component and continues until the withdrawal of the component from the service. It heavily depends on non-destructive testing (NDT) techniques. Based on the design considerations, the damage tolerance philosophy permits the growth of the crack to a limiting value, which is below the critical crack length. Damage tolerance philosophy necessitates the identification of the size of the existing crack or flaw and the prediction of the remaining fatigue cycles required for the crack to grow to the limiting crack length. This philosophy is based on characterizing the growth of cracks as a function of in-service loads, and periodic inspections ensuring that undetected damage will not become critical before the next inspection.

For inspection of the structural components to measure the probable size of the crack, NDT techniques are widely used. The expensive NDT can evaluate even small values of the crack length and thus leads to a longer inspection interval. On the other hand, inexpensive NDT is associated with the large values of minimum detectable crack size and thus shorter inspection intervals. This is schematically illustrated in Fig. 1.3.

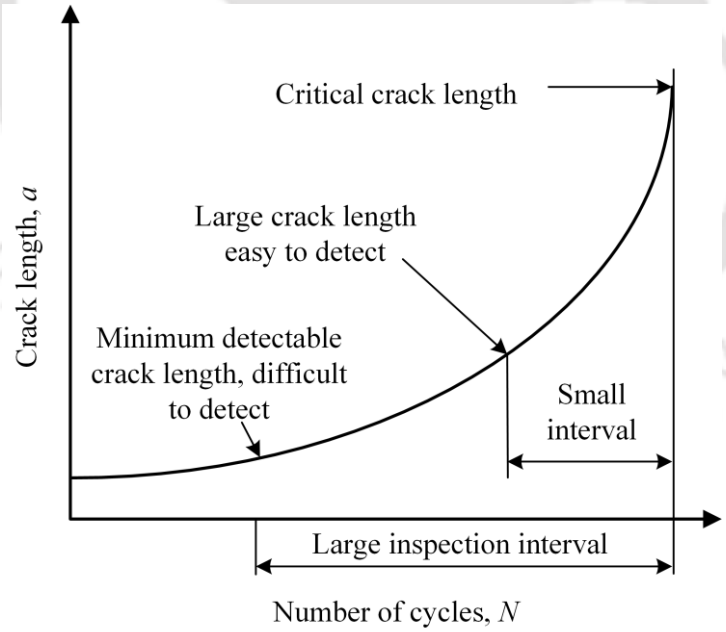

Figure 1.3 Illustration of inspection interval using the crack length versus the number of cycles (Tavares and de Castro, 2017)

This indicates that a trade-off between the inspection interval and the cost is required. Also, the probability of detection of a crack using NDT techniques are more for the longer cracks as compared to shorter cracks.

For the adoption of fracture control measures such as replacement and repair of the structures and components, the inspection interval must follow the crack growth time calculated in the damage tolerance analysis (Broek, 1989). The following Fig. 1.4 illustrates the processes of deciding the inspection interval.

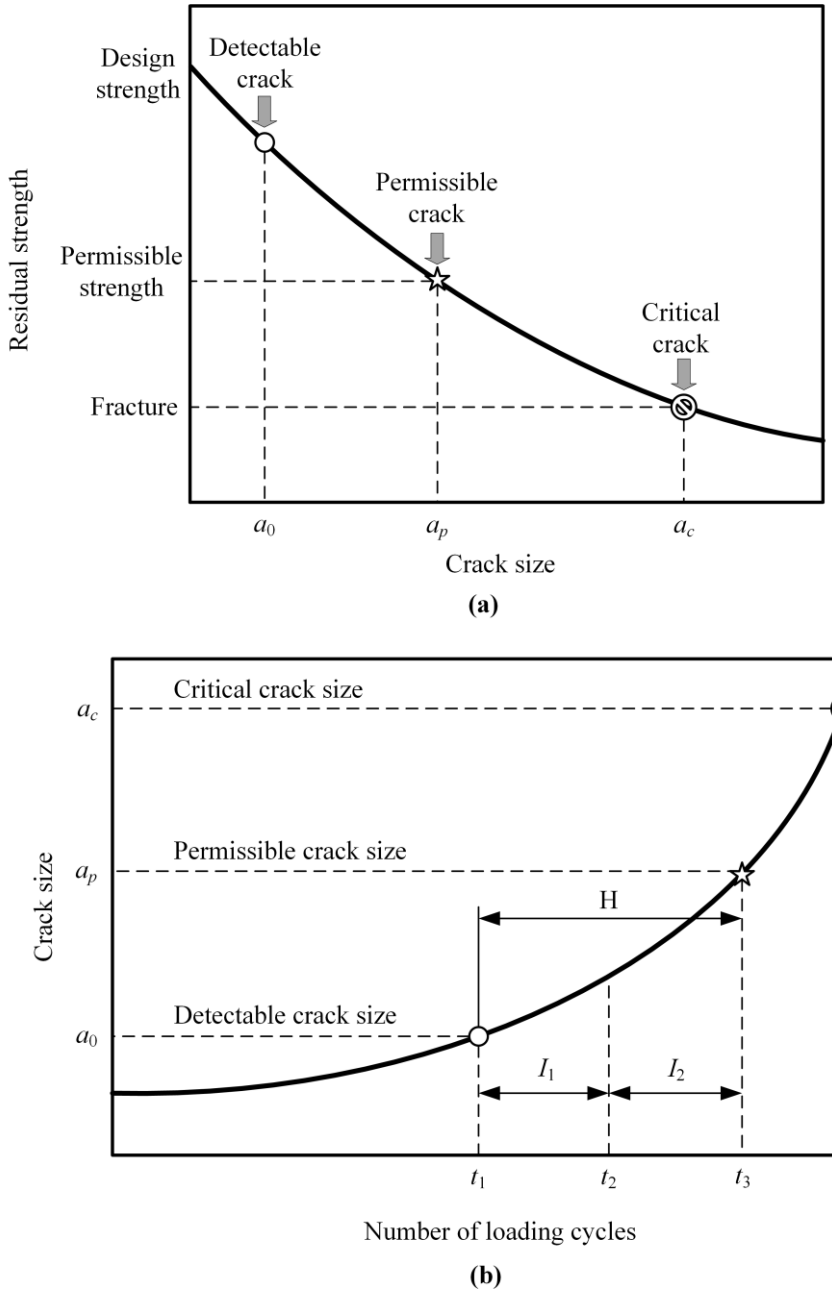

Figure 1.4 Principle of damage tolerance (a) residual strength diagram, and (b) crack growth curve (Broek, 1991)

Before the beginning of the service, the structure is inspected for the possible flaws and defects. If no flaws are detected, the size of the minimum detectable flaw using the NDT

techniques are taken as the initial crack size a_0 (Fig. 1.4) (Anderson, 2005; Broek, 1991). The fatigue crack growth life prediction and the inspection interval is based on this initial crack size a_0. The fatigue crack growth cycles for the crack to grow from initial crack size a_0 to the allowable crack size a_p, H, can be estimated. The first inspection interval, I_1, should be less than the loading cycles (H) required for the crack to grow from a_0 to a_t. A general thumb rule is to consider the first inspection interval I_1 equals to $H/2$ (Broek, 1989).

As discussed earlier, the damage tolerance analysis is a combination of the non-destructive inspections, and fracture mechanics and fatigue crack growth principles (to simulate and predict the fatigue life). The purpose of the NDT techniques is the timely detection of the crack, and the probability of the detection of the crack is less than 100 percent, and it depends on the crack size and the inspection technique used. An option to overcome the issue with the probability of detection is to shorten the inspection intervals since the more number of inspections will increase the probability of detection of the crack in due time (Zerbst et al., 2011; Zerbst and Beretta, 2011). Choosing a short enough inspection interval guarantee the cumulative probability of the detection of cracks prior to failure (Zerbst and Beretta, 2011). Even though the crack remains undetectable in the initial inspections, the probability of detection is higher in the subsequent inspections due to the increase in crack size between inspection.

It can be noticed from the above discussion that, prediction of crack length versus the number of loading cycles, i.e., fatigue crack growth curves of real engineering components are needed for the proper estimation of the inspection intervals (Fig.1.3 (b)). The experimental determination of such curves are limited only to simple benchmark specimens and for complex geometries, loading and boundary conditions (which is usually the case in the practical components) it is necessary to recourse to the numerical estimation of the fatigue crack growth curves. Various numerical techniques such as finite element method (FEM) and boundary element method (BEM) are in use for the above purpose. The numerical fatigue crack growth and life estimation tools perform the analysis using the actual component geometry and estimate the fatigue life (or the fatigue crack length) with the help of material dependent constants, fracture mechanics parameters, and a suitable crack growth law.

1.4 Mixed mode (I/II) fatigue

Fracture mechanics is the discipline, which deals with the study of the propagation of cracks in materials. The alteration in the loading direction with the crack leads to alteration of the singular stress fields around the crack and changes the modes of failure. As shown in Fig. 1.5, there are three general cases of load application leading to crack propagation. When the loading direction is normal to the crack plane, the opening mode or mode I condition prevails. When the loading direction is parallel to the crack plane, sliding mode (mode II) and the shearing mode (mode III) exists. Mode II causes kinking of the crack, whereas mode III causes crack front twisting. A combination of two or all of the aforementioned modes leads to the mixed mode case of loading. Under pure mode I loading, the fatigue crack grows in a self-similar manner (i.e., in the direction of the axis of the crack) whereas pure mode II loading causes non-self-similar fatigue crack growth. Mixed mode fatigue loading (superposition of modes I, II and/or III) create special crack surfaces (Fig. 1. 6), which can often be observed in practical cases (Richard et al., 2005).

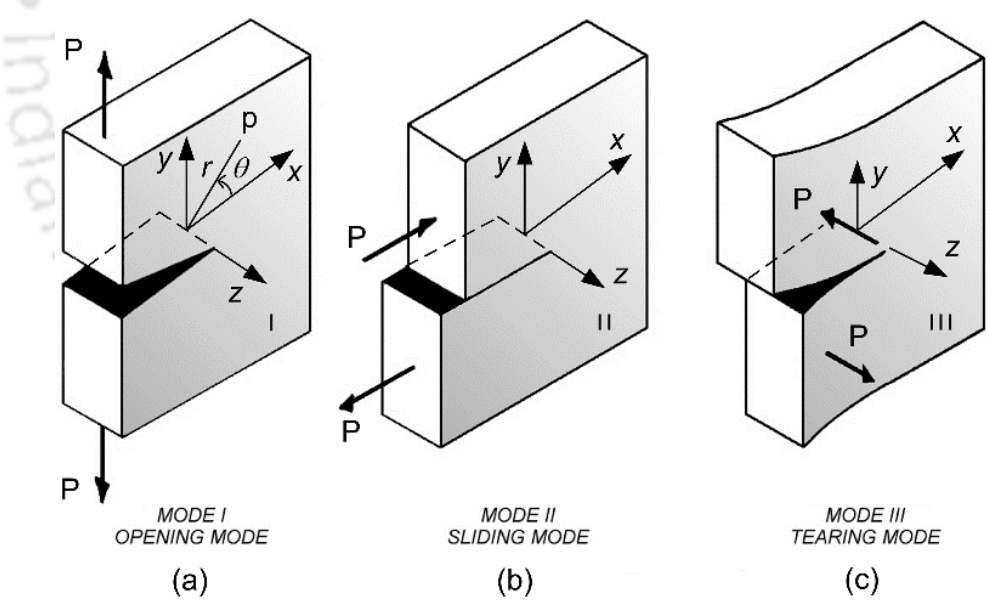

Figure 1.5 Three different modes of loading of a crack

Mixed mode fatigue crack growth (as is shown in Fig. 1.6) occurs when the applied cyclic load makes an angle with the crack axis. Due to complexities in geometries, complex loading, and boundary conditions, engineering components are often subjected to mixed mode cyclic loads. Many times damages arise due to the fact that the mechanism of fatigue crack growth is still not completely understood, particularly the cracks under mixed mode loading. The non-

symmetrical singular stress field exists at the crack front in case of mixed mode loading. Consequently, in addition to mode I SIF, mode II and/or mode III SIFs are also required to define the stress field around the crack tip (Richard et al., 2005).

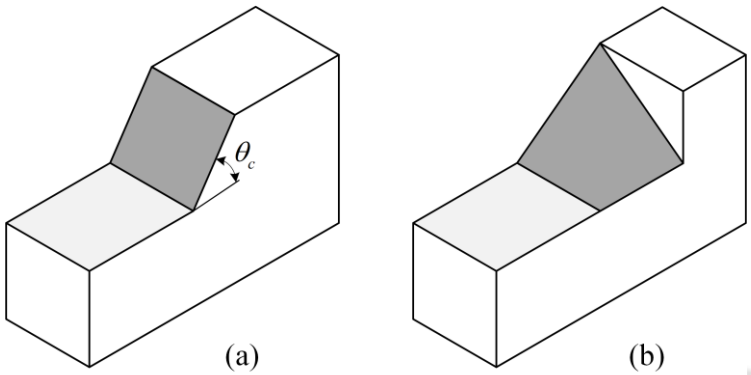

Figure 1.6 Typical mixed mode fracture surfaces under different loading conditions (a) mixed mode (I/II), (b) mixed mode (I/II/III)

Plane mixed-mode problem is the superposition of mode I and mode II, as shown in Fig. 1.5. When the LEFM conditions prevail (i.e., the size of the plastic zone is small compared to the crack length and other physical dimensions of the component), the corresponding SIFs K_I and K_{II} can be used to characterize the crack tip stress field (Richard et al., 2005). Under mixed mode (I/II) loading (Fig. 1.6 (a)), the crack deviates from the initial crack plane (grow in a non-self-similar manner), and thus the direction of the crack growth is also needed to be taken into consideration for the understanding of the mixed mode (I/II) fatigue crack growth. Thus the application of the damage tolerance design approach to the critical engineering component subjected to mixed mode (I/II) loading conditions require

1. Numerical prediction of mixed mode SIFs
2. Numerical prediction of the fatigue crack growth direction and,
3. Numerical prediction of mixed mode fatigue crack growth curve, ie, $a-N$ curve

are needed for the successful implementation of this philosophy.

1.5 Current status of fatigue life estimation

Paris' law (Paris et al., 1961) received wide attention for mode I fatigue crack growth studies and standardized test practice, ASTM E647-15e1 is available based on this law. Tanaka (1974) extended the Paris' law to the mixed-mode (I/II) loading and used an equivalent stress

intensity factor (ΔK_{eq}) based on the dislocation theory (Lardner, 1968; Weertman, 1966) to correlate with the fatigue crack growth rate. ΔK_{eq} is a function of both the mode I and mode II stress intensity factors K_I and K_{II}, respectively. Subsequently, a large number of ΔK_{eq} models have been proposed by the researchers for the last four decades to work with the modified form of the Paris law proposed by Tanaka. Some of these proposed ΔK_{eq} models are based on extension of the static fracture theories to the mixed mode (I/II) fatigue (Hussain et al., 1974; Irwin, 1957; Yan et al., 1992) while some others are the empirical models (Demir et al., 2018; Richard et al., 2003). These ΔK_{eq} models correlates the mode I and mode II stress intensity factors with or without considering the crack growth angles. All models assign a weightage of 1 (one) to the mode I SIF, whilst mode II SIF weightage varies across the models.

Currently, these ΔK_{eq} models are used along with the modified Paris' law to (a) understand the mixed mode fatigue crack growth phenomenon by conducting experiments and (b) compute or estimate the fatigue life of engineering components under mixed mode (I/II) loading conditions using numerical methods. Apart from the modified Paris' law, different other laws are also available for understanding the mixed mode fatigue crack growth phenomenon. A review of these laws can be found in Ref. (Qian and Fatemi, 1996a; Rozumek, 2014; Rozumek and Macha, 2009). Amongst these laws, the modified Paris' law proposed by Tanaka (Qand Fatemi, 1996b; Rozumek *et al., 2018; Ma et al., 2006; Biner, 2001; Demir et al.*, 2018) is widely used.

1.6 Motivation

Threat from the fatigue crack growth span over a wide spectrum of industries such as structural, aeronautical, naval, automotive, and locomotive etc. This problem continuously causes catastrophic failures of structural components. Thus, the designing of structures and components against fatigue damage and eventual failure persist as a crucial challenge even to date. Damage tolerance design philosophy is found to be extremely useful for safeguard against the fatigue failures of most critical components of the above engineering structures. It necessitates periodic inspection of the structural/engineering components to monitor the crack growth. These inspection intervals are decided based on the fatigue life prediction using numerical simulation methods.

Mixed mode (I/II) loading is often experienced by the engineering and structural components due to complex geometries, loading, and boundary conditions. Unlike mode I loading, no standardized test procedures are currently available for mixed mode (I/II) loading situations. Amongst various available mixed mode (I/II) fatigue crack growth laws, the modified Paris' law based on the equivalent SIF is widely employed for numerical predictions of engineering components. As has been stated earlier a large number of various equivalent SIF models are developed for the last four decades, and some of them are used for the numerical fatigue life prediction. To the knowledge of the author, the experimental and numerical examination of the effect of these different available ΔK_{eq} models on the predicted life are extremely scarce. In other words, no work is available to date on the comparison of these models to study the nature of predictability of the fatigue life or fatigue crack growth curves of engineering components. Further, when a new model was developed, no effort was also made on verification of the performance of the existing models available until that time. Due to the lack of information on the nature of the predictability capacity of the various ΔK_{eq} models, a question arises "*Which of these available model(s) predict fatigue life or provide the fatigue crack growth curves using the numerical methods close to the experimental results or provide conservative estimates*? No serious attempts are available to provide the answer to the above basic question for the last four decades. Because of the lack of answers to this question, the analysts would clearly be perplexed in the selection of the appropriate model for the prediction of mixed mode fatigue life using numerical methods. Further life predictions made without the knowledge about the capabilities of various ΔK_{eq} models do not provide useful data. Therefore, it is obligatory that these models need to be examined (in a common experimental program) to understand whether they offer nearly accurate or conservative predictions compared to the experimental life data. The availability of such knowledge is of great help for the engineers and designers in structural integrity and damage tolerance assessments.

Therefore, considering the nature and consequences of the mixed mode (I/II) fatigue fractures and considering importance of application of the modified Paris' law to safeguard the critical engineering components against the fatigue failures, the requirement of an attempt for a reasonable answer to the above question forms the motivation to the present investigation.

1.7 Thesis outline

The outline of the chapters for the remainder of the thesis is as follows.

In chapter 2, presents a detailed literature review. Various equivalent stress intensity factor models, their development and use over the years are also discussed in detail in this chapter. Various methods that predict the crack growth angle and various mixed mode fatigue specimens are also discussed.

Chapter 3 presents the necessary theoretical background for the understanding of the present work, which includes computation of the mixed mode fatigue life and fatigue crack growth path. A brief numerical formulation of various elements employed in the present investigation are also presented in this chapter.

In chapter 4, the theoretical formulation and the validation of the proposed stress intensity factor estimation technique are presented.

Chapter 5 describes the proposed three parameter double exponential model for best-fit of the experimental fatigue crack growth raw data. The comparison of the present curve fitting approach with the existing ones is also demonstrated in this chapter.

Chapter 6 describes the details and procedures of all the experiments carried out in the present study. Various aspects such as specimen geometry, loading fixture preparation, experimental procedures, tensile testing, Paris' constants determination from the mode I fatigue tests, mixed mode fatigue tests, and crack growth measurement approach are discussed.

In chapter 7, results of the mixed mode (I/II) experimental fatigue life and finite element prediction of the fatigue life of Al 6061-T6 alloy using the selected ΔK_{eq} models are compared with the help of error analysis.

In chapter 8, results of the mixed mode (I/II) experimental fatigue life and finite element prediction of the fatigue life of SS 316 using the selected ΔK_{eq} models are compared with the help of error analysis.

Chapter 9 discusses the predictability of the selected ΔK_{eq} models by conducting the finite simulation of the fatigue crack growth of the published specimens having available fatigue crack growth data in the literature.

In chapter 10, the summary of the present work, and important conclusions drawn from the present investigation are discussed. The future directions in this field are also listed in this chapter.

Chapter 2

Literature review

LEFM based models are useful tools for the accurate assessment of potency of the crack in engineering structures under small scale yielding (SSY) conditions. Stress intensity factor (K) is the most widely used LEFM parameter for the fracture analysis and fatigue crack growth (FCG) studies. The Paris' law (Paris et al., 1961) is the most widely used law for FCG studies in mode I loading conditions due to its simplicity and accuracy in the prediction of the FCG rate and life. The apparent simplicity in applying such laws makes them widely applicable in the context of engineering design practices (Chowdhury and Sehitoglu, 2016). The widespread usage of the Paris' law to a wide spectrum of materials has essentially formed the basis for further research to rationalize the observed power-law dependence of the fatigue crack growth to more complicated loading conditions.

Ever since the success of the FCG rate correlation to the SIF by the Paris' law (Paris et al., 1961), several investigations are carried out utilizing the various field variables around the crack tip to quantify the FCG rate. Most of such investigations under cyclic loading are limited to the crack growth under opening mode or mode I. However, in practice, due to the random orientation of the crack with the loading direction or due to the external constraints, the cracks are often subjected to mixed mode (I/II) loading. The effect of individual mode SIFs needs to be considered in the mixed mode loading conditions. Several crack growth models or laws are developed to quantify and describe the FCG under mixed mode (I/II) loading. One of the notable contributions is the modified Paris' law in terms of equivalent stress intensity factor (ΔK_{eq}) proposed by Tanaka (1974). Essentially, ΔK_{eq} is defined as a function of the individual mode SIFs. Other models available for mixed mode FCG studies are crack closure model (Newman, 2009, 1984), Chen and Keer model (Chen and Keer, 1991), strain energy density model (Erdogan and Sih, 1963; Patel and Pandey, 1981; Sih and Barthelemy, 1980), *J*-integral model (Chow and Lu, 1991; Hoshide and Socie, 1987; Srivastava and Garg, 1988), equivalent strain intensity factor model (Fatemi and Socie, 1988; Reddy and Fatemi, 1992; Socie et al.,

1987) and Gao's model (Hua et al., 1985). Among the above FCG models, the modified Paris' law defined in terms of ΔK_{eq} is the most widely used approach for FCG rate correlation and fatigue life prediction using numerical methods under SSY conditions.

Load ratio or stress ratio (R) is another factor, which influences the mixed mode FCG rate. In case of mode I fatigue loading, it is well known that as the stress ration R is increased, the crack growth rate (without changing the slope of the sigmoidal curve) is also increased and vice versa. The most widely used models which incorporate the R in case of mode I loading are Walker model (Walker, 1970), Forman model (Forman et al., 1967) and NASGRO model (Forman and Mettu, 1990). However, the effect of load ratio on the FCG rate is a complicated phenomenon (Zheng and Powell, 1999) and depends on the factors such as material (Allen et al., 1988), specimen geometry (Dover and Boutle, 1978), sign (whether positive or negative) and the range of stress ratio (Musuva and Radon, 1979). A detailed discussion on the above models for mode I loading conditions can be found in Refs. (Pook and Frost, 1973; Rozumek and Macha, 2009; Schijve, 2003). As far as mixed mode FCG is concerned, very limited works have been reported on study of effect of the R on the crack growth rate and this aspect needs further extensive investigations.

Another important aspect of cracks under the mixed mode loading is non-self-similar growth of the cracks, i.e., they grow at an angle to their initial crack orientation. Therefore, under such loading conditions, not only the crack growth rate but also the crack growth direction (crack path) is also important. Several criteria are available for the prediction of fatigue crack growth direction. Some of them are the maximum tangential stress criterion (MTS) (Erdogan and Sih, 1963), the minimum strain energy density theory (SED) (Sih, 1974), the maximum tangential principal stress theory (MTPS) (Maiti and Smith, 1983a), the maximum energy release rate criterion (MERR) (Hussain et al., 1974), the apparent crack extension force criterion (CEF) (Strifors, 1974), the maximum dilatational strain energy criterion (T-criterion) (Theocaris and Andrianopoulos, 1982) and the modified MTS criteria (Khan and Khraisheh, 2000). Among the aforesaid criteria, the MTS criterion and the SED criterion are widely employed for the mixed mode (I/II) fatigue crack path prediction (Qian and Fatemi, 1996a; Rozumek and Macha, 2009) in numerical simulation studies.

2.1 Review of development of various ΔK_{eq} models

Due to its simple form, dependency on the SIFs and widespread use of the Paris' law in pure mode I loading, the modified Paris' law proposed by Tanaka (1974) in terms of ΔK_{eq} has been widely referred in the mixed mode (I/II) fatigue crack growth studies. The modified Paris' law for the mixed mode (I/II) fatigue loading is given as

$$da/dN = C\left(\Delta K_{eq}\right)^{m} \tag{2.1}$$

where da/dN is the FCG rate, C and m are Paris constants: ΔK_{eq} is the equivalent SIF which is functions of SIFs K_I and K_{II}.

As a consequence of its popularity, a large number of various ΔK_{eq} models have been proposed for the last four decades to use with the modified Paris' law. Various criteria have been considered in the development of ΔK_{eq} models, which finally leads to assigning different weights to the individual mode SIFs to estimate the ΔK_{eq}. Some of these models are based on the dislocation based crack initiation theory, some are based on the static fracture theories under mixed mode (I/II) loading whilst other models are empirically formulated. A review of the development of various available ΔK_{eq} models are presented in this section after the review of early experimental studies on mixed mode (I/II) fatigue fractures.

The first experimental study on the mixed mode (I/II) fatigue crack growth was carried out by Iida and Kobayashi (1969) in 1969. They conducted experiments using a center cracked plate made of Al 7075-T6 alloy for the loading angles 0°, 30°, and 45°. The stress intensity factors were estimated using numerical methods. The crack growth rates were obtained from the experimental data, and plotted against the mode I stress intensity factor. During mixed mode loading, they observed that the crack changes the direction normal to the applied load, and mode II SIF decreases to a much lower value. The comparison of the crack growth rates under mode I and mixed mode (I/II) loading indicated that the crack growth rate was increased in the presence of the mode II stress intensity factor. Similar experiments were also performed by Robert and Kibler (1971) and observed that the crack growth rate was accelerated in the presence of mode II SIF. These tests indicated that a new parameter incorporating the effect of both the modes I and mode II SIFs are required for the fatigue crack correlation under mixed mode (I/II) loading conditions.

Historically, another important work on experimental mixed mode (I/II) fatigue crack growth studies were carried out by Pustejovski (1979a). He performed experiments using a center cracked titanium plate (Ti-6Al-4V) for two different loading angles viz, 30°, and 45°. The change in crack growth rate with the loading angle was discussed in this study. It was observed that the crack growth rate differed at the tips. In another work, Pustejovski (1979b) also discussed the numerical simulation of the fatigue crack growth using the dislocation superposition technique. In both of these works, Pustejovski did not attempt to propose any ΔK_{eq} model.

In 1983, Richards and Benitz (1983) introduced the compact tension shear (CTS) specimen along with a special loading device for introducing the mixed mode (I/II) loading easily at the crack tip using the uniaxial tensile testing machines. Here, the specimen is rotated relative to the loading axis so as to produce the mixed mode loading. Due to which the specimen can be fabricated with relatively less complications. This specimen setup laid the foundations of acceleration in mixed mode (I/II) experimental and numerical FCG studies.

Srinivas and Vasudevan (1993a, 1993b) conducted a series of mixed mode (I/II) experiments using the CTS specimen made of an Al alloy for five loading angles and three loading ratios. They observed that the load ratio did not influence the crack initiation angle. They identified that fatigue life was higher for the higher load ratio. They also observed that the crack growth rate was less at a higher load ratio even though the mean stress was high. In another study (1993c), they observed the effect of mode I overload on mixed mode (I/II) FCG rate. The influence of mode II SIF on the FCG rate was studied and found the necessity of inclusion of the mode II SIF while evaluating the crack growth rate.

Coming to the development of various ΔK_{eq} models, Tanaka (1974) was the first to propose the modified Paris' law for the mixed mode (I/II) loading in terms of the equivalent stress intensity factor ΔK_{eq} as an extension of the mode I Paris' law. He performed the mixed mode (I/II) fatigue crack growth experiments for loading angles 0°, 18°, 45°, and 60° using a center cracked specimen made of aluminum for the verification of the proposed law. The ΔK_{eq} term is a function of both mode I and mode II SIFs to include the effect of individual modes of loading. Tanaka originally suggested two forms of ΔK_{eq} models, and these were formulated using the dislocation based microscopic FCG models suggested by Weertman (1966) and Lardner (1968). Tanaka verified the proposed ΔK_{eq} models experimentally for the FCG rate

correlation and found that the ΔK_{eq} model proposed based on the Weertman's dislocation theory correlates well with the experimental data as compared with the model based on Lardner's theory. Further, Tanaka noticed that the fatigue crack grows in a direction roughly perpendicular to the applied load direction when the applied tensile load exceeds the threshold value.

Hussain et al.'s model (Hussain et al., 1974) was initially developed for the static mixed mode fracture and later suggested to use this model for the fatigue crack growth studies. They used a path independent integral and the complex variable mapping function to obtain the energy release rate for the cracks subjected to mixed mode (I/II) loading. They determined the crack growth direction from the maximum energy release rate and observed an excellent agreement between theory and experimental results. In this model, the energy release rate was expressed as functions of mode I and mode II SIFs and the crack deflection angle. Miranda et al. (2007) suggested the possibility of using the ΔK_{eq} model for use in the modified Paris' law. To the author's knowledge, this model has not been employed to date in any mixed mode fatigue crack growth studies.

Richard et al. (1991) developed a generalized fracture criterion and a ΔK_{eq} model for the mixed mode loading, which was comparable to the equivalent stress in the classical stress hypothesis (Broszeit et al., 1986). In this model, the weight of ΔK_I is 1, and that of ΔK_{II} is 1.155. These weights were obtained from the classical stress hypothesis. Later, Richard et al. (2003) performed experiments for the verification of their model and compared the fracture limit curves predicted with the available criteria.

Yan et al. (1992) extended the maximum tangential stress criterion proposed by Erdogan and Sih (1963) to the case of cyclic loading to predict the crack growth behavior under mixed mode (I/II) loading and proposed a new ΔK_{eq} model derived from this criterion. Similar to the Hussain et al.'s model, Yan et al.'s model also expressed ΔK_{eq} as a function of the mixed mode (I/II) SIFs and the crack propagation angle. They performed boundary element based numerical fatigue crack growth simulations using the proposed model on an inclined center cracked plate loaded biaxially.

Biner (2001) employed a ΔK_{eq} model based on the energy release rate principle proposed by Irwin (1957). Irwin (1957) introduced the concept of the energy release rate, which is the

energy required for the unit extension of the crack and defined it as a fracture parameter. Using the relation between the energy release rate and the stress intensity factors, a ΔK_{eq} model was proposed by assigning equal weight to individual mode stress intensity factors. Biner (2001) employed this model for the correlation of the fatigue crack growth data obtained using the CTS specimens made of AISI 304 stainless steel for the loading angles 0°, 30°, 45°, and 75°.

Forth et al. (2002) proposed the same ΔK_{eq} model that was proposed by Biner (2001) using Irwin's energy release rate. However, no experimental or numerical simulations are available in their study using the proposed model.

Using a unified model of Lo et al. (1996), Tamilselvan et al. (2005) proposed a new ΔK_{eq} model for the mixed mode (I/II) fatigue crack growth studies. In this ΔK_{eq} model, a weight of 1 was assigned to ΔK_I, whilst, the ΔK_{II} weight was expressed as the ratio of mode I and mode II fracture toughnesses and thus, requires fracture toughness values apriori. They employed the proposed ΔK_{eq} model for the FCG rate correlation of the mixed mode (I/II) experimental data. Although the authors discussed some of the available ΔK_{eq} models, no comparison with the existing ΔK_{eq} models was made in their work.

Recently, Demir et al. (2018) proposed another empirical model for ΔK_{eq} using a nonlinear regression analysis of numerical and experimental results of the CTS specimen. For the development of the model, they (Demir et al., 2018, 2017) performed experiments and FE based numerical studies using a CTS specimen made of Al 7075-T661 alloy. It was claimed that the proposed model is useful at higher load mixity levels, and its usefulness was demonstrated using a new T-type mixed mode specimen. A limited comparison between their proposed model and some available ΔK_{eq} models was made in the mixed mode (I/II) fatigue life prediction. To the best of author's knowledge, this is the first work devoted to comparing some of the available ΔK_{eq} models for predictability of the mixed mode fatigue life. However, their findings did not provide any definitive conclusions regarding the predictability of the selected ΔK_{eq} models.

2.2 Review of application of the available ΔK_{eq} models

Many researchers employed the developed ΔK_{eq} models (discussed in section 2.1) in various mixed mode FCG studies. The ΔK_{eq} models have been employed primarily for (a) FCG rate correlation studies, i.e., to see whether a linear relationship exists between ΔK_{eq} and the rate of crack growth da/dN and (b) numerical prediction of the mixed mode (I/II) fatigue life of various specimens and comparison with the experimental data. This section is devoted to reviewing works that have employed various ΔK_{eq} models in mixed mode studies.

Ingraffea et al. (1983) performed the boundary element simulation of the mixed mode (I/II) fatigue crack growth of the center cracked specimen employed by Pustejovski (1979a). They used the MTS criterion for the prediction of the crack path and one of the two Tanaka's ΔK_{eq} models for the fatigue life prediction. A reasonable agreement between the experimental and numerical results was observed in this study. Later, Ingraffea et al. (1994) developed a finite element based software FRANC2D (1994) for the mixed mode (I/II) quasi-static as well as fatigue crack growth studies. They estimated the fatigue life using the developed software and one of the Tanaka's ΔK_{eq} models. However, no satisfactory agreement was found between the predicted and the experimental life.

Reimers (1991) used Richard's ΔK_{eq} model for the finite element fatigue crack growth rate correlation using the CTS specimen. This study indicated that the mode II SIF vanishes after the first crack growth step and ΔK_{eq} coincides with ΔK_I after the first step of the simulation. Experiments were performed using the CTS specimens made of PMMA for verification of the crack initiation angle and the crack path. A good agreement between the predicted (using the MTS criterion) and experimental crack paths were observed.

Portela et al. (1993) used the dual boundary element method for the mixed mode crack growth studies in LEFM. Fatigue crack growth was introduced as a post-processing technique in their studies, and one of the Tanaka's ΔK_{eq} models was used for predicting the fatigue life. An incremental crack extension method was used for the simulation of the crack growth and the MTS theory was used to predict the crack path. Mixed mode SIFs were estimated using the J-integral method and it was also noticed that the mode II SIF was vanishing after the first step of crack growth simulation.

Yan and Nguyen-Dang (1995) performed boundary element based numerical simulation of the mixed mode (I/II) FCG and fatigue life estimation for a single and multiple cracked panels using the dual boundary element method. One of the Tanaka's ΔK_{eq} model was used for FCG rate correlation and life prediction. They suggested the use of Paris' constants obtained from mode I FCG tests for the mixed mode fatigue life prediction.

Qian and Fatemi (1996b) performed the mixed mode (I/II) experimental and finite element FCG simulation studies using the four-point bend specimens under different asymmetric load conditions. One of the Tanaka's ΔK_{eq} model was used for the FCG rate correlation. They identified that the MTS and SED criterion could be used for the successful prediction of the fatigue crack path. They also suggested the use of FCG test data from mode I FCG tests for conservative estimates of the mixed mode fatigue life using numerical methods.

Kim and Kim (2002) studied the mixed mode (I/II) fatigue crack growth by conducting experiments for two different loading angles (30°, and 60°) and two different load ratios (0.1 and 0.5). Three different ΔK_{eq} models, viz, Tanaka's model, Yan's model, and Richard's model were employed for the fatigue crack growth rate correlation. Contrary to the previous observations, they observed that fatigue crack growth rates were higher under mode I loading than that under mixed mode (I/II) loading. They recommended Richard's ΔK_{eq} model to evaluate the FCG rate of rail steel under mixed mode loading.

Sander and Richard (Sander and Richard, 2006, 2005) performed experimentally and FE based numerical FCG studies using the CTS specimen made of Al 7075-T651 alloy to investigate the effect of overload on the FCG rate. They employed Richards's ΔK_{eq} model for the FCG rate correlation. Crack retardation following an overload was also studied.

In 2006, Ma et al. (Ma et al., 2006; Zhang et al., 2006) performed mixed mode (I/II) FCG experimental and finite element simulation studies using two different materials (S460 stainless steel and Al 7005 aluminum alloy) for three different loading angles (0°, 30°, and 60°). For the correlation of the mixed mode FCG rate, they used one of the ΔK_{eq} models proposed by Tanaka.

Borrego et al. (2006) studied the mixed mode FCG behavior in Al 6082-T6 using the CTS specimen for three different loading angles. Both the experiments and finite element simulations were carried out. The Richard's ΔK_{eq} model was used for the correlation of the

FCG rate and found a satisfactory correlation between numerical and experimental crack growth rates under the mixed mode (I/II) loading using the above ΔK_{eq} model.

Yan (2007) performed an automated simulation of multiple fatigue crack propagation in 2D bodies using the boundary element method (BEM). The mixed mode fatigue life of a center cracked plate was predicted using Yan's ΔK_{eq} model. The fatigue crack path was predicted using the MTS theory.

Mohanty et al. (2009, 2008) performed an experimental FCG study using single edge notched tension (SENT) specimens made of Al 7020-T6. They introduced an exponential fatigue crack growth model for estimating the crack length and used Richard's ΔK_{eq} model for the mixed mode FCG rate correlation. The effect of overload on the FCG rate was also studied.

Fatigue crack growth behavior of a crack with a circular micro defect in the vicinity of the probable crack path was investigated experimentally and numerically based on the FE by Seo et al. (2010). They employed one of the Tanaka's model for the FCG rate correlation. A modified CTS specimen made of hot rolled steel containing a circular hole as a micro defect near the crack tip was used in the experiments. Deviation in the crack path due to the micro defect and the fatigue life differences as compared to the defect-free specimen was also observed.

Mixed mode FCG behavior of a crack emanating from a central hole of a plate was studied using experiments and numerical analysis using the FE method by Boljanovic and Maksimovic (2011). The study addressed both the aspects viz., the fatigue crack path, and fatigue life. They employed one of Tanaka's models for fatigue life prediction, and the MTS theory was used for the crack path prediction. Results indicated that the predicted fatigue life was in good agreement with some of the test results.

Apart from the above works, a large number of mixed mode FCG studies are available on the use of various ΔK_{eq} models. A summary of such numerous works are outlined in the following Table 2.1. This table provides a compendium of the present state of use of the ΔK_{eq} models in two-dimensional mixed mode FCG studies.

Table 2.1 Use of the various ΔK_{eq} models in the mixed mode (I/II) FCG studies

Year	Reference	ΔK_{eq} Model used	Description
2006	(Zhang et al., 2006)	Tanaka's model	Performed experimental and FE simulation studies using the CTS specimen made of Al alloy and steel and used Tanaka's ΔK_{eq} model for the FCG rate correlation. The MTS criterion was used for the crack path prediction.
2010	(Zhang et al., 2010)	Yan's model	FCG studies were conducted using the numerical manifold method. They used Yan's ΔK_{eq} modal for fatigue life prediction and studied the effect of crack increment in numerical simulations. The MTS criterion was used for the crack path prediction.
2011	(Leonel and Venturini, 2011)	Yan's model	They carried out a boundary element simulation of single and multiple crack growth problems and used the Yan's ΔK_{eq} model for the fatigue life prediction. They found a variation between the reference and predicted life. The MTS criterion was used for the crack path prediction.
2013	(Seifi and Eshraghi, 2013)	Richard's model	Effects of the mixed-mode overload on the mixed-mode fatigue crack growth were studied experimentally as well as numerically. The crack path was estimated using the MTS criterion and fatigue life using the Richard's ΔK_{eq} model. They used FE based FRANC2D software for numerical simulations (Wawrzynek and Ingraffea, 1994).
2014	(Boljanović and	Tanaka's model	They performed FE based mixed mode (I/II) FCG studies and predicted fatigue life using the Tanaka's ΔK_{eq} model. The crack path was

	Maksimović, 2014)		predicted using the MTS theory under constant amplitude loading with a single overload.
2014	(Varfolomeev et al., 2014)	Richard's model	They performed experimental and XFEM based FCG studies using a 4-point bend and edge cracked specimens. They used Richard's ΔK_{eq} model for the FCG rate correlation.
2014	(Ayatollahi et al., 2015, 2014)	Yan's model	They investigated the effect of stop hold in the FCG rate retardation with a modified CT specimen under the mixed mode (I/II) loading using experiments and FE studies. Fatigue life in presence of stop holes was predicted using the Yan's ΔK_{eq} model and crack trajectory was predicted based on the MTS criterion.
2015	(Kumar et al., 2015)	Yan's model	They performed XFEM based FCG studies for the fatigue crack path and life estimation. They used theYan's ΔK_{eq} model for the fatigue life prediction and MTS criteria for path estimation.
2015	(Albuquerque et al., 2015)	Tanaka's model	They investigated the fatigue assessment of in-service railway bridges considering multiple and complex loading histories using FE studies and experiments. They used the Tanaka's ΔK_{eq} model and mode I Paris constants for the fatigue life prediction and the MTS criterion for the crack path modeling.
2015	(He et al., 2015)	Yan's model	They developed a FE based numerical simulation program to simulate the fatigue crack path and to compute the corresponding fatigue life. They used Yan's ΔK_{eq} model for the fatigue life prediction and MTS criterion for the crack trajectory estimation.

2015	(Li et al., 2015)	Richard's model	Cohesive zone modeling was introduced for the mixed mode (I/II) crack growth studies and performed experiments using the CT and CTS specimens made of AISI 304 stainless steel to verify the numerical results. The fatigue life was predicted using the Richard's ΔK_{eq} model and fatigue crack path using the MTS criterion.
2016	(Jameel and Harmain, 2016)	Yan's model	They performed XFEM based FCG simulations in the presence of material discontinuities and used Yan's ΔK_{eq} model for the FCG rate correlation and life prediction.
2016	(Muzvidziwa et al., 2016)	Yan's model	They performed experimental studies to assess the crack growth rate in the friction stir welded zone and base metal. They used the Yan's ΔK_{eq} model for the FCG rate correlation under mixed mode (I/II) loading.
2016	(Duchaczek and Mańko, 2016)	Yan's model	They performed FE based mixed mode (I/II) FCG studies of steel girders in military bridges using FRANC2D and they used the Yan's ΔK_{eq} model for the FCG rate correlation.
2016	(Lesiuk et al., 2019, 2017, 2016)	Tanaka's model	Experimental fatigue crack growth studies were performed using the CTS specimen cut from a long operated steel bridge structures. The change in the crack growth rate with the rolling direction was discussed. They used one of the Tanaka's ΔK_{eq} models for the mixed mode FCG rate correlation. They also studied the variation in the crack initiation angles when using various path prediction criteria. However, none of them found suitable for this material.

2017	(Peixoto and de Castro, 2017)	Richard's model	They carried out experimental mixed mode (I/II) FCG studies using the CTS specimens cut from a high-speed rail wheel. They also performed FE based studies using the Richard's ΔK_{eq} model for the FCG rate correlation and MTS criteria for the crack trajectory prediction.
2017	(Zarrinzadeh et al., 2017)	Richard's model	They conducted XFEM analysis and experimental FCG studies of an aluminum pipe repaired by the composite patch using the Richard's ΔK_{eq} model for the fatigue life prediction. Reasonable agreement between experimental and predicted cycles was observed.
2017	(Nasri and Zenasni, 2017)	Tanaka's model	They performed XFEM based FCG simulations for the crack growth behavior at bi-metallic interfaces in the galvanized panels and used one of the Tanaka's ΔK_{eq} model for the fatigue life prediction.
2017	(Wang et al., 2017)	Richard's and Tanaka's model	They studied the FCG behavior of Ni-Cr-Mo-V high strength steel welded joints using the CTS specimen experimentally as well as numerically using FE method. They also used the Tanaka's and Richard's ΔK_{eq} models for the FCG rate correlation. However, no recommendations were made regarding the suitability of the models. The MTS and SED criteria were used for the path prediction and good agreement with the MTS predictions and experimental data were observed.
2018	(Cao et al., 2018)	Tanaka's model	They studied the anisotropic crack growth behavior in Al 7050-T7451 alloy with the CTS specimen using experiments and FE simulations. They used one of the Tanaka's ΔK_{eq} model for the FCG rate

			correlation and MTS, SED, and R-criterion for the crack initiation angle prediction.
2018	(Horas et al., 2018)	Tanaka's model	Mixed mode (I/II) FCG studies of large railway bridges were performed by taking into consideration of the loads due to the traffic. They used one of the Tanaka's ΔK_{eq} model for the FCG rate correlation and the MTS criterion for the path prediction.
2018	(Heirani and Farhangdoost, 2018)	Tanaka's and Richard's model	They studied the influence of compressive mode I loading on the FCG rate using experiments on the CTS specimen. They used the Tanaka's and Richard's ΔK_{eq} models for the rate correlation. Neither the Richard's nor the Tanaka's models are particularly satisfying.
2018	(Dirik and Yalçinkaya, 2018)	Tanaka's model	They performed automated FCG studies using XFEM under mixed mode (I/II) variable amplitude loading and used one of the Tanaka's ΔK_{eq} model for the fatigue life prediction. The MTS and MERR theories were used for the crack path prediction. Both theories predict the path with good agreement with the experimental data.
2019	(Leite and Gomes, 2019)	Tanaka's model	Mixed mode (I/II) FCG studies employing dual boundary element method were performed and compared the results with the available experimental results. They used one of the Tanaka's ΔK_{eq} model for the fatigue life prediction and MTS criterion for the crack trajectory estimation. They observed disagreement between predicted and experimental fatigue life.

2019	(Grbović et al., 2019b, 2019a)	Yan's model	They performed experimental studies and numerical simulation of the FCG in aircraft wing spars using XFEM and used the MTS criterion for the crack path prediction. They predicted fatigue life using Yan's the ΔK_{eq} model, and the predicted fatigue life was not in good agreement with the experimental fatigue life.

The application of the modified Paris' law with ΔK_{eq} is not limited to mixed mode consisting of mode I and mode II loading conditions, but employed for mixed mode (I/II/III) loading conditions as well. For the purpose of completion, Table 2.2 shows some studies available on the use of the three-dimensional form of ΔK_{eq} models (i.e., models include all the three SIFs, K_I, K_{II} and K_{III}) to study the mixed mode (I/II/III) fatigue fractures.

Table 2.2 Use of the various ΔK_{eq} models in the mixed mode (I/II/III) studies

Year	Reference	ΔK_{eq} Model used	Description
2010	(Shi et al., 2010)	Irwin's model for 3D	They performed numerical mixed mode (I/II/III) FCG simulations using XFEM and estimated the FCG rate and fatigue life using the Irwin's model containing all the three SIFs, K_I, K_{II} and K_{III} i.e., Irwin's 3D model. The fatigue crack path is predicted using the MTS theory.
2011	(Madia et al., 2011)	Richard's 3D model	FE based mixed mode (I/II/III) FCG studies for cracks in railway axles were carried out using the Richard's model containing all the three SIFs, K_I, K_{II} and K_{III}.
2012	(Farjoo et al., 2012)	Richard's 3D model	Numerical (FE) mixed mode FCG studies for 3D elliptical cracks in rail surfaces were carried out

			using the Richard's 3D ΔK_{eq} model. They used the Richard/Henn's criterion for crack path prediction.
2014	(He et al., 2014)	Irwin's 3D model	Three dimensional FE based FCG studies for the fatigue life prediction in marine structures (stiffened panel) using the Irwin's 3D ΔK_{eq} model were carried out. They used the MTS theory for the crack path prediction.
2015	(Ghaffari et al., 2015)	Richard's 3D model	They performed 3D FE FCG simulations of the crack initiation and propagation in gear tooth. They used the Richard's 3D ΔK_{eq} model for the fatigue life prediction. Reasonable agreement were observed between predicted and published experimental fatigue life.
2015	(Srilakshmi et al., 2015)	Irwin's 3D model	Experimental and FE FCG studies in CFRP patch repaired Al 2014-T6 panel were performed and they used the Irwin's 3D ΔK_{eq} model for the fatigue life prediction.
2016	(Martins et al., 2016)	Richard's and Yan's 3D model	They performed numerical (FEM) and experimental FCG studies under cyclic tension-torsion loading using the CT specimen, and used both the Richard's and Yan's 3D ΔK_{eq} models for the FCG rate correlation. However, no conclusive remarks were made regarding the appropriateness of these models. They also employed the MTS theory for the crack path prediction in numerical studies.
2016	(Li et al., 2016)	Irwin's 3D model	Three dimensional FE modeling of FCG of the surface cracks in pressurized pipes were performed and used the Irwin's 3D ΔK_{eq} model for the FCG rate estimation under 3D conditions.

2016	(Sadeghirad et al., 2016)	Irwin's 3D model	They performed XFEM based three-dimensional FCG simulations of nonplanar 3D embedded and surface cracks in helicopter components and used the Irwin's 3D ΔK_{eq} model for the FCG rate correlation.
2017	(Yang and Vormwald, 2017)	Yan's 3D model	They performed experimental and numerical FCG studies (using FRANC3D) in thin-walled hollow cylinders under non-proportional cyclic-tension and torsion loading. They used the Yan's 3D ΔK_{eq} model for the fatigue life prediction and MTS criterion for the crack path estimation.
2018	(Vormwald et al., 2018)	Yan's 3D model	Mixed mode (I/II/III) FCG studies of cracks originating from slits in the thin-walled tube specimens subjected to cyclic axial tension-torsion loading were performed experimentally as well as using FE method. They used the Yan's 3D ΔK_{eq} model for the FCG rate correlation.

The above review of the literature indicates that various ΔK_{eq} models have been employed primarily for (a) FCG rate correlation, i.e., studies to see whether or not a linear relationship could be obtained between the selected model of ΔK_{eq} and experimental values of the mixed mode da/dN on a logarithmic scale and (b) employed one of the available ΔK_{eq} models to determine the mixed mode (I/II) fatigue life using numerical methods. In fact, not all the proposed models are employed in the above studies. Irwin's, Richards, Tanaka and Yan's models are widely employed in the experimental and numerical studies. It is worth mentioning here that even to observe the linear relationship between ΔK_{eq} and da/dN, one need to recourse to the numerical methods for determination of the mixed mode SIFs on the experimental path of the crack. It is also worth noting here that only very few works are available, which considered more than one ΔK_{eq} model in their study, and no serious attempts are made on comparison of these selected models to understand their predictability of the mixed mode (I/II) fatigue life.

It can be noticed from the above review that starting with the Tanaka's first ΔK_{eq} model (Tanaka, 1974) in 1974 to the model proposed by Demir et al. (2018) in 2018, i.e., nearly during four decades, a large number of equivalent SIF, ΔK_{eq} models have been developed/suggested to use with the modified Paris' law. It is also evident that these models are used to correlate the FCG rate, and they are also used for the numerical prediction of mixed mode (I/II) fatigue life of engineering components. It can be noticed from the previous discussion that no serious attempts are available on the comparison of available ΔK_{eq} models for understanding their predictive capabilities in numerical fatigue life estimation of engineering components. In other words, till date, no attempts have been made to know *"which of the available ΔK_{eq} models provide fatigue life predictions close to the experimental data or provides conservative estimates of the life?"* Clearly, lack of answer to the above question makes the analyst to perplex on selection of the appropriate model for the mixed mode (I/II) fatigue life prediction of engineering components.

2.3 Review of criteria for crack initiation direction

An important aspect of the mixed mode fatigue crack growth is the propagation of the crack in a non-self-similar fashion. As a consequence, apriori prediction of the crack path direction from a given increment of the crack growth is an important variable for accurate prediction of the mixed mode (I/II) fatigue life of the engineering components. A large number of criteria are available for prediction of the crack path in mixed mode loading conditions. All these criteria are primarily developed in static mixed mode fracture conditions. The current practice in fatigue simulation studies is to directly employ these criteria developed for the static fractures cases to the cyclic loading of engineering components under the mixed mode loading conditions. In this section, some of these widely employed criteria are briefly reviewed.

2.3.1 Maximum tangential stress (MTS) criterion

The maximum tangential stress criterion is proposed by Erdogan and Sih (1963) and is the most widely used criterion for prediction of the direction of crack growth under in-plane mixed mode loads. This theory postulates that the crack growth occurs in the radial direction from the crack tip, and the direction is normal to the maximum circumferential (hoop or tangential) stress (σ_θ) at the crack tip, which can be treated as a material constant. The only

parameters needed for determining the crack propagation direction θ are the stress intensity factors. Once K_I and K_{II} along with their sings are known, the possible propagation direction can be obtained. It has also been observed that the θ direction coincides with the zero shear (principal) direction. The predictions using this theory are in good agreement with the experimental data of the through-thickness cracks as compared to the elliptical cracks.

2.3.2 Minimum strain energy density (SED) criterion

The minimum strain energy density (SED) criterion, proposed by Sih (1974, 1973) is based on local strain energy density in a confined area around the crack tip. This criterion postulates that the crack initiates and grows in a direction where local strain energy density around the crack tip at a constant radius is minimum. The region within this constant radius (where the SED is minimum) is known as the core region. According to this theory, the crack grows in the direction of minimum strain energy density (SED) and crack extension onsets when the minimum value of the strain energy density factor reaches a critical value, which is a material parameter. While the MTS is a two-dimensional criterion, SED is a three-dimensional criterion.

2.3.3 Maximum energy release rate (MERR) criterion

Hussain et al. (1974) proposed the maximum energy release rate (MERR) criterion based on the Griffith energy principle (1921) for brittle fracture under SSY conditions and showed that the crack initiates in the direction of the maximum value of the energy release rate. The underlying assumption behind this criterion is that for the mixed mode (I/II) loading, the crack moves along its initial plane.

2.3.4 Maximum tangential principal stress (MTPS) criterion

Maiti and Smith (1983a, 1983b) argued that the MTS criterion contains only the singular stress terms of Williams' eigen series expansion and suggested to include the contribution of the non-singular stress term. They suggested using the principal tangential stress. This forms the basis of the maximum principal stress (MTPS) criterion. According to the MTPS criterion, the crack extends in a radial direction corresponding to the maximum tangential principal stress, and the crack extension begins when this maximum reaches a critical value.

2.3.5 Maximum stress triaxiality criterion (M-criterion)

Kong et al. (1995) investigated the effects of triaxial crack tip stress state in the mixed-mode crack initiation direction and proposed the M-criterion. According to this theory, the direction of the crack initiation coincides with the direction of the maximum stress triaxiality along a contour at a constant radius around the crack tip (Fayed, 2002; Khan and Khraisheh, 2000; Mróz and Mróz, 2010). They expressed the maximum stress triaxiality (M) as the ratio of the hydrostatic stress σ_H and the equivalent stress σ_{eq}. Irrespective of the plane stress or plane strain, the M-criterion predicts the same crack propagation angle.

2.4 Review of various mixed mode (I/II) fatigue specimens

A vital element in obtaining valid mixed mode (I/II) fatigue crack growth data is the proper form of the experimental specimen. The specimen should be designed in such a way that it is amicable to produce all mode mixities, including pure mode I and pure mode II using standard uniaxial tensile loading machines. Indeed, most of the specimens and their associated test fixtures developed are useful for both the static and cyclic mixed mode studies. Mixed mode (I/II) FCG experiments are not yet standardized, and thus a variety of specimens are available in the literature for the FCG tests. This section briefly discusses some planar specimens available in the literature for the mixed mode (I/II) fatigue crack growth studies.

2.4.1 Compact tension shear (CTS) specimen

The compact tension shear (CTS) specimen, as shown in Fig. 2.1, is proposed by Richard et al. (Richard, 1981; Richard et al., 1991; Richard and Benitz, 1983) and is the most widely used specimen for the mixed mode (I/II) fatigue crack growth studies. It is an edge cracked plate with three holes on top and bottom to impart the applied load from the test fixture. The test fixture contains holes for producing different mode mixities and is connected to the clevis grip of the testing machine. This specimen can create mode mixities ranging from pure mode I, pure mode II and mixed mode (I/II). Many researchers, Richard et al. (2014), Ma et al. (2006), Zhang et al. (2006), Kim et al. (2002), Biner (2001), Ayatollahi et al. (2012) Rozumek et al. (2018), Demir et al. (2018), Miao et al. (2018), Qi et al. (2019) and others frequently used the CTS specimen for static and fatigue fracture studies under mixed mode (I/II) conditions.

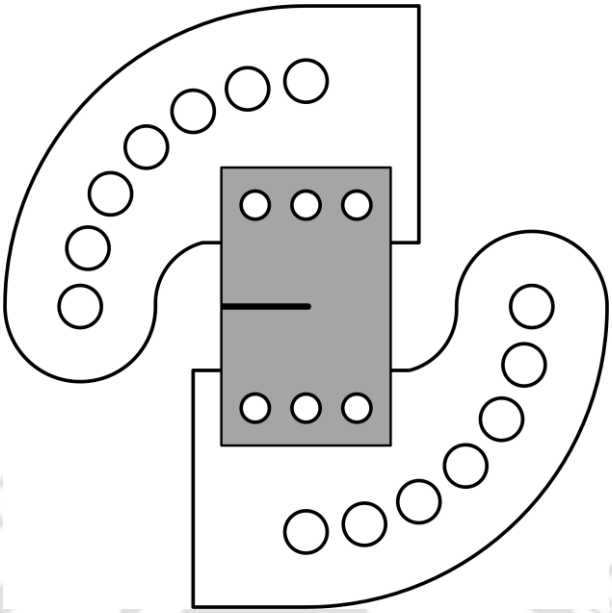

Figure 2.1 Richard's CTS specimen and its associated test fixture

2.4.2 Compact shear (C(S)) test specimen

Lo et al. (2003) proposed a specimen similar to the Richard's specimen named as compact shear (C(S)) specimen (Fig. 2.2) for conducting the mixed mode fatigue test. It is noticed that (Lo et al., 2003; Tamilselvan et al., 2005) the proposed specimen exhibits better qualities than the CTS specimen, and is also suitable for pure mode II fracture toughness tests. This also necessitates a special fixture for loading similar to the CTS specimen.

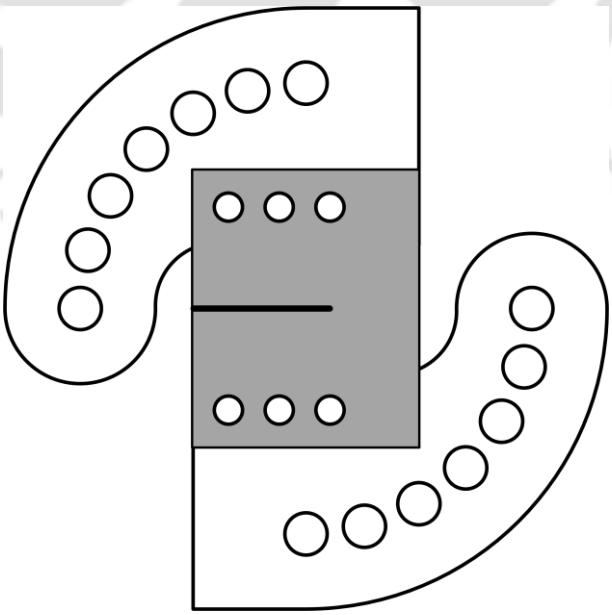

Figure 2.2 Compact shear specimen and the loading fixture

2.4.3 Modified compact tension specimen

Mahanty and Maiti (Mahanty and Maiti, 1990; Maiti and Mahanty, 1990) proposed a modified form of the CT specimen, as shown in Fig. 2.3 (a) suitable for the mixed mode (I/II) fracture studies. Although it resembles and provides all the advantages of the standard CT specimen used in mode I fatigue studies, it could only produce limited mode mixities. It doesn't require additional fixtures for loading the specimen. Miranda et al. (2002, 2003a, 2003b) also used a similar specimen for the mixed mode (I/II) fracture and fatigue tests (Fig. 2.3 (b)). The additional hole in the specimen is designed to produce mixed mode loading conditions by deflecting the crack towards the hole. Again it is able to generate limited mode mixities.

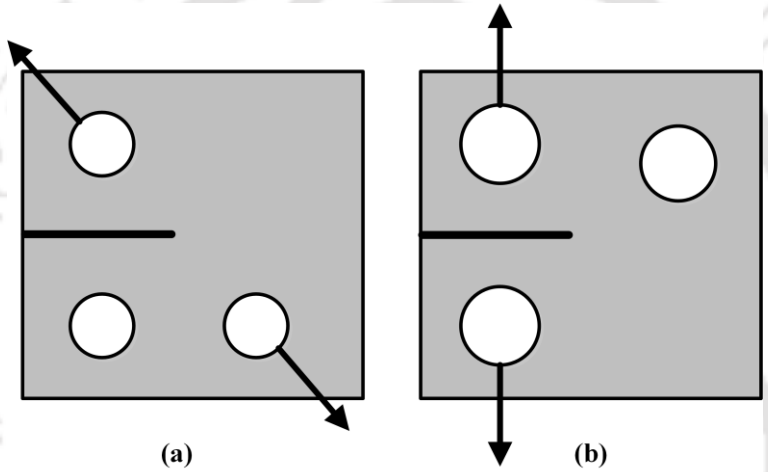

Figure 2.3 Modified compact tension specimen used by (a) Mahanty and Maiti and (b) Miranda et al.

2.4.4 Arcan specimen

The arcan specimen along with its test fixture is developed by Banks-Sills et al. (1984). Fig. 2.4 shows the schematic view of the Arcan specimen. Hallback (1997) studied further the effect of geometry and material of the arcan specimen in mixed mode (I/II) fatigue crack growth studies. Another variant of this specimen known as butterfly specimen is due to Hosseini et al. (2008). This specimen is also used for the biaxial fatigue crack growth studies by utilizing the proper loading fixture.

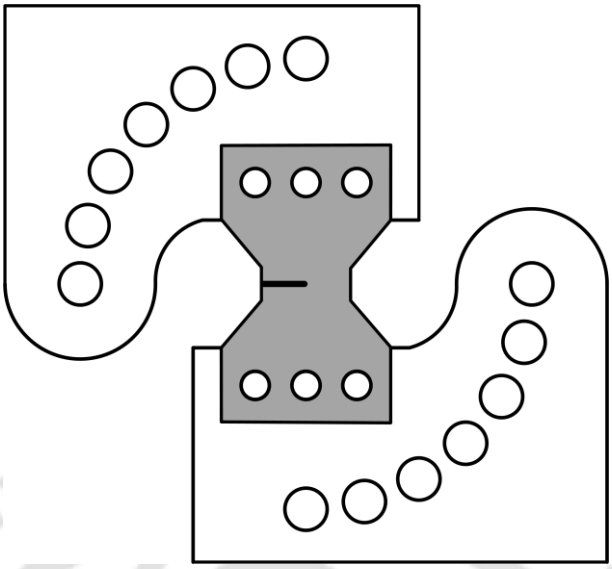

Figure 2.4 Arcan specimen and the loading specimen for the mixed mode fatigue studies

2.4.5 T-specimen

Recently, Demir et al. (2017) proposed a new T-specimen for in-plane mixed mode fracture and fatigue testing. The specimen contains four loading holes to prevent free rotation under mixed mode loading. This specimen also requires a special loading device similar to the Richard's loading device (1983) developed for the CTS specimen. The size of the T-specimen is significantly small as compared to the dimensions of the CTS specimen, thus requires less material and the lower failure load. The geometry of the specimen and the loading fixture are shown in Fig. 2.5.

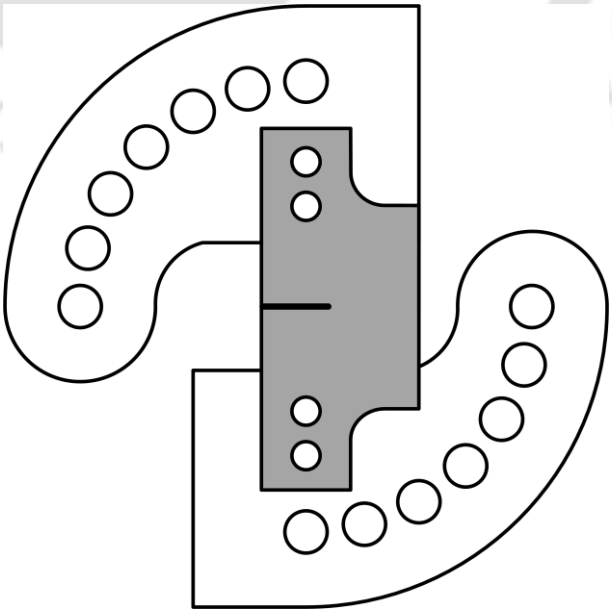

Figure 2.5 T-specimen for the mixed mode (I/II) fatigue crack growth studies

It is evident from the above review that the CTS specimen introduced by Richard et al. (1981) is the most widely used specimen for mixed mode (I/II) fatigue crack growth studies. One of the limitations of the CTS specimen is the requirement of an additional heavy loading fixture. The specimen is rugged in design and allows accurate mixed mode loading can be imparted to the specimen.

2.5 Summary of the literature review and research gap

2.5.1 Summary

- A number of mixed mode (I/II) fatigue crack growth laws have been proposed in the literature. These laws assume that the tensile crack growth dominates during the fatigue crack propagation.
- No standard test procedure is available to date for correlating the mixed mode (I/II) fatigue crack growth rate with the mode I and mode II SIFs.
- The modified Paris' law with the ΔK_{eq} model proposed by Tanaka (1974) is the most widely used LEFM based law for the fatigue crack growth studies in mixed mode (I/II) loading conditions.
- The modified Paris' law is widely used in mixed mode (I/II) fatigue for (a) the FCG rate correlation of various engineering materials and (b) numerical estimation of the mixed mode fatigue life of the engineering components.
- A large number of various ΔK_{eq} models have been proposed for the last five decades based on (a) microscopic fatigue models (b) static mixed mode (I/II) fracture theories and (c) empirical models.
- The finite element method is widely employed for numerical estimation of the mixed mode (I/II) fatigue life using the modified Paris' law with various ΔK_{eq} models.
- The maximum tangential stress (MTS) criterion and minimum strain energy density criterion (S-criterion) are widely used for the estimation of the crack growth direction in the numerical simulation studies.
- The incremental crack extension approach is widely employed in numerical simulation of the mixed mode (I/II) fatigue crack growth.

- The current practice is to use mode I Paris' constants (obtained from pure mode I FCG experiments) as material constants in the modified Paris' law for the numerical simulation of the mixed mode (I/II) FCG and estimation of the corresponding fatigue life.
- The CTS (compact tension shear) specimen, along with Richard's loading device have been widely used for mixed mode (I/II) FCG studies.

2.5.2 Research gap

- Very limited studies are available on the effect of the use of various ΔK_{eq} models in the modified Paris' law for finite element estimation of the mixed mode (I/II) fatigue life of engineering components. In other words, the literature on the study of the mixed mode (I/II) fatigue life predictive capabilities of various available ΔK_{eq} models when using the modified Paris' law is very scarce.
- From the above limited studies, no concrete suggestions/recommendations or observations are available to date to know which of the ΔK_{eq} models provide consistently the close/conservative life estimations when compared with the experimental test results.
- Nearly after 40 years, no comparative study is available.

2.6 Objectives of the present study

Based on the literature review and gaps in the current status on numerical prediction of the mixed mode (I/II) fatigue life, the objectives of the present investigation are laid as

1. To conduct mode I fatigue crack growth experiments using the standard CT specimens made of SS 316 and Al 6061 materials in order to determine the Paris' material constants C and m of the above materials.
2. To conduct mixed mode (I/II) fatigue crack growth experiments using the CTS specimens made of SS 316 material in order to obtain the crack length versus the number of loading cycle data. Next, to conduct finite element simulations of the mixed mode (I/II) fatigue crack growth of the CTS specimens made of SS 316 material in order to study the predictive capabilities of various ΔK_{eq} models in estimation of the

mixed mode (I/II) fatigue life (using the modified Paris' law) by comparing experimental data with the numerical results.

3. To conduct mixed mode (I/II) fatigue crack growth experiments using the CTS specimens made of Al 6061 material in order to obtain the crack length versus the number of loading cycle data. Next, similar to SS 316 material, to conduct finite element simulations of the mixed mode (I/II) fatigue crack growth of the CTS specimens made of Al 6061 material in order to study the predictive capabilities of various ΔK_{eq} models in estimation of the mixed mode (I/II) fatigue life (using the modified Paris' law) by comparing experimental data with the numerical results.
4. To develop a new finite element post-processing technique for accurate estimation of the mixed mode SIFs, K_I and K_{II} along with their signs for use in the computation of the required quantities while conducting finite element simulations of the present investigation.
5. To develop a new curve fitting technique for best-fit of the scattered mixed mode (I/II) experimental data of the measured crack length versus the number of loading cycles.
6. To conduct finite element simulations of the mixed mode (I/II) fatigue crack growth of the specimens having published experimental fatigue life data in order to study the predictive capabilities of various ΔK_{eq} models in estimation of the mixed mode (I/II) fatigue life using the modified Paris' law.
7. Based on the results corresponding to the objectives (1), (3) and (4), the present investigation recommends/suggests the ΔK_{eq} model(s) that would provide consistently close or conservative numerical predictions of the mixed mode (I/II) fatigue life of engineering components.

Chapter 3

Theoretical background

Theoretical background for various approaches adopted in the present investigations are presented in this chapter. The generalized Westergaard approach required for the proposed SIF estimation technique is described in this chapter. This chapter also describes the theoretical background for the prediction of fatigue crack growth path and the fatigue life under mixed mode (I/II) loading conditions. Various equivalent stress intensity factor models available in the literature are also discussed in this chapter. Finally, finite element formulation along with the details of the discretization of the cracked specimens used for the numerical analysis of the present investigations are also discussed.

3.1 Crack tip stress field

Two major approaches are in use for obtaining the stress fields around the crack tip in LEFM. One is the Williams' asymptotic eigenfunction expansion method (Williams, 1957) and the generalized Westergaard approach proposed by Sanford (1979). The generalized Westergaard approach (Sanford, 2003, 1979) is a generalization of the familiar Westergaard stress function approach (Westergaard, 1939) to include the finite bodies subjected to arbitrary surface tractions and containing a single ended crack and double ended crack (internal crack) with traction free crack faces. For the case of a single ended crack, the method is functionally equivalent to the well-known Williams eigenfunction expansion method (Hello, 2018; Hello et al., 2012; Williams, 1957).

The equivalence among various multi-parameter stress field equations obtained using the Williams eigenfunction expansion method and that of generalized Westergaard approach can be found in (Ramesh et al., 1996). In the present work, generalized Westergaard's approach has been used to obtain the field equations near the crack tip. The following section discusses

the theoretical formulations for the development of stress and displacement equations at the vicinity of the crack tip using the generalized Westergaard approach.

In the context of the Westergaard–Sanford complex approach, the stress field at a given point $z = x + iy$ (as shown in Fig. 3.1) is expressed with two pairs of potentials (Z_i, Y_i) where $i=I, II$ corresponding to the fracture modes mode I and mode II, respectively.

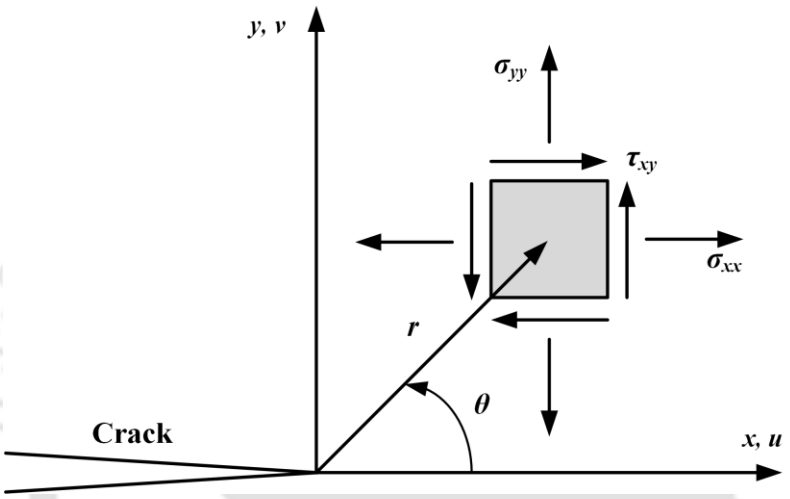

Figure 3.1 Crack tip coordinate system

3.2 Generalized Westergaard approach for the near field equations

The near field equations are the expressions of the stresses, strains, and displacements near the crack tip under SSY conditions. These equations consist of the leading term and a few higher order terms.

3.2.1 Mode I near field equations

In the generalized Westergaard approach (Sanford, 1979), the stress field around the crack tip is expressed in the series form as

$$\sigma_{ij} = \sum_{n=0}^{\infty} A_n z^{n-1/2} f_{ij}(\theta) \sum_{m=0}^{M} B_m r^m g_{ij}(\theta) \tag{3.1}$$

where A_n and B_m are unknown coefficients, and $f_{ij}(\theta)$ and $g_{ij}(\theta)$ are trigonometric functions.

The Airy stress function in this approach is given by

$$\phi_I = \mathrm{Re}\,\overline{\overline{Z_I}}(z) + y\,\mathrm{Im}\,\overline{Z_I}(z) + y\,\mathrm{Im}\,\overline{Y_I}(z) \tag{3.2}$$

where

$$\frac{d\bar{\bar{Z}}_i}{dz} = \bar{Z}_i, \quad \frac{d\bar{Z}_i}{dz} = Z_i, \text{ and } \frac{d\bar{Y}_i}{dz} = Y_i \tag{3.3}$$

In this approach, an additional term $y\,\mathrm{Im}\bar{Y}_I(z)$ is added to the conventional Westergaard approach. The complex analytic function $Z_I(z)$ and $Y_I(z)$ for opening mode are defined as (Sanford, 1979)

$$Z_I(z) = \sum_{n=0}^{\infty} A_n z^{n-1/2} = \frac{K}{\sqrt{2\pi z}} + \sum_{n=1}^{\infty} A_n z^{n-1/2} \tag{3.4}$$

$$Y_I(z) = \sum_{m=0}^{\infty} B_m z^m = \frac{\sigma_{0x}}{2} + \sum_{m=1}^{\infty} B_m z^m \tag{3.5}$$

which are series types of functions (in terms of a complex variable $z = x + iy$) containing the infinite number of coefficients $(A_0, A_1, ..., B_0, B_1, ...)$ that can be determined using the boundary condition of a given problem.

For a complex analytic function, such as $Z_I(z)$ the Cauchy-Riemann equations are given by,

$$\begin{aligned} \frac{\partial \mathrm{Re}\, Z_I}{\partial y} &= -\frac{\partial \mathrm{Im}\, Z_I}{\partial x} = -\mathrm{Im}\, Z_I' \\ \frac{\partial \mathrm{Im}\, Z_I}{\partial y} &= \frac{\partial \mathrm{Re}\, Z_I}{\partial x} = \mathrm{Re}\, Z_I' \end{aligned} \tag{3.6}$$

The Airy stress function ϕ is related to the cartesian components of the stresses as

$$\sigma_x = \frac{\partial^2 \phi}{\partial y^2}, \quad \sigma_y = \frac{\partial^2 \phi}{\partial x^2}, \text{ and } \tau_{xy} = -\frac{\partial^2 \phi}{\partial x \partial y} \tag{3.7}$$

Using Cauchy-Reimann relations (Eq. (3.6)), and Eq. (3.2), the first partial derivatives of ϕ can be obtained as

$$\begin{aligned} \frac{\partial \phi}{\partial x} &= \mathrm{Re}\, \bar{Z}_I + y\,\mathrm{Im}\, Z_I + y\,\mathrm{Im}\, Y_I \\ \frac{\partial \phi}{\partial y} &= \mathrm{Im}\, \bar{Z}_I + y\,\mathrm{Re}\, Z_I + y\,\mathrm{Re}\, Y_I \end{aligned} \tag{3.8}$$

Using Eqs. (3.6), (3.2) and (3.7), the stress components for mode I in the absence of body forces, then can be given as

$$\begin{aligned}\sigma_{xx} &= \mathrm{Re}\, Z_I - y\,\mathrm{Im}\, Z_I' - y\,\mathrm{Im}\, Y_I' + 2\,\mathrm{Re}\, Y_I \\ \sigma_{yy} &= \mathrm{Re}\, Z_I + y\,\mathrm{Im}\, Z_I' + y\,\mathrm{Im}\, Y_I' \\ \tau_{xy} &= -y\,\mathrm{Re}\, Z_I' - y\,\mathrm{Re}\, Y_I' - \mathrm{Im}\, Y_I\end{aligned} \tag{3.9}$$

Substitution of the series form of complex analytic functions $Z_I(z)$ and $Y_I(z)$ from Eqs. (3.4) and (3.5) gives equations for the stress field in the whole domain which consists of the infinite number of unknown coefficients A_n and B_m. Thus equations for the stress components are given by

$$\begin{Bmatrix}\sigma_{xx}\\ \sigma_{yy}\\ \tau_{xy}\end{Bmatrix} = \sum_{n=0}^{N} A_n r^{(n-\frac{1}{2})} \begin{Bmatrix}\cos(n-\frac{1}{2})\theta - (n-\frac{1}{2})\sin\theta\sin(n-\frac{3}{2})\theta \\ \cos(n-\frac{1}{2})\theta + (n-\frac{1}{2})\sin\theta\sin(n-\frac{3}{2})\theta \\ -(n-\frac{1}{2})\sin\theta\cos(n-\frac{3}{2})\theta\end{Bmatrix} + \sum_{m=0}^{M} B_m r^m \begin{Bmatrix}2\cos m\theta - m\sin\theta\sin(m-1)\theta \\ m\sin\theta\sin(m-1)\theta \\ -m\sin\theta\cos(m-1)\theta - \sin m\theta\end{Bmatrix} \tag{3.10}$$

Assuming plane stress conditions, the strain components are obtained using the generalized Hooke's law as

$$\begin{aligned}E\varepsilon_{xx} &= (1-\nu)\,\mathrm{Re}\, Z_I - (1+\nu)y\,\mathrm{Im}\, Z_I' - (1+\nu)y\,\mathrm{Im}\, Y_I' + 2\,\mathrm{Re}\, Y_I \\ E\varepsilon_{yy} &= (1-\nu)\,\mathrm{Re}\, Z_I + (1+\nu)y\,\mathrm{Im}\, Z_I' + (1+\nu)y\,\mathrm{Im}\, Y_I' - 2\nu\,\mathrm{Re}\, Y_I \\ E\gamma_{xy} &= -2(1-\nu)\,\mathrm{Im}\, Y_I - 2(1+\nu)y\,\mathrm{Re}\, Z_I' - 2(1+\nu)y\,\mathrm{Re}\, Y_I'\end{aligned} \tag{3.11}$$

and substitution of series forms of complex functions $Z_I(z)$ and $Y_I(z)$ from Eqs. (3.4) and (3.5) gives the exact representation of the strain field as

$$\begin{Bmatrix}\varepsilon_{xx}\\ \varepsilon_{yy}\\ \gamma_{xy}\end{Bmatrix} = \sum_{n=0}^{N} \frac{A_n}{E} r^{(n-\frac{1}{2})} \begin{Bmatrix}(1-\nu)\cos(n-\frac{1}{2})\theta - (n-\frac{1}{2})(1+\nu)\sin\theta\sin(n-\frac{3}{2})\theta \\ (1-\nu)\cos(n-\frac{1}{2})\theta + (n-\frac{1}{2})(1+\nu)\sin\theta\sin(n-\frac{3}{2})\theta \\ -(n-\frac{1}{2})(1+\nu)\sin\theta\cos(n-\frac{3}{2})\theta\end{Bmatrix} + \sum_{m=0}^{M} \frac{B_m}{E} r^m \begin{Bmatrix}2\cos m\theta - (1+\nu)m\sin\theta\sin(m-1)\theta \\ (1+\nu)m\sin\theta\sin(m-1)\theta - 2\nu\cos m\theta \\ -2(1+\nu)m\sin\theta\cos(m-1)\theta - 2(1+\nu)\sin m\theta\end{Bmatrix} \tag{3.12}$$

The displacement components can be obtained by integrating the strain components and can be obtained for mode I loading conditions as

$$
\begin{aligned}
Eu_1 &= (1-\nu)\,\mathrm{Re}\,\overline{Z}_I - (1+\nu)\,y\,\mathrm{Im}\,Z_I - (1+\nu)\,y\,\mathrm{Im}\,Y_I + 2\,\mathrm{Re}\,\overline{Y}_I \\
Ev_I &= 2\,\mathrm{Im}\,\overline{Z}_I - (1+\nu)\,y\,\mathrm{Re}\,Z_I - (1+\nu)\,y\,\mathrm{Re}\,Y_I + (1-\nu)\,\mathrm{Im}\,\overline{Y}_I
\end{aligned}
\tag{3.13}
$$

Substitution of the series form of complex functions $Z_I(z)$ and $Y_I(z)$ results to

$$
\begin{aligned}
\begin{Bmatrix} u_I \\ v_I \end{Bmatrix} = &\sum_{n=0}^{N} \frac{A_n}{E} r^{(n+\frac{1}{2})} \begin{Bmatrix} \dfrac{2(1-\nu)}{2n+1}\cos(n+\frac{1}{2})\theta - (1+\nu)\sin\theta\sin(n-\frac{1}{2})\theta \\ \dfrac{4}{2n+1}\sin(n+\frac{1}{2})\theta - (1+\nu)\sin\theta\cos(n-\frac{1}{2})\theta \end{Bmatrix} \\
&+ \sum_{m=0}^{M} \frac{B_m}{E} r^{(m+1)} \begin{Bmatrix} \dfrac{2}{m+1}\cos(m+1)\theta - (1+\nu)\sin\theta\sin m\theta \\ \dfrac{1-\nu}{m+1}\sin(m+1) - (1+\nu)\sin\theta\sin m\theta \end{Bmatrix}
\end{aligned}
\tag{3.14}
$$

Considering the terms corresponding to the coefficients A_0, A_1, and B_0 only, the near field stress components in mode I can be obtained as

$$
\begin{aligned}
\sigma_{xx} &= A_0 r^{-1/2}\cos\frac{\theta}{2}\left(1-\sin\frac{\theta}{2}\sin\frac{3\theta}{2}\right) + 2B_0 + A_1 r^{1/2}\cos\frac{\theta}{2}\left(1+\sin^2\frac{\theta}{2}\right) \\
\sigma_{yy} &= A_0 r^{-1/2}\cos\frac{\theta}{2}\left(1+\sin\frac{\theta}{2}\sin\frac{3\theta}{2}\right) + A_1 r^{1/2}\cos\frac{\theta}{2}\left(1-\sin^2\frac{\theta}{2}\right) \\
\tau_{xy} &= A_0 r^{-1/2}\sin\frac{\theta}{2}\cos\frac{\theta}{2}\cos\frac{3\theta}{2} - A_1 r^{1/2}\sin\frac{\theta}{2}\cos^2\frac{\theta}{2}
\end{aligned}
\tag{3.15}
$$

and similarly the strain components are given by

$$
\begin{aligned}
E\varepsilon_{xx} &= A_0 r^{-1/2}\cos\frac{\theta}{2}\left[(1-\nu)-(1+\nu)\sin\frac{\theta}{2}\sin\frac{3\theta}{2}\right] + 2B_0 \\
&\quad + A_1 r^{-1/2}\cos\frac{\theta}{2}\left[(1-\nu)+(1+\nu)\sin^2\frac{\theta}{2}\right] \\
E\varepsilon_{yy} &= A_0 r^{-1/2}\cos\frac{\theta}{2}\left[(1-\nu)+(1+\nu)\sin\frac{\theta}{2}\sin\frac{3\theta}{2}\right] - 2\nu B_0 \\
&\quad + A_1 r^{-1/2}\cos\frac{\theta}{2}\left[(1-\nu)-(1+\nu)\sin^2\frac{\theta}{2}\right] \\
2G\gamma_{xy} &= A_0 r^{-1/2}\left[\sin\theta\cos\frac{3\theta}{2}\right] - A_1 r^{1/2}\left[\sin\theta\cos\frac{\theta}{2}\right]
\end{aligned}
\tag{3.16}
$$

Finally, the displacement components u_I and v_I in terms of coefficients A_0, A_1, and B_0 using Eq. (3.14) can be represented as

$$
\begin{aligned}
u_I &= \frac{A_0}{2G} r^{1/2}\left[(\kappa-1)\cos\frac{\theta}{2}+\sin\theta\sin\frac{\theta}{2}\right] \\
&+ \frac{A_1}{2G} r^{3/2}\left[\frac{\kappa-1}{3}\cos\frac{3\theta}{2}-\sin\theta\sin\frac{\theta}{2}\right]+\frac{B_0(\kappa+1)}{4G} r\cos\theta \\
v_I &= \frac{A_0}{2G} r^{1/2}\left[(\kappa+1)\sin\frac{\theta}{2}-\sin\theta\cos\frac{\theta}{2}\right] \\
&+ \frac{A_1}{2G} r^{3/2}\left[\frac{\kappa+1}{3}\sin\frac{3\theta}{2}-\sin\theta\cos\frac{\theta}{2}\right]-\frac{B_0\nu(\kappa+1)}{4G} r\sin\theta
\end{aligned}
\tag{3.17}
$$

where

$$
\begin{aligned}
&\kappa = \frac{3-\nu}{1+\nu} \text{ for plane stress and} \\
&\kappa = 3-4\nu \text{ for plane strain}
\end{aligned}
\tag{3.18}
$$

The above Eqs. (3.15), (3.16) and (3.17) are termed as three parameter stress, strain, and displacement equations, respectively under mode I loading. These equations can represent stresses, strains, and displacements from the crack tip to a point (r,θ) that is sufficiently away from the crack-tip (Fig. 3.1) but not very far away from crack-tip. The above equations are used extensively in experimental fracture mechanics (Dally and Sanford, 1987; Sarangi et al., 2012, 2010) and are termed as near field equations. The leading terms of stresses, strains and displacement components can be obtained by omitting the coefficients A_1, and B_0 and retaining terms associated with the term A_0 in the above field equations.

It is clear from Eqs. (3.15), and (3.16) that each stress and strain component is inversely proportional to the square of the radial distance r of a point from the crack tip and they tend to infinity as r approaches to zero. Such solutions are also called as *singular solutions*. Unlike the stress and strain components, the displacement equations (Eq. (3.17)) do not contain singularity and are finite near the crack tip. This is a typical characteristic of LEFM.

3.2.2 Mode II field equations

The Airy stress function in the generalized Westergaard approach for mode II fracture problems is given by (Sanford, 1979)

$$
\phi_{II} = \mathrm{Im}\,\overline{Y}_{II}(z) - y\,\mathrm{Re}\,\overline{Y}_{II}(z) - y\,\mathrm{Re}\,\overline{Z}_{II}(z) \tag{3.19}
$$

In this approach, an additional term $-y\,\mathrm{Re}\,\overline{Z}_{II}(z)$ is added to the conventional Westergaard approach. The complex analytic function $Z_{II}(z)$ and $Y_{II}(z)$ for the shear mode are defined as

$$Z_{II}(z)=\sum_{n=0}^{\infty}C_n z^{\frac{n-1}{2}}$$
$$Y_{II}(z)=\sum_{m=0}^{\infty}D_m Z^m \tag{3.20}$$

which are series types of functions (in terms of a complex variable $z=x+iy$) containing the infinite number of coefficients $(C_0,C_1,.....,D_0,D_1,.....)$ that can be determined using the boundary condition of a given problem. Using Eqs. (3.6), (3.7) and (3.19), the shear mode stress components for the entire domain can be obtained as

$$\begin{aligned}\sigma_{xx}&=y\,\mathrm{Re}\,Z_{II}^{'}+2\,\mathrm{Im}\,Z_{II}+y\,\mathrm{Re}\,Y_{II}^{'}+\mathrm{Im}\,Y\\ \sigma_{yy}&=-y\,\mathrm{Re}\,Z_{II}^{'}-y\,\mathrm{Re}\,Y_{II}^{'}+\mathrm{Im}\,Y_{II}\\ \tau_{xy}&=\mathrm{Re}\,Z_{II}-y\,\mathrm{Im}\,Z_{II}^{'}-y\,\mathrm{Im}\,Y_{II}^{'}\end{aligned} \tag{3.21}$$

Substitution of the series form of complex analytic functions $Z_{II}(z)$ and $Y_{II}(z)$ from Eq. (3.20) gives equations for the stress field in the whole domain which consists of the infinite number of unknown coefficients C_n and D_m. Thus equations for the stress components are given by

$$\begin{Bmatrix}\sigma_{xx}\\ \sigma_{yy}\\ \tau_{xy}\end{Bmatrix}=\sum_{n=0}^{N}C_n r^{(n-1/2)}\begin{Bmatrix}(n-\frac{1}{2})\sin\theta\cos(n-\frac{3}{2})\theta+2\sin(n-\frac{1}{2})\theta\\ -(n-\frac{1}{2})\sin\theta\cos(n-\frac{3}{2})\theta\\ \cos(n-\frac{1}{2})\theta-(n-\frac{1}{2})\sin\theta\sin(n-\frac{3}{2})\theta\end{Bmatrix}$$
$$+\sum_{m=0}^{M}D_m r^m\begin{Bmatrix}\sin m\theta+m\sin\theta\cos(m-1)\theta\\ \sin m\theta-m\sin\theta\cos(m-1)\theta\\ m\sin\theta\sin(m-1)\theta\end{Bmatrix} \tag{3.22}$$

Assuming plane stress conditions, the strain components are given by

$$\begin{aligned}E\varepsilon_{xx}&=(1-\nu)\,\mathrm{Im}\,Y_{II}+(1+\nu)y\,\mathrm{Re}\,Y_{II}^{'}+(1+\nu)y\,\mathrm{Re}\,Z_{II}^{'}+2\,\mathrm{Im}\,Z_{II}\\ E\varepsilon_{yy}&=(1-\nu)\,\mathrm{Im}\,Y_{II}-(1-\nu)y\,\mathrm{Re}\,Y_{II}^{'}-(1-\nu)y\,\mathrm{Re}\,Z_{II}^{'}-2\nu\,\mathrm{Im}\,Z_{II}\\ 2G\gamma_{xy}&=-2(1+\nu)\,\mathrm{Im}\,Y_{II}^{'}-2(1+\nu)y\,\mathrm{Im}\,Z_{II}^{'}+2(1+\nu)\,\mathrm{Re}\,Z_{II}\end{aligned} \tag{3.23}$$

Substitution of the series form of complex functions $Z_{II}(z)$ and $Y_{II}(z)$ from Eq. (3.20) gives the exact representation of the strain field and is given by

$$\begin{Bmatrix}\varepsilon_{xx}\\ \varepsilon_{yy}\\ \gamma_{xy}\end{Bmatrix}=\sum_{n=0}^{N}\frac{C_n}{E}r^{(n-\frac{1}{2})}\begin{Bmatrix}(1+\nu)(n-\frac{1}{2})\sin\theta\cos(n-\frac{3}{2})\theta+2\sin(n-\frac{1}{2})\theta\\ -(1+\nu)(n-\frac{1}{2})\sin\theta\cos(n-\frac{3}{2})\theta-2\nu\sin(n-\frac{1}{2})\theta\\ 2(1+\nu)\cos(n-\frac{1}{2})\theta-2(1+\nu)(n-\frac{1}{2})\sin\theta\sin(n-\frac{3}{2})\theta\end{Bmatrix}$$
$$+\sum_{m=0}^{M}\frac{D_m}{E}r^{m}\begin{Bmatrix}(1-\nu)\sin m\theta+(1+\nu)m\sin\theta\cos(m-1)\theta\\ (1-\nu)\sin m\theta-(1+\nu)m\sin\theta\cos(m-1)\theta\\ -2(1+\nu)m\sin\theta\sin(m-1)\theta\end{Bmatrix} \tag{3.24}$$

The displacement components in mode II loading conditions can be obtained by integrating the strain components in Eq. (3.24) and are given by

$$\begin{aligned}Eu_{II}&=(1+\nu)\,\mathrm{Re}\,Z_{II}+(1+\nu)y\,\mathrm{Re}\,Y_{II}+(1+\nu)y\,\mathrm{Im}\,\overline{Y}_{II}+2\,\mathrm{Im}\,\overline{Z}_{II}\\ Ev_{II}&=-(1+\nu)y\,\mathrm{Im}\,Z_{II}-(1+\nu)y\,\mathrm{Im}\,Y_{II}-(1-\nu)\,\mathrm{Re}\,\overline{Z}_{II}-2\,\mathrm{Re}\,\overline{Y}_{II}\end{aligned} \tag{3.25}$$

and substitution of series forms of complex functions $Z_{II}(z)$ and $Y_{II}(z)$ results to

$$\begin{Bmatrix}u_{II}\\ v_{II}\end{Bmatrix}=\sum_{n=0}^{N}\frac{C_n}{E}r^{(n+\frac{1}{2})}\begin{Bmatrix}\frac{4}{2n+1}\sin(n+\frac{1}{2})\theta+(1+\nu)\sin\theta\cos(n-\frac{1}{2})\theta\\ -\frac{2(\nu-1)}{2n+1}\cos(n+\frac{1}{2})\theta-(1+\nu)\sin\theta\sin(n-\frac{1}{2})\theta\end{Bmatrix}$$
$$+\sum_{m=0}^{M}\frac{D_m}{E}r^{(m+1)}\begin{Bmatrix}\frac{1-\nu}{m+1}\sin(m+1)\theta+(1+\nu)\sin\theta\cos m\theta\\ -\frac{2}{m+1}\cos(m+1)\theta-(1+\nu)\sin\theta\sin m\theta\end{Bmatrix} \tag{3.26}$$

The stresses and strains in the vicinity of the crack tip can be represented by the first term C_0 or the leading term in Eqs. (3.22) and (3.24) respectively. More number of terms should be added for stresses and strains at points that are away from the crack tip. Considering the terms corresponding to the coefficients $C_0, C_1,$ and D_0, the stress components are given by

$$\begin{aligned}\sigma_{xx}&=C_0r^{-1/2}\left(-\frac{1}{2}\sin\theta\cos\frac{3\theta}{2}-2\sin\frac{\theta}{2}\right)+0D_0+C_1r^{1/2}\left(\frac{1}{2}\sin\theta\cos\frac{\theta}{2}+2\sin\frac{\theta}{2}\right)\\ \sigma_{yy}&=C_0r^{-1/2}\left(\frac{1}{2}\sin\theta\cos\frac{3\theta}{2}\right)+0D_0+C_1r^{1/2}\left(-\frac{1}{2}\sin\theta\cos\frac{\theta}{2}\right)\\ \tau_{xy}&=C_0r^{-1/2}\left(\cos\frac{\theta}{2}-\frac{1}{2}\sin\theta\sin\frac{3\theta}{2}\right)+0D_0+C_1r^{1/2}\left(\cos\frac{\theta}{2}+\frac{1}{2}\sin\theta\sin\frac{\theta}{2}\right)\end{aligned} \tag{3.27}$$

and strain components are given by

$$
\begin{aligned}
E\varepsilon_{xx} &= -C_0 r^{-1/2}\sin\frac{\theta}{2}\left[(1+\nu)\cos\frac{\theta}{2}\cos\frac{3\theta}{2}+2\right] \\
&\quad + C_1 r^{1/2}\sin\frac{\theta}{2}\left[(1+\nu)\cos^2\frac{\theta}{2}+2\right]+0D_0 \\
E\varepsilon_{yy} &= -C_0 r^{-1/2}\sin\frac{\theta}{2}\left[2\nu+(1+\nu)\cos\frac{\theta}{2}\cos\frac{3\theta}{2}\right] \\
&\quad - C_1 r^{1/2}\sin\frac{\theta}{2}\left[(1+\nu)\cos^2\frac{\theta}{2}+2\nu\right]+0D_0 \\
G\gamma_{xy} &= C_0 r^{-1/2}\cos(\frac{\theta}{2})\left[1-\sin\frac{\theta}{2}\sin\frac{3\theta}{2}\right] \\
&\quad - C_1 r^{1/2}\cos\frac{\theta}{2}\left[1+\sin^2\frac{\theta}{2}\right]+0D_0
\end{aligned}
\tag{3.28}
$$

The displacement components u_{II} and v_{II} in terms of coefficients $C_0, C_1,$ and D_0 can be obtained using Eq. (3.26) as

$$
\begin{aligned}
u_{II} &= \frac{C_0}{2G} r^{1/2}\left[(\kappa+1)\sin\frac{\theta}{2}+\sin\theta\cos\frac{\theta}{2}\right] \\
&\quad + \frac{C_1}{2G} r^{3/2}\left[\frac{(\kappa+1)}{3}\sin\frac{3\theta}{2}+\sin\theta\cos\frac{\theta}{2}\right]+\frac{D_0(\kappa+1)}{4G}r\sin\theta \\
v_{II} &= \frac{C_0}{2G} r^{1/2}\left[(1-\kappa)\cos\frac{\theta}{2}+\sin\theta\sin\frac{\theta}{2}\right] \\
&\quad + \frac{C_1}{2G} r^{3/2}\left[\frac{(1-\kappa)}{3}\cos\frac{3\theta}{2}+\sin\theta\sin\frac{\theta}{2}\right]-\frac{D_0(\kappa+1)}{4G}r\cos\theta
\end{aligned}
\tag{3.29}
$$

where

$$
\begin{aligned}
\kappa &= \frac{3-\nu}{1+\nu} \text{ for plane stress and} \\
\kappa &= 3-4\nu \text{ for plane strain}
\end{aligned}
\tag{3.30}
$$

The above Eqs.(3.27), (3.28) and (3.29) are termed as three parameter stress, strain, and displacement equations respectively for mode II loading. These equations can represent stresses, strains, and displacements from the crack tip to a point (r,θ) that is sufficiently away from the crack-tip but not very far away from crack-tip (Dally and Sanford, 1987; Sarangi et al., 2012, 2010).

3.2.3 Leading terms for mode I, mode II and mixed mode I/II loading

The leading terms of stresses, strains, and displacement components can be obtained by omitting the coefficients $A_1, C_1, B_0,$ and D_0 and retaining terms associated with the coefficients

A_0 and C_0 in the near field equations. Thus the displacement leading terms near the crack tip under plane stress conditions corresponding to mode I loading can be written as (using Eq. (3.17))

$$\begin{aligned} u_I &= \frac{A_0}{2G} r^{1/2} \left[(\kappa - 1)\cos\frac{\theta}{2} + \sin\theta \sin\frac{\theta}{2} \right] \\ v_I &= \frac{A_0}{2G} r^{1/2} \left[(\kappa + 1)\sin\frac{\theta}{2} - \sin\theta \cos\frac{\theta}{2} \right] \end{aligned} \tag{3.31}$$

Similarly, for mode II loading, the displacements in terms of the leading term can be written as (using Eq. (3.29))

$$\begin{aligned} u_{II} &= \frac{C_0}{2G} r^{1/2} \left[(\kappa + 1)\sin\frac{\theta}{2} + \sin\theta \cos\frac{\theta}{2} \right] \\ v_{II} &= \frac{C_0}{2G} r^{1/2} \left[(1 - \kappa)\cos\frac{\theta}{2} + \sin\theta \sin\frac{\theta}{2} \right] \end{aligned} \tag{3.32}$$

In case of mixed mode (I/II) loading the displacement components can be obtained using the principle of superposition as

$$\begin{aligned} u &= u^I + u^{II} \\ v &= v^I + v^{II} \end{aligned} \tag{3.33}$$

$$\begin{aligned} u &= \frac{A_0}{2G} r^{1/2} \left[(\kappa - 1)\cos\frac{\theta}{2} + \sin\theta \sin\frac{\theta}{2} \right] + \frac{C_0}{2G} r^{1/2} \left[(\kappa + 1)\sin\frac{\theta}{2} + \sin\theta \cos\frac{\theta}{2} \right] \\ v &= \frac{A_0}{2G} r^{1/2} \left[(\kappa + 1)\sin\frac{\theta}{2} - \sin\theta \cos\frac{\theta}{2} \right] + \frac{C_0}{2G} r^{1/2} \left[(1 - \kappa)\cos\frac{\theta}{2} + \sin\theta \sin\frac{\theta}{2} \right] \end{aligned} \tag{3.34}$$

The mode I stress intensity factor K_I is formally defined as

$$K_I = \lim_{r \to 0} \sqrt{2\pi r}\ \sigma_{yy}(r, \theta = 0^0) \tag{3.35}$$

which relates K_I to A_0 as

$$K_I = \sqrt{2\pi}\ A_0 \tag{3.36}$$

Similarly, mode II stress intensity factor K_{II} can be defined as

$$K_{II} = \lim_{r \to 0} \sqrt{2\pi r}\ \tau_{xy}(r, \theta = 0^0) \tag{3.37}$$

which leads to the relationship between K_{II} and C_0 as

$$K_{II} = \sqrt{2\pi}\ C_0 \tag{3.38}$$

Thus the coefficients A_0 and C_0 are related to the SIFs K_I and K_{II} respectively.

3.3 Prediction of mixed mode (I/II) fatigue life

Ever since the fatigue crack growth correlation by Paris et al. (1961), several investigations are carried out utilizing the physical and field variables around the crack tip to quantify the FCG rate. Most of such investigations under cyclic tensile loading are for the crack growth under opening mode or mode I. However, in practice, due to the random orientation of the crack with the loading direction or due to the external constraints, the cracks are often subjected to mixed mode loading. In the presence of shear loading, sliding forces between the crack surfaces and the crack wedging mechanism are influential in the FCG behavior of materials. The effect of individual mode SIFs (or any other fracture mechanics parameter) needs to be considered in mixed mode loading conditions. Several crack growth models are developed to quantify the FCG rate under mixed mode (I/II) loading. One of the notable contributions is the modified Paris' law in terms of the equivalent stress intensity factor, ΔK_{eq} proposed by Tanaka (1974). Within the context of the linear elastic fracture mechanic (LEFM), this modified Paris law along with various ΔK_{eq} models, is the most widely employed for the numerical estimation of mixed mode (I/II) fatigue life the cracked bodies. This section describes the current practice of numerical estimation of the mixed mode (I/II) fatigue life of engineering components.

The well-known Paris law for mode I fatigue crack growth is given as

$$\frac{\mathrm{d}a}{\mathrm{d}N} = C\left(\Delta K\right)^m \tag{3.39}$$

where C and m are known as Paris' material constants. On the other hand, the modified Paris' law for mixed mode (I/II) fatigue crack growth as a function of the mixed mode SIFs (Fig. 3.2 (a)) is given as

$$\frac{\mathrm{d}a}{\mathrm{d}N} = C\left(\Delta K_{eq}\right)^m \tag{3.40}$$

where ΔK_{eq} is the equivalent stress intensity factor and is the function of

$$\Delta K_{eq} = f\left(\Delta K_I, \Delta K_{II}\right) \tag{3.41}$$

for the mixed mode (I/II) loading conditions and

$$\Delta K_I = K_{I,\max} - K_{I,\min} \text{ and } \Delta K_{II} = K_{II,\max} - K_{II,\min} \tag{3.42}$$

where $K_{I,\max}$ and $K_{I,\min}$ are the maximum and minimum mode I SIFs and $K_{II,\max}$ and $K_{II,\min}$ are the maximum and minimum mode II SIFs.

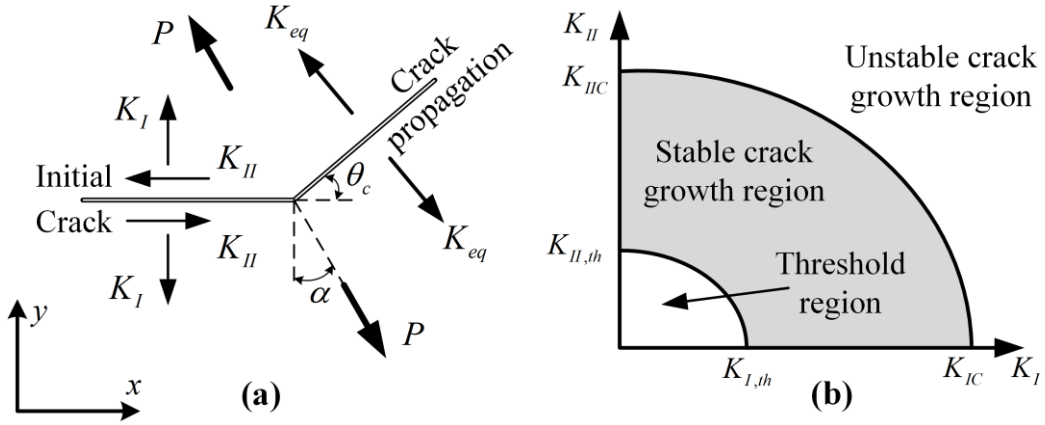

Figure 3.2 (a) K_{eq} as a function of K_I and K_{II} (b) Fracture limit curve under mixed mode (I/II) loading

Figure 3.2 (b) shows a typical fracture limit curve for the mixed mode (I/II) loading where the threshold region, stable and unstable crack growth regions are shown. Fatigue crack growth occurs if the equivalent SIF exceeds the material dependent threshold value (Reimers, 1991; Richard et al., 2014)

$$\Delta K_{eq} \geq K_{I,th} \tag{3.43}$$

and unstable fracture occurs if

$$K_{eq-\max} \geq K_{IC} \tag{3.44}$$

For a finite, predefined crack increment Δa, the associated fatigue life can be estimated as

$$\int_0^{\Delta a} \frac{da}{C\left(\Delta K_{eq}\right)^m} = \int_0^{\Delta N} dN = \Delta N \tag{3.45}$$

If an increment $\Delta a_i \,(= a_{i+1} - a_i)$ is very small, then the Eq. (3.45) can be discretized and ΔN in the above equation for an i^{th} step can be estimated as

$$\frac{\Delta a_i}{C\left(\Delta K_{eq}^i\right)^m} = \Delta N_i \tag{3.46}$$

Eq. (3.46) is employed in the present investigation for the numerical estimation of the fatigue life for a predefined crack increment of Δa. Although some recommendations are available on the selection of the value of Δa, smaller sizes of Δa provides an accurate prediction of fatigue life. as indicated by the Eq. (3.42). In the present investigation, a Δa value of 0.5 mm is selected by conducting numerical simulations. In the incremental crack growth

simulations, it is assumed that the ΔK_{eq} remains same during the crack increment. The ΔK_{eq}^{i} for an i^{th} step is computed at a crack length of a_i (Ma et al., 2006), and the mixed mode SIFs are calculated using the proposed crack flank displacement method. As far as the Paris' material constants C and m are concerned in Eq. (3.40), the current practice in numerical simulation of the mixed mode fatigue crack propagation is to use the values from mode I experiments (Blažić et al., 2014; Kim and Lee, 2007; Portela et al., 1993; Reimers, 1991; Yan et al., 1992). The approach in which a pre-defined value crack increment (Δa) is used for estimation of fatigue life is known as the incremental crack extension method, and this approach is used for all the mixed mode FCG simulations discussed in the subsequent chapters. Figure 3.3 illustrates the typical procedure in the incremental crack growth approach adopted in the present investigation. Steps involved in this approach are as follows.

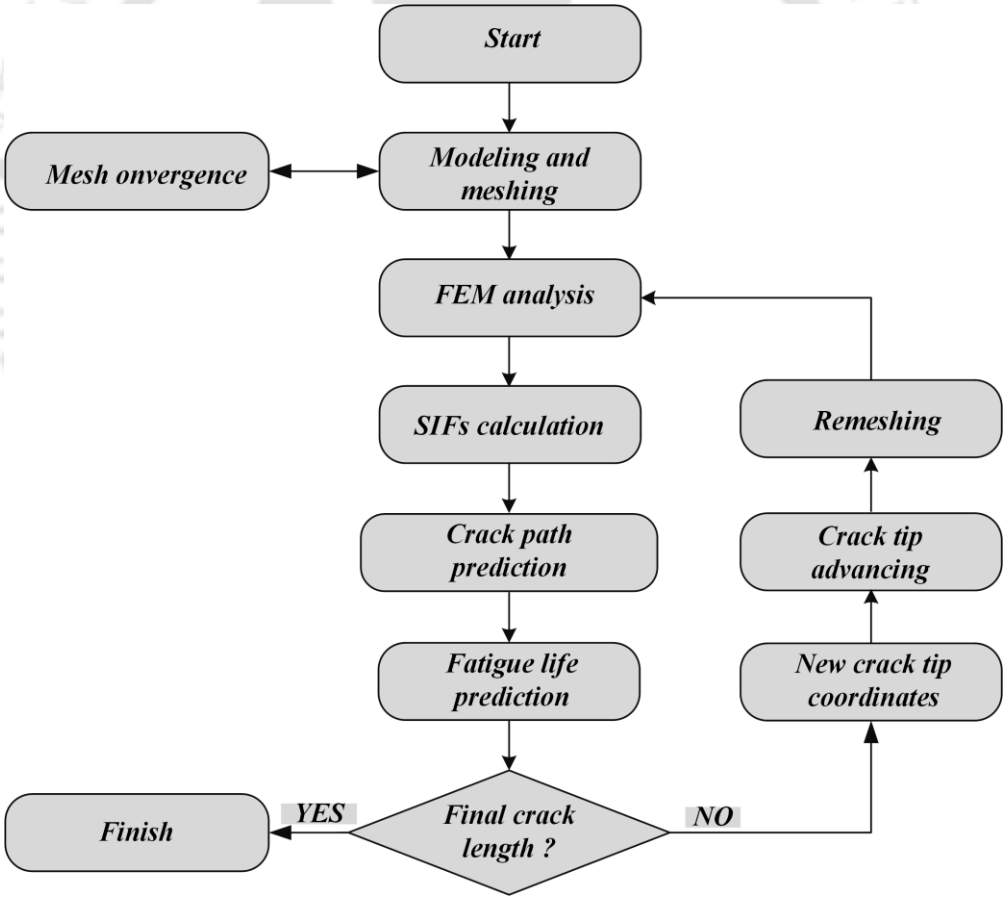

Figure 3.3 Incremental crack growth approach for the FCG simulation

1. Assume the fatigue life at the initial step is zero
2. Finite element analysis of the selected cracked configuration is carried out

3. Compute the mode I and mode II SIFs (K_I and K_{II})
4. Compute the crack growth direction using a crack growth criterion. In the present investigation, MTS criterion is used
5. Assume a virtual crack increment Δa = 0.5 mm.
6. Calculate the fatigue life using Eq. (3.46) and this incremental life to the previous life
7. Extended the existing crack by an amount of Δa in the direction computed using the MTS criterion.
8. Remesh the whole cracked body with extended crack length
9. Repeat the steps from 2 to 8 until the critical crack length is reached or required crack length is reached.

3.4 Equivalent SIF (ΔK_{eq}) models

After the introduction of ΔK_{eq} concept by Tanaka (1974), a large number of various ΔK_{eq} have been proposed over the last three decades. The theoretical background of various available ΔK_{eq} models in the literature are presented in the following sections.

3.4.1 Tanaka's ΔK_{eq} model

Tanaka proposed two ΔK_{eq} models along with the modified Paris law. He assumed that there is no interaction between the deformations coming from individual modes of loading. The first model is based on the dislocation theory proposed by Weertman (1966). It is hypothesized that the fatigue crack grows when the absolute value of the crack tip displacement reaches a critical value. It is assumed that the plastic deformation at the crack tip due tip opening and shearing mode are not interactive. Also, the effective crack tip displacement is assumed to be the vector sum of mode I and mode II crack tip displacements. Following these assumptions, Tanaka proposed a ΔK_{eq} model as

$$\Delta K_{eq} = (\Delta K_I^4 + 8\Delta K_{II}^4)^{1/4} \tag{3.47}$$

Based on the dislocation based fatigue crack growth model by Bilby et al. (1963) and its extension by Lardner (1968), Tanaka proposed another ΔK_{eq} model. In this model, Tanaka

postulated that the effective crack tip displacement is the sum of absolute values of the mode I and mode II displacements, and the crack growth rate is equal to the reverse component of the displacement at the crack tip. This leads to the following ΔK_{eq} model

$$\Delta K_{eq} = (\Delta K_I^2 + 2\Delta K_{II}^2)^{1/2} \tag{3.48}$$

3.4.2 Irwin's ΔK_{eq} model

Using Irwin's energy release rate criterion, the total energy release rate can be expressed as the sum of individual mode energy release rates.

$$G = G_I + G_{II} + G_{III} \tag{3.49}$$

where G_I, G_{II}, and G_{III} are the energy release rates for mode I, mode II, and mode III, respectively. In LEFM, the relationship between G and K can be written as

$$G_I = K_I^2 / E', \quad G_{II} = K_{II}^2 / E', \quad \text{and} \quad G_{III} = K_{III}^2 (1+\nu) / E' \tag{3.50}$$

where

$$\begin{aligned} E' &= E && \text{for plane stress} \\ E' &= E/(1-\nu^2) && \text{for plane strain} \end{aligned} \tag{3.51}$$

Assuming

$$G = K_{eq}^2 / E' \tag{3.52}$$

then in the mixed mode,

$$\begin{aligned} K_{eq}^2 &= K_I^2 + K_{II}^2 + K_{III}^2 (1+\nu) && \text{for plane stress} \\ K_{eq}^2 &= K_I^2 + K_{II}^2 + K_{III}^2 / (1-\nu) && \text{for plane strain} \end{aligned} \tag{3.53}$$

and thus for plane stress (Miranda et al., 2007)

$$\Delta K_{eq} = \left(\Delta K_I^2 + \Delta K_{II}^2 + \Delta K_{III}^2 (1+\nu) \right)^{1/2} \tag{3.54}$$

In case of two dimensional mixed mode fatigue crack growth problems Irwin's model Eq. (3.54) can be simplified to

$$\Delta K_{eq} = \left(\Delta K_I^2 + \Delta K_{II}^2 \right)^{1/2} \tag{3.55}$$

Although Irwin's ΔK_{eq} model in Eq. (3.55) is originally developed for elastostatic mixed mode (I/II) fracture conditions, but the above model has been extensively used in the modified Paris law (Eq. (3.40)) for prediction of the mixed mode (I/II) fatigue lives.

3.4.3 Richard's ΔK_{eq} model

In the generalized fracture criterion proposed by Richard (Henn et al., 1988; Richard et al., 1991) the ΔK_{eq} is defined in the same way as the equivalent stress in the classical hypothesis. Following this, the ΔK_{eq} model given by Richard (Henn et al., 1988; Richard et al., 2003, 1991) is

$$\Delta K_{eq} = \frac{\Delta K_I}{2} + \frac{1}{2}\sqrt{\Delta K_I^2 + 4(\beta \Delta K_{II})^2} \tag{3.56}$$

The term $\beta = 1.155$ is set by considering the relation between K_I and K_{II} in the fracture limit curve of the maximum tangential stress criterion. Henn et al. (1988) and Richard et al. (1991) also proposed a modified form of their ΔK_{eq} model (Eq. (3.56)) of the following form

$$\Delta K_{eq} = \frac{\Delta K_I}{2} + \frac{1}{2}\sqrt{\Delta K_I^2 + 6\Delta K_{II}{}^2} \tag{3.57}$$

Eq. (3.56) is widely used for the mixed mode (I/II) FCG rate correlation and life prediction.

3.4.4 Yan's ΔK_{eq} model

Based on the maximum tangential stress (MTS) criterion proposed by Erdogan and Sih (1963), Yan et al. (1992) proposed another ΔK_{eq} model for in-plane mixed mode fatigue loading. According to the MTS criterion, under mixed mode (I/II) loading, the crack starts to grow in a direction (θ_0) in which the tangential tensile stress reaches the maximum. Using the expression of maximum tangential stress, Yan et al. (1992) identified the possibility of the following ΔK_{eq} model that can be used along with the modified Paris' law

$$\Delta K_{eq} = \frac{1}{2}\cos\frac{\theta_0}{2}\left[\Delta K_I(1+\cos\theta_0) - 3\Delta K_{II}\sin\theta_0\right] \tag{3.58}$$

3.4.5 Hussain's ΔK_{eq} model

For solving the elasticity problem of a deflected crack under plane loading conditions, Hussain et al. (1974) used a complex variable mapping function to map a crack into a unit circle. Using the variable mapping and the path independent integral, the energy release rate is also obtained. The fundamental assumption behind this criterion is that the crack extension occurs in a direction $\theta = \theta_o$ that maximizes G, leading to the maximum fracturing energy

release rate $(G_{\max})$ criterion. Miranda et al. (2007) suggested the presence of a ΔK_{eq} model in the expression of $G_{\max}$, which is given as follows.

$$\Delta K_{eq} = \sqrt{\frac{4}{\left(3+\cos^2\theta_0\right)^2}\left(\frac{1-\theta_0/\pi}{1+\theta_0/\pi}\right)^{\theta/\pi}\begin{bmatrix}\left(1+3\cos^2\theta_0\right)\Delta K_I^2 \\ +4\sin 2\theta_0\,\Delta K_I \Delta K_{II} \\ +\left(9-5\cos^2\theta_0\right)\Delta K_{II}^2\end{bmatrix}} \tag{3.59}$$

3.4.6 Forth's ΔK_{eq} model

Based on the mixed mode experiments on an aluminum alloy Forth et al. (2002) proposed an empirical ΔK_{eq} model as

$$\Delta K_{eq} = \left(\Delta K_I^2 + A\Delta K_{II}^2\right)^{1/2} \tag{3.60}$$

where A is a material dependent constant.

3.4.7 Tamilselvan's ΔK_{eq} model

Tamilselvan et al. (2005) proposed a mixed-mode fatigue crack growth based on a unified model as

$$\Delta K_{eq} = \sqrt{\Delta K_{I\theta}^2 + K_{CR}^2 \Delta K_{I\theta}^2} \tag{3.61}$$

where K_{CR} is the ratio of the fracture toughness and is given by

$$K_{CR} = \frac{K_{Ic}}{K_{IIc}} \tag{3.62}$$

3.4.8 Sih's ΔK_{eq} model

Based on the strain energy density principle, Sih (1974) proposed the minimum strain energy density $S_{\min}$ criterion, assuming that the crack propagates in a direction $\theta = \theta_o$ that minimizes the strain energy S around the crack tip. The associated equivalent SIF is then calculated at $\theta = \theta_o$ that minimizes the expression as

$$\Delta K_{eq}^2 = \frac{1}{4(8\kappa-5)}\begin{Bmatrix}(\kappa-\cos\theta_0)(1+\cos\theta_0)\Delta K_I^2 \\ +2\sin\theta_0\left[\cos\theta_0-(\kappa-1)\right]\Delta K_I\Delta K_{II}+ \\ \left[4(\kappa+1)(1-\cos\theta_0)+(1+\cos\theta_0)(3\cos\theta_0-1)\right]\Delta K_{II}^2 \\ +4\Delta K_{III}^2\end{Bmatrix} \tag{3.63}$$

The material constants C and m of Paris' law are not applicable to this model, equivalent values of C and m needs to be estimated by equating it to the Paris' law for mode I loading.

3.4.9 Demir's ΔK_{eq} model

Recently, Demir et al. (2018) proposed another empirical model for ΔK_{eq} using the nonlinear regression analysis of the numerical and experimental results of the CTS specimen. The proposed ΔK_{eq} model is given by

$$\Delta K_{eq} = \left(1.0519\ \Delta K_I^4 - 0.035\ \Delta K_{II}^4 + 2.3056\ \Delta K_I^2 \Delta K_{II}^2\right)^{1/4} \tag{3.64}$$

Apart from the above expressions, many other ΔK_{eq} models can be found in review papers (Qian and Fatemi, 1996a; Rozumek and Macha, 2009) and articles (Miranda et al., 2007; Richard et al., 2005; Tavares et al., 2019; Wang et al., 2017).

3.5 Prediction of fatigue crack growth direction

In the mixed mode fatigue, the crack does not grow in a self-similar direction; instead, it grows at an angle to the axis of the crack. In order to predict the direction of crack growth, a large number of criteria are available (Qian and Fatemi, 1996a; Richard et al., 2005; Rozumek and Macha, 2009). In the present investigation, two criteria are employed for prediction of the direction of growth of the fatigue crack. The background theory of these two criteria presented in the following sections.

3.5.1 Maximum tangential stress (MTS) criterion

Accurate prediction of fatigue crack path is essential as the inaccurate path estimation can lead to erroneous fatigue life prediction. It is worth noting that various criteria employed for numerical simulation of the crack path in mixed mode fatigue loading conditions are developed for elastostatic cases (Mróz and Mróz, 2010; Qian and Fatemi, 1996a; Rozumek and Macha,

2009; Sajjadi et al., 2015). Among the established criterion, the maximum tangential stress (MTS) criterion proposed by Erdogan and Sih (1963) is widely in use. According to this criterion, the crack propagates in a radial direction (θ_c) from the crack tip in which the tangential stress $(\sigma_{\theta\theta})$ becomes maximum $(\sigma_{\theta\theta,\max})$, and the unstable fracture takes place when the tangential stress (hoop stress) reaches a critical value. Accordingly, the hoop stress in the vicinity of the crack tip is given by (Erdogan and Sih, 1963)

$$\sigma_{\theta\theta} = \frac{K_I}{\sqrt{2\pi r}}\left(\frac{3}{4}\cos\frac{\theta}{2} + \frac{1}{4}\cos\frac{3\theta}{2}\right) + \frac{K_{II}}{\sqrt{2\pi r}}\left(-\frac{3}{4}\sin\frac{\theta}{2} - \frac{3}{4}\sin\frac{3\theta}{2}\right) \tag{3.65}$$

The crack will grow when

$$\frac{\partial\sigma_{\theta\theta}}{\partial\theta} = 0, \text{ and } \frac{\partial^2\sigma_{\theta\theta}}{\partial\theta^2} < 0 \tag{3.66}$$

that is

$$\tan^2\frac{\theta}{2} - \frac{K_I}{2K_{II}}\tan\frac{\theta}{2} - \frac{1}{2} = 0 \tag{3.67}$$

and

$$-\frac{3}{2}\left[\left(\frac{1}{2}\cos^3\frac{\theta}{2} - \cos\frac{\theta}{2}\sin^2\frac{\theta}{2}\right) + \frac{K_{II}}{K_I}\left(\sin^3\frac{\theta}{2} - \frac{7}{2}\sin\frac{\theta}{2}\cos^2\frac{\theta}{2}\right)\right] < 0 \tag{3.68}$$

By maximizing the tangential stress component $\left(\partial\sigma_{\theta\theta,\max}/\partial\theta = 0\right)$, the crack extension direction θ_c can be found as

$$K_I \sin\theta_c + K_{II}(3\cos\theta_c - 1) = 0 \tag{3.69}$$

The solution of the above equation can be expressed as

$$\begin{aligned} \theta_c &= 2\tan^{-1}\left[\frac{1}{4}\frac{K_I}{K_{II}} - \frac{1}{4}\sqrt{\left(\frac{K_I}{K_{II}}\right)^2 + 8}\right] \quad \text{for} \quad K_{II} > 0 \\ \theta_c &= 2\tan^{-1}\left[\frac{1}{4}\frac{K_I}{K_{II}} + \frac{1}{4}\sqrt{\left(\frac{K_I}{K_{II}}\right)^2 + 8}\right] \quad \text{for} \quad K_{II} < 0 \end{aligned} \tag{3.70}$$

where positive θ_c is defined as the angle measured in the anticlockwise direction with respect to the initial crack orientation direction (Fig. 3.4).

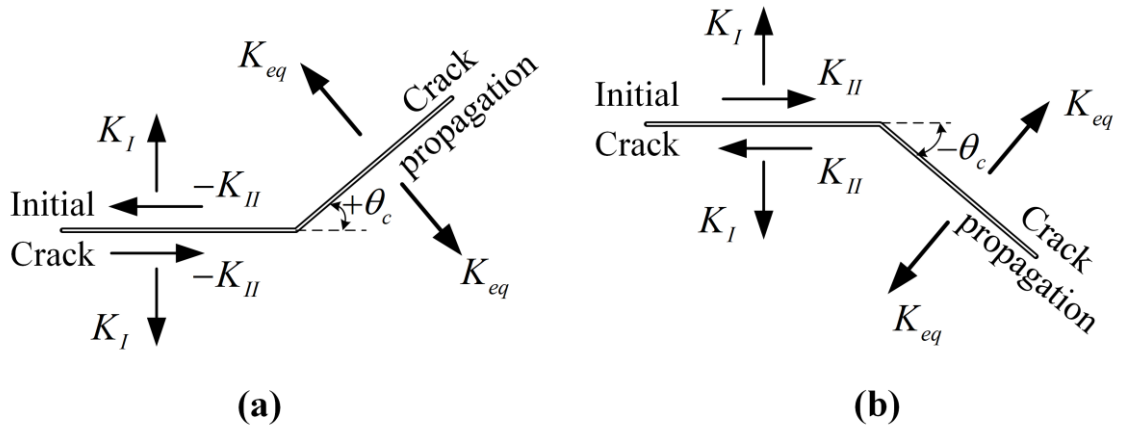

Figure 3.4 Direction of the K_{II} and crack growth angle (a) positive θ_c (b) negative θ_c

It is evident from Eq. (3.70) that the crack initiation angle in the mixed mode (I/II) is independent of the state of stress and the material properties.

3.5.2 Minimum strain energy density (SED) criterion

The minimum strain energy density (SED) criterion, proposed by Sih (1973), is based on the local strain energy density at a confined area around the crack tip. This criterion postulates that the crack initiates and grows in the direction in local strain energy density around the crack tip at a constant radius is minimum. The region within this constant radius is known as the core region. The main hypotheses of this theory state that the crack initiates and grows in the direction of minimum strain energy density (SED) and crack extension onsets when the minimum value of the strain energy density factor reaches a critical value $(S_{cr} = S_{in})$. Accordingly, the strain energy density can be written as

$$S = a_{11}K_I^2 + 2a_{12}K_I K_{II} + a_{22}K_{II}^2 \tag{3.71}$$

where

$$a_{11} = \frac{1}{16G}\left(3 - 4\nu - \cos\theta\right)\left(1 + \cos\theta\right) \tag{3.72}$$

$$a_{12} = \frac{1}{16G}2\sin\theta\left(\cos\theta - 1 + 2\nu\right) \tag{3.73}$$

$$a_{22} = \frac{1}{16G}\left(4(1-\nu)(1+\cos\theta) + (3\cos\theta - 1)(1+\cos\theta)\right) \tag{3.74}$$

and

$$a_{33} = \frac{1}{16G}4 \tag{3.75}$$

ν is the Poisson's ratio and G is the shear modulus. θ is the polar coordinate component. In mathematical form, *S*-criterion can be stated as

$$\frac{\partial S}{\partial \theta} = 0, \qquad \frac{\partial^2 S}{\partial \theta^2} > 0 \tag{3.76}$$

Using the above expressions, the propagation angle θ_c corresponding to a minimum S can be obtained. In the SED criterion, the crack initiation angle is dependent on the state of stress and the material properties.

3.6 Finite element formulation

In the present investigation, the mixed mode (I/II) fatigue life is estimated using finite element (FE) simulation of various specimens. As a part of the simulation, linear elastic finite element analysis of various cracked configurations has been carried out using displacement based FE method. For this purpose, commercial software ANSYS® has been utilized for FE analysis. In the present work, PLANE183 element available in ANSYS® is used for discretization of the cracked domains. PLANE183 is a higher order 2D, eight noded isoparametric quadrilateral element (Q8). These elements are well suited for both plane stress and plane strain conditions. The crack tip elements have been modeled using quarter point elements (QPEs) obtained using PLANE 183 to incorporate the square root singularity which arises in LEFM (Barsoum, 1976). The details of these elements, including the FE formulation, have been presented in the following sections.

3.6.1 Eight noded quadrilateral element

The eight noded isoparametric quadrilateral element (Q8), which permits modeling of complicated shapes, is generally used to solve fracture mechanics problems. The Q8 is shown in Fig. 3.5.

Being an isoparametric element, the geometric variables are expressed in a similar way as the field variable. Thus, in Q8

$$x = \sum_{i=1}^{8} N_i x_i \tag{3.77}$$

$$y = \sum_{i=1}^{8} N_i y_i \tag{3.78}$$

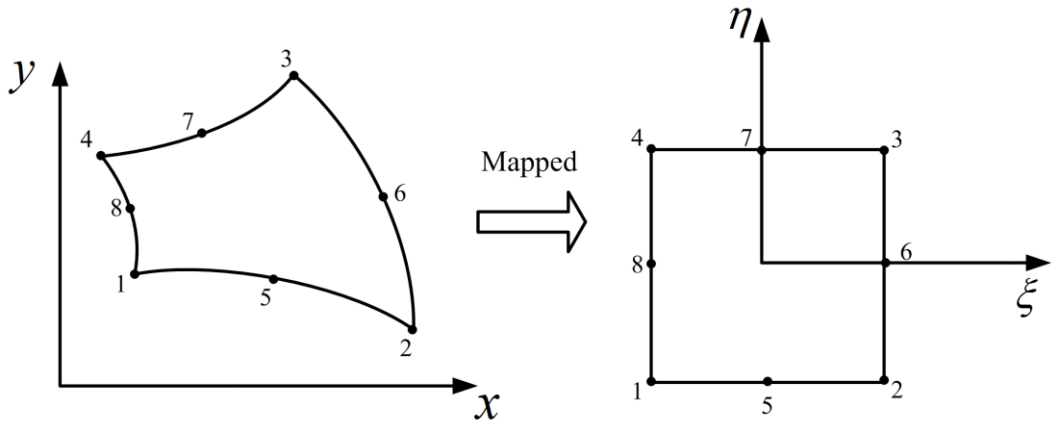

Figure 3.5 Eight noded quadrilateral isoparametric element represented in natural coordinates

Similarly, the field variables are also represented as

$$u = \sum_{i=1}^{8} N_i u_i \tag{3.79}$$

$$v = \sum_{i=1}^{8} N_i v_i \tag{3.80}$$

where the $N_i (i = 1, 2..., 8)$ are shape functions, (x_i, y_i) are nodal coordinates and (u_i, v_i) are nodal displacements. Shape function must be expressed in a natural coordinate system for numerical integration. Natural coordinate (ξ, η) systems are dimensionless and have a maximum absolute magnitude of one. They are defined with reference to the element rather than with reference to the global coordinate system in which the element resides (Fig. 3.5). The shape functions for a Q8 element are expressed in natural coordinates as

$$\begin{aligned}
N_1 &= \frac{1}{4}(1+\xi)(1-\eta) - \frac{1}{2}(N_8 + N_5) & N_5 &= \frac{1}{2}(1-\xi^2)(1-\eta) \\
N_2 &= \frac{1}{4}(1-\xi)(1+\eta) - \frac{1}{2}(N_5 + N_6) & N_6 &= \frac{1}{2}(1+\xi)(1-\eta^2) \\
N_3 &= \frac{1}{4}(1-\xi)(1-\eta) - \frac{1}{2}(N_6 + N_7) & N_7 &= \frac{1}{2}(1-\xi^2)(1-\eta) \\
N_4 &= \frac{1}{4}(1+\xi)(1-\eta) - \frac{1}{2}(N_7 + N_8) & N_8 &= \frac{1}{2}(1+\xi)(1-\eta^2)
\end{aligned} \tag{3.81}$$

The displacements within the element in terms of nodal displacements can be expressed as

$$\{U\} = \begin{Bmatrix} u \\ v \end{Bmatrix} = [N]\{X\}_e \tag{3.82}$$

where $\{U\}$ is the displacement vector of an element, with the shape function matrix

$$[N]=\begin{bmatrix} N_1 & 0 & N_2 & 0 & \cdots & N_7 & 0 & N_8 & 0 \\ & N_1 & 0 & N_2 & \cdots & 0 & N_7 & 0 & N_8 \end{bmatrix} \tag{3.83}$$

and nodal displacement

$$\{X\}_e^T=\{u_1 \quad v_1 \quad u_2 \quad v_2 \quad u_3 \quad v_3 \quad u_4 \quad v_4 \quad u_5 \quad v_5 \quad u_6 \quad v_6 \quad u_7 \quad v_7 \quad u_8 \quad v_8\} \tag{3.84}$$

The governing equations of equilibrium for the plane elastostatic problems are given by

$$\frac{\partial \sigma_{xx}}{\partial x}+\frac{\partial \tau_{xy}}{\partial y}+f_x=0 \tag{3.85}$$

$$\frac{\partial \tau_{xy}}{\partial x}+\frac{\partial \sigma_{yy}}{\partial y}+f_y=0 \tag{3.86}$$

where f_x and f_y denote the body force per unit volume along the x and y direction; σ_{xx} and σ_{yy} are the normal stresses and τ_{xy} is the in-plane shear stress. The strain matrix associated with the plane stress and plane strain problems in terms of the nodal displacement vector is then given by

$$\{\varepsilon\}=\begin{Bmatrix} \varepsilon_{xx} \\ \varepsilon_{yy} \\ \gamma_{xy} \end{Bmatrix}=\begin{Bmatrix} \dfrac{\partial u}{\partial x} \\ \dfrac{\partial v}{\partial y} \\ \dfrac{\partial u}{\partial y}+\dfrac{\partial v}{\partial x} \end{Bmatrix}=\begin{bmatrix} \dfrac{\partial}{\partial x} & 0 \\ 0 & \dfrac{\partial}{\partial y} \\ \dfrac{\partial}{\partial y} & \dfrac{\partial}{\partial x} \end{bmatrix}\begin{Bmatrix} u \\ v \end{Bmatrix}=\begin{bmatrix} \dfrac{\partial}{\partial x} & 0 \\ 0 & \dfrac{\partial}{\partial y} \\ \dfrac{\partial}{\partial y} & \dfrac{\partial}{\partial x} \end{bmatrix}[N]\{X\}_e \tag{3.87}$$

According to the standard notation, the strain matrix is

$$\{\varepsilon\}=[B]\{X\}_e \tag{3.88}$$

The matrix $[B]$ is also called the strain displacement matrix and can be represented as

$$[B]=\begin{bmatrix} \dfrac{\partial}{\partial x} & 0 \\ 0 & \dfrac{\partial}{\partial y} \\ \dfrac{\partial}{\partial y} & \dfrac{\partial}{\partial x} \end{bmatrix}[N] \tag{3.89}$$

Then the stress-strain relationship for an element is given by

$$\{\sigma\} = \begin{Bmatrix} \sigma_{xx} \\ \sigma_{yy} \\ \tau_{xy} \end{Bmatrix} = [D]\{\varepsilon\} = [D][B]\{X\}_e \tag{3.90}$$

where $[D]$ is the elasticity matrix and is given for plane stress and isotropic materials as

$$[D]_{Plane-Stress} = \begin{bmatrix} \frac{E}{1-\nu^2} & \frac{\nu E}{1-\nu^2} & 0 \\ \frac{\nu E}{1-\nu^2} & \frac{E}{1-\nu^2} & 0 \\ 0 & 0 & G \end{bmatrix} \tag{3.91}$$

Here E, ν, and G are Young's modulus, Poisson's ratio, and shear modulus, respectively. The displacements, derivatives of displacements, strains and stresses at any point within the element can be easily computed once $\{X\}_e$ of an element is known. The element stiffness matrix which relates the unknown nodal displacements to the applied forces on an element can be given as

$$[K]_e = t\int_{A_e} [B]^T [D][B]\,dxdy \tag{3.92}$$

where $[D]$ is the elasticity matrix consisting of element material constants. The matrix $[B]$ which relates strains and displacements is a function of (x, y) and t is the thickness of the element (assumed constant). The differential area $dxdy$ can be replaced by

$$dxdy = |J|\; d\xi\, d\eta \tag{3.93}$$

where $|J|$ is the determinant of the Jacobian matrix and is given by

$$|J| = \frac{\partial x}{\partial \xi}\frac{\partial y}{\partial \eta} - \frac{\partial x}{\partial \eta}\frac{\partial y}{\partial \xi} \tag{3.94}$$

Then Eq. (3.92) becomes

$$[K]_e = t\int_{-1}^{1}\int_{-1}^{1} \left[B(\xi,\eta)\right]^T [D]\left[B(\xi,\eta)\right]|J|\,d\xi d\eta \tag{3.95}$$

The above equation is now entirely a function of local co-ordinates (ξ,η). Numerical integration is required to be employed over the area for the evaluation of the element stiffness matrix $[K]_e$.

3.6.2 Quarter point elements (QPEs)

Quarter point singular elements are extensively used in LEFM for modeling the inverse square root singularity occurs at the crack tip. Barsoum (1976) and Henshell and Shaw (1975) were first to discover the quarter point elements which can be easily generated from any isoparametric elements containing mid-side nodes. The singularity in the QPE is achieved by shifting the mid-side nodes on edges that are connected to the crack tip by an amount of quarter of the length of the edge towards the crack tip. Such a simple and bodily movement of nodes ensures accurate estimation of the SIFs and modeling of $1/\sqrt{r}$ singularity with less number of elements around the crack tip. The conventional Q8 elements are first collapsed to six noded triangular elements and arranged in a standard *spider-web pattern* around the crack tip. Finally, the mid-side nodes are shifted to build the QPEs. All these steps are carried out by ANSYS® automatically using its inbuilt command KSCON. The $1/\sqrt{r}$ singularity in these QPEs is demonstrated in the following section.

3.6.3 Collapsed six-noded triangular quarter point elements

Figure 3.6 shows a collapsed Q8 crack-tip element, in which nodes 1, 4 and 8 are collapsed at the crack tip. This triangle is generated by collapsing the side 1-4 of the quadrilateral in Fig. 3.5.

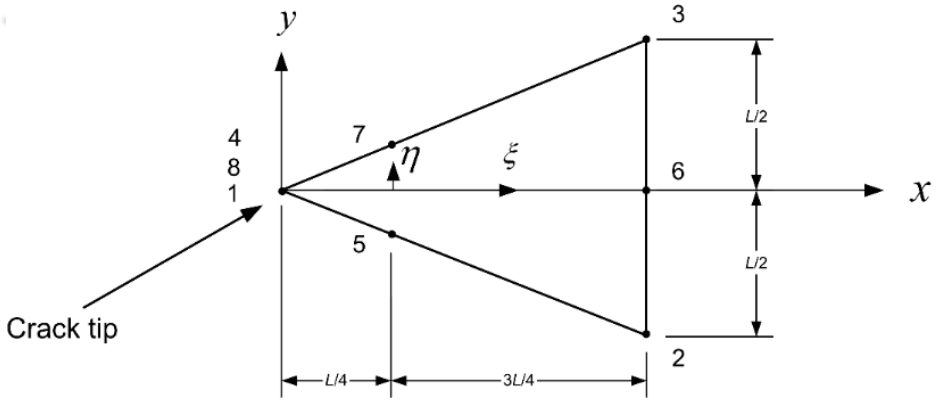

Figure 3.6 Six noded quadrilateral isoparametric element with mid-side nodes at the quarter point

Here the singularity is investigated along the $x-$ axis (i.e., $\eta=0$). Using

$$x=N_1x_1+N_2x_2+N_3x_3+N_4x_4+N_5x_5+N_6x_6+N_7x_7+N_8x_8 \tag{3.96}$$

the x - coordinate along the $x-$ axis in terms of natural coordinate ξ is given by

$$x = -\frac{1}{4}(1+\xi)(1-\xi)l_1 - \frac{1}{4}(1+\xi)(1-\xi)l_1 + \frac{1}{2}(1-\xi^2)\frac{l_1}{4} + \frac{1}{2}(1+\xi)l_1 + \frac{1}{2}(1-\xi^2)\frac{l_1}{4} \tag{3.97}$$

which simplifies to

$$x = (\xi^2 + 2\xi + 1)\frac{l_1}{4} \tag{3.98}$$

Therefore, ξ in terms of x can be given as

$$\xi = \left[-1 + 2\sqrt{\frac{x}{l_1}}\right] \tag{3.99}$$

The displacement u along $x-$axis is given by

$$u = N_1u_1 + N_2u_2 + N_3u_3 + N_4u_4 + N_5u_5 + N_6u_6 + N_7u_7 + N_8u_8 \tag{3.100}$$

Substituting shape functions and Eq. (3.99) into Eq. (3.100) and differentiating w.r.t x, the strain in the x-direction is then given by

$$\begin{aligned}\varepsilon_{xx} = \frac{\partial u}{\partial x} = &-\frac{1}{2}\left[\frac{1}{\sqrt{(xL)}} - \frac{2}{L}\right]u_2 + \frac{1}{2}\left[-\frac{1}{\sqrt{(xL)}} + \frac{2}{L}\right]u_3 \\ &+\left[\frac{1}{\sqrt{(xL)}} - \frac{2}{L}\right]u_7 + \frac{1}{2}\left[\frac{1}{\sqrt{(xL)}}\right]u_6 + \left[\frac{1}{\sqrt{(xL)}} - \frac{2}{L}\right]u_5\end{aligned} \tag{3.101}$$

Thus, Eq. (3.101) shows that the strain singularity in the form of $\frac{1}{\sqrt{x}}$ along the $x-$axis as $x \to 0$.

3.7 Error estimation

In order to estimate the error in the predicted fatigue life in comparison with the experimental fatigue life, different global, as well as local error estimates are used in the present investigation. Percentage relative error is an example for the local error estimates which provides the deviation in the predicted value with reference to the experimental value for each instance. One the other hand, the L_2 norm, and RMS quantities are examples of the global error estimates. Different error estimates have been calculated using the following formulas in the present investigation.

$$\text{Percentage relative error} = \frac{N_{i\_prediction} - N_{i\_experiement}}{N_{i\_experiement}} \times 100 \tag{3.102}$$

$$L_2 \text{ - Norm} = \frac{\sum_{1}^{n}\sqrt{(N_{i\_prediction} - N_{i\_experiement})^2}}{\sum_{1}^{n}\sqrt{(N_{i\_experiement})^2}} \tag{3.103}$$

$$\text{RMS} = \frac{\sum_{1}^{n}\sqrt{(N_{i\_prediction} - N_{i\_experiement})^2}}{n} \tag{3.104}$$

where the $N_{i\_experiement}$ denotes the number of loading cycles corresponding to crack length a_i obtained from experiments and $N_{i\_prediction}$ denotes the number of loading cycles corresponding to crack length a_i obtained from numerical simulations.

The percentage relative error provides the error at each stage of the life prediction and clearly portrays the stages of life prediction with substantial and low errors. Moreover, this type of error estimation clearly shows the relative performance of each of the models considered more explicitly for the crack growth up to the final fracture. On the other hand, the L_2 norm and RMS quantities provide overall accuracy (or gross error in terms of a single value) of the models considered as compared to the reference data. They cannot show the pointwise scenario at every stage of life prediction. By studying results from both the pointwise error prediction (i.e., percent relative error approach) and gross error predictors (i.e., L_2 and RMS quantities), the final qualification of models can be made on a scientific basis. This approach has been implemented in the present work to arrive at the final conclusions.

3.8 Summary

In this chapter, the detailed background of near field equations has been presented with the help of the generalized Westergaard approach. The procedure for the numerical estimation of mixed mode (I/II) fatigue life using the incremental crack extension method is also presented in this chapter. The formulations of the various ΔK_{eq} models are also discussed in this chapter. Various error estimation techniques employed in the present work are also discussed here.

Chapter 4

Proposed crack flank displacement technique

This chapter presents the proposed technique for the estimation mixed mode (I/II) stress intensity factors utilizing the crack flank displacements obtained from the finite element analysis. First, a brief literature review is presented followed by the theoretical formulation of the proposed technique is described. The SIFs are then estimated using the proposed technique and compared with the reference solutions for a variety of mode I, mode II and mixed mode (I/II) benchmark examples. The convergence characteristics of the proposed technique have also been studied using meshes of varying quarter point element sizes (mesh densities).

4.1 Mixed mode (I/II) SIF estimation techniques: A brief review

Stress intensity factor (SIF), K proposed by Irwin (1957) plays a vital role in the strength and structural integrity assessment of the cracked structures. It is used to describe the crack driving force, the level of singularity (Paris, 2014), and the material's resistance to fracture. Further, it is also useful in fatigue crack growth studies. To this end, numerous analytical (Sih, 1973), experimental (Kaushik et al., 2008; Ravi-Chandar, 2008; Swamy et al., 2008) and numerical methods (Banks-Sills and Sherman, 1986; Barsoum, 1976; Henshell and Shaw, 1975; Lim et al., 1992a; Mukhopadhyay et al., 2000; Murthy and Mukhopadhyay, 2001; Qian et al., 2016; Yan et al., 2010) are available for the SIF determination.

Analytical and semi-analytical SIF solutions of some simple configurations are available in various handbooks (Laham, 1998; Tada et al., 2000; Yukitaka Murakami, 1987). For complex configurations, numerical methods such as the FE method and boundary element (BE) method are employed. Amongst the available numerical methods, the FE method has been extensively used for the accurate estimation of SIFs of complex configurations. Other important areas that demand accurate estimation of the SIFs is FE simulations of quasi-static crack growth and fatigue crack growth in damage tolerance design philosophy. In these studies, a large number of finite element analyses of a given cracked configuration are necessary due

to the incremental increase of the crack length. In such cases, it is cost effective if accurate SIFs are estimated for a given mesh in the simulation process. Moreover, the signs of the individual SIFs are also important in the estimation of the crack growth directions both in quasi-static and fatigue crack growth simulations.

In the FE method, quarter point elements (QPEs) (Barsoum, 1976; Henshell and Shaw, 1975) are employed at the crack tip for modeling the inverse square root singularity. In relation to the QPEs and FE method, a number of SIF estimation techniques have been developed over past five decades. A review of some of these commonly used techniques are available in works (Banks-Sills and Sherman, 1986; Lim et al., 1992a; Mukhopadhyay et al., 2000; Murthy and Mukhopadhyay, 2001; Qian et al., 2016).

The SIF estimation techniques (usually post-processing techniques) are broadly classified into stress based, displacement based and energy based. The displacement based techniques includes limited displacement extrapolation technique by Lim et al. (1992b), displacement correlation technique (Tracey, 1977), displacement extrapolation techniques (DETs) (ANSYS, 2007; Chan et al., 1970; Guinea et al., 2000; Kirthan et al., 2016; Rahulkumar et al., 1997; Shih et al., 1976), quarter point displacement technique (Barsoum, 1976; Henshell and Shaw, 1975; Lim et al., 1992b) and interior collocation technique (Jogdand and Murthy, 2010). Some of the stress based methods are stress extrapolation (Chan et al., 1970) and force method (Raju and Newman, 1977). Examples of energy based SIF extraction methods are modified crack closure integral (Ramamurthy et al., 1986; Rybicki and Kanninen, 1977; Sethuraman and Maiti, 1988), virtual crack closure integral (Rybicki and Kanninen, 1977; Shivakumar et al., 1988), J-integral (Rice, 1968), stiffness derivative (Parks, 1974), virtual crack extension (Hellen, 1975) and interaction integral (I-integral) (Nakamura, 1991; Shih et al., 1986) techniques.

Amongst the above techniques, *J*-integral, interaction integral, and a kind of DET are integrated into various commercial software such as ANSYS® and ABAQUS®, etc. Although the path independent integral techniques (*J*-integral and interaction integral) neatly avoid crack tip complications, they only provide accurate solutions of the SIFs by computing over several paths, which complicates the mesh generation process. The interior collocation technique (Jogdand and Murthy, 2010), although it provides accurate values of the SIFs, demands a special mesh pattern around the crack tip. As a consequence, these are difficult to implement into the existing FE codes. On the other hand, techniques such as stiffness derivative and virtual

crack extension require the calculation of structural stiffness matrix twice, which increases the computational cost. It is evident that the above techniques, apart from difficult to incorporate into the existing codes, are also not very appropriate for employing in the crack growth simulations where large numbers of analysis steps are usually needed.

While the displacement based techniques are simple and easy to implement into existing FE codes (they demand no other than quarter point elements), techniques such as displacement correlation (Tracey, 1977) and quarter point displacement techniques (Barsoum, 1977, 1976; Henshell and Shaw, 1975; Lim et al., 1992b) do not show convergence as the meshes are refined (Murthy and Mukhopadhyay, 2001). Clearly, use of these techniques is prohibitive, especially in crack growth simulations. Coming to the case of displacement extrapolation methods, a form of displacement extrapolation was first proposed by Chan et al. (1970) which has the limitation of carrying out regression analysis for the best-fit straight line. Subsequently, many variants of displacement extrapolation techniques have been proposed in the past (Guinea et al., 2000; Kirthan et al., 2016; Rahulkumar et al., 1997; Shih et al., 1976).

The above extrapolation methods have been devised based on two types of formulations. In the first type of formulations (ANSYS, 2007; Rahulkumar et al., 1997), the crack opening displacement (COD) and crack sliding displacement (CSD) are approximated using the singular solutions and these displacements are approximated using an assumed profile (containing singular and higher order displacements) fitted to the edges of the finite elements attached to the crack flanks. In the second type of formulation, the relative displacement of nodes on one of the two flanks of the crack were expressed in terms of known analytical expressions containing singular and higher order terms and obtained the SIFs by correlating these expressions with the elemental displacement field (Guinea et al., 2000; Kirthan et al., 2016; Shih et al., 1976). It has been shown using extensive numerical analyses that the techniques based on the second type of formulation (Guinea et al., 2000; Kirthan et al., 2016; Shih et al., 1976) do not converge as the meshes are refined (Murthy and Mukhopadhyay, 2001). Clearly, these existing displacement techniques are not reliable while estimating the mixed mode (I/II) SIFs of complex configurations and also during the fatigue crack propagation simulations. A technique based on the first type of formulation (ANSYS, 2007; Rahulkumar et al., 1997), implemented in commercial software ANSYS®, although it estimates accurate values of the SIFs, but has a major limitation of not providing signs of the SIFs which are extremely important in mixed mode fatigue crack growth simulations.

In view of the importance of accurate estimation of the SIFs along with their signs and various limitations of the existing SIF extraction methods (as described above) a new simple and efficient displacement extrapolation type technique which also provides signs of the estimated SIFs, is proposed in the present investigation. This work takes advantage of both the types of formulations implemented in the existing techniques (Rahulkumar et al., 1997; Shih et al., 1976; Zhu and Smith, 1995) and formulates the COD and CSD using a combination of singular and higher order terms. Due to the presence of higher order terms, the technique can be used on coarse meshes to get the accurate values of the SIFs. The mixed mode SIFs are then estimated directly by comparing the analytical expressions of COD and CSD with the computed values obtained at the nodes of the crack flanks. Further, the proposed technique employs a more elegant approach of the Generalized Westergaard proposed by Sanford (1979). It is very easy to implement into the existing FE codes and provides very accurate SIFs even in the relatively coarse meshes. Solutions of the proposed technique converge, as the meshes are refined. The efficacy of the proposed technique is substantiated by solving the SIFs of mode I, mode II and mixed mode (I/II) benchmark problems and comparing the results with the values computed using J-integral and interaction integral and published results.

4.2 Proposed crack flank displacement technique for the estimation of mixed mode (I/II) SIFs

In the generalized Westergaard method (Sanford, 1979), the displacement components in terms of three parameters A_0, A_1 and B_0 are given as (recalling Eq. 3.17)

$$\begin{aligned} u_I &= \frac{A_0}{2G} r^{1/2}\left[(\kappa-1)\cos\frac{\theta}{2}+\sin\theta\sin\frac{\theta}{2}\right] \\ &\quad + \frac{A_1}{2G} r^{3/2}\left[\frac{\kappa-1}{3}\cos\frac{3\theta}{2}-\sin\theta\sin\frac{\theta}{2}\right]+\frac{B_0(\kappa+1)}{4G} r\cos\theta \\ v_I &= \frac{A_0}{2G} r^{1/2}\left[(\kappa+1)\sin\frac{\theta}{2}-\sin\theta\cos\frac{\theta}{2}\right] \\ &\quad + \frac{A_1}{2G} r^{3/2}\left[\frac{\kappa+1}{3}\sin\frac{3\theta}{2}-\sin\theta\cos\frac{\theta}{2}\right]-\frac{B_0\nu(\kappa+1)}{4G} r\sin\theta \end{aligned} \tag{4.1}$$

where u_I and v_I represents the mode I displacements in x and y directions, respectively (Fig. 4.1) and $\kappa = 3-4\upsilon$ for plane strain and $\kappa = (3-\upsilon)/(1+\upsilon)$ for plane stress conditions.

Similarly, the displacement components in terms of three parameters C_0, C_1 and D_0 for mode II can be obtained as (recalling Eq. 3.29)

$$\begin{aligned} u_{II} &= \frac{C_0}{2G} r^{1/2}\left[(\kappa+1)\sin\frac{\theta}{2}+\sin\theta\cos\frac{\theta}{2}\right] \\ &+ \frac{C_1}{2G} r^{3/2}\left[\frac{(\kappa+1)}{3}\sin\frac{3\theta}{2}+\sin\theta\cos\frac{\theta}{2}\right]+\frac{D_0(\kappa+1)}{4G} r\sin\theta \\ v_{II} &= \frac{C_0}{2G} r^{1/2}\left[(1-\kappa)\cos\frac{\theta}{2}+\sin\theta\sin\frac{\theta}{2}\right] \\ &+ \frac{C_1}{2G} r^{3/2}\left[\frac{(1-\kappa)}{3}\cos\frac{3\theta}{2}+\sin\theta\sin\frac{\theta}{2}\right]-\frac{D_0(\kappa+1)}{4G} r\cos\theta \end{aligned} \tag{4.2}$$

where u_{II} and v_{II} are the mode II displacements (Fig. 4.1). G and υ are the shear modulus and Poisson's ratio, respectively. A_0, A_1, B_0, and C_0, C_1, D_0 represents coefficients of the generalized Westergaard (Sanford, 2003) in mode I and mode II, respectively. In case of the mixed mode (I/II) loading the displacement components can be obtained using the principle of superposition as

$$\begin{aligned} u &= u_I + u_{II} \\ v &= v_I + v_{II} \end{aligned} \tag{4.3}$$

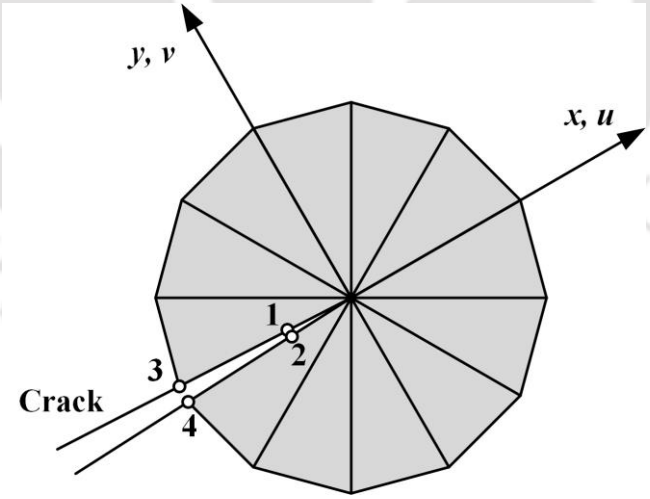

Figure 4.1 Crack tip coordinate system and associated displacements

Figure 4.1 shows a typical crack tip mesh pattern with the QPEs deployed at the crack tip. The nodes 1-2 represents quarter point nodes on the crack flanks (with node 1 being at $\theta = +180°$ and node 2 at $\theta = -180°$ respectively) and nodes 3-4 represents corner nodes of the QPEs attached to the crack flanks. It is assumed that Eqs (4.1) and (4.2) are sufficient to represent the displacement components along the length of the QPEs lying on the crack flanks

in any loading. Referring to Fig. 4.1, for $\theta = \pm 180°$ the v component of the displacement in mixed mode loading conditions is given as

$$\begin{aligned} v_{180} &= \frac{A_0(\kappa+1)}{2G} r^{1/2} - \frac{A_1(\kappa+1)}{6G} r^{3/2} + \frac{B_0(\kappa+1)}{4G} r \\ v_{-180} &= -\frac{A_0(\kappa+1)}{2G} r^{1/2} + \frac{A_1(\kappa+1)}{6G} r^{3/2} + \frac{B_0(\kappa+1)}{4G} r \end{aligned} \tag{4.4}$$

Similarly, the u component of the displacement as

$$\begin{aligned} u_{180} &= \frac{C_0(\kappa+1)}{2G} r^{1/2} - \frac{C_1(\kappa+1)}{6G} r^{3/2} - \frac{D_0(\kappa+1)}{4G} r \\ u_{-180} &= -\frac{C_0(\kappa+1)}{2G} r^{1/2} + \frac{C_1(\kappa+1)}{6G} r^{3/2} - \frac{D_0(\kappa+1)}{4G} r \end{aligned} \tag{4.5}$$

Therefore, from Eqs. (4.4) and (4.5) the crack opening and sliding displacements Δv and Δu can be obtained as

$$\begin{aligned} \Delta v &= v_{180} - v_{-180} = \frac{A_0(\kappa+1)}{G} r^{1/2} - \frac{A_1(\kappa+1)}{3G} r^{3/2} \\ \Delta u &= u_{180} - u_{-180} = \frac{C_0(\kappa+1)}{G} r^{1/2} - \frac{C_1(\kappa+1)}{3G} r^{3/2} \end{aligned} \tag{4.6}$$

In the present investigation, the unknown coefficients A_0 and C_0 are solved using the FE solutions of Δv and Δu at two different radial locations r_1(or r_2) and r_3(or r_4) on the crack flank, as shown in Fig. 4.1. Then the mixed mode SIFs K_I and K_{II} can be estimated as

$$K_I = \sqrt{2\pi} A_0 \quad \text{and} \quad K_{II} = \sqrt{2\pi} C_0 \tag{4.7}$$

It can be noticed from Eqs. (4.6) and (4.7) that actual signs (positive or negative) of the SIFs (which depends on the orientation of the crack with the loading) can also be furnished by the proposed technique.

4.3 Numerical examples

In order to validate the performance of the proposed technique, numerical evaluation is carried out in this section using a number of benchmark problems. Finite element analysis of all the examples is carried out using the commercial software ANSYS® (2007). Meshing is done using eight noded isoparametric quadrilateral (Q8) elements and collapsed Q8 QPEs are employed at the crack tip in a spider web pattern. Plane stress conditions, Young's modulus E

=1.0, Poisson's ratio υ = 0.3, and the applied stress σ = 1.0 are assumed in all the example problems. Units of all examples are consistent. SIFs are also computed using the DET, *J*-integral and *I*-integral techniques available in ANSYS®. In order to study the efficacy of the proposed technique, solutions using the above technique along with the published solutions are compared with that obtained using the proposed technique. The percentage relative error in the estimated SIF is calculated as

$$\% \text{ relative error} = \left| \frac{\text{computed value - reference value}}{\text{reference value}} \right| \times 100 \qquad (4.8)$$

where computed value refers to the value of SIF estimated using the proposed technique and the reference value is the available analytical or numerical value.

4.3.1 Example 1: Centre cracked plate under mode I loading

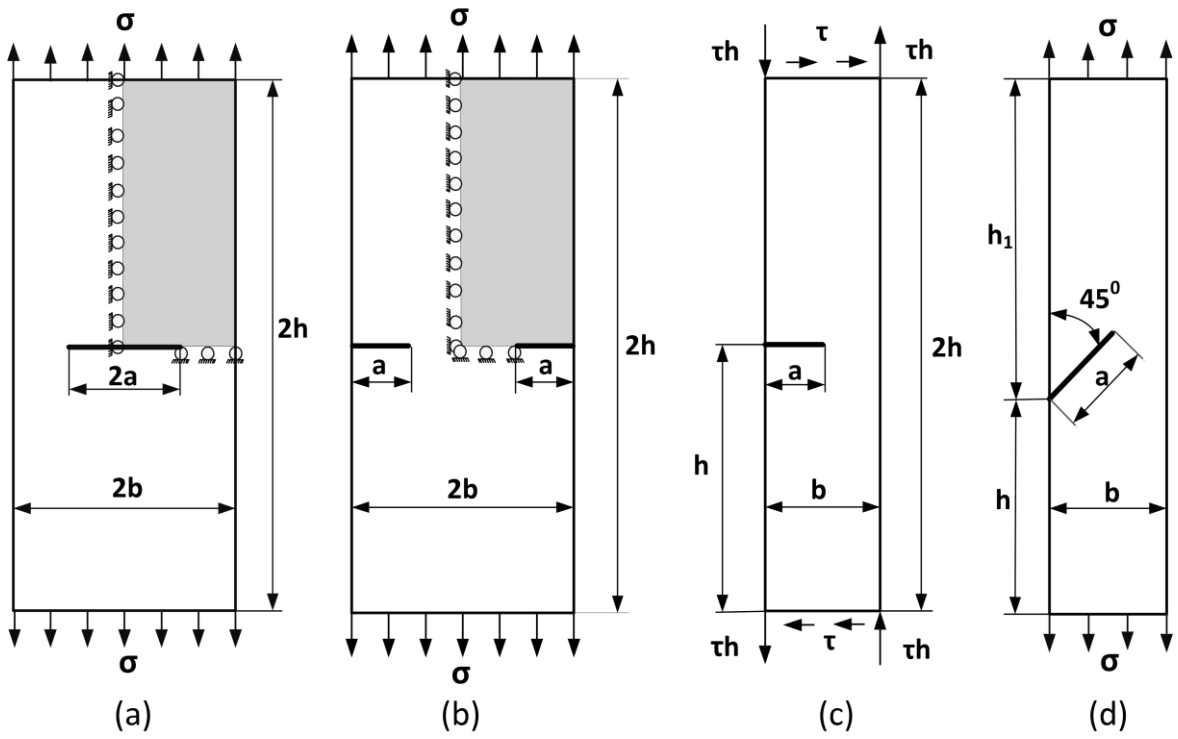

Figure 4.2 Geometry and boundary conditions of the various crack configurations

The first example discussed here is a mode I problem of a centre cracked plate (CCP) under uniform tensile loading (Fig. 4.2 (a)) with $h/b = 3$. Three configurations of CCP with a/b = 0.2, 0.4, and 0.6 have been considered for the study. Due to symmetry, only one quarter of the CCP is simulated (shaded area in Fig. 4.2 (a)). Figure 4.2 (a) also shows symmetry boundary conditions used in FE analysis. Figure 4.3 shows a sequence of finite element meshes

having the QPE length to crack length ratio (L_Q / a) of 0.4, 0.2 and 0.1, respectively, employed for convergence study. The number of elements (NE) and the number of nodes (NN) are also shown in Fig. 4.3. The mesh pattern around the crack tip is shown in Fig. 4.3 (d).

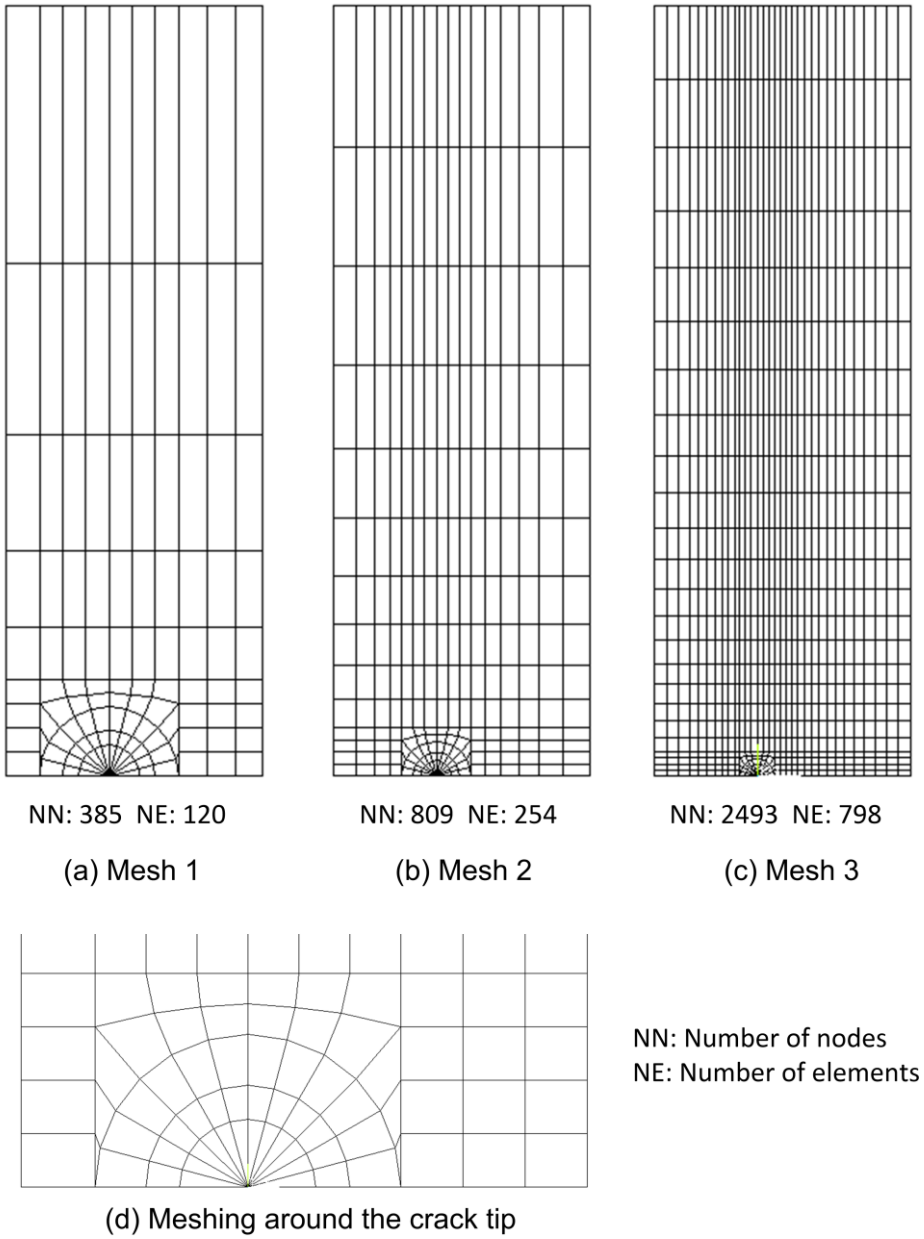

Figure 4.3 Different finite element meshes used for the analysis of CCP

Table 4.1 shows the results of the estimated normalized SIF obtained using the proposed approach and other techniques. The values given in brackets indicate the percentage relative error based on the reference solutions given by Isida (1971) in Eq. (4.8).

Table 4.1 Comparison of the normalized SIFs for CCP ($h/b = 3$, $a/b = 0.2, 0.4, 0.6$)

		$K_I/\sigma\sqrt{\pi a}$				
a/b	Mesh	(Isida, 1971)*	Present	DET	J-int	I-int
0.2	Mesh 1	1.025	1.0272	1.0272	1.0246	1.0249
			(0.21)#	(0.22)	(0.04)	(0.01)
	Mesh 2		1.0263	1.0264	1.0246	1.0246
			(0.13)	(0.13)	(0.04)	(0.04)
	Mesh 3		1.0258	1.0258	1.0246	1.0246
			(0.08)	(0.07)	(0.04)	(0.04)
0.4	Mesh 1	1.109	1.1120	1.1120	1.1094	1.1097
			(0.27)	(0.27)	(0.03)	(0.06)
	Mesh 2		1.1109	1.1109	1.1094	1.1093
			(0.17)	(0.17)	(0.03)	(0.03)
	Mesh 3		1.1105	1.1105	1.1094	1.1093
			(0.14)	(0.14)	(0.03)	(0.03)
0.6	Mesh 1	1.303	1.3052	1.3052	1.3033	1.3037
			(0.17)	(0.17)	(0.02)	(0.05)
	Mesh 2		1.3047	1.3046	1.3033	1.3033
			(0.13)	(0.13)	(0.02)	(0.02)
	Mesh 3		1.3044	1.3045	1.3033	1.3033
			(0.11)	(0.12)	(0.02)	(0.02)

**** Reference solution, # Percentage relative error***

It can be noticed from Table 4.1 that the results obtained using the proposed technique converges to the reference value with the mesh refinement. This is true for all a/b values considered. It is interesting to notice from the results in Table 4.1 that in all the meshes, the SIFs are determined with an accuracy that is comparable with that obtained using *J*-integral and *I*-integral. Very accurate SIFs are estimated using the proposed technique even in the relatively coarse meshes. The maximum percentage error observed using coarse meshes (Mesh 1) is 0.27%, and using fine meshes (Mesh 3) is 0.14%. It can also be noticed that the results

obtained in this section are in excellent agreement with the reference value, and the proposed technique computes very accurate values of the SIFs.

4.3.2 Example 2: Double edge cracked plate under mode I loading

The second example problem considered is also a mode I problem of double edge cracked plate (DECP) subjected to uniform far field tensile stresses as shown in Fig. 4.2 (b). The geometry parameters used for FE analysis are $h/b = 3$, $a/b = 0.2$, 0.4, and 0.6. Only one quarter of the plate is modeled as shown (with boundary conditions) in Fig. 4.2 (b) due to the symmetry of the problem. Meshes that are similar to Fig. 4.3 are employed for FE analysis. However, results corresponding to the Mesh 1 and Mesh 3 are presented here. Table 4.2 shows the comparison of computed mode I normalized SIFs using the proposed approach and other techniques. The % relative error is shown in brackets. Solutions of Benthem and Koither (1973) are considered as the reference solution in Eq. (4.8).

Table 4.2 Comparison of the normalized SIFs for DECP ($h/b = 3$, $a/b = 0.2$, 0.4, 0.6)

a/b	Mesh	$K_I/\sigma\sqrt{\pi a}$					
		(Benthem and Koiter, 1973)*	(Yan et al., 2010)	Present	DET	J-int	I-int
0.2	Mesh 1	1.1180	1.1123	1.1104 (0.68)#	1.1105 (0.67)	1.1118 (0.56)	1.1121 (0.53)
	Mesh 3			1.1124 (0.50)	1.1124 (0.50)	1.1118 (0.56)	1.1117 (0.56)
0.4	Mesh 1	1.1361	1.1377	1.1309 (0.46)	1.1309 (0.46)	1.1321 (0.35)	1.1325 (0.32)
	Mesh 3			1.1329 (0.28)	1.1329 (0.28)	1.1321 (0.35)	1.1321 (0.35)
0.6	Mesh 1	1.2333	1.2446	1.2361 (0.23)	1.2362 (0.23)	1.2360 (0.22)	1.2364 (0.25)
	Mesh 3			1.2371 (0.30)	1.2371 (0.30)	1.2360 (0.22)	1.2360 (0.22)

**** Reference solution, # Percentage relative error***

It is seen that the results of the present displacement based method is in very good agreement with the results using the other three methods and the published results in all the meshes. Like in the previous example, the estimated SIF is converged as the meshes are refined and very accurate solutions are determined using even in relatively coarse meshes such as Mesh 1. This is true for all a/b values considered. The solutions of the proposed technique are comparable to that of path independent integral techniques. The maximum error using Mesh 1 is 0.68%, and that in the Mesh 3 is 0.56%.

4.3.3 Example 3: Edge cracked plate under mode II loading

In this section, a pure mode II problem of an edge cracked plate under antisymmetric loading is presented, as shown in Fig. 4.2 (c). For this problem h/b is set to 1.0, and different configurations with $a/b =$ 0.2, 0.4, and 0.6 have been analyzed. As there is no symmetry exists in this problem, the full model is considered in FE analysis. The bottom edge of the plate is restrained from all the degrees of freedom, and the top face is loaded with the forces, as shown in Fig. 4.2 (c). Like in the previous examples, the convergence of the computed mode II SIF K_{II} using the proposed technique is observed on three meshes with varying mesh density, as shown in Fig. 4.4, and the corresponding results are presented in Table 4.3.

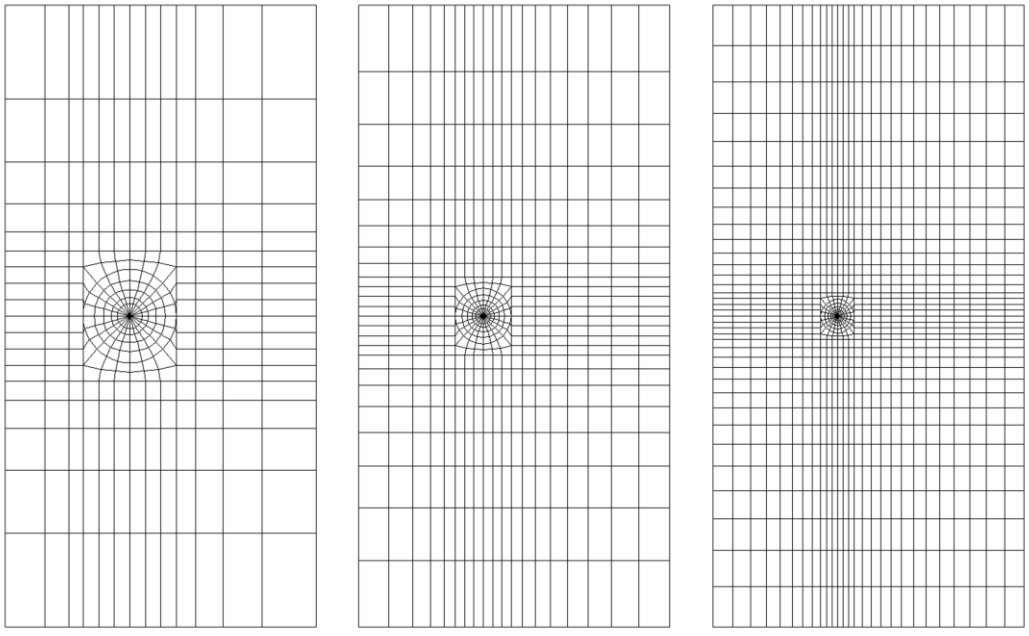

Figure 4.4 Finite element meshes used for the analysis of ECP under mode II loading

For the % relative error calculations in the normalized SIF (Eq. (4.8)), the results of Treifi (2008) are considered as the reference solution.

Table 4.3 Normalized mode II stress intensity factors for ECP ($h/b=1$, $a/b=0.2, 0.4, 0.6$)

a/b	Mesh	$K_{II}/\tau\sqrt{\pi a}$ (Treifi et al., 2008)*	Present	DET	J-int	I-int
0.2	Mesh 1	0.694	0.6906 (0.49)#	0.6906 (0.49)	0.7065 (1.79)	0.7039 (1.43)
	Mesh 2		0.6887 (0.77)	0.6883 (0.82)	0.6960 (0.29)	0.6960 (0.29)
	Mesh 3		0.6905 (0.51)	0.6905 (0.50)	0.6959 (0.27)	0.6959 (0.27)
0.4	Mesh 1	1.179	1.1718 (0.56)	1.1718 (0.56)	1.1794 (0.03)	1.1798 (0.06)
	Mesh 2		1.1739 (0.40)	1.1740 (0.38)	1.1794 (0.03)	1.1794 (0.03)
	Mesh 3		1.1748 (0.33)	1.1752 (0.29)	1.1794 (0.03)	1.1794 (0.03)
0.6	Mesh 1	1.552	1.5468 (0.33)	1.5466 (0.34)	1.5503 (0.11)	1.5507 (0.08)
	Mesh 2		1.5469 (0.32)	1.5471 (0.31)	1.5509 (0.07)	1.5509 (0.07)
	Mesh 3		1.5474 (0.29)	1.5473 (0.30)	1.5510 (0.06)	1.5510 (0.06)

**** Reference solution, # Percentage relative error***

It may be observed from the results of Table 4.3 that similar to the previous examples, extremely accurate values of the mode II SIFs are extracted by the proposed method and are converged as the meshes are refined. This can be seen in all a/b values employed. The results

obtained using Mesh 3 are in very good agreement with the published results as well as with the other methods. In this example also the accuracy of the proposed method is similar to the *J*-integral and *I*-integral techniques. A maximum error of 0.56% is noticed in Mesh 1 of $a/b =$ 0.4. However, with the fine meshes (Mesh 3), the maximum error is 0.51%.

4.3.4 Example 4: Slant edge cracked plate under mixed mode (I/II) loading

Finally, to demonstrate the efficacy of the proposed technique in the mixed mode (I/II) loading conditions, a slant edge cracked plate (SECP) subjected to tension loads (as shown in Fig. 4.2 (d)) is considered here. The geometric parameters for this problem are $h/b = 1$, $h_1/h =$ 1.5, and $a/b = 0.2$, 0.4, and 0.6. Due to the lack of symmetry, the whole domain is modeled using finite elements. The bottom face of the plate is restrained in x, and y directions and the top face is loaded as shown in Fig. 4.2 (d). The convergence study has also been carried out using the three meshes of varying mesh density, as shown in Fig. 4.5. Tables 4.4 and 4.5 show the results of the analyses for the normalized K_I and K_{II} respectively.

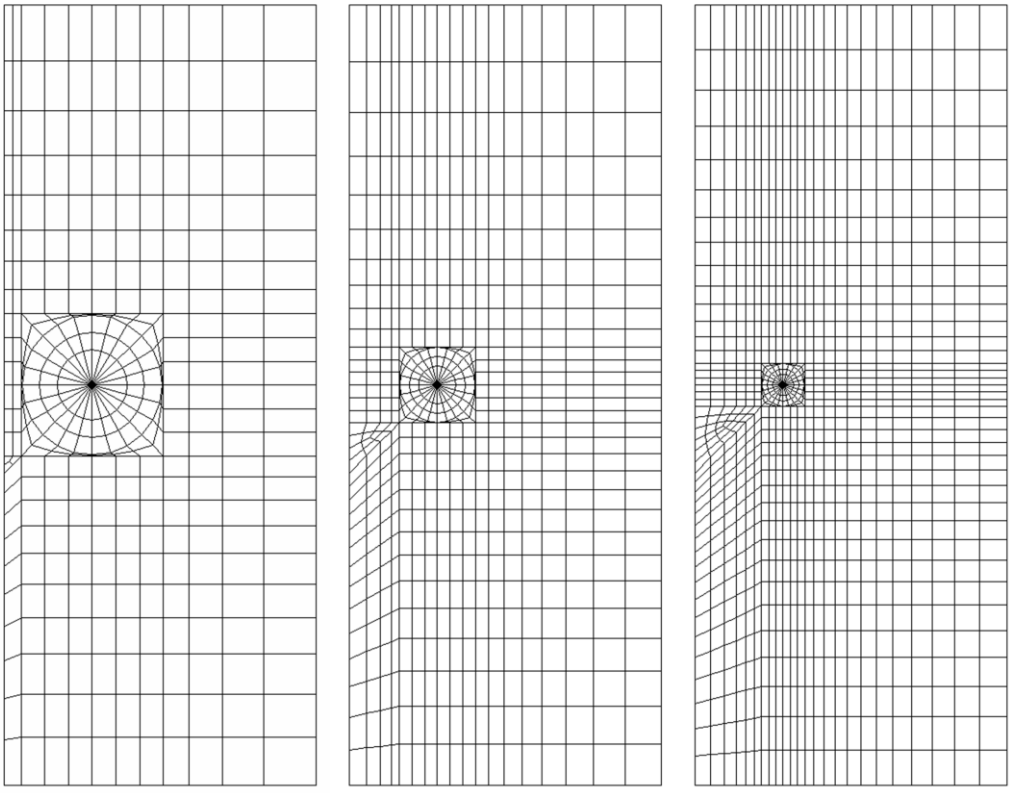

Figure 4.5 Finite element meshes used for the analysis of SECP under tension

Table 4.4 Normalized mode I stress intensity factors for SECP under tension

($h/b=1,\ h_1/h=1.5,\ a/b=0.3, 0.4, 0.6$)

a/b	Mesh	$K_I/\sigma\sqrt{\pi a}$				
		(Chen and Wang, 2008)*	(Wilson, 1969)	Present	DET	I-int
0.3	Mesh 1	0.883	0.883	0.8811 (0.21)#	0.8811 (0.22)	0.8828 (0.02)
	Mesh 2			0.8821 (0.10)	0.8826 (0.05)	0.8826 (0.04)
	Mesh 3			0.8830 (0.00)	0.8831 (0.01)	0.8826 (0.04)
0.4	Mesh 1	1.017	1.011	1.0155 (0.15)	1.0155 (0.15)	1.0177 (0.07)
	Mesh 2			1.0175 (0.05)	1.0177 (0.07)	1.0176 (0.06)
	Mesh 3			1.0178 (0.08)	1.0179 (0.09)	1.0177 (0.07)
0.6	Mesh 1	1.459	1.437	1.4584 (0.04)	1.4584 (0.04)	1.4590 (0.00)
	Mesh 2			1.4595 (0.03)	1.4596 (0.04)	1.4590 (0.00)
	Mesh 3			1.4596 (0.04)	1.4598 (0.05)	1.4590 (0.00)

**** Reference solution, # Percentage relative error***

It is very interesting to notice from the results of Tables 4.4 and 4.5 that like the previous examples, very accurate values of both the SIFs K_I and K_{II} have been estimated by the present technique. The percent relative error in the present results are of the similar order as that of path independent integrals specifically in the refined meshes. Furthermore, the convergence of the extracted SIFs can be noticed from Tables 4.4 and 4.5 as the meshes are

refined. The results in tables clearly show that the proposed technique is capable of providing accurate mixed mode SIFs even in the relatively coarse meshes similar to that of *J* and *I*-integrals.

Table 4.5 Normalized mode II stress intensity factors for SECP under tension

($h/b=1,\ h_1/h=1.5,\ a/b=0.3, 0.4, 0.6$)

a/b	Mesh	$K_{II}/\sigma\sqrt{\pi a}$				
		(Chen and Wang, 2008)*	(Wilson, 1969)	Present	DET	I-int
0.3	Mesh 1	0.448	0.450	0.4383 (2.17)#	0.4381 (2.20)	0.4469 (0.24)
	Mesh 2			0.4423 (1.27)	0.4425 (1.24)	0.4466 (0.30)
	Mesh 3			0.4441 (0.88)	0.4443 (0.84)	0.4466 (0.31)
0.4	Mesh 1	0.507	0.505	0.4955 (2.28)	0.4955 (2.27)	0.5055 (0.30)
	Mesh 2			0.5012 (1.15)	0.5010 (1.19)	0.5051 (0.38)
	Mesh 3			0.5021 (0.98)	0.5020 (0.99)	0.5051 (0.38)
0.6	Mesh 1	0.685	0.674	0.6782 (1.00)	0.6782 (0.99)	0.6833 (0.24)
	Mesh 2			0.6806 (0.64)	0.6805 (0.66)	0.6831 (0.27)
	Mesh 3			0.6807 (0.62)	0.6808 (0.61)	0.6831 (0.27)

**** Reference solution, # Percentage relative error***

4.4 Summary

A simple and efficient displacement extrapolation technique for the accurate estimation of SIFs of mode I, mode II and mixed mode (I/II) loading conditions is proposed in this chapter. The technique uses the crack flank displacement components from finite element analysis to compute the SIFs along with their signs. The technique is developed based on the Generalized Westergaard approach. The results of the present investigation clearly show that (a) the present technique provides very accurate SIFs even in the relatively coarse meshes (b) the estimated SIFs shows convergence as the meshes are refined (c) the computed SIFs using the proposed technique show a very good agreement with the published results and solutions obtained using the *J*-integral and *I*-integrals and (d) the accuracy of the estimated SIFs using the proposed technique is of the similar order as obtained using path independent integrals. Apart from the accuracy of the SIFs, another important feature of the proposed technique is that it provides the SIFs with their correct sign, which is vital in fatigue crack growth simulation studies in the damage tolerance design philosophy. Thus the present technique is also extremely useful in the fatigue crack growth simulations. Owing to the simplicity and ease of implementation, it can easily be incorporated into the existing FE codes.

Chapter 5

Proposed best-fit model

5.1 Best-fit models for fatigue data: A brief review

In damage tolerance and structural integrity analyses, the assessment of the length of fatigue crack (a) as a function of the number of loading cycles (or fatigue life, N) is important. The macroscopic analysis assumes that the fatigue crack propagation under constant amplitude load is a smooth process. However, the laboratory fatigue crack growth test results show a significant amount of scattering in the crack length versus the number of loading cycles $(a-N)$ data (Mukherjee, 1972; Schijve, 2009). Scatter can occur in the FCG data due to numerous reasons such as variability in fatigue testing procedures, measurement technique used for crack length, and irregularity in the microstructure of the material (Virkler et al., 1979) etc.

The fatigue crack appears to grow in an exponential manner, and the Paris law (Paris et al., 1961) is used to describe the relationship between the fatigue crack growth rate da/dN and the stress intensity factor range ΔK in mode I loading. Their relation, in turn, can be used to determine the Paris material constants C and m (Eq. 3.36) of the engineering materials. However, the da/dN is calculated using the $a-N$ data obtained from the experiments. Smooth data is required for the accurate calculation of the da/dN and hence the Paris constants, such data is essential for the accurate prediction of the fatigue life of structural components (Zheng and Powell, 1997). From this point of view, various data fitting techniques are widely employed for an accurate representation of the fatigue crack length as a function of the fatigue life $\left(a=f(N)\right)$. Due to the scatter in the fatigue crack growth data, various methods for fitting and smoothing the experimental $a-N$ data have been developed for the mode I loding (Davies and Feddersen, 1973; Munro, 1973; Smith, 1973; Zheng and Powell, 1997).

An early attempt to fitting a curve to the fatigue crack growth data was by Davies et al. using the polynomial curve (Davies and Feddersen, 1973), in which they used a seventh-degree polynomial to fit the $a-N$ data. Munro (1973) suggested an orthogonal polynomial approach, in which five consecutive data points are considered, and a cubic polynomial expression is fitted to them. In this approach, in a data set with k the number of data points, the data points from N_3 to N_{k-2} are modified, and the first two and the last two data values remain unchanged. Then the actual data points from N_3 to N_{k-2} were replaced by the smooth points. The procedure has to be repeated a number of times to complete all the data points. A special requirement for the use of this method is that all the crack length measurements must be equally spaced, which is hard to obtain in the studies like mixed mode fatigue crack growth.

Smith (1973) used a three parameter equation to fit the whole range of the experimental data. To represent the complete data set, three different equations are used. The first and third equation covers the top and bottom halves of the data. The second equation is an overlap that covers the second and third quarters of the data range. Polak and Knesl (1975) proposed the use of cubic spline techniques for both the data interpolation and data smoothing. Using spline techniques, he established a relationship between the successive points by a third order polynomial so that the requirement for continuous first and second order derivative are met.

It is well known that the mode I FCG test is standardized. As a result, standardized crack length measurement techniques are in use (ASTM E399-19). Due to the standardization, most of the best-fit techniques are in-built in the software of commercially available testing machines so that at the end of the test a smooth plot of $a=f(N)$ can be obtained automatically. On the other hand, mixed mode (I/II) FCG tests are not standardized to date. Consequently, no standardized crack length measurement technique is available. As the crack grows in a curvilinear manner in the mixed mode (I/II) FCG studies, therefore optical microscope is the most widely used device for measurement of the length of the growing crack. As the crack length measurement with this technique is manual, it is prone to the measurement error and variability in the measured data. Thus, fitting and smoothing are essential for the mixed mode (I/II) fatigue crack growth data. However, a very little amount of work appears in this direction. To the knowledge of the author, the only available work in this direction is due to Mohanty et al. (2009).

Mohanty et al. (2009) proposed a single term exponential model for representing the crack length as a function of the number of load cycles and vice versa under mixed mode (I/II)

loading. Their exponential model is based on the extension of the "law of growth" in biological studies to the fatigue crack growth phenomena. Exponential models are frequently employed in biological studies. However, no satisfactory best-fit and smoothened data have been noticed in the present experimental data by using the Mohanty et al. (2009) model. Nevertheless, this exercise showed promising results to work further with the "law of growth" models.

In view of (a) the inadequacy of the available models in providing satisfactory best fit of the $a-N$ experimental data in the mixed mode (I/II) loading, (b) the importance of need for the smoothened data in the present investigation, (c) inherent scatter while using the optical microscope and (d) the inherent limitations of higher order polynomials in representing scattered present mixed mode data, the present work proposes a better best-fit technique termed as "the double exponential model" for fitting the whole range of $a-N$ data obtained from the mixed mode (I/II) fatigue experiments. The proposed model is useful for both the mode I as well as mixed mode (I/II) loading conditions.

5.2 The proposed three-parameter double exponential model

The crack growth rate is infinitesimal at the initial stages of the fatigue crack propagation and increases, as the crack grows further. Fatigue crack growth is a continuous phenomenon. The exponential models are in use for modeling continuous growth that occurs naturally, such as populations, bacteria, radioactive decay, etc. The equation describing the exponential growth can be expressed as,

$$A = A_0 e^{pt} \tag{5.1}$$

where A_0 is the initial value of the dependent variable A, and t is the time. p is the specific growth rate, which is also known as the Malthusian parameter (Mohanty et al., 2009). Eq. (5.1) is widely known as the "law of growth." Considering the continuous and uncontrollable nature of the fatigue crack growth, Mohanty et al. (2009) extended the model in Eq. (5.1) to the fatigue crack growth as

$$a_i = a_0 e^{pN_i} \tag{5.2}$$

where a_i is the instantaneous crack length and the a_0 is the initial crack length. N_i is the fatigue life cycles for the crack to grow from a_0 to a_i. Due to the inability to properly best-fit the present experimental data by Eq. (5.4), a new double exponential model is proposed here.

The suitability of Eq. (5.2) in representing the mixed mode (I/II) fatigue crack length vs cycles to failure $(a-N)$ can be improved by incorporating additional exponential term, thus making it as a double exponential model as

$$a_i = (a_0 - k)e^{pN_i} + ke^{qN_i} \tag{5.3}$$

where a_i is the crack length at i^{th} step and N_i is the corresponding number of cycles. a_0 is the initial length of the crack, k is a constant and p and q are exponents to be determined. The proposed model in Eq. (5.3) is thus, passing through the point $(0, a_0)$ which is the main requirement of the a versus N function. Unlike the widely used polynomial models, this model utilizes only three parameters $(k,\ p \text{ and } q)$ and can easily be obtained using the commercial curve fitting tools such as MATLAB® cftool and Origin pro, etc. In the present work, MATLAB® cftool is used for obtaining the best-fit constants. Also, the proposed function is continuous and continuously differentiable over the range $a_0 - a_f$ where a_f is the final or the required crack length. The proposed exponential model is tested with a large number of experimental data, and a few of the tests are illustrated in the following sections to demonstrate the efficacy of the proposed model.

The above unknown three parameters $(k,\ p \text{ and } q)$ can be found by minimizing the sum of the squares of the residuals using MATLAB® cftool. Accordingly, the sum of the squares of error (SSE) in the present case can be written as

$$SSE = \sum_{i=1}^{n} \left[\bar{a}_i - a_i\right]^2 \tag{5.4}$$

where $\bar{a}_i$ is crack length obtained from the experiments. Thus, according to the present approach, Eq. (5.4) can be written as

$$SSE = \sum_{i=1}^{n} \left[\bar{a}_i - \left((a_0 - k)e^{pN_i} + ke^{qN_i}\right)\right]^2 \tag{5.5}$$

5.3 Numerical validation of the proposed model

In order to validate the proposed model, three other available data fitting techniques along with the proposed double exponential model are fitted to the published experimental data. Various other methods selected for comparison purpose are

a. Polynomial fits (Order 3 to 6) (Munro, 1973)
b. Cubic Spline fit (Polak and Knesl, 1975)
c. Smoothing spline fit (Polak and Knesl, 1975)

The experimental data selected for the present analysis is shown in Table 5.1. In fatigue testing, the crack growth rate depends on a number of factors such as loading range, frequency, the material used and more importantly the final number of data points measured. The number of data points depends on the selected measurement technique used for the crack length and the interval between crack length measurements. By applying low applied loads and the lesser time interval between measurements, more number of data points $(a-N)$ can be achieved. However, this may not be always the case. Thus, a best-fit model is expected to provide as good best fit as possible even in the case where less number of data points are available. In this regard, data points of 7, 16 and 32 are selected as shown in Table 5.1.

Table 5.1 Details of the experimental data selected for the analysis.

Author and Year	Specimen type	Loading angle	Number of data points
(Kim and Kim, 2013)	Compact Tension (CT)	0°	32
(Zhang et al., 2006)	Compact Tension Shear (CTS)	0°	16
(Zhang et al., 2006)	Compact Tension Shear (CTS)	60°	7

The least-square regression is used in all the techniques mentioned above for the purpose of fitting the best fit line. All the required codes are developed in MATLAB®. A 95% confidence level is considered for constructing the best-fit line. Figures 5.1-5.3 show the best fit lines using all the selected four methods along with the experimental data mentioned in Table 5.1 for 32, 16, and 7 data points, respectively. The corresponding regression and goodness of fit parameters are presented in Tables 5.2-5.4, respectively.

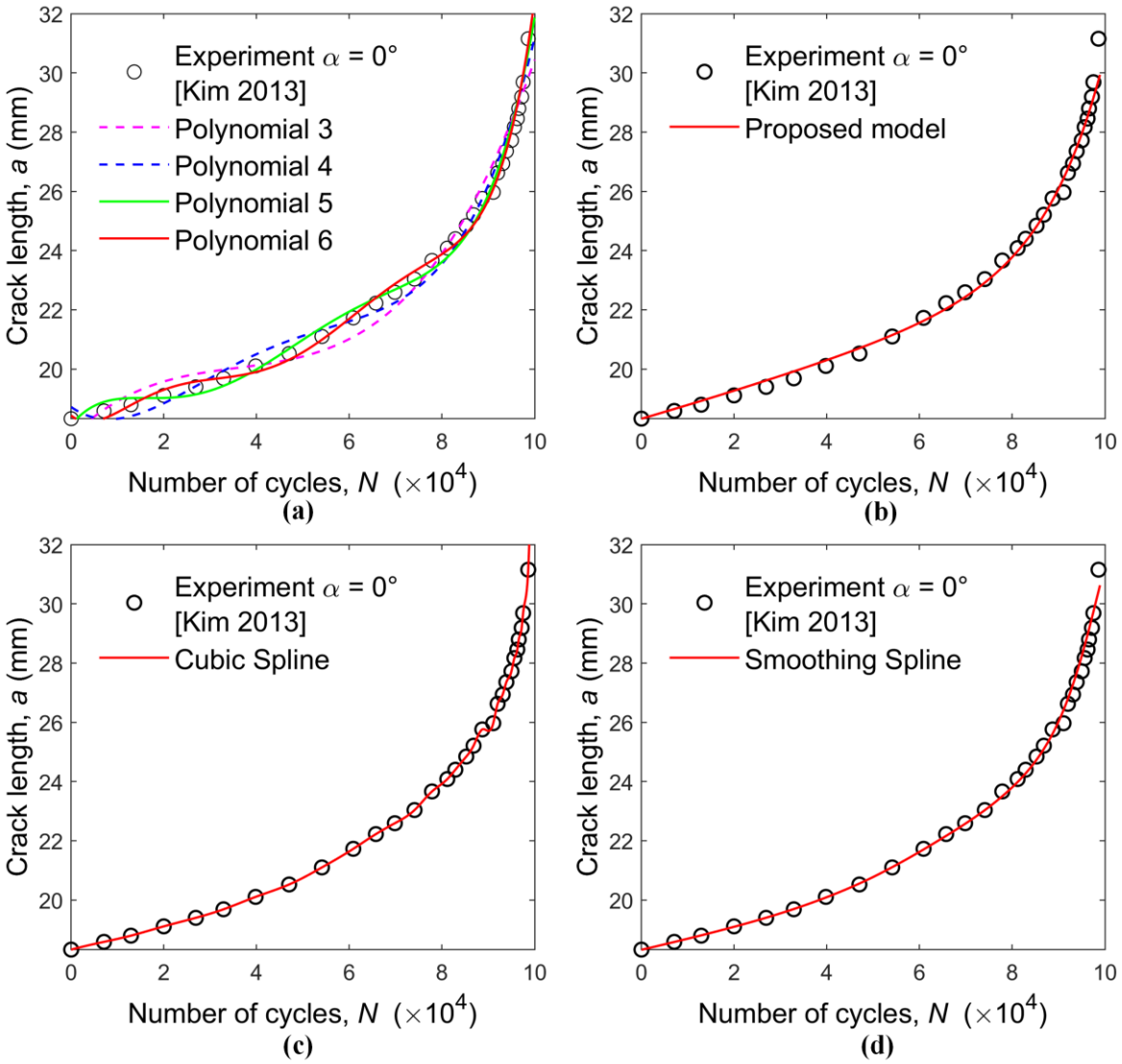

Figure 5.1 Experimental $a-N$ data and the fitted curves for the CT Specimen (32 data points, (Kim and Kim, 2013)) (a) polynomial fits (b) double exponential fit (c) cubic spline fit and (d) smoothing spline fit

Table 5.2 Best-fit parameter values for the CT Specimen (Kim and Kim, 2013)

Parameter	Fit type						
	Poly 3	Poly 4	Poly 5	Poly 6	Present	Cubic Spline	Smoothing Spline
SSE	15.0746	8.7564	5.2201	3.2261	2.4476	0	5.5683
r^2	0.9691	0.9821	0.9893	0.9934	0.9950	1	0.9886

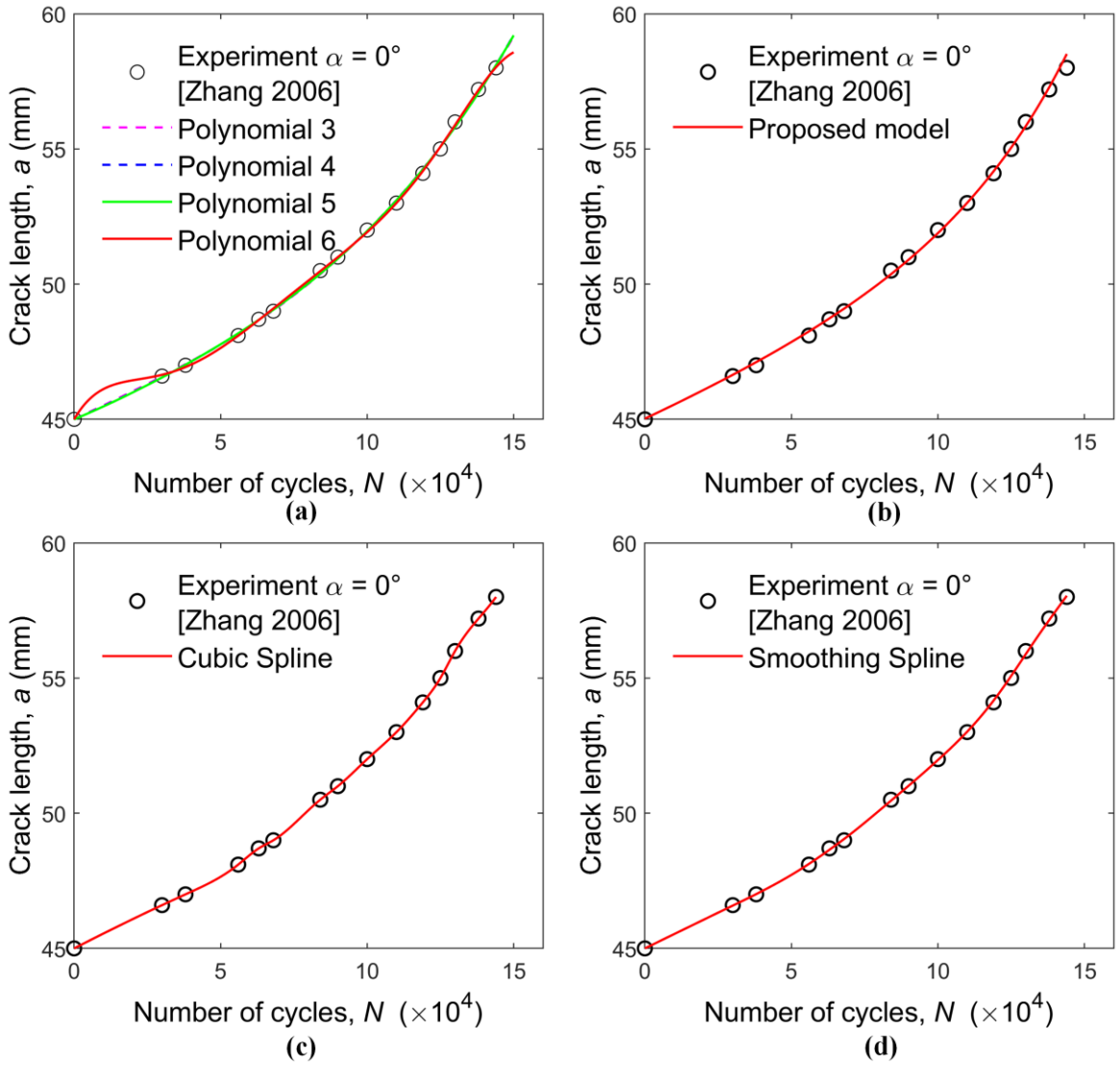

Figure 5.2 Experimental $a-N$ data and the fitted curves for the CTS Specimen of 0° (16 data points, (Zhang et al., 2006)**) (a) polynomial fits (b) double exponential fit (c) cubic spline fit and (d) smoothing spline fit**

Table 5.3 Best-fit parameter values for the CTS Specimen of 0° (Zhang et al., 2006)

Parameter	Fit type						
	Poly 3	Poly 4	Poly 5	Poly 6	Double Exp.	Cubic Spline	Smoothing Spline
SSE	1.2131	1.1275	1.1174	1.0555	0.2423	0	0.0363
r^2	0.9947	0.9951	0.9951	0.9954	0.9989	1	0.9998

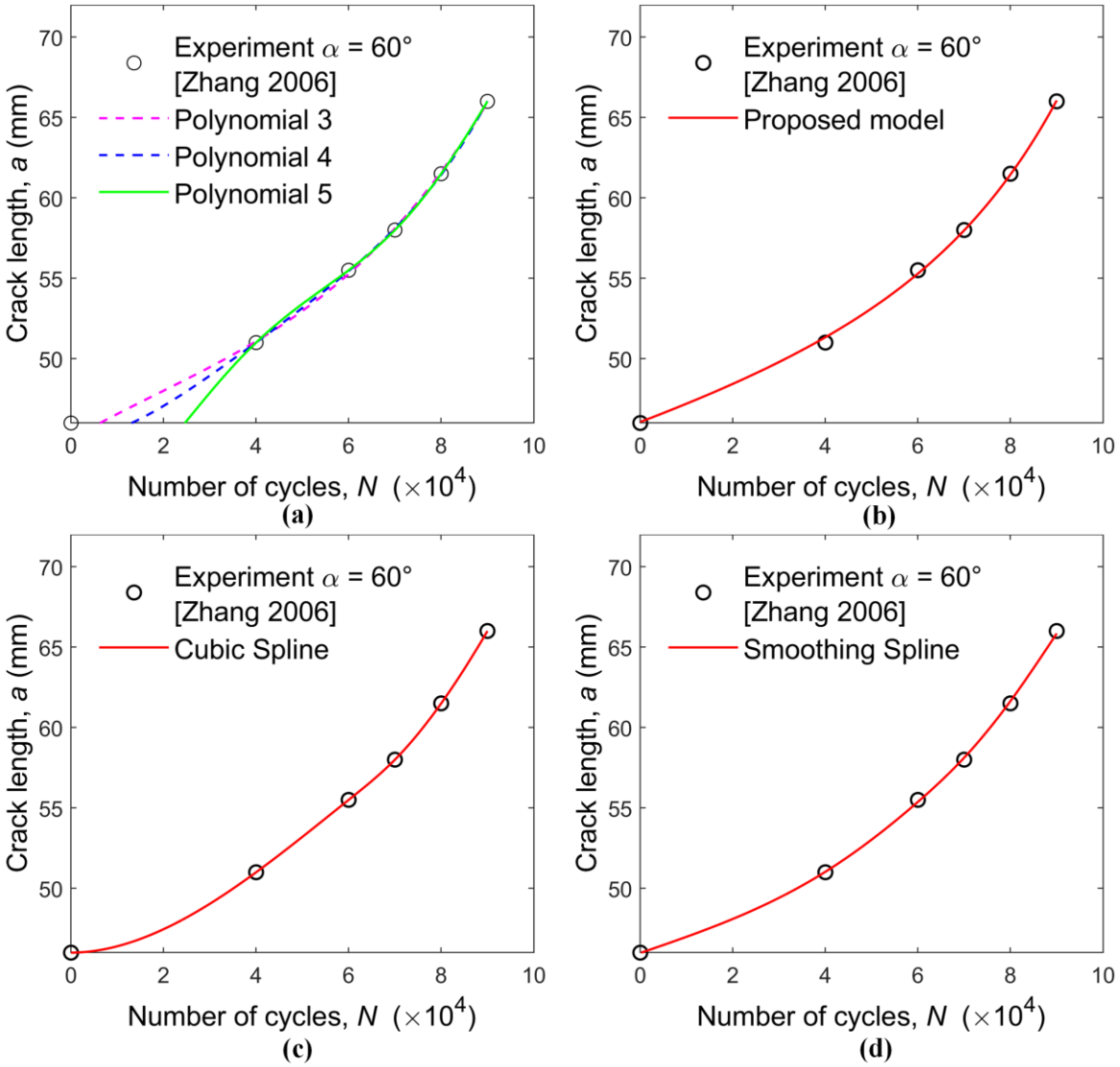

Figure 5.3 Experimental $a-N$ data and the fitted curves the CTS Specimen of 60° (7 data points, (Zhang et al., 2006)**) (a) polynomial fits (b) double exponential fit (c) cubic spline fit and (d) smoothing spline fit**

Table 5.4 Best-fit parameter values for the CTS Specimen of 60° (Zhang et al., 2006)

Parameter	Fit type						
	Poly 3	Poly 4	Poly 5	Poly 6	Double Exp.	Cubic Spline	Smoothing Spline
SSE	0.1057	0.0151	2.09e-19	--	0.0907	0	0.0763
r^2	0.9996	0.9999	1	--	0.9994	1	0.9997

In the first set of experimental data using 32 data points (Fig. 5.1), the higher order polynomial fits (Order 5, Order 6) are able to reasonably represent the experimental raw data with goodness of fit values of 0.9893 and 0.9934 respectively as compared to the lower order polynomial fits (Order 3, Order 4). One can see from Fig. 5.1 (a) that the higher order polynomial fits have many inflection points, which shows that the curve is not a smooth curve. Further, the oscillatory nature of the polynomial fits can also be seen in the higher order fits. Figure 5.1 (b) clearly shows the best-fitted plot using the proposed double exponential model is smooth without having any inflection points and with a goodness of fit (r^2) value of 0.9950. Although, a good quality of fits are obtained using the cubic spline and smoothing spline techniques, the corresponding best-fit curves, however, are not smooth and have multiple inflection points (as in the case of polynomials) due to the use of piecewise functions. Similar observations can also be noticed with the 16 numbers of data points in Fig. 5.2.

For the data with 7 data points, only the polynomial of order 3 was able to represent the series accurately, and the order 6 polynomial was unable to fit due to the insufficient number of data points as expected. However, the proposed double exponential function undoubtedly provides a good best-fit and smooth representation of the fatigue data even when the data points are less as compared to other methods considered.

Thus, due to the presence of multiple inflection points and lack of a unique order of polynomial fit for all data sets, and due to the utilization of piecewise functions in spline and smoothing spline techniques, these techniques are not preferable for the accurate representation of the $a-N$ experimental data. On the other hand, the results of all the examples clearly show that the proposed double exponential model is able to fit accurately with the goodness of fit values close to unity and provides a smooth representation of the data as per the expectation of the analyst. The curve of the double exponential model is smooth, and it does not have any inflection points. The double exponential model utilizes only three parameters (k, p and q) and can easily be fitted using commercial software such as MATLAB®, Origin®, etc.

In order to further demonstrate the advantage of fitting the experimental data using the proposed double exponential model, a mode I fatigue crack growth example is considered here (Kim and Kim, 2013). The Paris law (Paris et al., 1961) for mode I FCG rate is given as

$$\frac{da}{dN} = C\left(\Delta K\right)^m \tag{5.6}$$

where C and m are material constants and ΔK is the stress intensity factor range.

The mode I experimental data of Kim and Kim (2013) is fitted using the proposed double exponential model and obtained the material constants C and m as shown in Table 5.5. Table 5.5 also shows the material constants obtained by Kim and Kim using the raw experimental data.

Table 5.5 Paris constants reported by Kim and Kim (Kim and Kim, 2013) and calculated values using the proposed double exponential model

Parameter	(Kim and Kim, 2013)	Proposed model
$C\left((m/\text{cycle})/(MPa\sqrt{m})\right)^m$	1.10×10^{-11}	1.82×10^{-11}
m	2.78	2.6096

Next, the numerical prediction of the mode I fatigue life of the CT specimen used by Kim and Kim is carried. The fatigue life is evaluated using both the C and m values given in Table 5.5, and the estimated fatigue life is compared with the experimental data given by Kim and Kim (2013) as shown in Fig. 5.4.

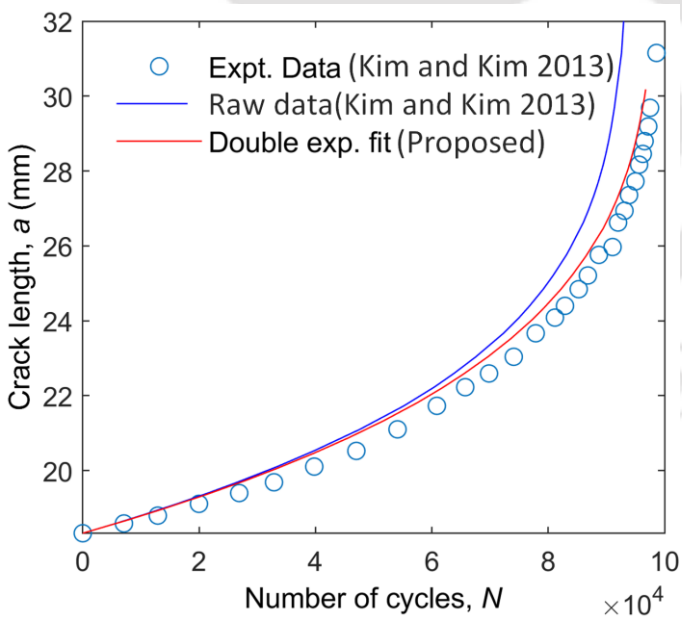

Figure 5.4 Comparison of the fatigue lives using the C and m values in Table 5.5

It can be clearly evident from Fig. 5.4 that the fatigue life calculated using the material constants C and m obtained using the proposed double exponential equations is more accurate as compared to the C and m values obtained directly from the experimental raw data by Kim

and Kim (2013). Thus, all these results of the example problems clearly show the efficacy of the proposed double exponential model under mode I and mixed mode (I/II) loading conditions. The results presented in subsequent chapters further indicates the usefulness of the proposed model.

5.4 Summary

A double exponential model for best-fitting of the experimental fatigue crack growth data for mode I and mixed mode (I/II) loading conditions is proposed in the present chapter. The proposed model utilizes only three parameters, and the same function can be used for the entire range of fatigue crack propagation, i.e., from the beginning of the crack propagation to the final rupture. The accuracy of the proposed model is verified by comparing it with the other models available for fitting fatigue crack growth data. The results of the present investigation clearly show that the proposed double exponential type function provides a good best-fit with the smooth representation of the experimental data without any inflection points as anticipated by the analyst. It has also been shown the fatigue life predictions using the C and m values obtained from the proposed function is very close to the experimental data.

Chapter 6

Experimental procedures

This chapter describes the experimental procedures implemented in the present investigation for the predictability assessment of various ΔK_{eq} models. Initially, the details of different test specimens and loading devices are described. The fabrication procedure of these specimens is also described in this chapter. Then the procedures for the mode I and mixed mode (I/II) fatigue crack growth experiments are discussed in detail. Procedures for the precracking and the crack length measurement during the mixed mode (I/II) experiments are also described in this chapter.

6.1 Details of the test specimens and loading devices

In the present investigation, two materials viz., SS 316 steel and Al 6061 T6 alloy are considered in the experimental studies in order to achieve the stated objectives. Apart from the tensile test specimens, two types of testing specimens, i.e., one for the mode I FCG tests and another one for the mixed mode (I/II) FCG studies are considered in the present investigation. The following specimens are fabricated for the FCG experiments

1. Compact tension specimen (CT specimen) made of SS 316 and Al 6061-T6 for the mode I FCG tests.
2. Compact tension shear specimen (CTS specimen) made of SS 316 and Al 6061-T6 for the mixed mode (I/II) FCG studies.

In addition to the above two types specimens, the mixed mode fatigue experiments require the use of a special loading device (known as Richard's fixture) to apply the mixed mode I/II loading on the CTS specimens using a uniaxial tensile testing machine. Pins are used for connecting the CTS specimen to Richard's fixture, and this fixture, along with the

specimen, in turn, is connected to the testing machine using the clevis grips. The following are the additional details of the fixtures and pins used for in the present work.

1. Richard's loading device or loading fixture is made of EN 24 (AISI 4340) steel.
2. Pins (for connecting the fixture and CTS specimen) are made of H13 steel.

The complete details of all the specimens and fixtures used are described in the subsequent sections.

6.1.1 Compact tension specimen

Mode I fatigue crack growth experimental studies using the CT specimen are required for the determination of the Paris' material-dependent constants C and m which appear in the mode I Paris law as well as in the modified Paris law (Eq. 3.39 and Eq. 3.40). Accurate values of these constants are needed for the correct estimation of the mixed mode (I/II) fatigue life. All mode I FCG tests have been conducted according to the ASTM E647-15e1 standard. For this purpose, standard CT specimens have been made using both the materials SS 316 and Al 6061-T6. Dimensions and other details of the CT specimen fabricated in the present investigation are shown in Fig. 6.1 (a). A crack length (a) of 45 mm, a width (b) of 60 mm, and a thickness (t) of 22 mm are set to all the CT specimens. All dimensions and tolerances of the specimen are chosen according to the ASTM E647-15e1 and E399-19 standards. The details of the notch are shown in Fig. 6.1 (b). The surfaces of the specimens are machined using the face milling operation. All the CT specimens are fabricated using the wire electric discharge machine (EDM). The wedges provided on the front faces of the CT specimen are to facilitate the crack length measurement using the crack opening displacement (COD) gauge. The specimens are connected to the clevis grips of the testing machine using pins for imparting the cyclic axial loads.

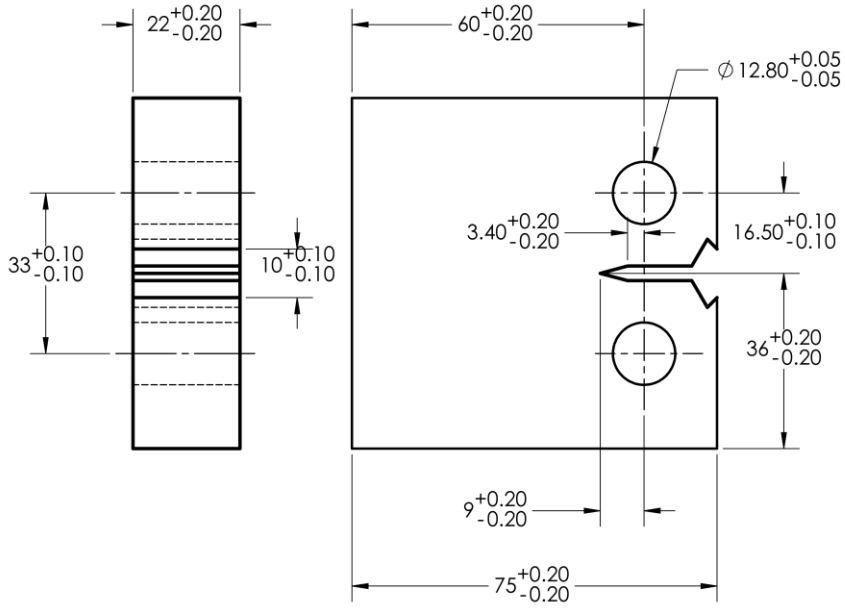

(a)

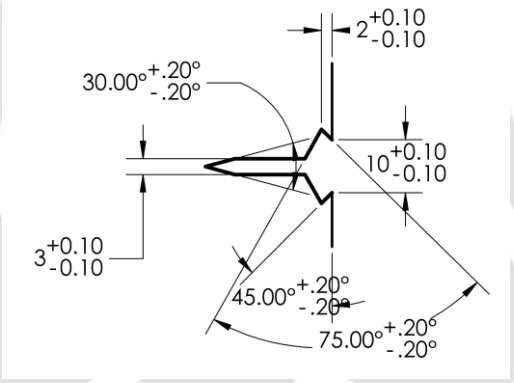

(b)

Figure 6.1 Dimensions of the (a) CT specimen and (a) notch

6.1.2 Compact tension shear specimen

The compact tension shear (CTS) specimen is widely used for the mixed mode (I/II) FCG experimental studies. In the present investigation, these specimens are made using both the SS 316 steel and Al 6061-T6 materials. As there is no standard test procedure available for the mixed mode (I/II) FCG studies to date, the dimensions of the CTS specimen provided by Richard (1983) have been employed in the present investigation. These suggested geometrical proportions are widely employed by the earlier researchers. Further, for the same reason of no standard, ASTM E647-15e1 guidelines are usually adopted for the mixed mode cyclic loading as well. The geometry and dimensions of the CTS specimen used are shown in Fig. 6.2. All the CTS specimens are fabricated using the wire EDM. A width (b) of 90 mm and a thickness (t) of 15 mm have been chosen for the CTS specimens. The starter notch for the crack is made

according to the ASTM E647-15e1 standard. In all the specimens, the initial machined notch length is 40 mm, and after a fatigue pre-crack of length 5 mm from the notch tip, the initial crack length (a) for the fatigue testing is 45 mm and $a/b = 0.5$. The holes provided near the top and bottom edge of the plate are aid to connect to Richard's loading fixture. All tolerances in Fig. 6.2 are according to the ASTM E647-15e1 standards.

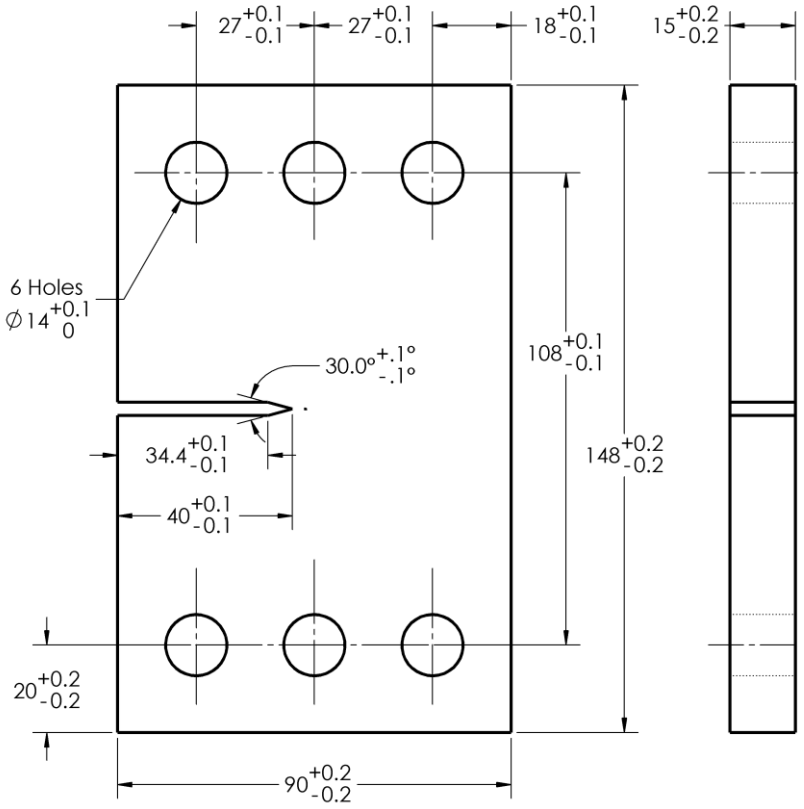

Figure 6.2 Geometry and dimensions of the CTS specimen.

6.1.3 Richard's loading device

In mixed mode (I/II) fatigue testing, Richard's loading device (Richard and Benitz, 1983) or Richard's loading fixture facilitates the simultaneous application of both the in-plane tensile and shear loadings on the CTS specimen. This fixture consists of four identical loading plates. The geometry, dimensions, and tolerances of a loading plate employed in the present experiments are shown in Fig. 6.3. All the four loading plates of Richard's fixture are made of high strength alloy steel EN 24 (AISI 4340), (which has a yield strength of 750 MPa) and fabricated using the wire EDM.

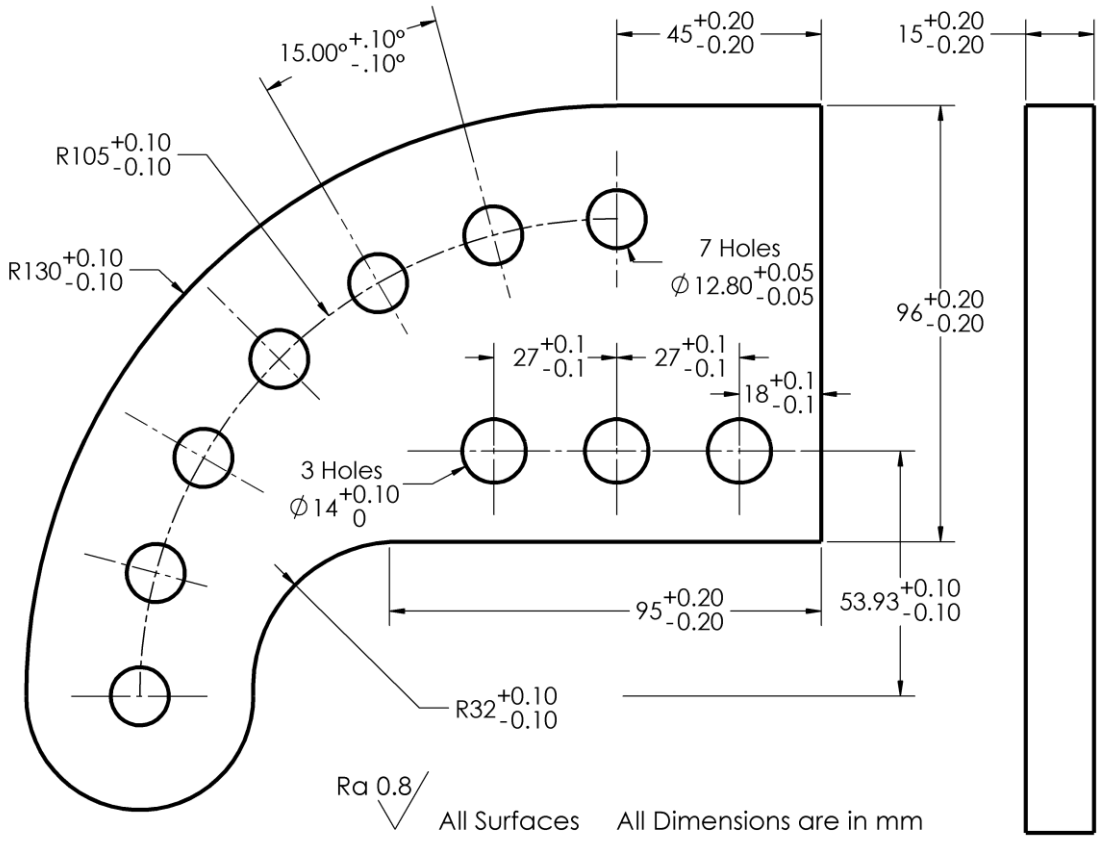

Figure 6.3 Geometry and dimensions of the Richard's loading device

Two such loading plates are connected to the CTS specimen (with the specimen being in between the two plates) through the three holes ($\phi = 14$ mm) located on top of the specimen by means of a 14 mm diameter pins. The remaining two plates are connected to the bottom holes of the specimen. The seven holes located circumferentially on each of the loading plates are used to connect the fixture to the clevis grips of the tensile testing machine. In the present study, these seven holes are graduated at an interval of 15° and produces different required mode mixity ratios in steps of 15°. Further, it is also possible to apply pure mode I (0°) and pure mode II (90°) loadings apart from the required mode mixities using the present fixture shown in Fig. 6.3.

6.1.4 Tensile test specimens

The FCG experiments and the numerical simulations of the mixed mode (I/II) FCG require accurate values of the material properties. Therefore, tensile test specimens have been fabricated using both the SS 316 steel and Al 6061-T6 materials. The geometry of the tensile test coupons used in the present investigation is shown in Fig. 6.4. It should be noted here that,

the tensile test specimens, the CT and CTS specimens are made from the same stock plates of SS 316 and Al 6061-T6. The tensile tests have been conducted on these specimens according to ASTM (ASTM E8/E8M-16a) procedure.

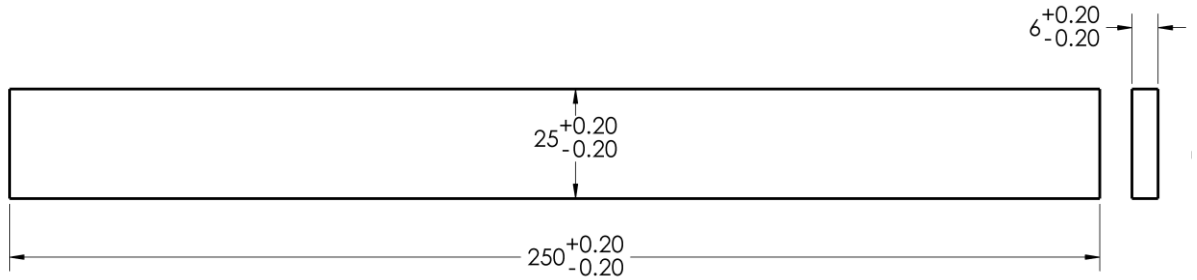

Figure 6.4 Dimensions of the rectangular tensile test specimen

6.2 Details of fabrication of the specimens, loading plates and pins

This section discusses the further details of fabrication of the CT, CTS, Richard's loading device, tensile test specimens, and the pins used for different connections. The heat treatment processes for the loading device and pins are also described in this section.

6.2.1 Specimens preparation

Figure 6.5 shows the material coordinate system and orientation of the specimens used in the present study. In L-T orientation, the specimen is loaded in the longitudinal direction (rolling direction), and the crack is expected to grow in the transverse direction. In the present investigation, all the CT (Fig. 6.6), CTS (Fig. 6.7), and tensile testing (Fig. 6.8) specimens are cut in the L-T orientation and fabricated from the same stock plate. All these three types of specimens have been fabricated using wire cut electrical discharge machining (EDM) as per the dimensions shown in Figs. 6.1, 6.2 and 6.4.

CT specimens of thickness 22 mm and CTS specimen of thickness 15 mm are fabricated using both the SS 316 steel and Al 6061-T6 alloys. In the present investigation, two CT specimens and two tensile test specimens from each of the two selected materials have been fabricated and tested. On the other hand, one CTS specimen for each of the loading angles 30°, 45°, and 60° has been fabricated and tested using the two selected materials. The notches have been cut in the fatigue specimens (CT and CTS) in the L-T orientation ((Fig. 6.5) and maintained the root radius within the limits specified by ASTM E647-15e1 standard (notch root diameter < 0.5 mm). The surfaces of the CTS specimens were mirror-polished so that even

a very small increase in crack length can be observed using the digital microscopes. Starting from the crack tip, gridlines are marked on the surface of the CTS specimen at an interval of 1 mm. The intersection of the crack with the gridline act as a reference point during the crack length measurement using the digital microscope. Polishing of the surfaces has been done using sandpaper of different grit sizes. Initially, the sandpapers of coarse grit size (100 and 120) are used. Finally, for fine finishing, more fine grades are used. The mirror polished surface finishing of SS 316 has been finally achieved using 800 and 1000 grit size. On the other hand, for the CTS specimens made of Al 6061-T6, the mirror-polished surfaces have been achieved using grit sizes of 1200 and 2000. Figures 6.6-6.8 shows photographs of the CT, CTS, and tensile testing specimens fabricated using the SS 316 steel and Al 6061-T6 alloy.

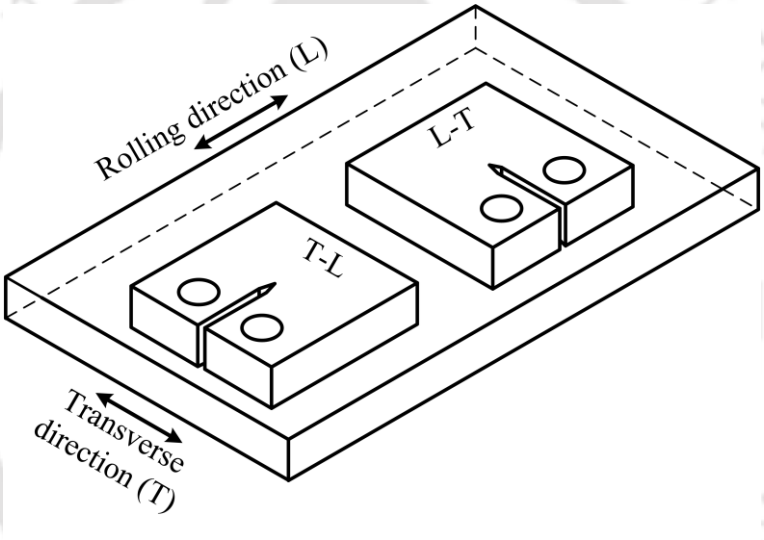

Figure 6.5 Definition of the material coordinate system and orientation of the fatigue test specimens

Figure 6.6 Photograph of the fabricated CT specimen Al 6061-T6 (left) and SS 316 (right)

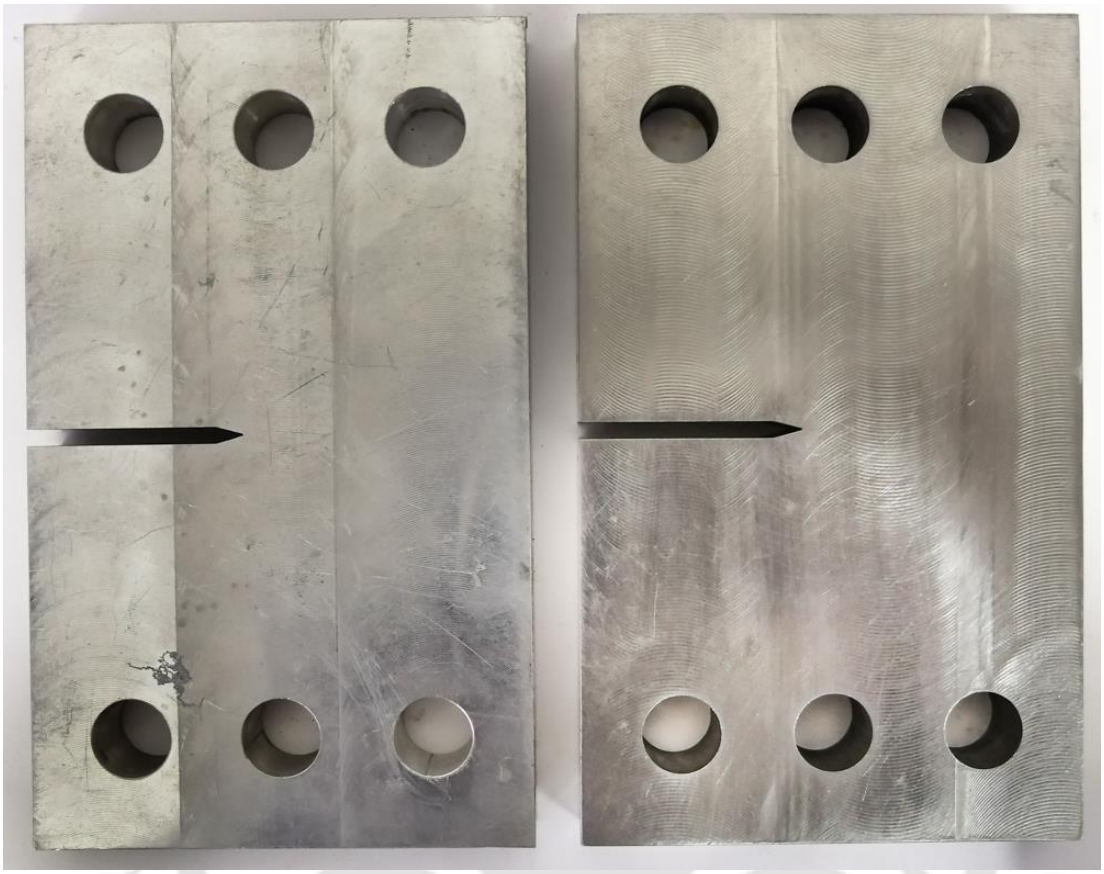

Figure 6.7 Photograph of the fabricated CTS specimen Al 6061-T6 (left) and SS 316 (right)

Figure 6.8 Photograph of the fabricated tensile test specimen Al 6061-T6 (top) and SS 316 (bottom)

6.2.2 Richard's loading fixture and pins preparation

CNC milling is used for drilling the holes and cutting the profile of all four loading plates (Fig. 6.3) of Richard's fixture. The material chosen for the loading device fabrication is EN 24 (AISI 4340 stainless steel), which is a high strength alloy steel with a yield strength of 750 MPa. The loading fixtures are finally hardened and tempered. For the hardening, the fixture is heated to 840° C in a muffle furnace and then quenched by covering the fixture with a mixture

of alumina and graphite powders to prevent the oxidation. Again, the fixture is heated to 650° C for tempering and kept at that temperature for 2 hours. After soaking, it is allowed to cool in the furnace to relieve the stresses.

Pins for connecting the Richard's fixture to the CTS specimen and connecting the fixture to the clevis grips of the testing machine are fabricated using H13 steel. The former pins are of the size 80 mm in length and 14 mm diameter. The diameter and length of the later pins are 12.5 mm and 100 mm, respectively. The pins are also hardened and tempered following the recommended procedures (Ghosh and Mallik, 2010) for hardening and tempering. Photograph of Richard loading device and pins are shown in Fig. 6.9.

Figure 6.9 Photograph of Richard's loading device and pins

6.3 Details of the experimental setup

This section describes the details of the experimental setup and the various equipment used in the present study. All the tensile tests, mode I and mixed mode FCG experiments are conducted on a 250 kN closed-loop servo-hydraulic universal testing machine (Make: Biss-ITW, Model: Median 250). In all the tests, perfect alignment of the grips of the testing machine is ensured before conducting the tests. As the CT and CTS specimens need to be connected to the testing machine via clevis grips, therefore only tensile-tensile cyclic loads have been applied on these specimens under load control mode. The required nature of the cyclic loading can be selected in the testing machine software, and the actuator applies the required cyclic loads under computer control. In all the FCG tests of the present investigation, a load ratio (R) of 0.1 and the load frequency of 10 Hz is maintained. The loads for all the FCG tests are greater than the forces during pre-cracking.

6.3.1 Mode I fatigue experiments

In the mode I FCG tests, two repeated tests until final fracture have been conducted for each of the selected materials SS 316 steel and Al 6061-T6 alloy for the determination of the Paris' material constants C and m (Eq.3.39) of the above materials. Thus, as stated earlier, two CT specimens have been made from each of the above materials. These specimens are connected to the top and bottom clevis grips of the testing machine using pins of diameter 12.7 mm as shown in Fig. 6.10. The COD gauge used in the present experiments is Biss AC-07-0020, which has a 10 mm gauge length and +4 mm/ -1 mm travel range. The gauge is firmly mounted to the knife edges provided on the front face of the CT specimen. The parallelism of both knife edges is checked to ensure that the COD gauge does not slip during the cyclic loading. This is ensured by moving the gauge along the knife edges and checking the gauge readings. The growing crack lengths are calculated using the VAFCP (Variable Amplitude Fatigue Crack Propagation) module in-built in the testing machine. The COD gauge measures the crack opening displacements and converts it into the compliance at the crack flanks following the ASTM E647-15e1 guidelines. The measured compliance is, in turn, converted into the crack length in the VAFCP module. The values of mode I SIF range are also calculated in the VAFCP module using the ASTM recommended formula (ASTM E399-19).

Figure 6.10 Mode I CT specimen with the COD gauge for fatigue test

The mode I FCG tests are carried out under constant load ($\Delta P = \text{constant}$) conditions. A load ratio (R) of 0.1 and a frequency (f) of 10 Hz have been considered. The maximum load in the cycle $P_{\max}$ is set according to the material of the specimen, as shown in Table 6.1. Some other details pertaining to the mode I FCG tests are also presented in Table 6.1. The initial crack length (after the pre-cracking) of all the four specimens is 14 mm (initial notch length (9 mm) + pre-crack length (5 mm)) so that $a/b = 0.23$, which is consistent with the ASTM E647-15e1 standards $(a/b > 0.2)$. All the mode I FCG tests are continued until fracture of the specimens. Using the data acquisition system, fatigue crack growth data is recorded at every 0.01 mm crack increment.

Table 6.1 Loading details of the mode I FCG tests

Sl. No.	Specimen	Material	$P_{\max}$ (kN)	R	Frequency (Hz)	No. of specimens tested
1	CT	Al 6061-T6	14	0.1	10	2
2	CT	SS 316	28	0.1	10	2

6.3.2 Mixed mode (I/II) fatigue experiments

Mixed mode (I/II) FCG experiments have been conducted for three different loading angles (mode mixities) of 30°, 45°, and 60°. One specimen for each loading angle had been tested for each of the SS 316 steel and Al 6061-T6 materials in order to record the data of crack length versus the number of loading cycles. However, one repeated test is conducted for the loading angle 30° on a CTS specimen made of Al 6061-T6 alloy. Thus, altogether seven mixed mode fatigue tests have been conducted. All the specimens have been fatigued until the final fracture. In these tests, first, the CTS specimen is connected to Richard's loading fixture, and the fixture is, in turn, connected to the clevis grips of the testing machine shown in Fig. 6.11.

Figure 6.11 Mixed mode CTS Specimen along with the digital microscope

As mentioned earlier, Richard's loading device is fabricated for applying 0°, 15°, 30°, 45°, 60°, 75°, and 90° loading, where 0° refers to the pure mode I loading and 90° refers to the pure mode II loading. Figure 6.12 shows the manner in which seven different levels of mode mixity can be achieved by changing the position of the clevis pin. As there is no standard test procedure available for the mixed mode (I/II) FCG studies, the current practice is to follow the guidelines provided by the ASTM E647-15e1 standard.

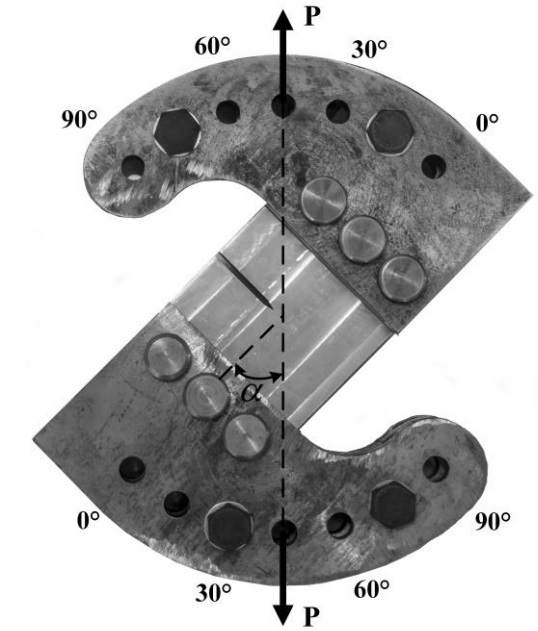

Figure 6.12 CTS Specimen with Richard's loading device

Similar to the mode I FCG tests, a load ratio of 0.1 and the loading frequency of 10 Hz is maintained in all the mixed mode (I/II) tests. The maximum load P_{max} on each of the seven CTS specimens tested is shown in Table 6.2. Other details of the tests are also presented in Table 6.2. The tests are performed under the load control mode. The sinusoidal waveform loading is considered in all experiments. The test builder module of the testing machine is used for applying the required cyclic loads under the load control. The initial crack length of all the seven specimens is 45 mm (initial notch length (40 mm) + pre-crack length (5 mm)) so that $a/b = 0.5$, which is consistent with the ASTM E647-15e1 standards $(a/w > 0.2)$.

Table 6.2 Details of mixed mode (I/II) fatigue experiments

Material	Loading angle ($\theta°$)	P_{max} kN	R	Frequency (f, Hz)	No. of repeated tests
Al 6061-T6	30	16	0.1	10	2
	45	16	0.1	10	1
	60	16	0.1	10	1
SS 316	30	36	0.1	10	1
	45	40	0.1	10	1
	60	47	0.1	10	1

Since the mixed mode FCG tests are not standardized, there is no provision available in the testing machine software for recording the crack length. In the present investigation, the length of the growing crack in the mixed mode (I/II) fatigue experiments is measured using the portable Dino-lite Pro AM4013 digital microscope (as shown in Fig. 6.11) with a magnification of 10x to 220x. The present measurements are made at 50x magnification. The microscope is kept perpendicular to the surface of the specimen during the experiments. The digital microscope is attached to the traveling microscope for precise movements. This arrangement is also necessary for providing the movement in three directions so that the viewing area of the digital microscope can be adjusted manually to follow the tip of the growing crack. The Dino-capture software (which comes along with the digital microscope) is used for recording the images from the digital microscope. The images are recorded at every 5-sec intervals (i.e., for every 50 cycles, since the loading frequency is 10 Hz). The crack length and the crack path have been measured from these stored images by post-processing them manually.

In order to provide a reference point for the crack length measurements, grid lines are marked on the mirror-polished surface of the CTS specimen. The gridlines are marked from 45 mm (crack tip) to 70 mm (probable final crack length) at 1 (one) mm interval. Figure 6.13 shows a typical CTS specimen with the grid lines. The point of intersection of the growing crack with these grid lines are taken as the reference point for the crack length measurement. The corresponding number of loading cycle data is obtained from the test builder. Using the measured crack length from the microscope images and loading cycles from the test builder the crack length (a) versus the number of loading cycles (N) data has been obtained, and the crack growth curves have been plotted manually using the measured $a-N$ data. It should be noted here that the time is synchronized between the microscope image data and the loading cycle data. Figure 6.14 shows the overall view of the mixed mode (I/II) fatigue crack growth tests. Figure 6.15 illustrates various stages of the mixed mode (I/II) FCG experiments.

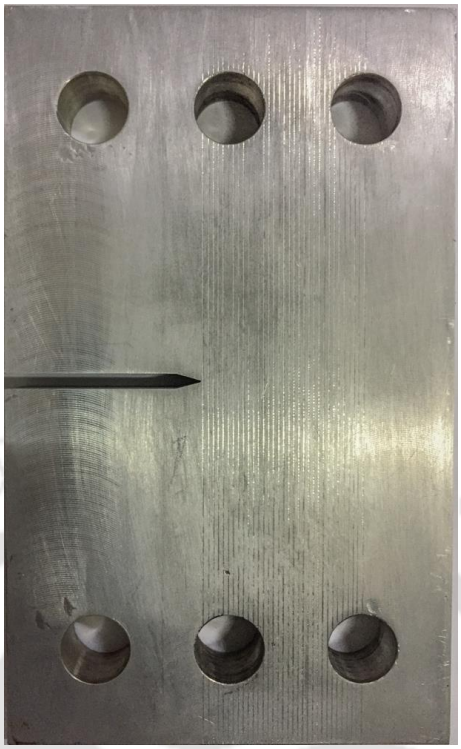

Figure 6.13 CTS specimen with the grid lines

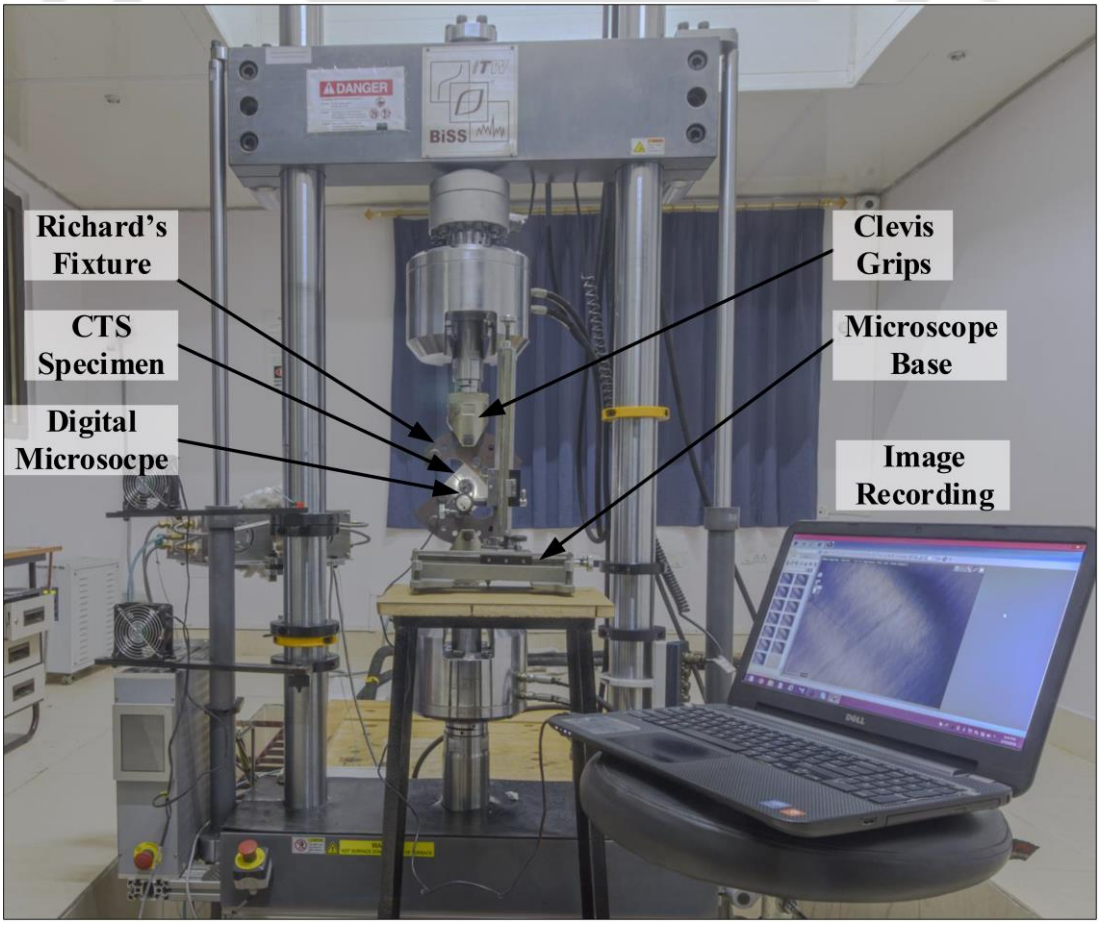

Figure 6.14 Experimental setup for mixed mode fatigue test

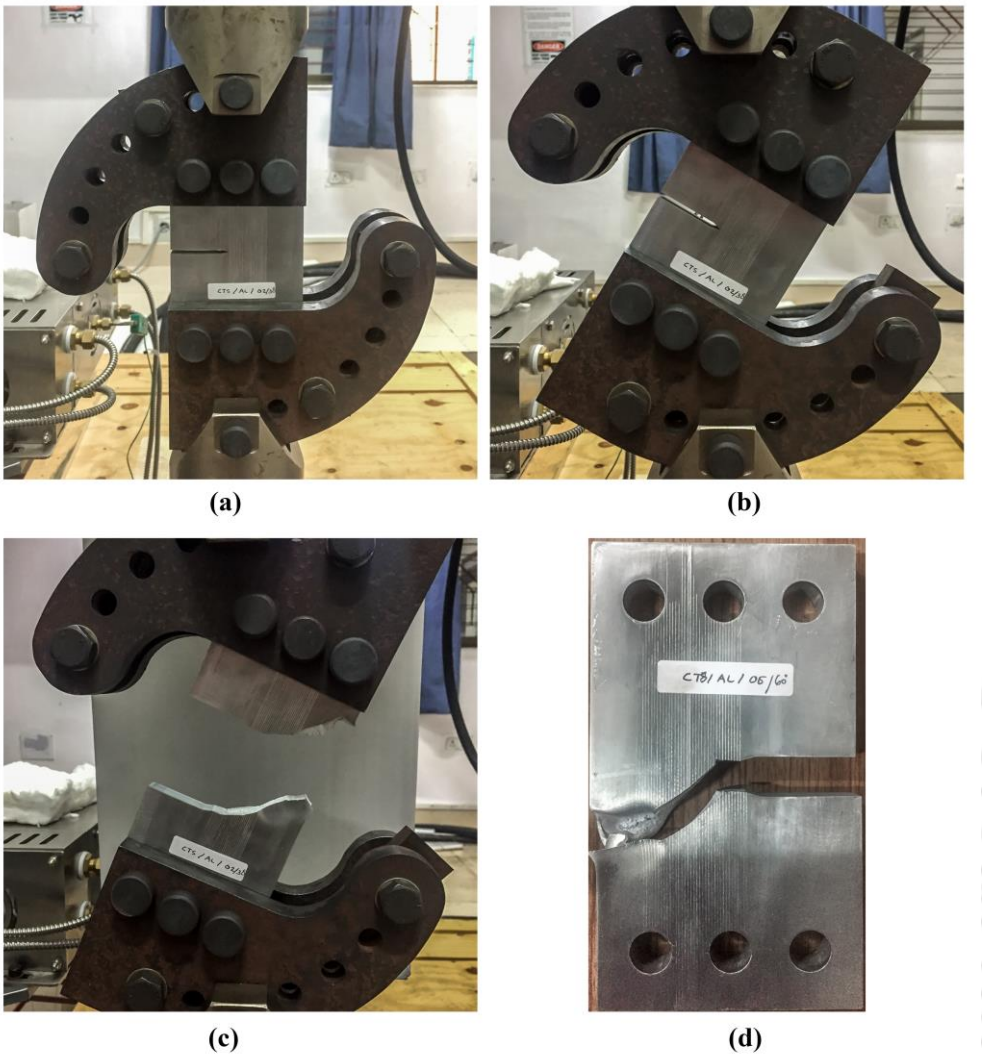

Figure 6.15 Different stages of mixed mode (I/II) fatigue crack growth experiment (a) precracking (b) fatigue crack growth test (c) at the end of the test and (d) fractured specimen

6.4 Precracking

Precracking is essential in fatigue tests since the crack growth has to be initiated from an idealized sharp crack. Fatigue pre-cracking under mode I loading is a common approach in fracture mechanics studies. The correctness and the reliability of the fatigue test largely depend on the quality of the machined notch and the correctness of the fatigue pre-crack. In the present investigation, all the specimens for the FCG studies are subjected to mode I cyclic loading (as per the guidelines of ASTM E647-15e1) at a constant frequency (under load control) so that the crack initiation takes place from the initial machined notch. The precracking process is continued until a sharp fatigue crack of length 5 mm is reached.

For the CT specimens, as the mode I FCG test is standardized, the pre-crack length can be monitored, and the process can be terminated automatically once the crack reaches to a predefined length. On the other hand, as there is no possibility for automatic detection of the length of the crack for the CTS specimens, the cyclic load is applied through the hole pairs labeled 0° (Fig. 6.12). The crack tip is then observed using the digital microscope. The pre-cracking process is stopped manually when the growing crack tip touches the gridline made at 45 mm. A load ratio of 0.1 and the loading frequency of 10 Hz is maintained during the pre-cracking process. The maximum load P_{max} on various specimens tested is shown in Table 6.3 along with the number of load cycles consumed for reaching a crack length of 5 mm. Figure 6.16 shows the enlarged view near the initial crack tip of a typical specimen after the pre-cracking.

Table 6.3 Details of the precracking

Sl. No.	Specimen	Material	P_{max} (kN)	R	Frequency (Hz)	Loading angle	Cycles to failure
1	CT	Al 6061-T6	14	0.1	10	0°	87421
2	CT	SS 316	28	0.1	10	0°	169368
3	CTS	Al 6061-T6	16	0.1	10	30° (Exp 1)	48952
						30° (Expt 2)	59824
						45°	54596
						60°	55000
4	CTS	SS 316	36	0.1	10	30°	120726
						45°	113008
						60°	105630

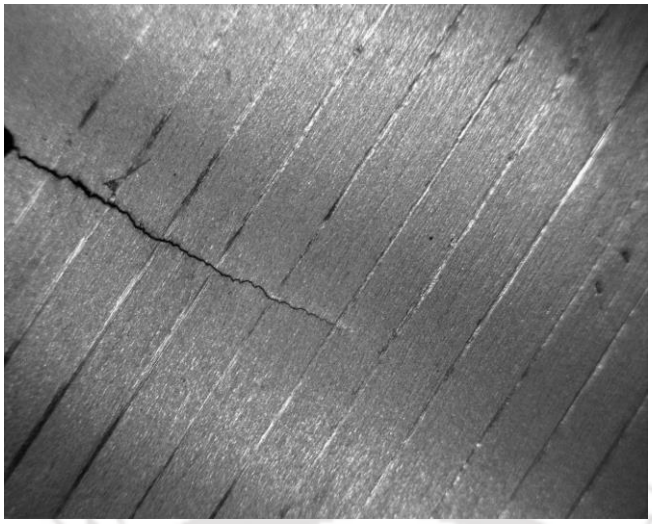

Figure 6.16 A typical view near the pre-crack

6.5 Mixed mode crack length determination procedure

Section 6.3 presents the details of the digital microscope measurement approach adopted in the present investigation for the determination of the length of the growing crack under mixed mode (I/II) cyclic loading conditions. This section discusses the image processing technique implemented in the present investigation for the determination of the length of the crack from the images captured by the digital microscope. Figure 6.17 illustrates the various steps involved in the measurement of crack length from the captured images. One of the major steps in the crack length measurement is the calibration. Calibration of the images is done by using grid lines; a length of 5 mm is considered for the calibration. It can be noted from Fig. 6.17 that, as expected, the crack path is not a straight line between two adjacent grid lines. In such cases, the crack path measurement is made over the zigzag path between the grid lines.

There are more than 600 images that have been taken for each of the seven mixed mode (I/II) FCG experiments. However, some of the images are unusable due to the blur in the images. Thus, the crack lengths are measured from the selected images only. The intersection of the crack with the gridline is considered as a reference point for the measurement of the crack length. After the calibration, from each image, the distance from the reference point to the crack tip is measured using the Dino-Capture software. The number of loading cycles corresponds to that image are obtained from the testing machine, and thus the crack length versus the number of loading cycles ($a-N$) data corresponding to that image is obtained. The process is repeated using all the selected images to obtain the $a-N$ curve for a particular specimen.

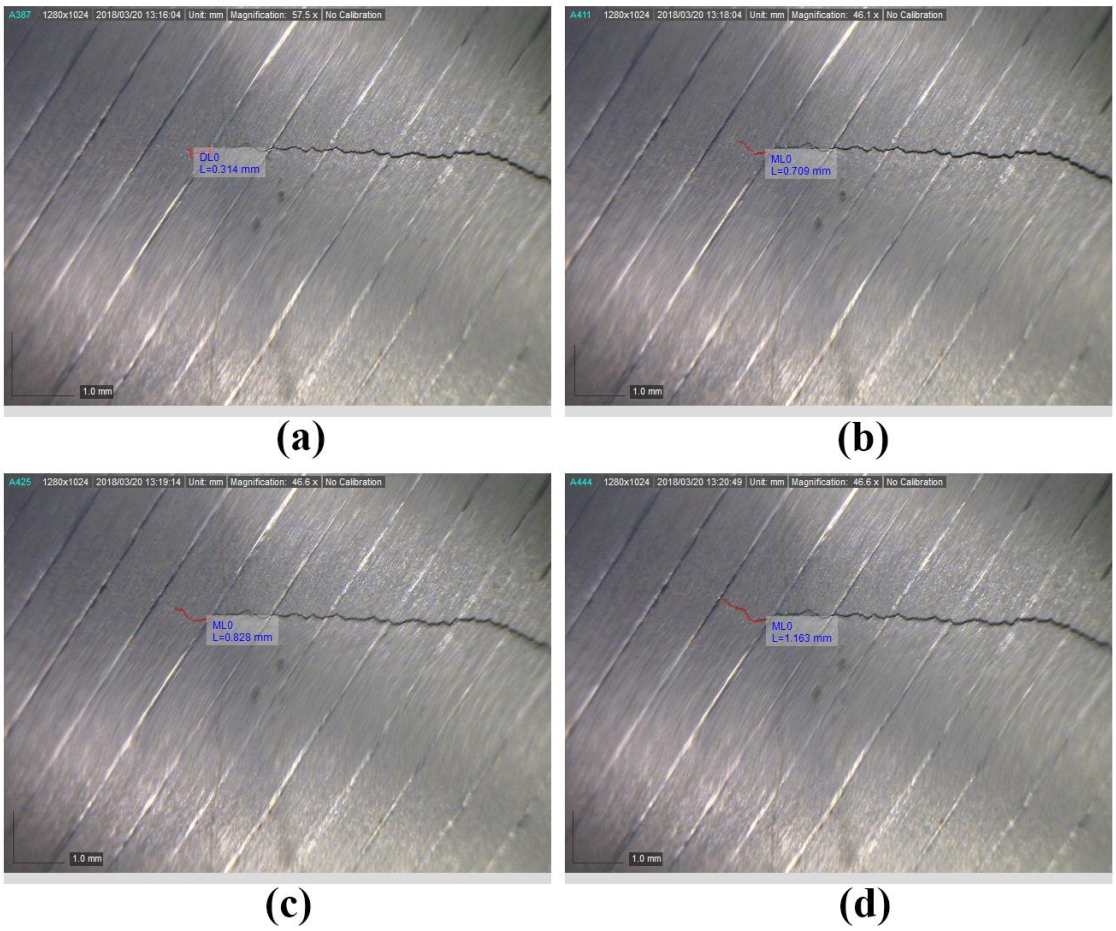

Figure 6.17 Sequence of crack length measurement: Length measurement from (a) reference point (point on grid line) to initial point (b), (c) from reference point to intermediate points (d) reference point to final point lies on the next reference point through intermediate points (a point on adjacent grid line)

6.6 Fractography studies

Fractography is an effective method of analyzing the fractured surfaces for studying the underlying microscopic mechanism behind the material failure. These microscopic mechanism helps to identify the causes of the failures. Also, different modes of failure leave different features on the fractured surface, which aid to identify the causes of failure. The field emission scanning electron microscope is an important tool for fractography studies. The fractography studies of the fractured mode I and mixed mode (I/II) specimens made of both the materials are performed. The fractography study of Al 6061-T6 alloy is performed using Zeiss sigma FESEM and that of SS 316 is performed using Jeol JSM 7610 machine (shown in Fig. 6.18)

Figure 6.18 FESEM equipment used in the present study (a) Zeiss Sigma (b) Jeol JSM 7610 (Image courtesy: Zeiss Germany, Jeol Japan)

6.7 Summary

In this chapter, a detailed description of the specimens and the loading fixtures used in the present investigation and the procedure for their fabrication is presented. Details about the mode I and mixed mode (I/II) precracking and the FCG tests are also discussed in this chapter. Further, the crack length measurement using the digital microscope during the mixed mode (I/II) fatigue tests are also detailed.

Chapter 7

Predictability assessment: Using Al 6061-T6 alloy

This chapter discusses the assessment of the nature of predictability of the mixed mode (I/II) fatigue life using the modified Paris law with the selected ΔK_{eq} models and experimental results of Al 6061-T6 alloy. Apart from experiments, numerical simulations of the mixed mode (I/II) FCG are also performed, and fatigue life is predicted using the seven selected ΔK_{eq} models. The error in predicted life is assessed using various global as well as pointwise error estimates. Finally, fractographic studies of the growing crack at various crack lengths are performed and discussed in this chapter to aid the present analyses.

7.1 Results of the tensile tests

The tensile test on two Al 6061-T6 specimens is performed following ASTM E8 standards. The details of the tensile test specimens are discussed in section 6.1.4. The material properties are not a prerequisite for the FCG experiments; however, they are necessary for the numerical simulation of the FCG. Table 7.1 presents the averaged tensile test results of the Al-6061-T6.

Table 7.1 Tensile test results of Al 6061-T6

Yield strength (MPa)	Ultimate tensile strength (MPa)	% Elongation	Young's modulus (GPa)	Poisson's ratio
270	307	14.8	68	0.33

7.2 Results of the mode I FCG experiments

The main purpose of the mode I FCG test in the present work is to obtain the Paris' constants C and m of Al 6061-T6 in Eq. 3.40, which is useful while carrying out numerical

predictions of mixed mode (I/II) fatigue life. As discussed in chapter 6, the tests are performed on the two CT specimens, as the test results are identical for both the specimens, the results of one specimen are presented here. In these tests, a maximum load of $P_{max} = 14$ kN, load ratio $R = 0.1\left(R = P_{min}/P_{max}\right)$, and a loading frequency of 10 Hz from pre-cracking to the final rupture are considered, as shown in Table 7.2. The number of loading cycles up to the final fracture of the specimen is also shown in Table 7.2. The instantaneous crack lengths are recorded using the COD gauges attached to the front face of the CT specimens. The crack growth rates are calculated using the VAFCP module of the testing machine. This module is built in compliance with the ASTM E399-17 and ASTM E647-15 standards. The crack length versus the number of cycles $(a-N)$ curve and the FCG rate $(da/dN - dK)$ curve obtained from the mode I fatigue test of a CT specimen are shown in Fig. 7.1. Figure 7.2 shows a fractured CT specimen at the end of the test. The Paris' constants of Al 6061-T6 using the experimental data from $a = 14$ mm to 36 mm are obtained as $C = 4.3378\times10^{-7}$ (mm/cycle)/(MPa^m m$^{m/2}$), and $m = 2.6183$. Nearly similar values of the material constants are obtained using both the CT specimens tested.

Table 7.2 Mode I FCG test details of Al 6061-T6

Specimen	Material	P_{max} (kN)	R	Frequency (Hz)	Cycles to fracture
CT	Al 6061-T6	14	0.1	10	41535

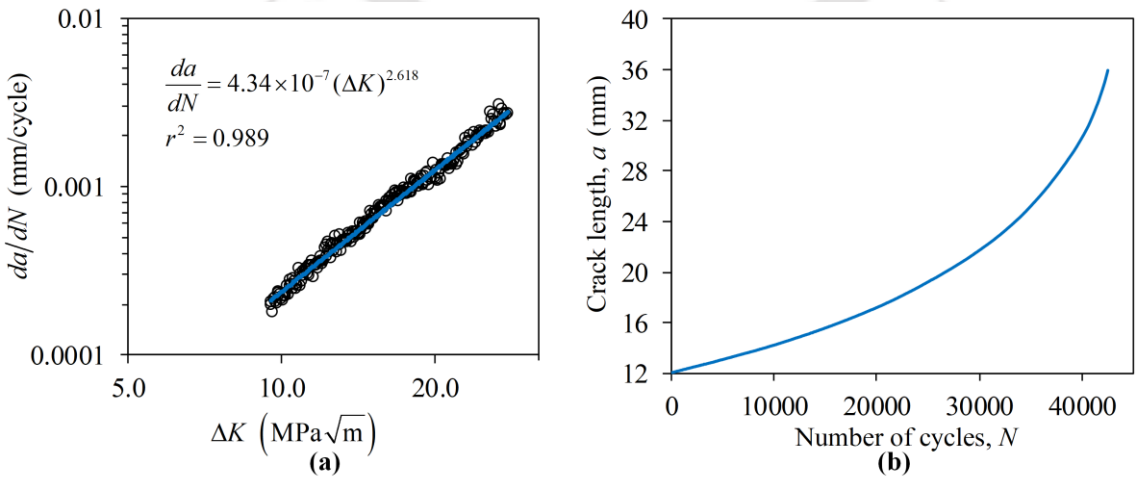

Figure 7.1 Fatigue crack growth curves for mode I loading (a) da/dN vs ΔK curve (b) a vs N curve

Figure 7.2 Fractured mode I specimen made of Al 6061-T6 alloy

7.3 Results of the mixed mode (I/II) FCG experiments

Mixed mode (I/II) fatigue crack growth experiments are carried out using the CTS specimen (Fig. 6.2) with the help of Richard's loading device (Fig. 6.3). Since there are no standards available for this test, ASTM E647-15 guidelines have been observed in the present experiments. As mentioned previously, three specimens with loading angles (angle between the direction of the applied tensile load and the crack axis) of 30°, 45°, and 60° are tested. All the three specimens are tested from the initial crack length to the final fracture. For all these three specimens, pre-cracking and FCG tests are carried out under load control with a constant load of $P_{\max}$=16 kN , load ratio $R=0.1$ and a frequency of 10 Hz. Two CTS specimens are tested for the loading angle 30° in order to study the precision with which all the mixed mode FCG experiments are carried out in the present work. For the rest of the loading angles, one specimen for each of the loading angles is employed. The other details of the mixed mode (I/II) FCG experiments, along with the number of loading cycles to the final fracture, are listed in Table 7.3.

Figure 7.3 shows photographs of the fractured CTS specimen for 30°, 45°, and 60° loadings angles. The crack initiation angles measured using the optical microscope and crack paths for all three specimens are shown in Fig. 7.4. These paths are compared with the paths estimated using the MTS criterion is presented in subsequent sections. Figure 7.5 shows $a-N$ plots of the raw experimental data (circled data points) obtained by analyzing crack growth images captured using the digital microscope (as discussed in chapter 6) and best-fit curves to

the raw data using the proposed double exponential model in Eq. (5.3). Coefficients in Eq. (5.3) corresponding to the four specimens are shown in Table 7.4. The corresponding goodness of fit $\left(r^2\right)$ is also given in Table 7.4. It can be noticed from Fig. 7.5 and Table 7.4 that the proposed best-fit model exhibits a highly satisfactory representation of the original raw data of the mixed mode experiments.

Table 7.3 Mixed mode (I/II) FCG test details of Al 6061-T6

Sl. No.	Specimen	Loading angle	P_{max} (kN)	R	Frequency (Hz)	Cycles to failure
1	CTS	30° (Exp-1)	16	0.1	10	34759
2		30° (Exp-2)				33216
3		45°				38535
4		60°				54847

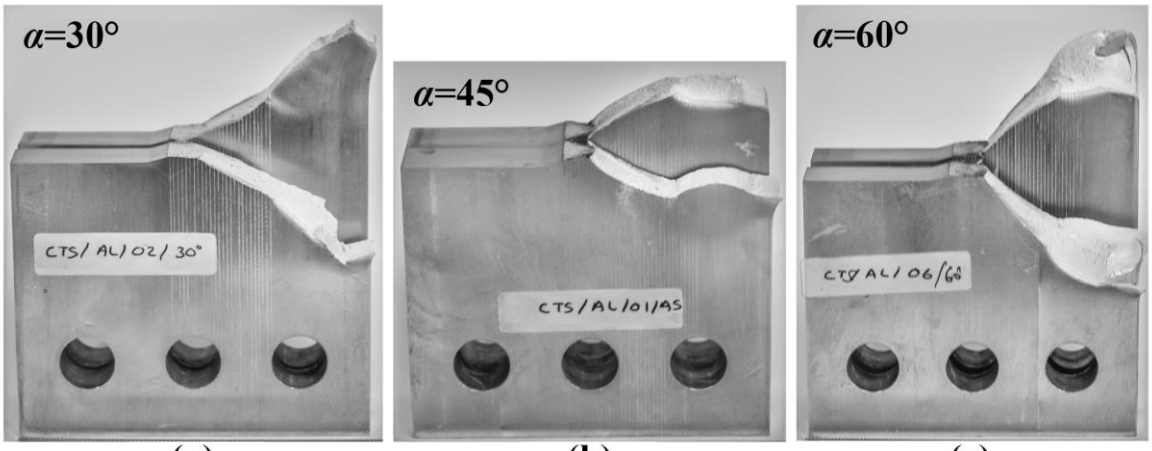

Figure 7.3 Fractured CTS specimens for the loading angles (a) 30°, (b) 45°, and (c) 60°

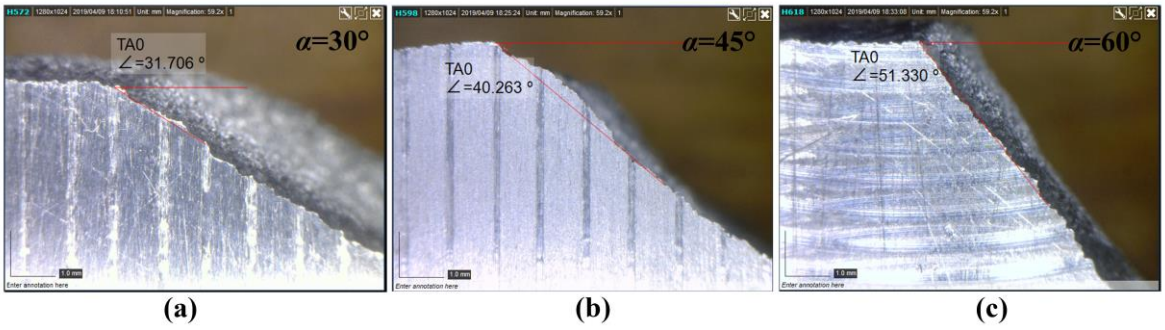

Figure 7.4 The fatigue crack initiation angle for (a) 30° (b) 45° and (c) 60° mixed mode (I/II) specimens

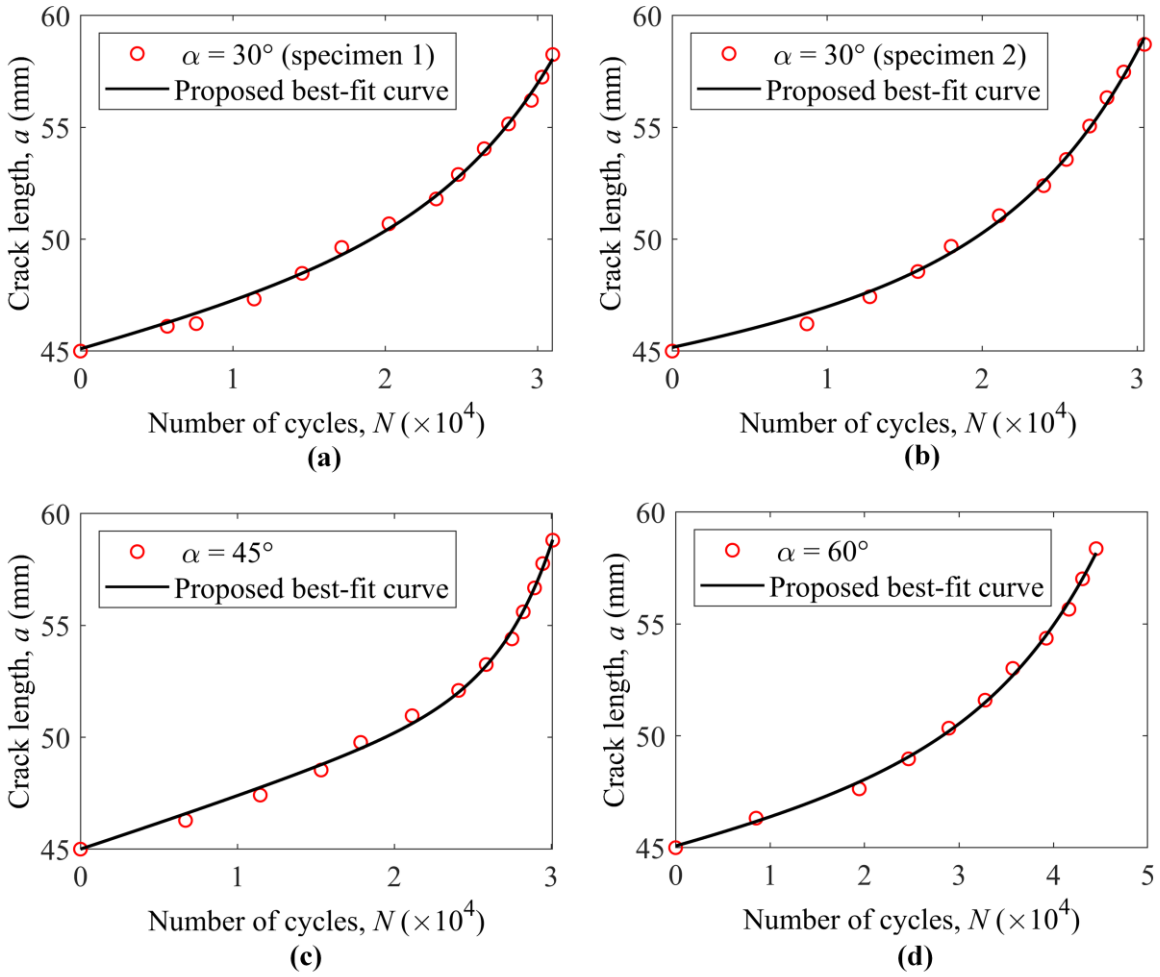

Figure 7.5 Experimental data and the best fit line using the three-parameter double exponential model for (a) Experiment-1 30° (b) Experiment-2 30° (c) 45° and (d) 60° loading angles

Table 7.4 Best fit parameters of the proposed double exponential model

Loading angle	p	k	q	r^2
30° (Experiment-1)	3.95×10^{-6}	1.08×10^{-1}	1.36×10^{-4}	0.9975
30° (Experiment -2)	2.59×10^{-6}	2.48×10^{-1}	1.22×10^{-4}	0.9965
45°	5.05×10^{-6}	4.24×10^{-4}	3.19×10^{-4}	0.9983
60°	3.21×10^{-6}	1.79×10^{-2}	1.33×10^{-4}	0.9978

7.4 Numerical simulation of the mixed mode (I/II) FCG

In this section, finite element simulation of the mixed mode (I/II) FCG using the selected three CTS experimental specimens has been carried out. As the main thrust of the present work is to study the nature of predictability of various ΔK_{eq} models , therefore seven such models are selected and presented in Table 7.5. More details of these models can be found in section 3.4. Using Eq. (3.40), and the procedure explained in section 3.3, the fatigue life is computed corresponding to each of the selected ΔK_{eq} models. Simulations of all three specimens have been carried out in ANSYS®. Eight noded quadratic quadrilateral elements are used, and plane stress conditions are assumed in all the simulations. Quarter point elements (QPEs) have been deployed at the tip of a growing crack for modeling the inverse square root singularly. Sixteen number of QPEs elements are employed around the crack tip, and the length of these elements is set at 0.08 mm throughout the crack growth in simulations. Figure 7.6 shows geometry, boundary conditions, and loads applied for finite element analysis of a typical CTS specimen. The pin loads P_1 to P_3 developed by the loading device at the top holes are also shown in Fig. 7.6. Half of the bottom holes of the CTS specimen are constrained in the direction of pin forces. The magnitude of these forces in terms of the applied load P from the testing machine is given as (Borrego et al., 2006; Sander and Richard, 2006)

$$\begin{aligned} P_1 &= P\left(0.5\cos\alpha + (c/b)\sin\alpha\right) \\ P_2 &= P\sin\alpha \\ P_3 &= P\left(0.5\cos\alpha - (c/b)\sin\alpha\right) \end{aligned} \tag{7.1}$$

where α is the loading angle (Fig. 7.6), c and b are as defined in Fig. 7.6. The loads P_1 to P_3 are calculated for different loading angles (30°, 45°, and 60°), and the two-dimensional finite element analysis is carried out for each loading angle. Here the applied loads employed in the experiments (Table 7.3) are applied to the finite element model to mimic the experiments. Figure 7.7 shows meshing features for the loading angle 30° to represent typical features of all the three specimens. Figure 7.7 (a) shows the initial finite element mesh employed for the mixed mode FCG simulation of the CTS specimen loaded at 30°. Figure 7.7 (b) shows mesh near the crack tip in the initial mesh. Figures 7.7 (c) and (d) show mesh near the crack tip at the 10th and 20th simulation step of the crack growth.

Table 7.5 List of the ΔK_{eq} models used in the present study

Model name	Equation	Eq. No.
Tanaka 1 (Tanaka, 1974)	$\Delta K_{eq} = \left(\Delta K_I^2 + 2\Delta K_{II}^2\right)^{1/2}$	Eq. (3.48)
Tanaka 2 (Tanaka, 1974)	$\Delta K_{eq} = \left(\Delta K_I^4 + 8\Delta K_{II}^4\right)^{1/4}$	Eq. (3.47)
Irwin (Irwin GR, 1957)	$\Delta K_{eq} = \sqrt{\Delta K_I^2 + \Delta K_{II}^2}$	Eq. (3.55)
Yan (Yan et al., 1992)	$\Delta K_{eq} = \frac{1}{2}\cos\frac{\theta}{2}\left[\Delta K_I\left(1+\cos\theta\right) - 3\Delta K_{II}\sin\theta\right]$	Eq. (3.58)
Hussain (Hussain et al., 1974)	$\Delta K_{eq} = \sqrt{\frac{4}{\left(3+\cos^2\theta\right)^2}\left(\frac{1-\theta/\pi}{1+\theta/\pi}\right)^{\theta/\pi}\begin{bmatrix}\left(1+3\cos^2\theta\right)\Delta K_I^2 + \\ 4\sin 2\theta\,\Delta K_I\Delta K_{II} \\ +\left(9-5\cos^2\theta\right)\Delta K_{II}^2\end{bmatrix}}$	Eq. (3.59)
Richard (Richard et al., 2003)	$\Delta K_{eq} = \frac{\Delta K_I}{2} + \frac{1}{2}\sqrt{\Delta K_I^2 + 4\left(1.155\Delta K_{II}\right)^2}$	Eq. (3.56)
Demir (Demir et al., 2018)	$\Delta K_{eq} = \left(1.0519\Delta K_I^4 - 0.035\Delta K_{II}^4 + 2.3056\Delta K_I^2\Delta K_{II}^2\right)^{1/4}$	Eq. (3.64)

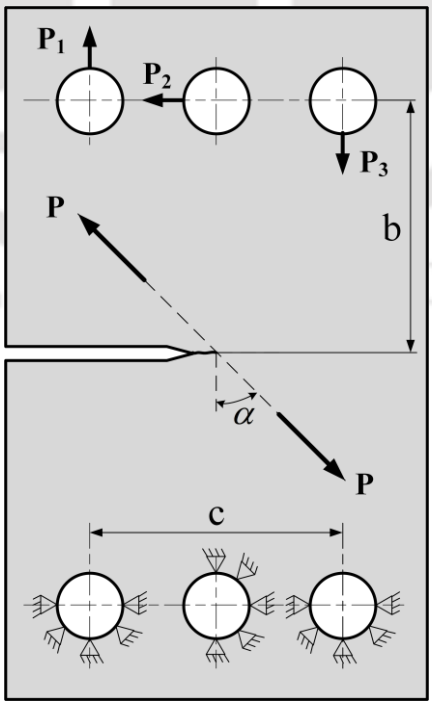

Figure 7.6 Loading and boundary conditions used for the numerical simulation of the CTS specimens. α is the angle between the applied tensile load P and crack axis (loading angle)

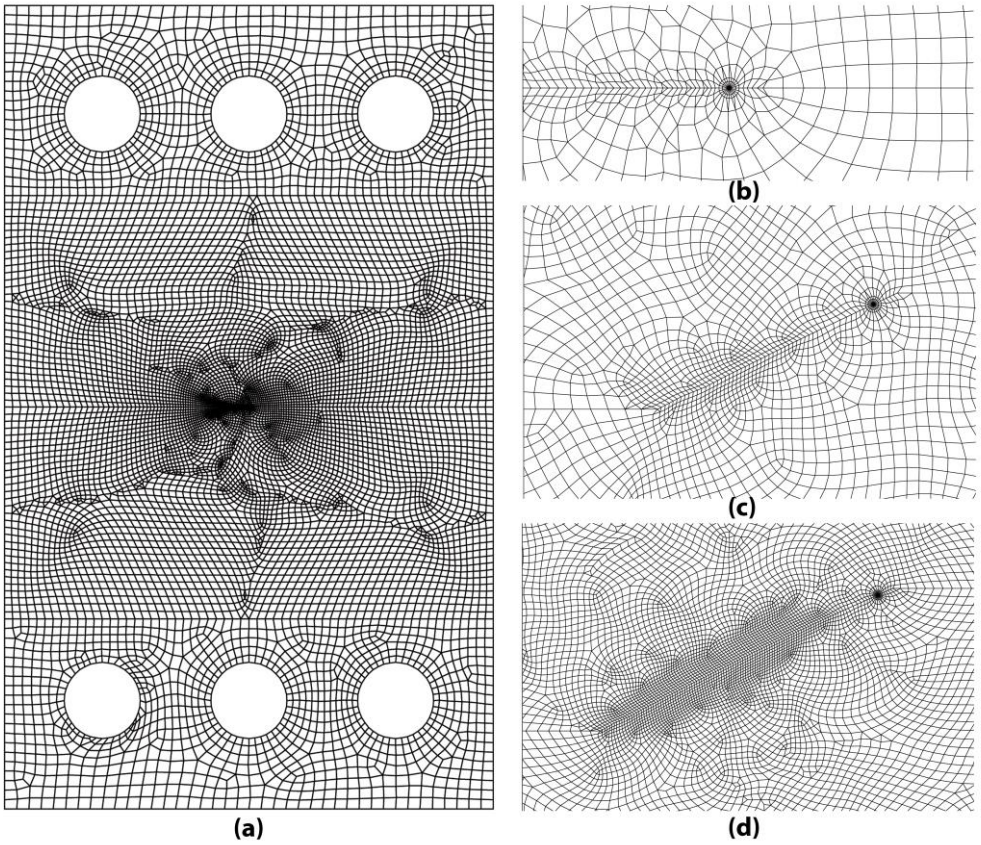

Figure 7.7 Finite element meshes used for the numerical simulation of CTS specimen loaded at 30° (a) initial mesh (b) view near the crack tip in initial mesh (c) crack tip mesh at 10th step and (d) crack tip mesh at 20th step

7.4.1 The convergence of computed mixed mode SIFs

In order to demonstrate the convergence of the mixed mode SIFs, K_I and K_{II} calculated using the proposed finite element based displacement technique, the CTS specimen as shown in Fig. 7.6, and $\alpha = 45^{o}$ is considered here. A solution to the mixed mode SIFs of this configuration are given by Richard (1981).

$$K_I = \frac{P}{Wt}\sqrt{\pi a}\,\frac{\cos\alpha}{(1-a/W)}\sqrt{\frac{0.26+2.65a/(W-a)}{1+0.55a/(W-a)-0.08\left(a/(W-a)\right)^2}}$$
$$K_{II} = \frac{P}{Wt}\sqrt{\pi a}\,\frac{\sin\alpha}{(1-a/W)}\sqrt{\frac{-0.23+1.40a/(W-a)}{1-0.67a/(W-a)+2.08\left(a/(W-a)\right)^2}} \qquad (7.2)$$

where P is the uniaxial force (Eq. (7.1)) applied to Richard's loading device (Fig. 6.12) a is the crack length, W is the specimen width and t is the specimen thickness. A value of $P = 16\,\text{kN}$, $a = 45\,\text{mm}$, $W = 90\,\text{mm}$ and $t = 15\,\text{mm}$ are considered for finite element analysis.

Eight finite element meshes (similar to Fig. 7.7) with increasing mesh density of the selected specimen have been employed to compute the mixed mode SIFs using the displacement technique. Figure 7.8 shows the plot of the variation of present computed mixed mode SIFs and the reference values obtained from Eq. (7.2) as a function of the length of the QPEs at the crack tip. It can be noticed from Fig. 7.8 that as the meshes are refined, the computed SIFs K_I and K_{II} are converging to the reference solutions. It can also be observed from the results in Fig. 7.8 that the QPE's length of 0.08 mm is adequate for the accurate estimation of mixed mode SIFs. Therefore, QPE length is set at 0.08 mm in all the simulations of the present investigation.

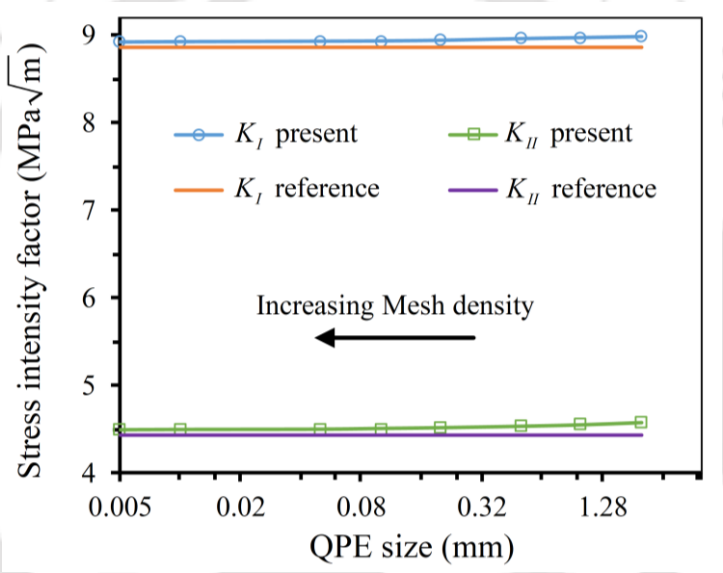

Figure 7.8 Results of the mesh convergence study

The crack growth direction (θ_c) at all stages of the crack growth is calculated using the MTS criteria (Erdogan and Sih, 1963), as given in Eq. 3.70. Figure 7.9 (a) shows the comparison of the experimental crack kinking angles (the first step of the crack growth) (Fig. 7.4) with both the MTS and SED criterion for all three loading angles. Figure 7.9 (b) shows the prediction of crack paths for all the loading angles. It can be noticed from Fig. 7.9 that the MTS criterion accurately predicts the measured angles and the crack path for all the loading angles. Using this simulated path, the mixed mode fatigue life is estimated for each increment. In all the simulations of the present study, a crack increment of $\Delta a = 0.5$ mm is set in all the crack growth increments of the simulations. After $i-1^{th}$ step of the crack growth, the crack tip is advanced to the next position (x_i, y_i) such that

$$x_i = x_{i-1} + \Delta a \cos(\theta_{r-i})$$
$$y_i = y_{i-1} + \Delta a \sin(\theta_{r-i}) \tag{7.3}$$

where θ_{r-i} is the angle between the crack growth direction and the x-axis for the i^{th} step determined using Eq. (3.70). This procedure is continued until the predefined crack length is reached. Then the fatigue lives are calculated using Eq. (3.46), and Paris' material constants obtained in section 7.2, and the selected ΔK_{eq} models given in Table 7.5 at each step of the crack growth. All necessary codes for computation of the fatigue life are developed in MATLAB®. The following sections describe the assessment of the nature of the predictability of all the seven ΔK_{eq} models by comparing the numerically estimated fatigue life with the above experimental results.

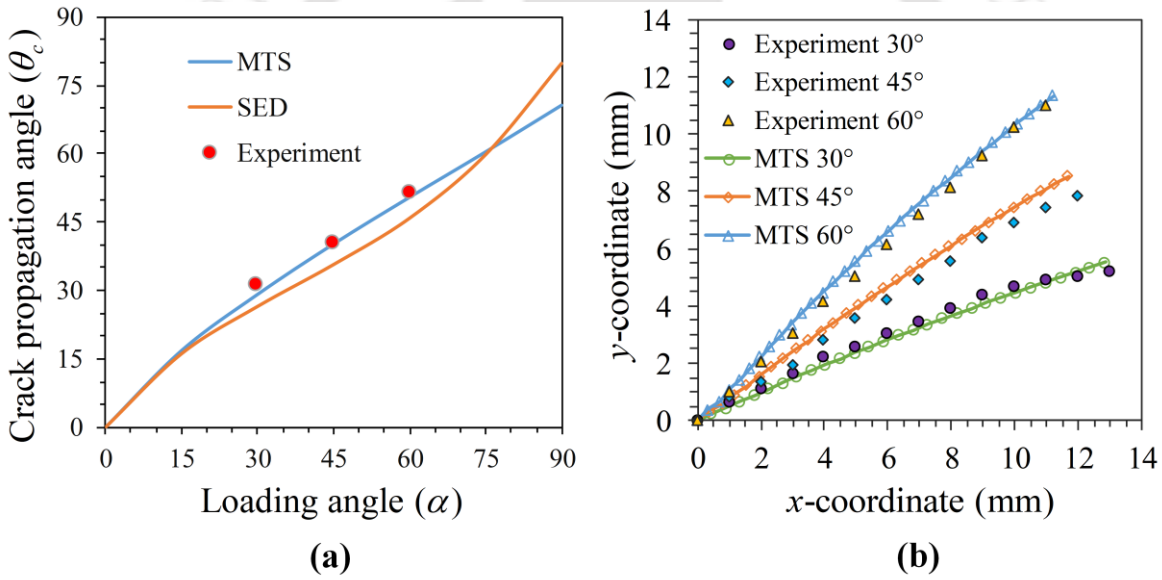

Figure 7.9 (a) comparison of crack initiation angle with the MTS and SED (b) experimental and predicted crack paths using the MTS of all the three specimens

7.4.2 Comparison of the fatigue lives: Loading angle 30°

Following the finite element simulation procedure described in the previous section, the predicted mixed mode fatigue life using various ΔK_{eq} models (Table 7.5) for the CTS specimen loaded at an angle of 30° is shown in Fig. 7.10. A total of 30 numerical simulations are performed from an initial crack length a_i = 45 mm to a_f = 60 mm with a crack increment of Δa = 0.5mm. The actual crack path and predicted crack path using the MTS criterion are shown in Fig. 7.9 (b). It can be seen from Fig. 7.9 (b) that the estimation of the fatigue crack

path by the MTS criterion is accurate. In order to assess the capability of ΔK_{eq} models considered, predicted fatigue lives are compared with the experimental fatigue life for the loading angle 30°, as shown in Fig. 7.10. Recall that two repeated experiments have been conducted for this loading angle. It can be noticed from Fig. 7.10 that nearly the same fatigue lives are obtained from both the experiments.

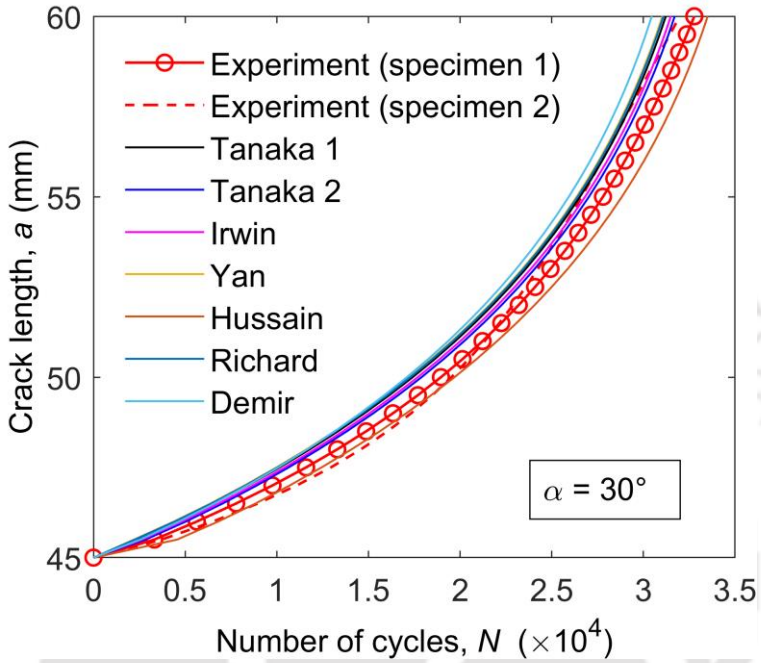

Figure 7.10 Comparison of the experimental and simulated fatigue life using various ΔK_{eq} models for the loading angle of 30°

Figure 7.11 shows the plots of percentage relative error in predicted life (with respect to the experimental life) by each of the seven models. Table 7.6 presents errors computed in terms of RMS and L_2 norm (in percentage) values with the best-fitted experimental values as the reference values. It should be noted that the percentage relative error represents the error in fatigue life prediction at each step of the crack growth. On the other hand, the RMS and the L_2 norm errors are global error estimators and provide an overall error (of the given range) in the life prediction. Results in Fig. 7.11 also shows that some models have small errors during the initial stages and acquired large errors at later stages of crack propagation and vice-versa. Considering the overall performance of the models during the entire range of crack propagation, it is evident from Figs. 7.10 and 7.11 that, predictions using Irwin's and Tanaka 2 ΔK_{eq} models are close to the experimental data as compared to the other models. Results presented in Table 7.6 also shows that Irwin's and Tanaka 2 models have made more accurate

predictions as compared with the other models as both the RMS and L_2 norm error values are minimum for these models. Again considering the overall performance during the entire crack growth range, Figs. 7.10 and 7.11 and Table 7.6 also show that Richard's, Yan's, and Demir's models provide conservative estimates of the mixed mode fatigue life.

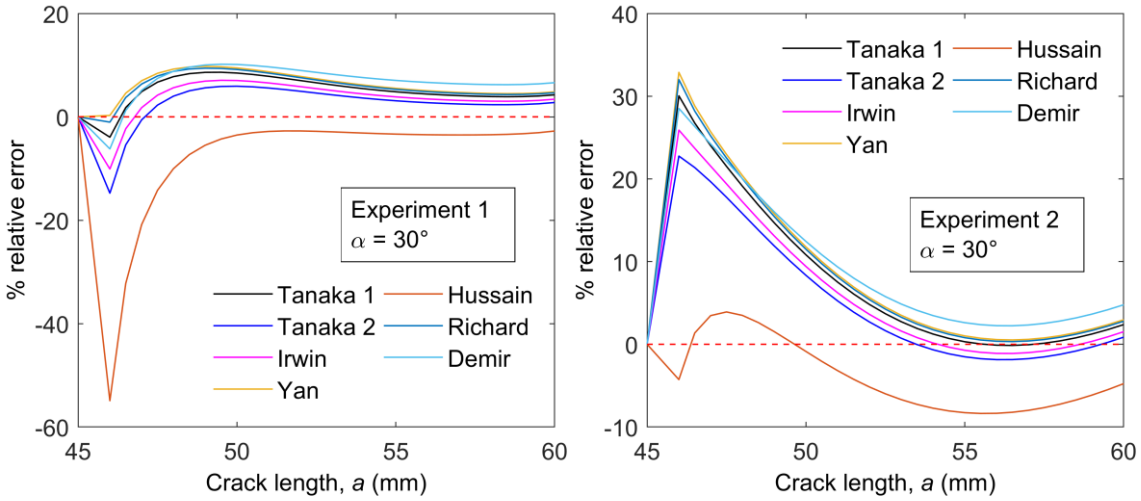

Figure 7.11 Percentage relative error in estimated fatigue life using various ΔK_{eq} models for the loading angle of 30°

Table 7.6. The RMS error and error in the L_2 norm in estimated fatigue life using the various ΔK_{eq} models for the loading angle of 30°

Specimen	Error	Tanaka 1	Tanaka 2	Irwin	Yan	Hussain	Richard	Demir
30° Specimen 1	RMS	1318	876	1063	1496	1125	1442	1807
	L_2 (%)	5.44	3.67	4.41	6.17	5.04	5.95	7.46
30° Specimen 2	RMS	1528	1214	1337	1671	1543	1627	1777
	L_2 (%)	6.51	5.15	5.69	7.13	6.52	6.94	7.53

7.4.3 Comparison of the fatigue lives: Loading angles 45° and 60°

A similar analysis was carried out for the CTS specimens with the loading angles of 45° and 60°. A total of 20 numerical simulations are performed from an initial crack length a_i = 45 mm to a_f = 55 mm with a crack increment of Δa = 0.5 mm for 45° loading angle. 30 numerical simulations are performed from an initial crack length a_i = 45 mm to a_f = 60 mm with a crack increment of Δa = 0.5 mm for 60° loading angle. Following the simulation

procedure as is carried out in the previous section, the predicted fatigue life using all the seven ΔK_{eq} models for the loading angles 45° and 60° are shown in Fig. 7.12 and Fig. 7.13, respectively. Experimental fatigue life data is also presented in Figs. 7.12 and 7.13 for the comparison purpose. Figures 7.14 and 7.15 show the plot of percentage relative error in predicted life by each model for the loading angles 45° and 60°, respectively. Similarly, Tables 7.7 and 7.8 present error in terms of RMS and L_2 norm values corresponding to 45° and 60°, respectively. The actual crack paths and predicted crack paths using the MTS criterion for the loading angles 45° and 60° are shown in Fig. 7.9 (b). It can be seen from Fig. 7.9 (b) that the estimation of the fatigue crack paths by the MTS criterion is accurate in all the loading angles.

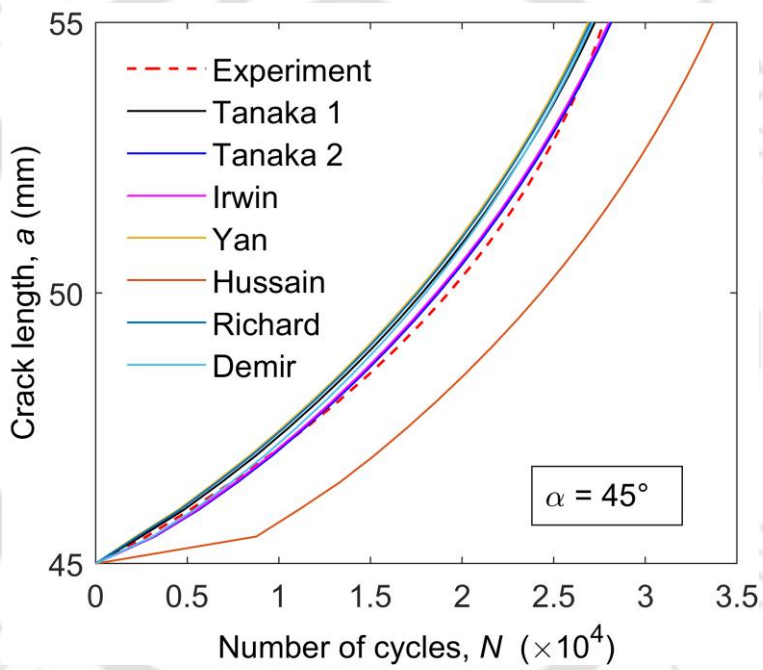

Figure 7.12 Comparison of the experimental and simulated fatigue life using various ΔK_{eq} models for the loading angle of 45°

Referring to Figs. 7.12-7.15, as in the case of 30°, some models exhibited relatively small errors during the initial stages of the crack propagation and acquired large errors at later stages. Nonetheless, considering the overall performance of the models during the entire range of crack propagation, an interesting observation can be noticed from the results presented in Figs. 7.12-7.15 that for the loading angles 45° and 60°, again the Irwin's and Tanaka 2 models consistently predicted the mixed mode fatigue life more closely to the experimental data. Furthermore, similar to the case of the loading angle 30°, Yan's and Richard's models provided a conservative life estimate as compared to the other models.

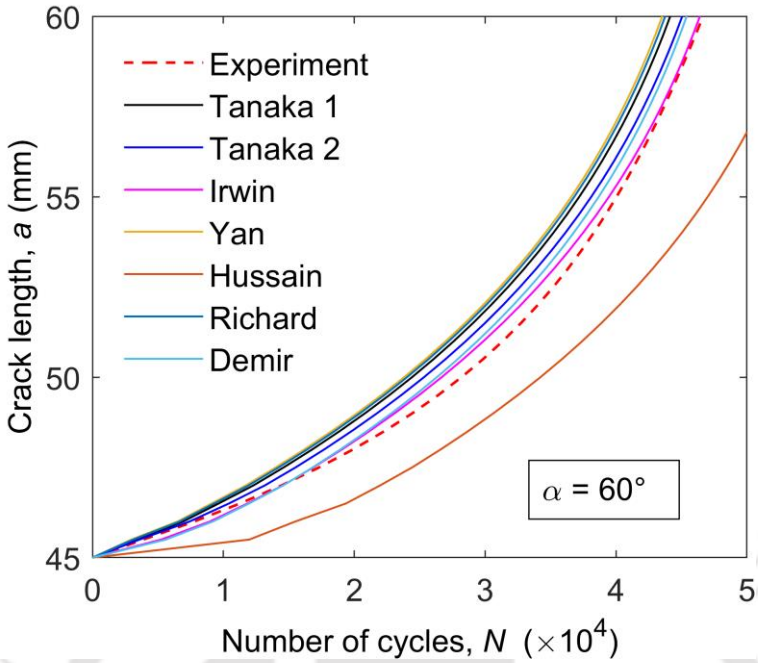

Figure 7.13 Comparison of the experimental and simulated fatigue life using various ΔK_{eq} models for the loading angle of 60°

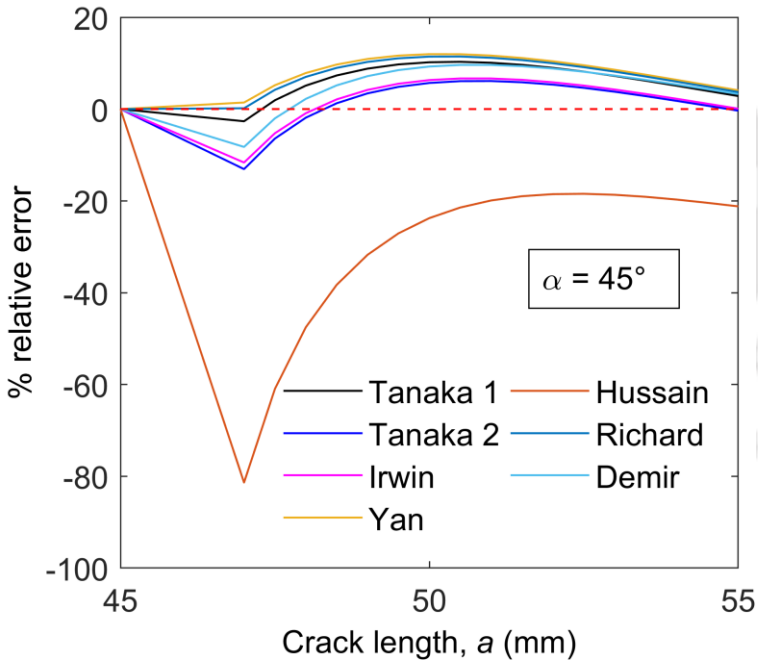

Figure 7.14 Percentage relative error in estimated fatigue life using various ΔK_{eq} models for the loading angle of 45°

Results in Tables 7.7 and 7.8 also clearly indicate that on overall, the Irwin's and Tanaka 2 model predictions are close to the experimental data while the Yan's and Richard's predictions are conservative as compared to other loads. However, for the 60° loading angle,

Demir's model (Demir et al., 2018) also provided very accurate predictions as compared to other loading angles. As claimed by Demir et al. (2018), this model is devised to provide accurate predictions at higher mode mixities.

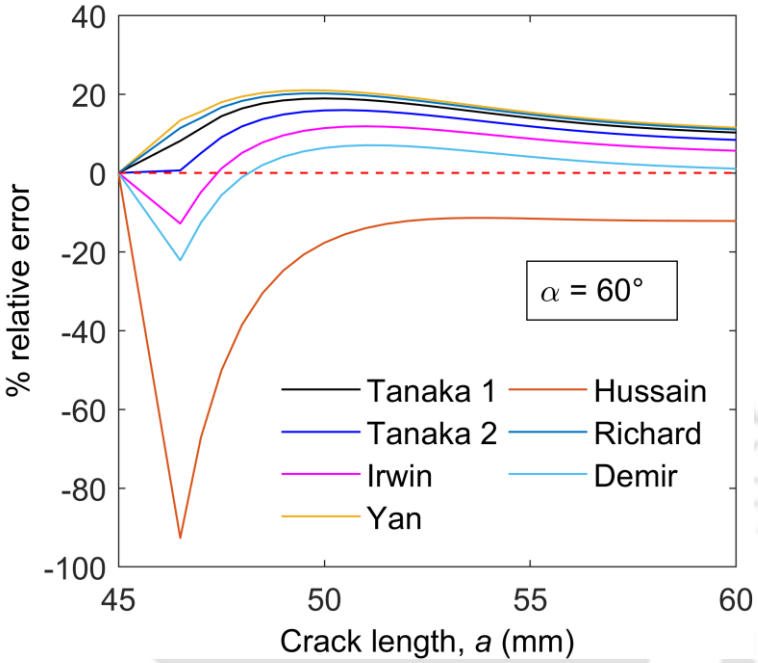

Figure 7.15 Percentage relative error in estimated fatigue life using various ΔK_{eq} models for the loading angle of 60°

Table 7.7 The RMS error and error in the L_2 norm in estimated fatigue life using the various ΔK_{eq} models for the loading angle of 45°

Error type	Tanaka 1	Tanaka 2	Irwin	Yan	Hussain	Richard	Demir
RMS	1633	925	1006	1953	5332	1854	1571
L_2 (%)	7.58	5.03	5.27	8.98	28.02	8.54	7.55

Table 7.8 RMS error and error in the L_2 norm in estimated fatigue life using the various ΔK_{eq} models for the loading angle of 60°

.Error type	Tanaka 1	Tanaka 2	Irwin	Yan	Hussain	Richard	Demir
MS	5012	4180	2975	5570	5481	5363	1401
L_2 (%)	13.04	10.87	7.84	14.50	15.77	13.96	4.11

7.5 Fractographic studies of the Al 6061-T6 fractured samples

Fractographic studies of both the mode I and mixed mode specimens are carried out, and results are presented in Fig. 7.16 for the mode I loading, and Figs. 7.17-7.19 for the mixed mode loading angles of 30°, 45°, and 60° respectively. These images have been obtained using the Zeiss Sigma field emission scanning electron microscope (FESEM).

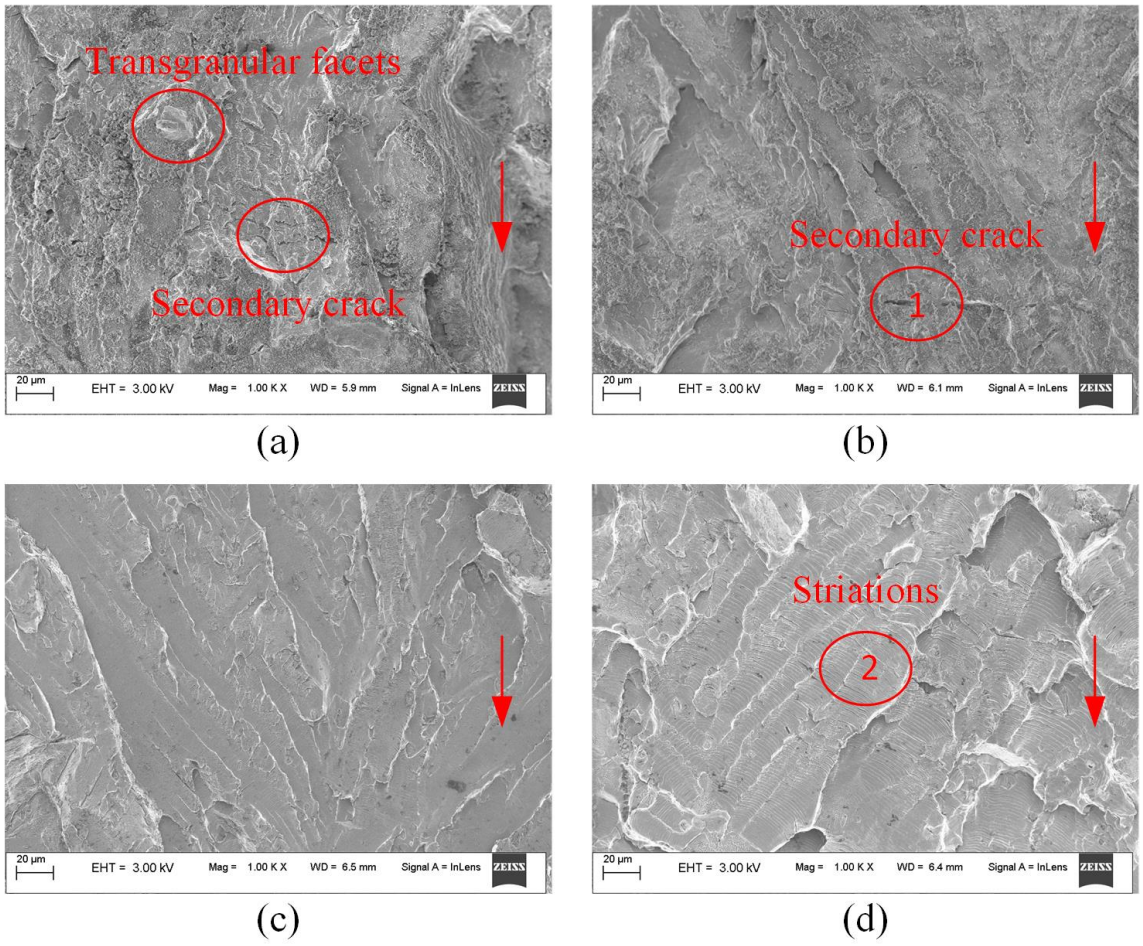

Figure 7.16 Fractographs of the mode I CT specimen showing the fractured surfaces at different crack lengths (a) 12.6 mm (b) 15.8 mm (c) 24.5 mm (d) 34.8 mm [arrows indicate the direction of crack growth]

Fatigue crack propagates by the formation of the ductile striations owing to the ductility of the material (Jogi et al., 2008). The presence of ductile striations can be observed in fractographs of both the mode I (Fig. 7.16 (c) and (d)) and mixed mode loading. The spacing between the striations can be attributed to the FCG rate at that instant. It can be observed from fractographs of both the mode I and mixed mode lading that the width of the striations is increasing as the crack grows further, indicating acceleration of the crack growth. In general, striations align perpendicular to the macroscopic crack growth direction (Fig. 7.16 (c), 7.17

(c), 7.18 (d), 7.19 (d)). However, due to the variations in local stresses and microstructure, a change in crack growth plane and striation alignment direction can also be observed (Fig. 7.16 (d)) (Mills et al., 1987). The present fractographs also displays the above observation.

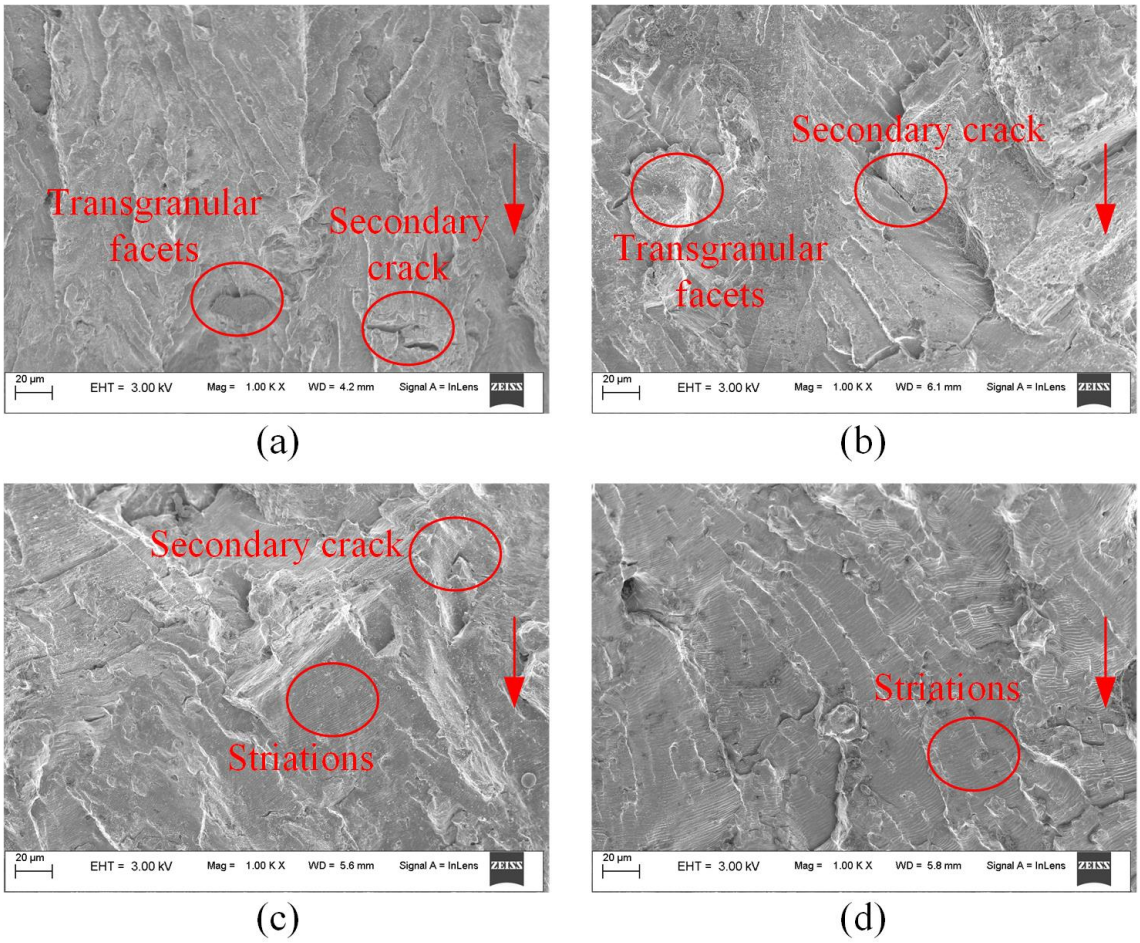

Figure 7.17 Fractographs of the mixed mode 30° CTS specimen showing the fractured surfaces at different crack lengths (a) 45.5 mm (b) 52.8 mm (c) 56.2 mm (d) 60.6 mm [arrows indicate the direction of crack growth]

The fractured surface of the mode I specimen (Fig. 7.16) shows the presence of both intergranular and transgranular crack growth (Rozumek et al., 2018). The presence of secondary cracks is also evident from the fractography of both the modes I and mixed mode (I/II) samples (Fig. 7.16-7.19). At the initial stages of the mixed mode fatigue crack growth, the fractured surfaces of all the specimens (Fig. 7.17 (a), 7.18 (a), 7.19 (a)) have higher roughness due to the presence of mode II component (which causes severe rubbing of the crack surfaces). Subsequently, the surfaces are relatively smooth at the later stages of the crack growth (Fig. 7.17 (c-d), 7.18 (c-d), 7.19 (c-d)) (Kim and Kim, 2013) indicating domination of

the mode I. In the mixed mode loading, as mode II SIF diminishes and mode I SIF increases continuously, the crack surfaces open up more, reduces the interference between surfaces and thereby produces relatively smooth surfaces. A notable distinction between the mode I (Fig. 7.16) and mixed mode (Fig. 7.17-7.19) loading lies in the roughness of the fracture surface. Due to the continuous decrease of ΔK_{II}, the fracture morphology changes from dominantly fatigue fracture to a mixture of fatigue fracture and transgranular quasi-cleavage failure (Kim and Kim, 2013; Wang et al., 2017).

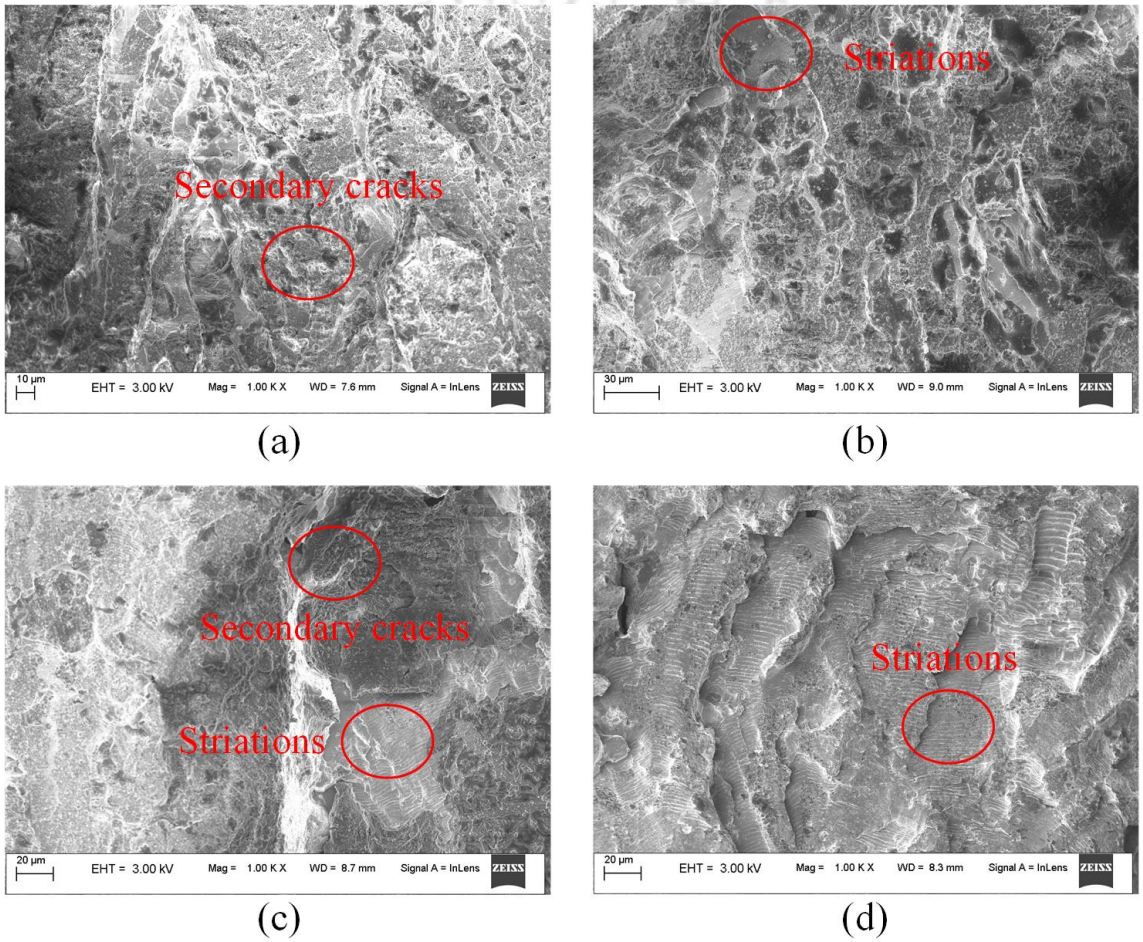

Figure 7.18 Fractographs of the mixed mode 45° CTS specimen showing the fractured surfaces at different crack lengths (a) 45.4 mm (b) 51.6 mm (c) 55.2 mm (d) 57.7 mm

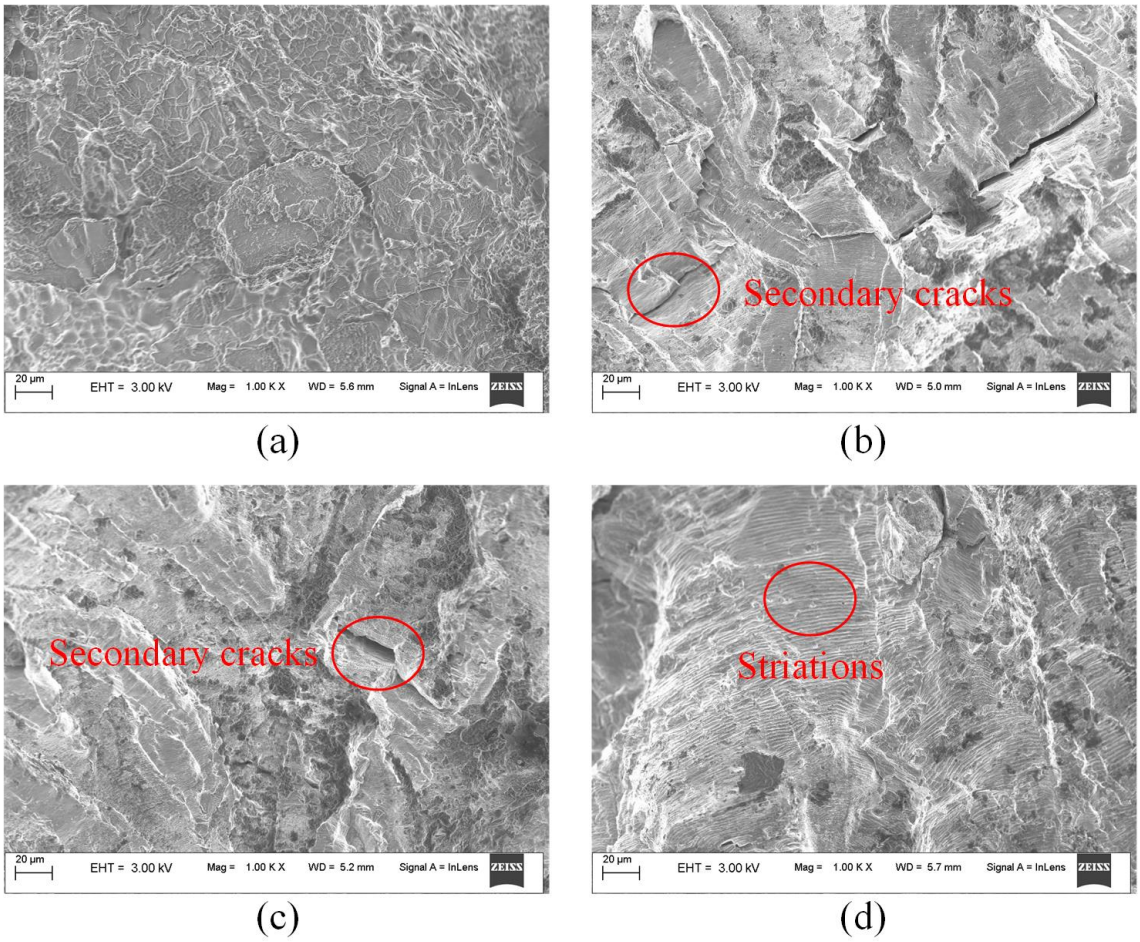

Figure 7.19 Fractographs of the mixed mode 60° CTS specimen showing the fractured surfaces at different crack lengths (a) 45.5 mm (b) 49.2 mm (c) 53.5 mm (d) 57.8 mm

7.6 Summary

In this chapter, the mixed mode (I/II) fatigue crack growth studies in the CTS specimens made of Al 6061-T6 alloy are carried out experimentally and numerically for various mode mixities. Using experimental and numerical results, an attempt has been made here to study the nature of the capability of various ΔK_{eq} models available for use in the mixed mode Paris' law for the numerical prediction of the mixed mode (I/II) fatigue life. Results of the present investigation show that very satisfactory best-fits can be obtained for the mixed mode (I/II) experimental data with the help of the proposed best-fit model. Based on the overall performance during the entire range of the fatigue crack propagation, the results of the present study clearly demonstrate that Irwin's ΔK_{eq} model is consistently predicting the mixed mode fatigue life closer to the experimental data. Moreover, one of the two Tanaka's models (Tanaka 2) is also consistently found to be a promising model for the prediction of the fatigue life close

to the experimental data. Again based on the overall performance, Richard's and Yan's models are found to be conservative as compared to the other models. Interestingly, the ΔK_{eq} model proposed by Demir et al. (2018) is found highly accurate in prediction of the life for 60° as claimed by Demir et al. (2018) and is conservative for other loading angles.

Chapter 8

Predictability assessment: Using SS 316 steel

This chapter presents the results of the assessment of the nature of predictability of the mixed mode (I/II) fatigue life using the modified Paris law with the selected ΔK_{eq} models and experimental results of SS 316 steel. Apart from the mixed mode experiments, numerical simulations of the mixed mode (I/II) FCG are also performed, and fatigue life is predicted using the previously selected seven ΔK_{eq} models. The error in predicted life is assessed using various global as well as pointwise error estimates. Finally, fractographic studies of the growing crack at various crack lengths are performed for both the mode I and mixed mode specimens and discussed here.

8.1 Results of the tensile tests

Tensile tests on two specimens are preformed following ASTM E8 standards, and the averaged results are presented in Table 8.1. The other details of the tensile test specimens are discussed in section 6.1.4. These material properties are needed in the numerical simulation of the mixed mode FCG.

Table 8.1 Tensile test results of SS 316

Yield strength (MPa)	Ultimate tensile strength (MPa)	% Elongation	Young's modulus (GPa)	Poisson's ratio
295	582	47	192	0.27

8.2 Results of the mode I FCG experiments

As a prerequisite for the mixed mode FCG numerical studies, the mode I FCG experiments are performed on the two CT specimens to obtain the Paris' material constant C

and the Paris' exponent m. The compact tension (CT) specimens of width 60 mm and thickness 22 mm are used for performing the test, all other specimen dimensions are as per ASTM E399-17 and ASTM E647-15e1 standards. In these tests, a maximum load $P_{max} = 28$ kN, load ratio $R(= P_{min}/P_{max}) = 0.1$, and loading frequency 10 Hz are set from pre-cracking to the final rupture. All the tests are carried out under load control mode. The COD gauge is mounted on the front face of the CT sample and is used for measuring the instantaneous crack lengths. The crack growth rates are estimated using the variable amplitude fatigue crack propagation (VAFCP) module of the universal testing machine. The fatigue tests are continued from the initial crack length of 14 mm until the final rupture of the specimen. All details pertaining to the mode I FCG experiments are presented in Table 8.2. The Paris' material constants are obtained from $a = 14\,\text{mm}$ to $32\,\text{mm}$ experimental data are presented in Table 8.3. The $da/dN - dK$ curve and $a - N$ curve obtained from the mode I fatigue tests are shown in Fig. 8.1 (a) and Fig. 8.1 (b), respectively. As nearly similar values of the material constants are obtained using both the CT specimens tested, only the results pertaining to one specimen are presented in this section. Figure 8.2 shows a fractured CT specimen made of SS 316 at the end of the test.

Table 8.2 Mode I FCG test details of SS 316

Specimen	Material	P_{max} (kN)	R	Frequency (Hz)	Cycles to failure
CT	SS 316	28	0.1	10	150784

Table 8.3 Paris constant and exponent of SS 316

Material	$C\ \left((\text{mm/cycle})/\left(\text{MPa}\sqrt{\text{m}}\right)^m\right)$	m
SS 316	$4.051\text{x}10^{-8}$	2.34

The Paris constants evaluated from the mode I fatigue tests are used for the mixed mode (I/II) fatigue crack growth simulations discussed in the succeeding sections.

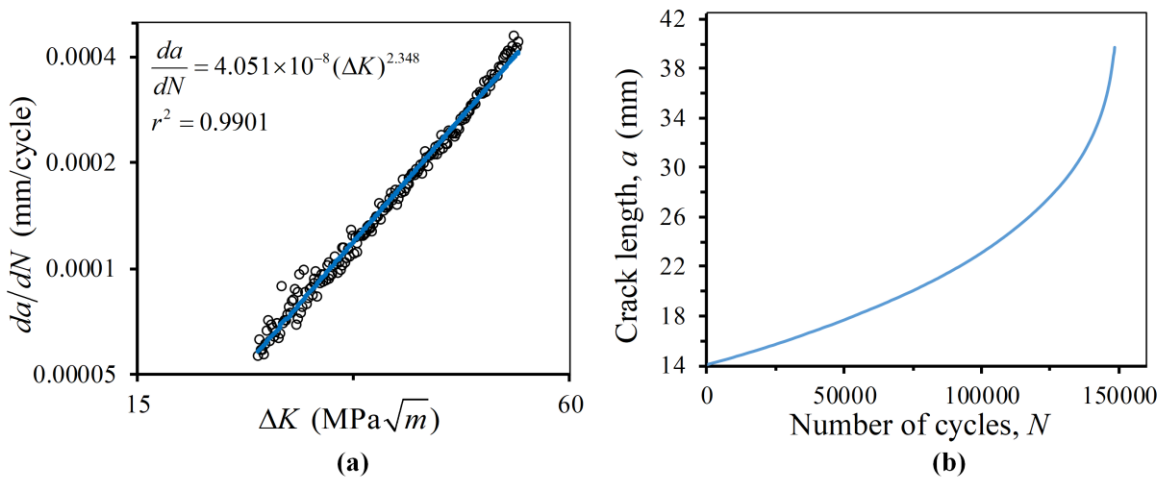

Figure 8.1 Mode I fatigue crack growth data (a) crack growth rate $(da/dN - dK)$ (b) crack length versus the number of cycles (a vs N)

Figure 8.2 Fractured CT specimen made of SS 316

8.3 Results of the mixed mode (I/II) FCG experiments

Mixed mode (I/II) fatigue crack growth experiments are performed using the CTS specimens (Fig. 6.2) made of SS 316 and loaded at angles 30°, 45°, and 60° with the help of Richard's loading device (Fig. 6.3). Since the mixed mode fatigue crack growth tests are not yet standardized, the standard for the mode I fatigue test (ASTM E647-15e1) is followed in this study. Initially, the pre-cracking of all the CTS specimens are carried out at a constant load of $P_{max} = 36$ kN, $R = 0.1$ and frequency of 10 Hz. Following the pre-cracking, the specimen is loaded at desired loading angles, and the fatigue crack growth test is performed. The loads

applied during the mixed fatigue testing are P_{max} = 40 kN, 38 kN, and 47 kN for loading angles 30°, 45°, and 60°, respectively. The load ratio and frequency are maintained the same as that of pre-cracking. The sinusoidal waveform is used for loading. The crack lengths are monitored at an equal time interval using the digital microscope. The fatigue test is continued until the final rupture of the specimen. Table 8.4 presents the details of the mixed mode (I/II) FCG experiments, along with the number of loading cycles took until the final fracture in the present experiments.

Table 8.4 Mixed mode (I/II) FCG test details of SS 316

Sl. No.	Specimen	Loading angle	P_{max} (kN)	R	Frequency (Hz)	Cycles to failure
1	CTS	30°	40	0.1	10	75352
2		45°	38			98522
3		60°	47			82097

The photographs of the fractured mixed mode specimens are shown in Fig. 8.3. Figure 8.4 shows the crack initiation angles measured using the digital microscope.

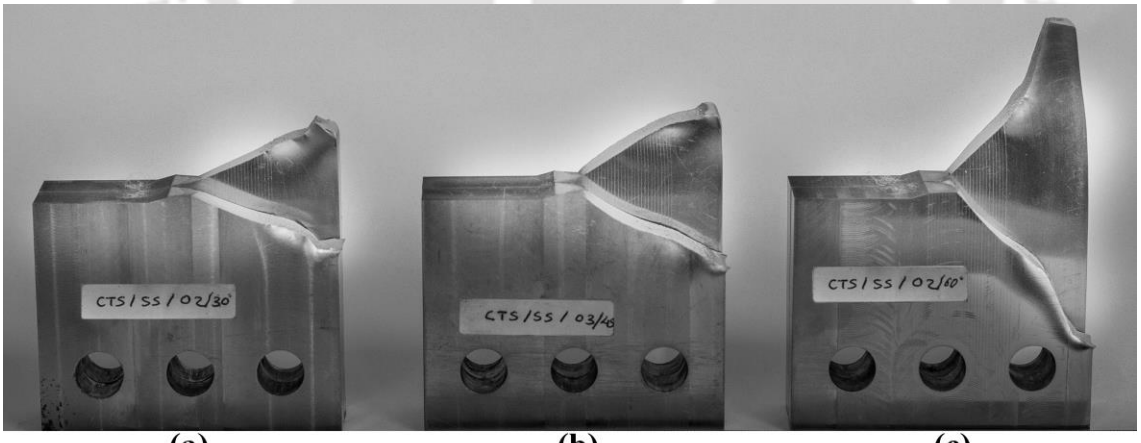

Figure 8.3 Broken mixed mode CTS specimens for the loading angles (a) 30°, (b) 45°, and (c) 60°

The crack length vs. the number of cycles $(a-N)$ curve obtained from experiments for three different loading angles along with the best fit curve using the proposed double exponential approach (Eq. 5.3) is shown in Fig. 8.5. The best-fit parameters (Eq. 5.3) and corresponding goodness of the fit $\left(r^2\right)$ are presented in Table 8.5. Again it can be noticed from

Fig. 8.5 and Table 8.5 that the proposed best-fit model exhibits a highly satisfactory representation of the original raw data of the mixed mode experiments even in case of SS 316 steel.

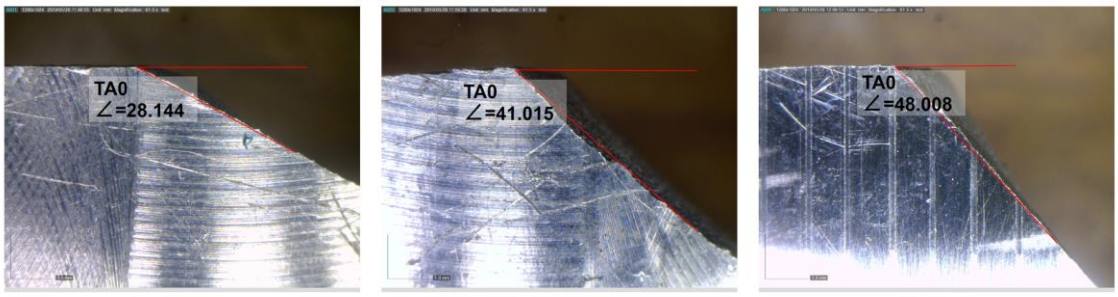

Figure 8.4 Fatigue crack initiation angle measurement for (a) 30° (b) 45° and (c) 60° mixed mode (I/II) CTS specimens

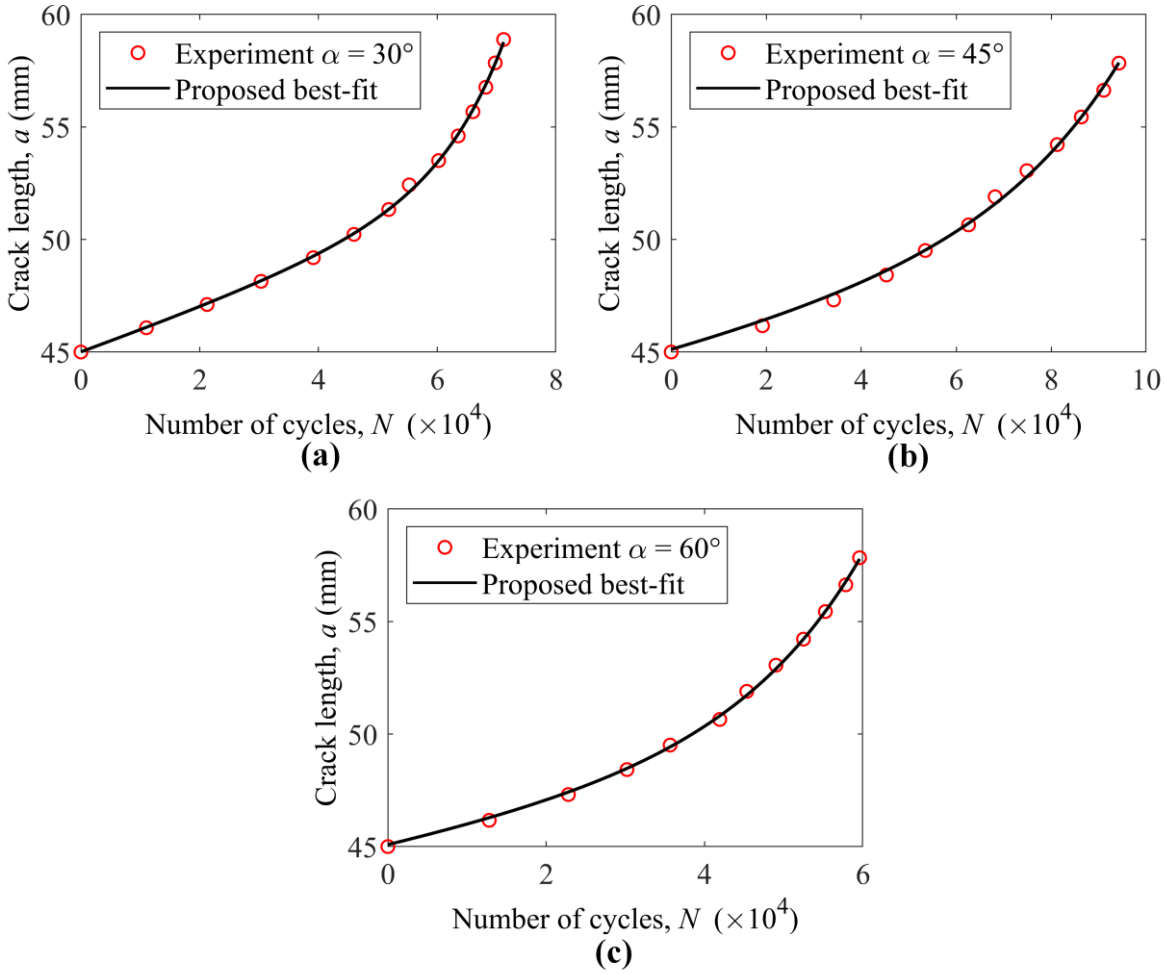

Figure 8.5 Experimental data and the fitted double exponential model for (a) 30° (b) 45° and (c) 60° loading angles

Table 8.5 Best fit parameters of the proposed double exponential model

Loading angle (α)	p	k	q	r^2
30°	1.64×10^{-6}	1.69×10^{-1}	6.51×10^{-5}	0.9987
45°	1.20×10^{-6}	1.95×10^{-1}	3.87×10^{-5}	0.9968
60°	2.15×10^{-6}	8.36×10^{-3}	9.32×10^{-5}	0.9993

8.4 Numerical simulation of the mixed mode (I/II) FCG

Similar to the FCG simulation discussed in section 7.4, finite element modeling and simulations are carried out using the CTS specimen in the ANSYS® APDL environment. Eight noded isoparametric quadrilateral (Q8) elements are used for meshing the geometry, and 24 number of quarter-point elements (QPEs) are used at the crack tip in a spider web pattern to model the inverse square root singularity. The length of crack tip QPE is maintained at 0.08 mm in all numerical simulations. Similar loading and boundary conditions, as discussed in section 7.45, are used for the analysis of SS 316 CTS specimens. Here also, the loads employed in the experiments (Table 8.4) are applied to the finite element model.

Figure 8.6 shows typical finite element meshes used for the loading angle 45°. Similar meshes are used for all loading angles. Figure 8.6 (a) shows the initial finite element mesh employed for the FCG simulation of the CTS specimen. The crack tip meshes in the initial step, 5th step, and 10th step are shown in Fig. 8.6 (b-d), respectively. For all three loading angles, a total of 30 numerical simulations are performed from an initial crack length $a_i = 45$ mm to $a_f = 60$ mm with a crack increment of $\Delta a = 0.5$ mm. The same seven ΔK_{eq} models selected in Chapter 7 (shown in Table 7.5) are selected here for the fatigue life predictability assessment using the SS 316 steel.

In all the simulations of the present study, a crack increment of $\Delta a = 0.5\,\text{mm}$ is maintained, and crack path simulation is performed as per the procedure discussed in section 3.3. At each step of the crack growth, the mixed mode SIFs, K_I and K_{II} are calculated using the proposed crack flank displacement technique discussed in chapter 4. The direction of crack growth (θ_c) is estimated using the MTS criterion (Eq. 3.70). Figure 8.7 (a) shows the initial crack growth direction obtained from the experiment against the crack growth directions predicted by the MTS and SED criteria for all the three loading angles. Figure 8.7 (a) shows a

good agreement between the prediction made by the MTS criterion and the experimental crack initiation direction. Figure 8.7 (b) shows the prediction of crack paths for all the loading angles. This figure shows an excellent agreement between the experimental data and the simulated path using the MTS criterion. Using this simulated path, the mixed mode fatigue life is estimated for each increment. The fatigue lives are calculated using Eq. 3.40 (discussed in section 3.3), Paris' constants in Table 8.3, and the selected ΔK_{eq} models (Table 7.5) at each step of the crack growth. The post-processing tasks for fatigue life estimation is performed using MATLAB®.

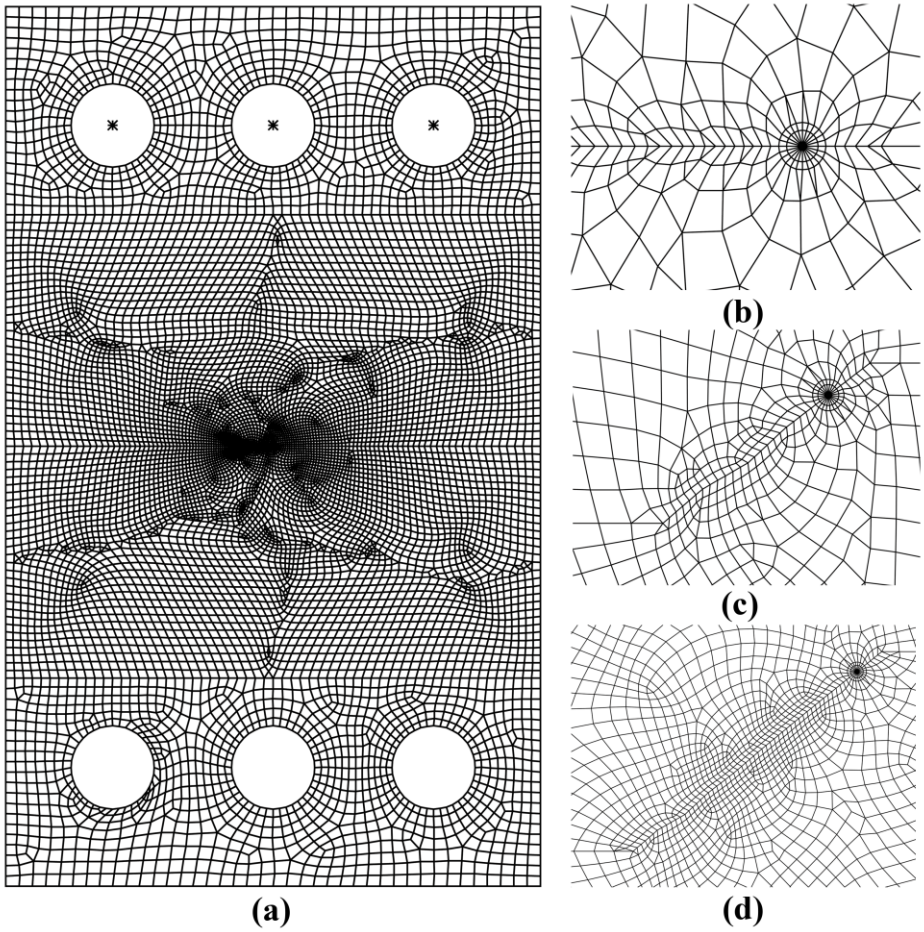

Figure 8.6 The typical finite element meshes used for the fatigue crack growth simulation using CTS specimen for the loading angle 45° (a) initial step mesh, (b) initial step crack tip, (c) 5th step crack tip mesh, and (d) 10th step crack tip mesh

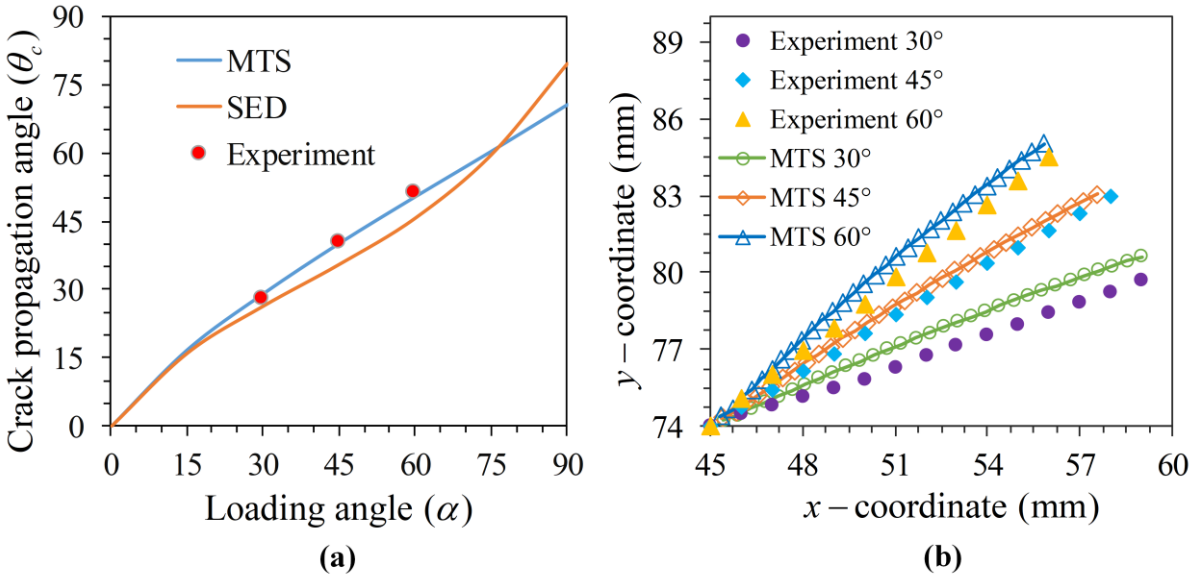

Figure 8.7 (a) FCG crack initiation angle predicted by the MTS and SED criterion against the experimental values (b) experimental and predicted fatigue crack paths using the MTS criterion

8.4.1 Comparison of the fatigue lives: Loading angles 30°, 45° and 60°

This section discusses the predicted fatigue life using the selected ΔK_{eq} models and its comparison with the experimental results of SS 316 steel. Following the procedure discussed in section 8.2, the fatigue life of the CTS specimen for loading angles 30°,45°, and 60° is estimated. Figures 8.8-8.10 shows the estimated fatigue life using seven selected ΔK_{eq} models (Table 7.5) as well as the experimental fatigue life for the loading angles 30°,45°, and 60°, respectively. The predictability of various ΔK_{eq} models (Table 7.5) for different loading angles is assessed by comparing it with the experimental fatigue life as shown in Figs. 8.8-8.10.

Figure 8.11-8.13 shows the plots of the percentage relative error in predicted life (with respect to the experimental life) for each of the seven models for all the three loading angles considered in this study.

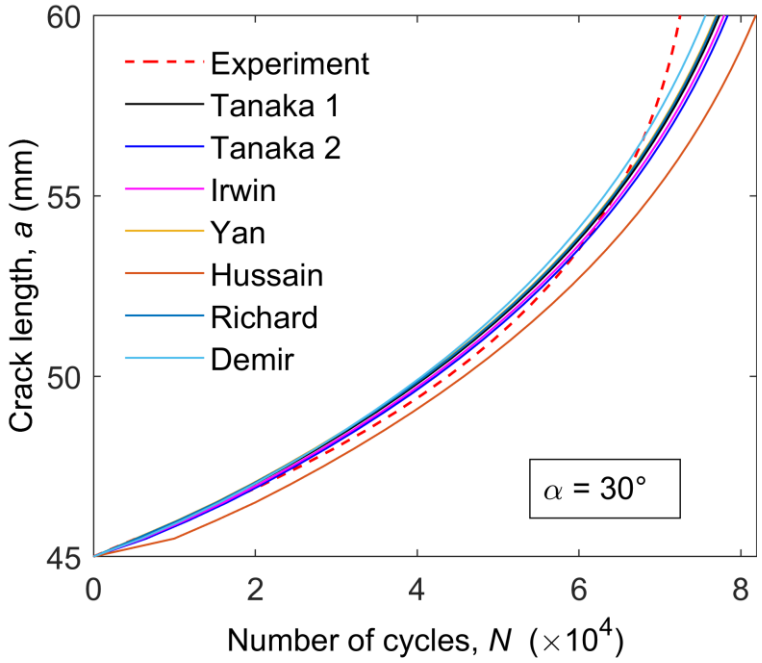

Figure 8.8 Experimental and predicted fatigue life using the CTS specimen of 30° loading angle

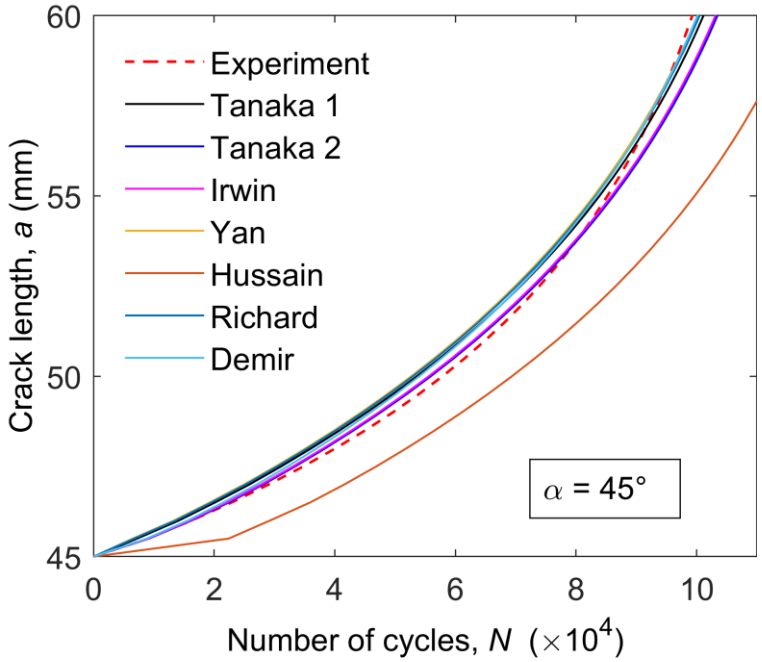

Figure 8.9 Experimental and predicted fatigue life using the CTS specimen of 45° loading angle

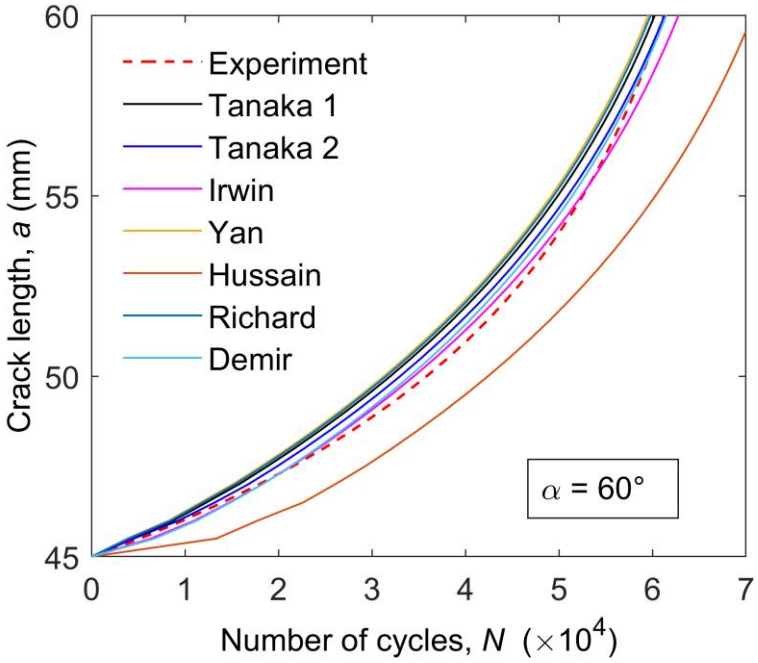

Figure 8.10 Experimental and predicted fatigue life using the CTS specimen of 60° loading angle

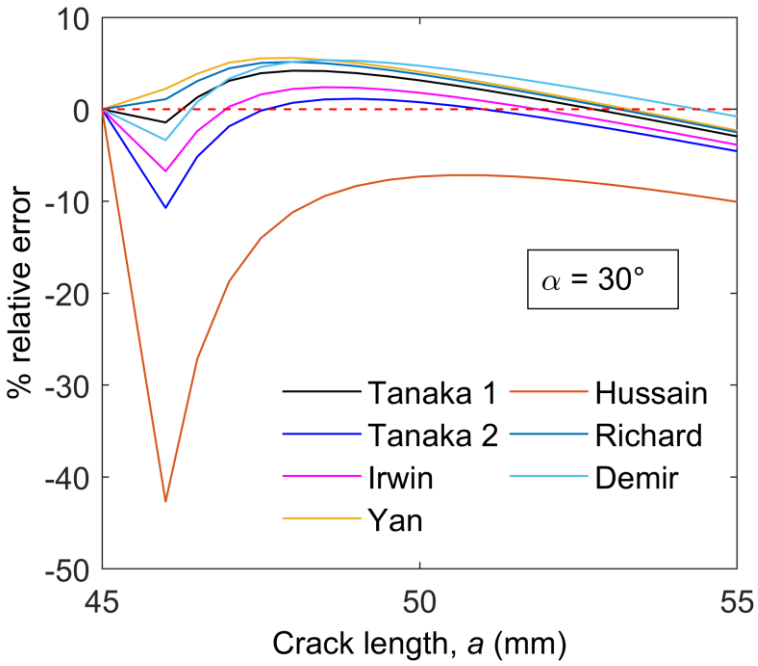

Figure 8.11 Percentage relative error in fatigue life prediction for the CTS specimen of 30° loading angle

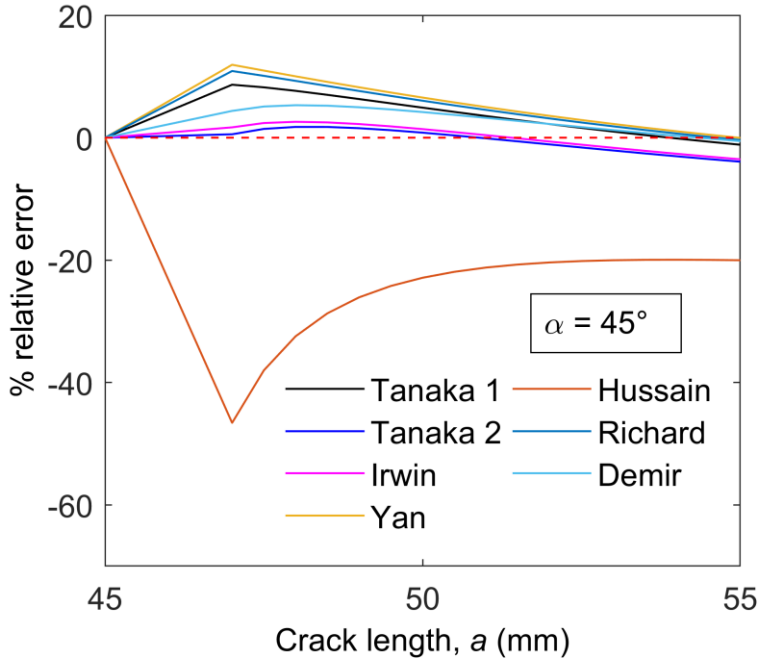

Figure 8.12 Percentage relative error in fatigue life prediction for the CTS specimen of 45° loading angle

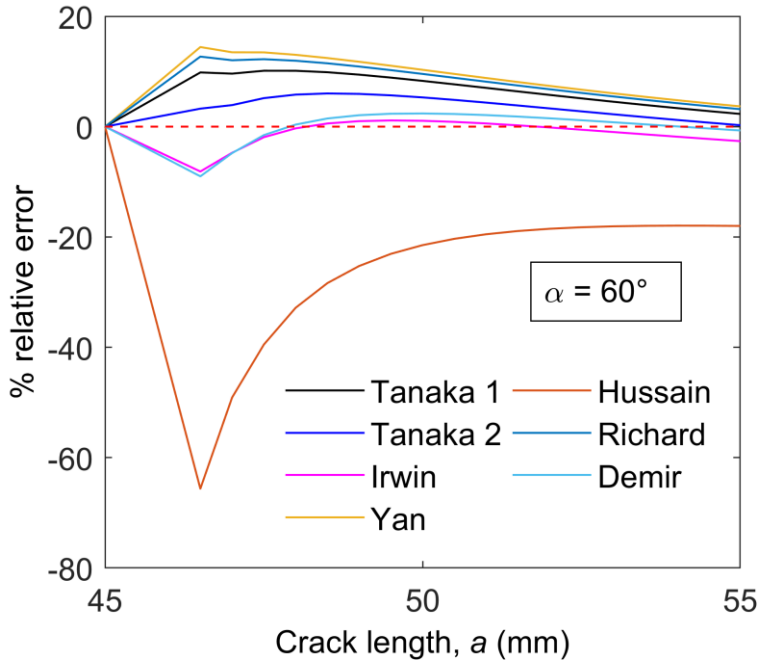

Figure 8.13 Percentage relative error in fatigue life prediction for the CTS specimen of 60° loading angle

In order to have an overall and conclusive view of error in the life prediction, the root mean square (RMS) error and the L_2 norm (in percentage) of error in the predicted fatigue life with respect to the experimental life are calculated and presented in Table 8.6.

Table 8.6 RMS error and the L_2 norm of percentage relative error.

Error	α	ΔK_{eq} model						
		Tanaka 1	Tanaka 2	Irwin	Yan	Hussain	Richard	Demir
RMS	30°	1171	1392	1195	1321	4483	1262	1366
	45°	2153	1373	1271	2968	14319	2704	1622
	60°	2251	1283	765	2926	8400	2673	827
L_2	30°	2.32	2.68	2.26	2.76	9.63	2.60	3.02
	45°	3.60	2.30	2.13	4.97	23.97	4.53	2.72
	60°	6.10	3.48	2.07	7.93	22.76	7.24	2.24

The percentage relative error plots (Figs. 8.11-8.13) indicates that some models exhibit relatively smaller error at the initial stages and however, at the later stages, the error is large and vice versa. It is evident from Figs. 8.11-8.13 that, taking into account the overall performance of models for the entire range of crack propagation, the ΔK_{eq} models viz., Irwin and Tanaka 2 are predicting fatigue life close to the experimental data. On the overall, Irwin model is predicting consistently close to the experimental data compared to other ΔK_{eq} models for all three loading angles examined in this study. This can also be clearly seen in the results of Table 8.6. Although the Demir model is expected to provide higher accuracy for higher mode mixity cases, it can be noticed from Table 8.6 that its prediction is close to the experimental data even for the case of loading angles 30° and 45°. As expected, predictions made by the Demir model are as close as the Irwin model for 60°. Results presented in Table 8.6 also shows that the RMS and L_2 norm values are least for Irwin and Tanaka 2 models, which further substantiate the observations from the error plots (Figs. 8.11-8.13). It is also observed from Figs. 8.11-8.13 and Table 8.6 that the ΔK_{eq} models proposed by Richard and Yan are providing conservative estimates of the fatigue life as compared to the other models

considered. Similar observations are also noticed in studies using Al 6061-T6 experimental data (Chapter 7).

8.5 Fractographic studies

Fatigue fractographic studies of the SS 316 steel for mode I and mixed mode specimens at different crack lengths are carried out using JEOL field emission scanning electron microscope (FESEM) and are presented in Fig. 8.14 for the mode I loading samples and Figs. 8.15-8.17 for the mixed mode loading angles 30°, 45° and 60°, respectively. These images are obtained at different crack lengths at a magnification of 1000x. In general, the fractured surfaces consist of flat facets surrounded by some irregular regions (Fig. 8.14 (a)). The flat facets indicate the failure mechanism, such as intergranular separation and grain boundary cracking (Gao et al., 1992; Gao and Wei, 1992). The presence of secondary cracks are also observed in this study (Figs. 8.14 (a-b), 8.15 (a-b), 8.16 (b)).

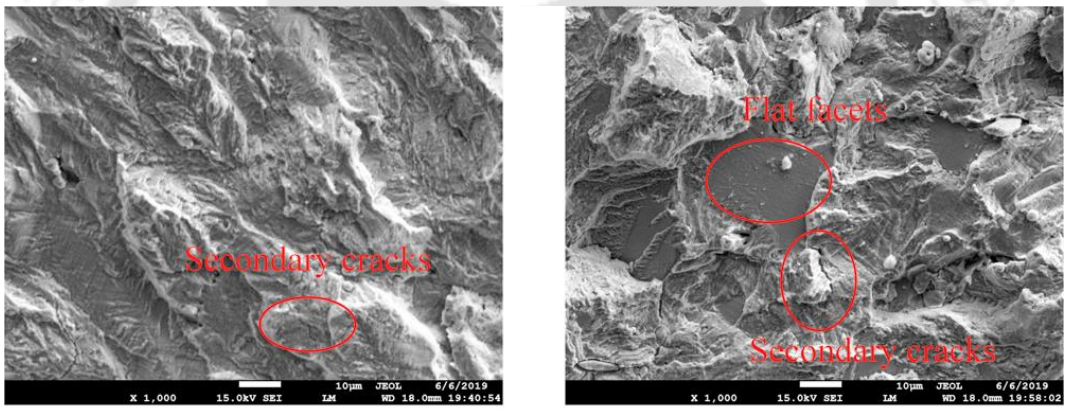

(a) (b)

Figure 8.14 SEM images of the fatigue fractured mode I specimen at (a) $a = 14.5$ mm and (b) $a = 17.2$ mm

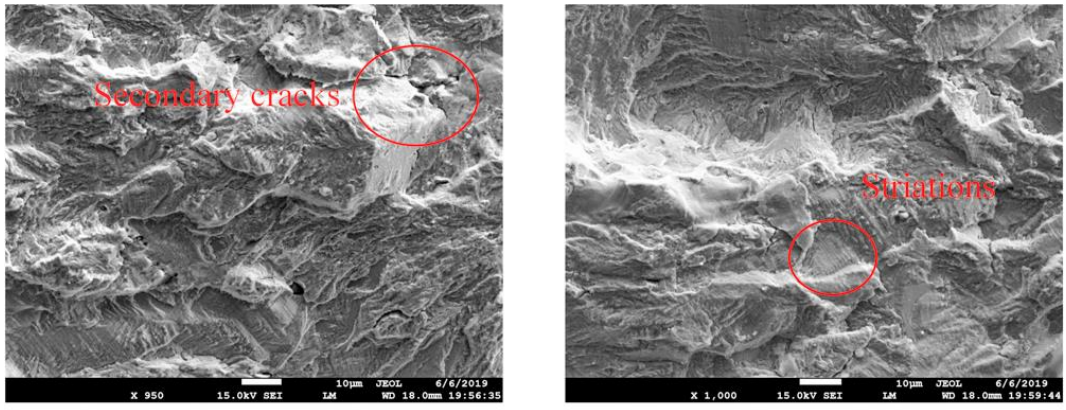

Figure 8.15 SEM images of the fatigue fractured mixed mode 30° specimen at (a) $a = 45.5$ mm and (b) $a = 49.1$ mm

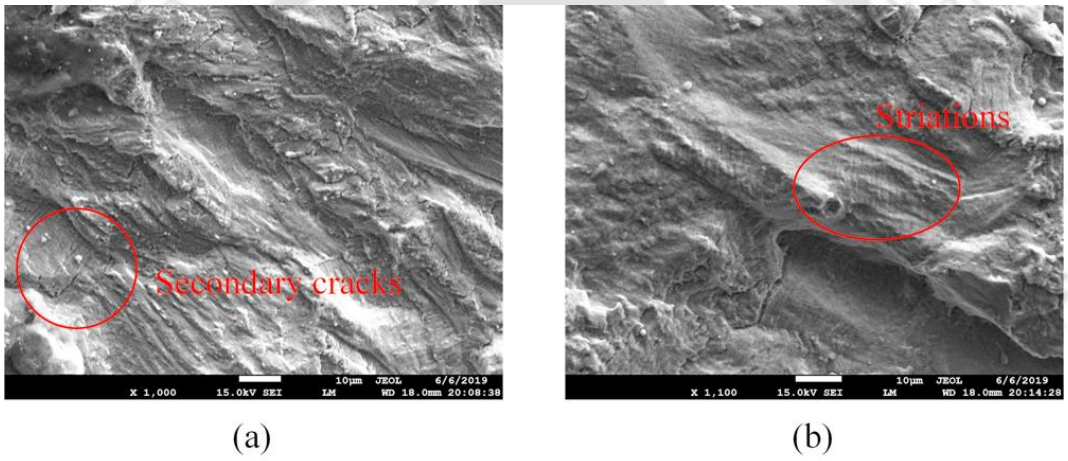

Figure 8.16 SEM images of the fatigue fractured mixed mode 45° specimen at (a) $a = 45.8$ mm and (b) $a = 49.4$ mm

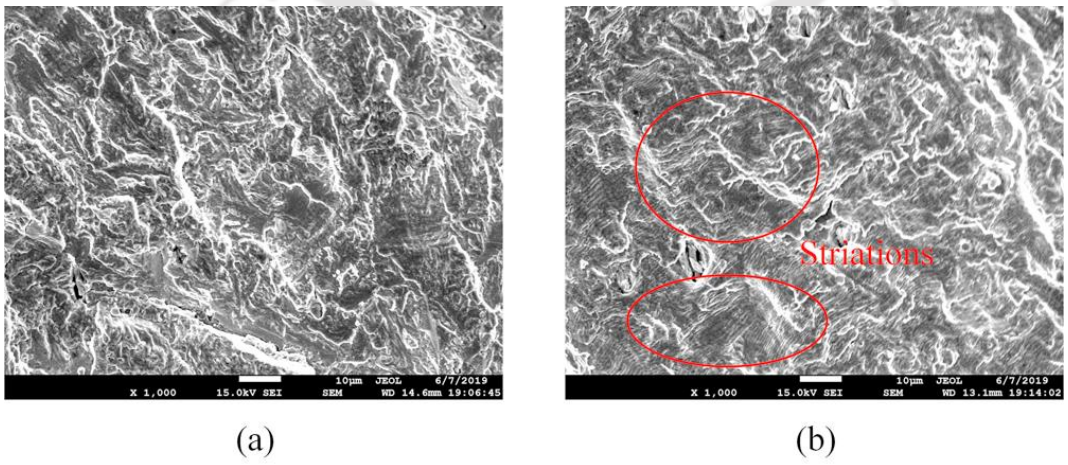

Figure 8.17 SEM images of the fatigue fractured mixed mode 60° specimen at (a) $a = 45.4$ mm and (b) $a = 51.3$ mm

The fractured surfaces also contain fatigue striations (Figs. 8.14 (b), 8.15 (b), 8.16 (b), 8.17 (b)). For mixed mode (I/II) fatigue fractured specimens, the surfaces are rough at the initial stages of the crack growth due to the presence of mode II component of loading (which causes rubbing of cracked surfaces) and are relatively smooth at the later stages of crack growth due to the domination of the mode I loading. Also, a significant difference in surface roughness observed between the mode I (Fig. 8.14) and mixed mode (I/II) (Figs. 8.15-8.17) fractured surfaces.

8.6 Summary

In the present investigation, finite element and experimental mixed mode (I/II) fatigue crack growth studies using the CTS specimen made of SS 316 stainless steel are performed for various loading angles. Using the mixed mode Paris law and the material dependent constants obtained from the mode I fatigue tests, the efficacy of various ΔK_{eq} models in fatigue life prediction is assessed. The quality of the proposed double exponential model in representing the fatigue crack growth curve is also demonstrated. Results of the present investigation again show that very satisfactory best-fits can be obtained for the mixed mode (I/II) experimental data with the help of the proposed best-fit model. Based on the performance throughout the fatigue crack propagation, the results of the present study clearly show that the ΔK_{eq} models viz., Irwin, Tanaka 2, and Demir predict fatigue life close to the experimental data. Further, predictions made by the Irwin model is consistently more close to the experimental data than Tanaka 2 and Demir. On the other hand, the ΔK_{eq} models viz., Richard, and Yan offering conservative estimates of the mixed mode fatigue life. It is very interesting to notice that similar observations have been noticed in the case of Al 6061-T6 material.

Chapter 9

Predictability assessment: Using published data

This chapter presents the assessment of the nature of the predictability of various ΔK_{eq} models using the already published results of other investigators. This is important because very similar conclusions are noticed in the present experiments, even with the different materials Al 6061-T6 and SS 316, and it is interesting to study whether the same conclusions can be reached using the already published experiments conducted by other investigators. It can be anticipated that these published works may contain different experimental specimens other than the CTS (considered in this investigation) and the materials other than considered in the present work. The work in this section starts with using the data of mixed mode experimental FCG studies on the center cracked specimen made of Ti-6Al-4V alloy by Pustejovsky (1979a). The second one is the data of the CTS specimen made of S460 steel by Ma et al. (2006) for the loading angle 30°. The third example considered is of the CTS specimen made of Al 7075-T6 alloy by Demir et al. (2018) for loading angles 45° and 60°.

9.1 Predictability assessment: Using Pustejovsky's data

Mixed mode fatigue crack growth simulations have been carried out on a center cracked (Fig. 9.1 (a)) specimen employed by Pustejovsky (1979a, 1979b). The specimen is made of Titanium alloy (Ti-6Al-4V) and containing center crack making an angle of 43° with the loading axis. The configuration in Fig. 9.1 (b) is employed to mimic the specimen in Fig. 9.1 (a). The validity of this simplification has been demonstrated by Ingraffea et al. (1983). Figure 9.1 (b) also shows boundary conditions used in the present finite element analysis where the bottom edge is restrained from all displacements.

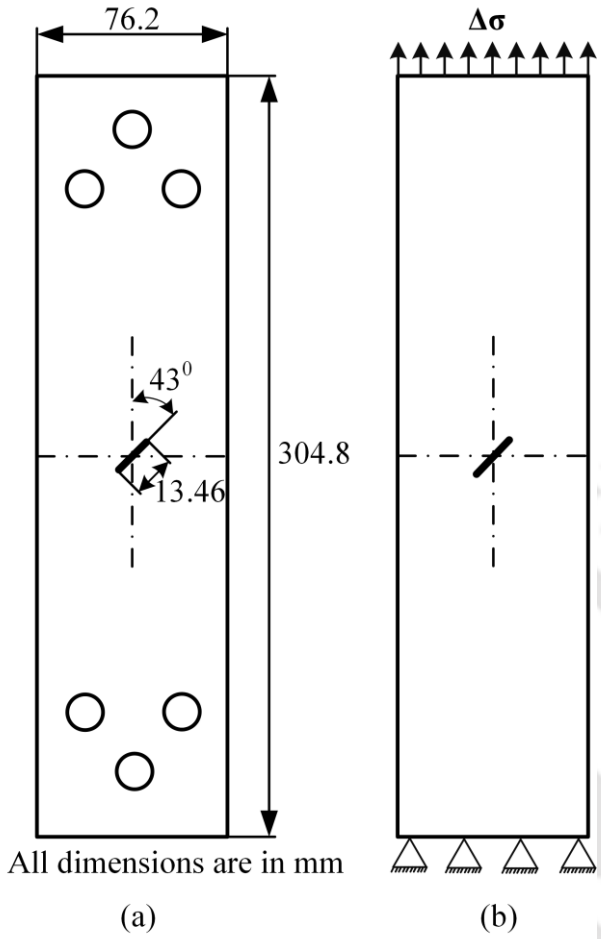

Figure 9.1 (a) Specimen used in experiments by Pustejovsky, (b) loading and boundary conditions of the specimen

Table 9.1 shows the material of the specimen and its properties, test conditions given by Pustejovsky (1979a), and other data useful for the present numerical simulation. In this simulation also, a small crack extension of $\Delta a = 0.5\,\text{mm}$ is employed, plane stress conditions have been assumed, and all other parameters useful in the numerical simulation are also presented in Table 9.1.

Figure 9.2 (a-c) shows the initial, intermediate, and final finite element meshes (near the crack tip) employed to reach to final crack length of $a_f = 13.231$ mm in 14 incremental simulations from an initial crack length of $a_i = 6.731$ mm. Figure 9.3 shows the comparison of the simulated and experimental paths. At both the crack tips, there is an excellent agreement between the experimental data and the simulated path using the MTS criterion. Using this simulated path, mixed mode fatigue life is estimated for each increment of the crack length using all the models of ΔK_{eq} presented in Table 7.5.

Table 9.1 Material properties and test conditions data for the center cracked plate

Parameter	Value
Material used	Ti-6Al-4V in mill annealed condition
Young's modulus, E	110.3 GPa
Poisson's ratio, ν	0.29
Plate thickness, t	3.175 mm
Paris constant, C	8.77E-12 $\left(\left(\text{m/cycle}\right)/\left(\text{MPa}\sqrt{\text{m}}\right)\right)^{\text{m}}$
Paris exponent, m	3.37
Load, $\Delta\sigma$	155.3 MPa
Load ratio, R	0.1
Frequency, f	10-40 Hz
Initial K_{II} / K_I	1.0523
Tensile yield strength	827.4 MPa
Ultimate tensile strength	930.8 MPa
Plane strain fracture toughness, K_{Ic}	82.4 $\text{MPa}\sqrt{\text{m}}$
Crack increment, Δa	0.5 mm
Initial crack length, a_i	6.731 mm
Final crack length, a_f	13.231 mm (left tip), 13.230 mm (right tip)

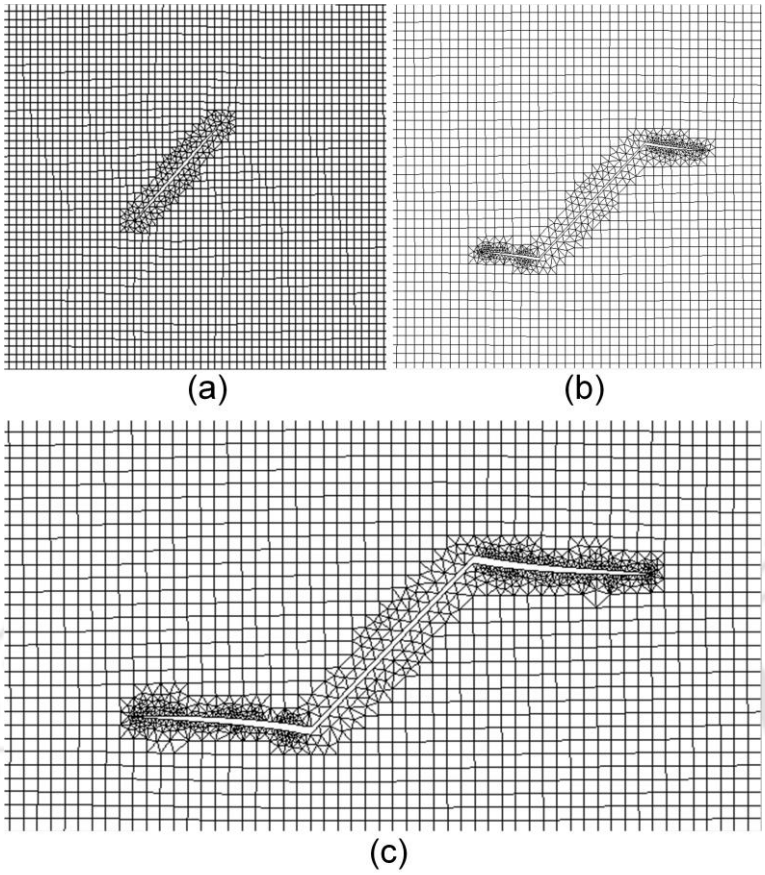

Figure 9.2 Sequence of meshes used for FE simulation of the mixed mode (I/II) FCG (a) initial, (b) intermediate and (c) final meshes near the crack tip

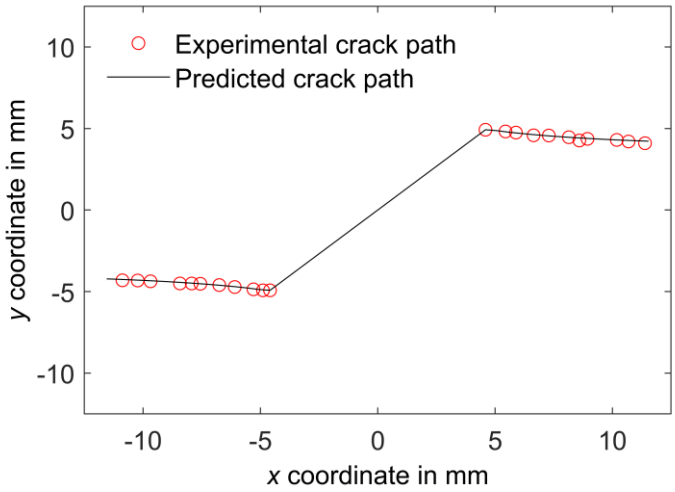

Figure 9.3 Comparison of the experimental and simulated crack path

Figures 9.4 and 9.5 shows the experimental data of $a-N$ curve obtained by Pustejovsky (1979a) and proposed double exponential fit to this experimental data at the right and left crack tips, respectively. The corresponding best-fit parameters are given in Table 9.2. One can see

from Figs. 9.4 and 9.5 that a little difference in the experimental life data due to the lack of perfect symmetric growth from both the tips. It can also be noticed from Figs. 9.4 and 9.5 that the proposed double exponential model fits accurately and satisfactorily represents the mixed mode (I/II) experimental data. Figures 9.6 and 9.7 show the predicted mixed mode fatigue crack growth curves, i.e., $(a-N)$ curves at the right and left tips, respectively, by employing all the selected ΔK_{eq} models (Table 7.5). Figures 9.6 and 9.7 also show the best-fits made in Figs. 9.4 and 9.5, which serves as a basis for the comparison of life predictive capability of various ΔK_{eq} models.

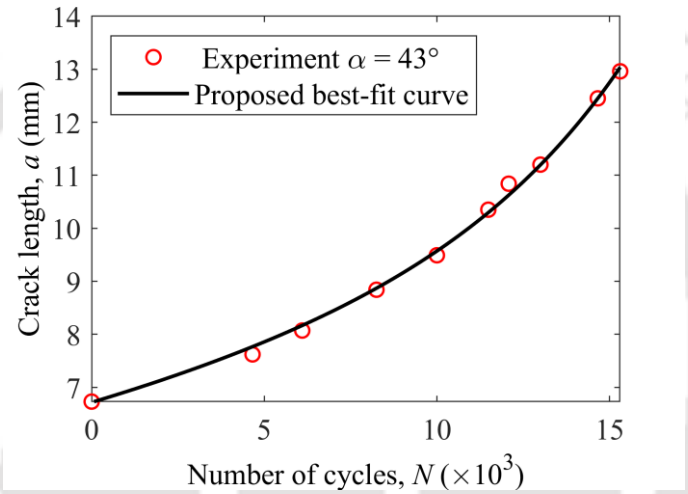

Figure 9.4 Experimental data and their best fit polynomials for the right crack tip (Pustejovsky, 1979a)

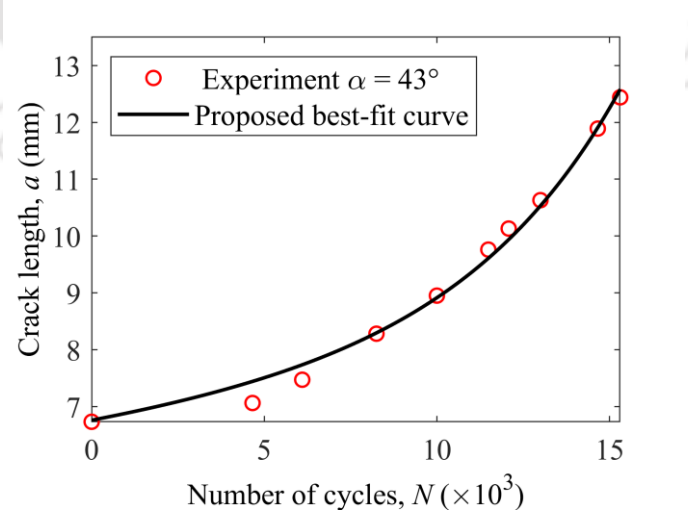

Figure 9.5 Experimental data and their best fit polynomials for the left crack tip (Pustejovsky, 1979a)

Table 9.2 Best fit parameters of the proposed double exponential model

Loading angle	p	k	q	r^2
43° (Right crack tip)	2.57×10^{-5}	8.07×10^{-2}	2.3×10^{-3}	0.9962
43° (Left crack tip)	1.26×10^{-5}	1.58×10^{-1}	2.2×10^{-3}	0.9913

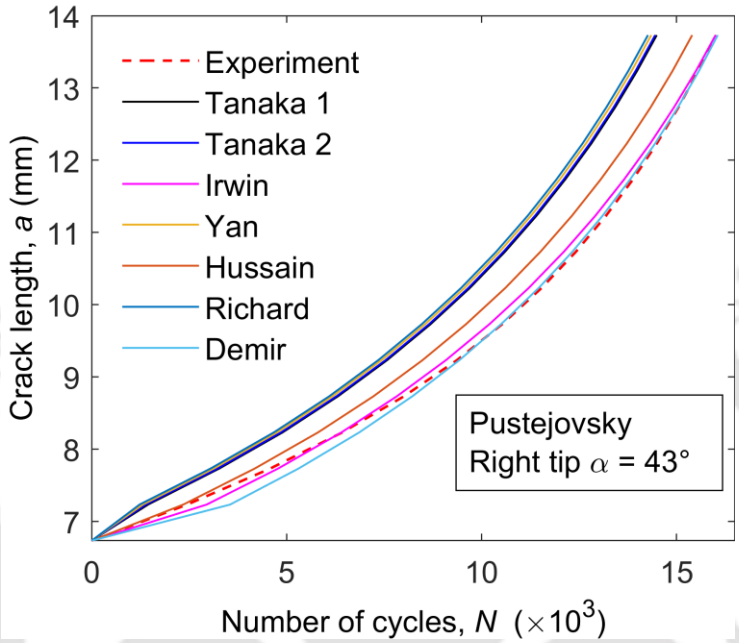

Figure 9.6 Comparison of crack length versus the number of loading cycles for the right crack tip (Pustejovsky, 1979a)

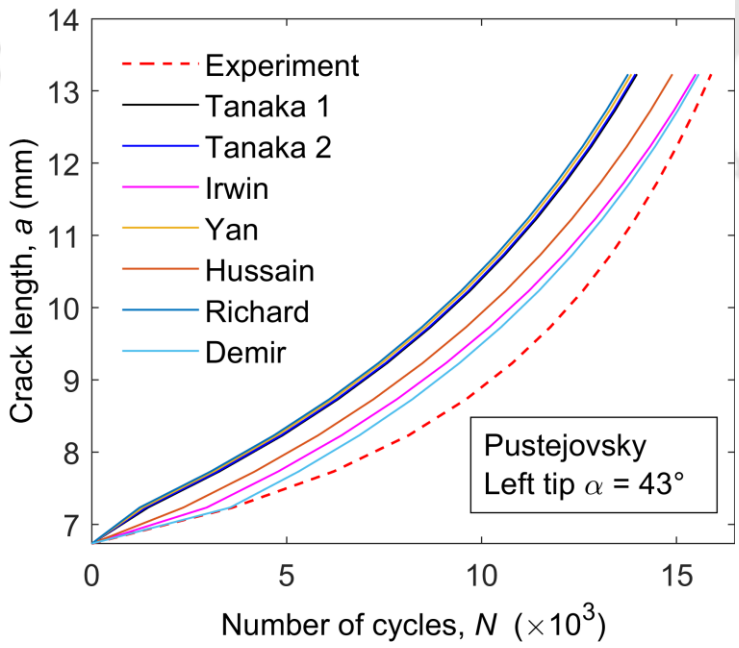

Figure 9.7 Comparison of the crack length versus the number of loading cycles for the left crack tip (Pustejovsky, 1979a)

Figures 9.8 and 9.9 shows % relative error in predicted life by various models with respect to the experimental values given in Figs. 9.4, and 9.5. Table 9.3 shows the % relative error in L_2 - norm and RMS error for all the models with the best-fitted experimental values as the reference values. It can be seen from Figs. 9.8 and 9.9 that all the ΔK_{eq} models show a high error at the initial stages of crack propagation and decreases as it propagates further. It is also very interesting to see from Figs. 9.6-9.9 that the life prediction made by Irwin's model is again very close to the experimental data as compared to all other models. Further, it is also interesting to notice from Figs. 9.6-9.9 that the predictions made using Demir et al.'s model are also very close to the experimental findings. The remaining ΔK_{eq} models are providing conservative estimates of the mixed mode fatigue life. Amongst, Richard et al. and Yan's models provide more conservative solutions. It is also interesting to see that the above observations are true at both the tips. Interestingly the error in the L_2 - norm and RMS value in Table 9.3 once again strongly substantiates all these previous observations.

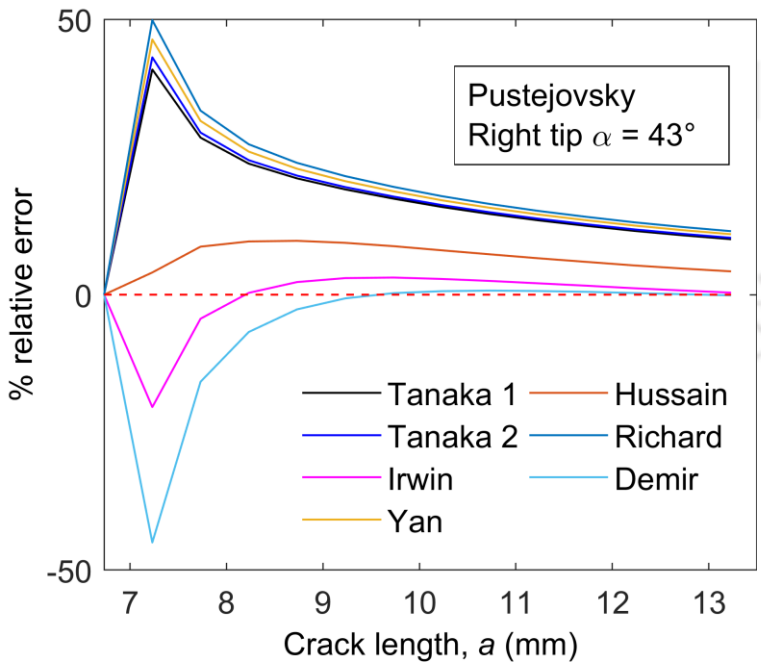

Figure 9.8 Percentage relative error in predicted life with respect to the experimental data for the right crack tip (Pustejovsky, 1979a)

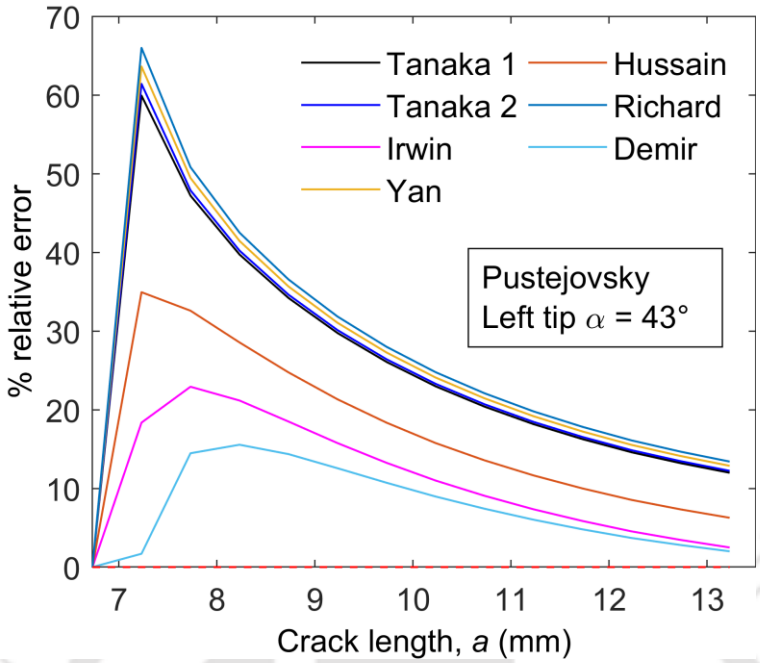

Figure 9.9 Percentage relative error in predicted life with respect to the experimental data for the left crack tip (Pustejovsky, 1979a)

Table 9.3 The RMS error and the L_2 norm in the estimated fatigue life for $\alpha = 43°$ (Pustejovsky, 1979a)

Crack tip	Error	ΔK_{eq} model						
		Tanaka 1	Tanaka 2	Irwin	Yan	Hussain	Richard	Demir
Left	RMS	2696	2736	1239	2834	1809	2919	952
	L_2	22.2	22.5	10.2	23.3	14.9	24.0	7.8
Right	RMS	1638	1678	252	1777	749	1862	379
	L_2	14.0	14.3	2.1	15.2	6.4	15.9	3.2

9.2 Predictability assessment: Using Ma et al.'s data

The second simulation carried out here is based on the experiments of Ma et al. (2006) using the CTS specimen made of steel and loaded using Richards loading device with the loading axis of 30° to the crack axis as shown in Fig. 7.5. As this specimen is the same as that employed in Chapters 7 and 8, finite element modeling is done as discussed in section 7.4.

Table 9.4 shows the details of the material, specimen, and other test conditions considered by Ma et al. (2006) and other data useful for the present numerical simulation. Plane

stress condition has been assumed. Employing a crack extension $\Delta a = 0.5\,\text{mm}$, a total of 40 finite element simulations steps have been carried out to reach a final crack of length $a_f = 65\,\text{mm}$ from an initial crack of length $a_i = 45\,\text{mm}$. Figure 9.10 shows the predicted crack path using the MTS criterion and Fig. 9.11 shows the experimental data of crack length and number of loading cycles measured by Ma et al. (2006) along with the double exponential best-fit curve to the experimental data. Table 9.5 shows the best-fit parameters.

Table 9.4 Material properties and test conditions data for the CTS specimen (Ma et al., 2006)

Parameter	Value
Material used	Steel S460
Young's modulus, E	200 GPa
Poisson's ratio, ν	0.25
Plate thickness, t	6 mm
Paris constant, C	7E-8 $\left(\left(\text{m/cycle}\right)/\left(\text{MPa}\sqrt{\text{m}}\right)\right)^{\text{m}}$
Paris exponent, m	2.1
Load ΔP	9 kN
Load ratio, R	0.5
Frequency, f	25 Hz
Initial K_{II}/K_I	0.3
Yield strength	460 MPa
Ultimate strength	610 MPa
Crack increment, Δa	0.5 mm
Initial crack length, a_i	45 mm
Final crack length, a_f	65 mm

Figure 9.12 shows the predicted crack length versus the number of loading cycles by employing all the selected ΔK_{eq} models (Table 7.5) along with the best-fitted experimental data (Fig. 9.11). Figure 9.13 shows % relative error in the predicted fatigue lives by all the ΔK_{eq} models with the experimental results as reference values. Interestingly, as in the previous

simulation, except at the initial stage of the crack propagation, the prediction based on Irwin's model is very close to the experimental results. Further, Tanaka 2 model is also predicting close to the experimental results. In a similar way, the predictions made by Richard's and Yan's models are conservative as compared to the other models. However, unlike the previous simulation, highly conservative predictions are made by Demir's model here. Table 9.6 shows the % relative error in L_2 - norm and RMS error in cycles for all the models with the best-fitted experimental values as the reference values. Once again, the above observations can also be noticed from the values of errors in Table 9.6.

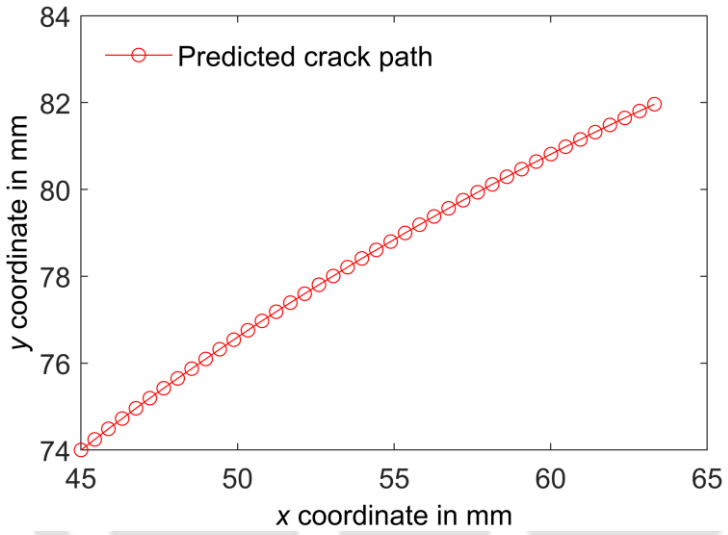

Figure 9.10 Simulated crack path for the CTS specimen (Ma et al., 2006) **(30°) using the MTS criterion**

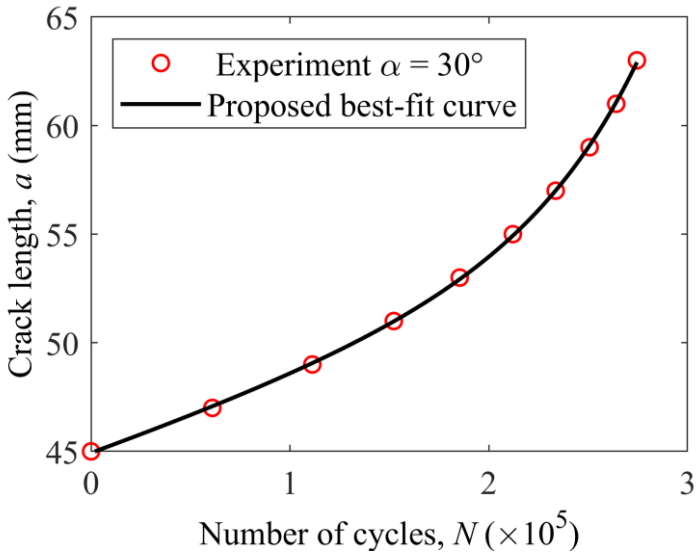

Figure 9.11 Experimental data and the best-fit curve (Ma et al., 2006) **(30°)**

Table 9.5 Best fit parameters of the proposed double exponential model

Loading angle	p	k	q	r^2
30°	4.37×10^{-6}	3.46×10^{-1}	9.27×10^{-3}	0.9953

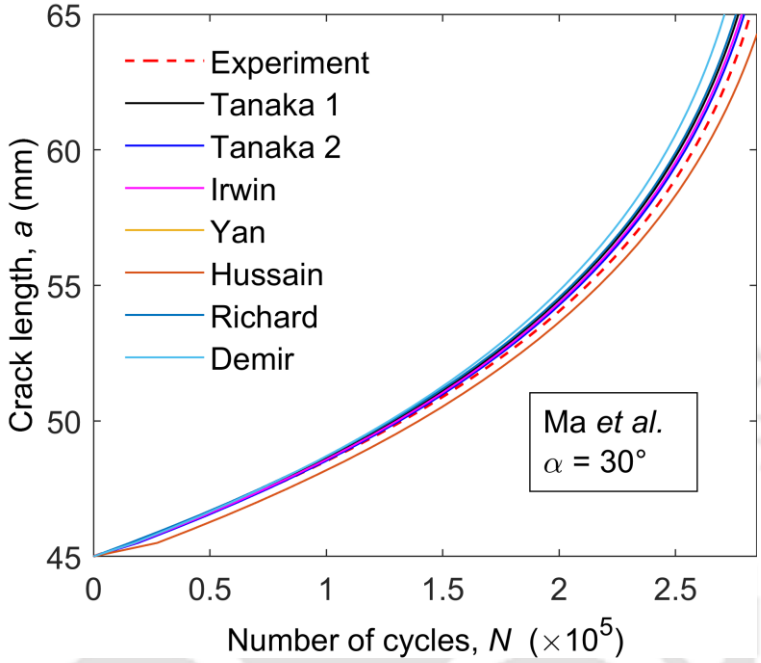

Figure 9.12 Comparison of the crack length versus the number of loading cycles (Ma et al., 2006) **(30°)**

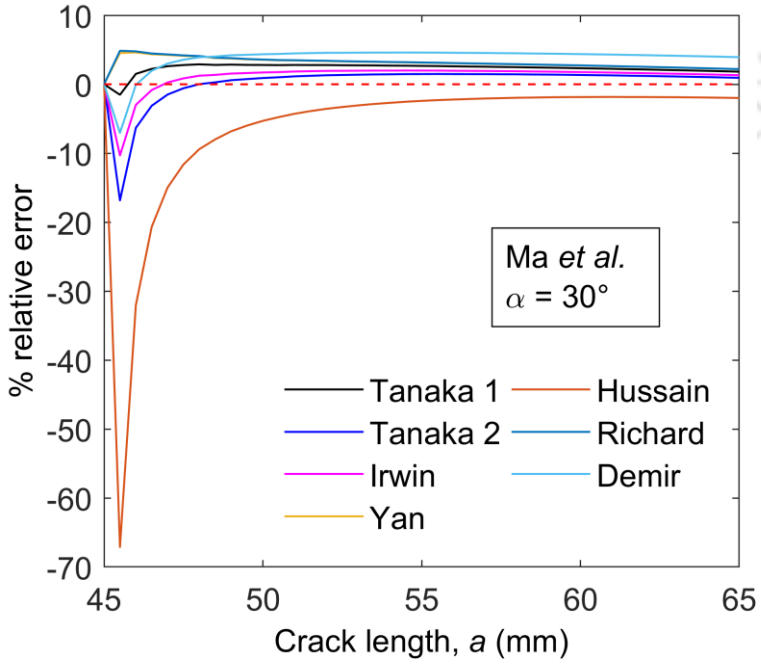

Figure 9.13 Percentage relative error in the fatigue life prediction (Ma et al., 2006) **(30°)**

Table 9.6 The RMS error and the L_2 norm in the estimated fatigue life for $\alpha =$ 30° (Ma et al., 2006)

α	Error	ΔK_{eq} model						
		Tanaka 1	Tanaka 2	Irwin	Yan	Hussain	Richard	Demir
30°	RMS	4934	2708	3610	5880	6350	5931	9002
	L_2	2.4	1.3	1.7	2.8	3.1	2.9	4.3

9.3 Predictability assessment: Using Demir et al.'s data

This section discusses the results obtained from the finite element FCG simulations based on Demir et al.'s experimental data (Demir et al., 2018) for the CTS specimens with loading angles 45° and 60°. Table 9.7 shows the details of the material, specimen, and test conditions considered by Demir et al. (2018) and other data useful for the present numerical simulation. Figures 9.14 and 9.15 shows the experimental data of crack length and number of loading cycles measured by Demir et al. (2018) for the loading angles 45° and 60°, respectively along with the present double exponential best-fit curve to this data. The corresponding best-fit parameters are given in Table 9.8. Figures 9.14 and 9.15 once again demonstrates the efficacy of the proposed double exponential method in fitting the mixed mode experimental data. As this specimen is the same as that employed in Chapters 7 and 8, finite element modeling for the present analyses is done as discussed in section 7.4.

Table 9.7 Material properties and other parameters used for the numerical simulation

Parameter	Value
Material	Al 7075-T651 alloy
Young's modulus E	70 GPa
Poisson's ratio ν	0.33
Thickness t	10 mm
Applied load P	11.40 kN (45°), 13.65 kN (60°)
Load ratio R	0.1
Paris' constant C	$1.46\times10^{-6}\,(\text{mm/cycle})/\left(\text{MPa}\sqrt{\text{m}}\right)^{m}$
Paris exponent m	2.44

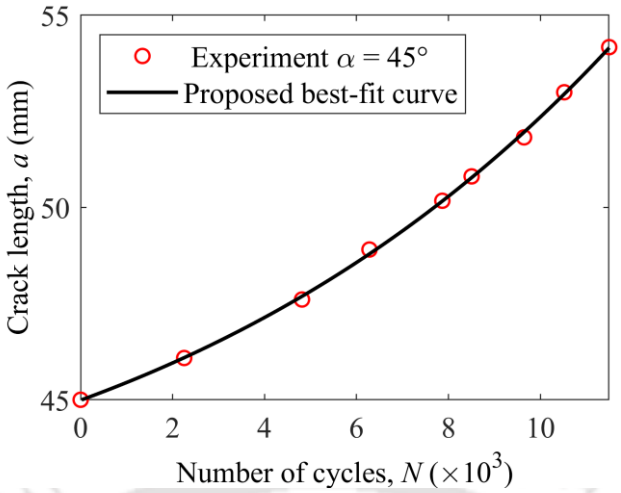

Figure 9.14 Experimental data and the best-fit curve (Demir et al., 2018) **(45°)**

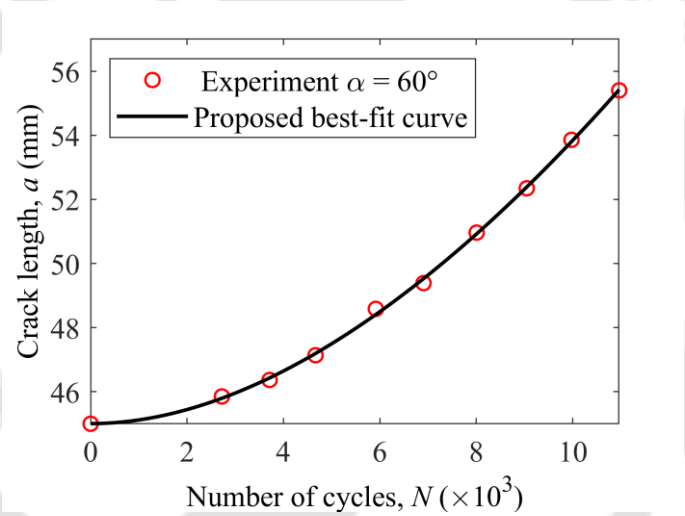

Figure 9.15 Experimental data and the best-fit curve (Demir et al., 2018) **(60°)**

Table 9.8 Best fit parameters of the proposed double exponential model

Loading angle	p	k	q	r^2
45°	1×10^{-5}	3.32×10^{-1}	2.2×10^{-3}	0.9992
60°	1.16×10^{-5}	1.34×10^{-1}	3.31×10^{-3}	0.9926

The fatigue life for both the loading angles 45° and 60° are estimated using seven selected ΔK_{eq} models (Table 7.5) and are plotted in Figs. 9.16 and 9.17. In order to assess the predictability of the ΔK_{eq} models, the numerical fatigue life is compared with the experimental fatigue life obtained by Demir et al. (2018). Three different error estimators, viz, percentage

relative error, the RMS value of the error, and the L_2 norm of the percentage relative error with reference to the experimental data are estimated for both the loading angles. Figures 9.18 and 9.19 shows the percentage relative error at every stage of the crack growth. Table 9.9 shows the global error values in terms of the RMS and L_2 norm.

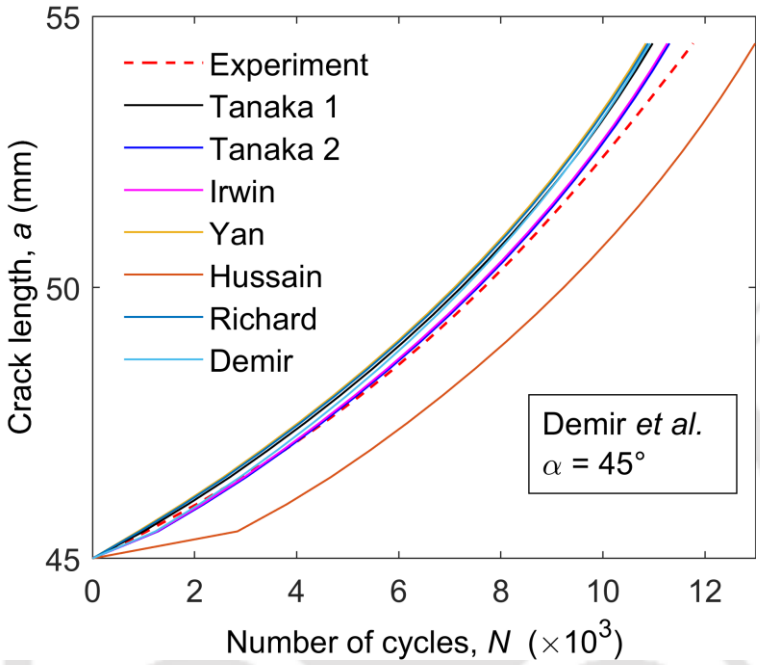

Figure 9.16 Comparison of the crack length versus the number of loading cycles (Demir et al., 2018) **(45°)**

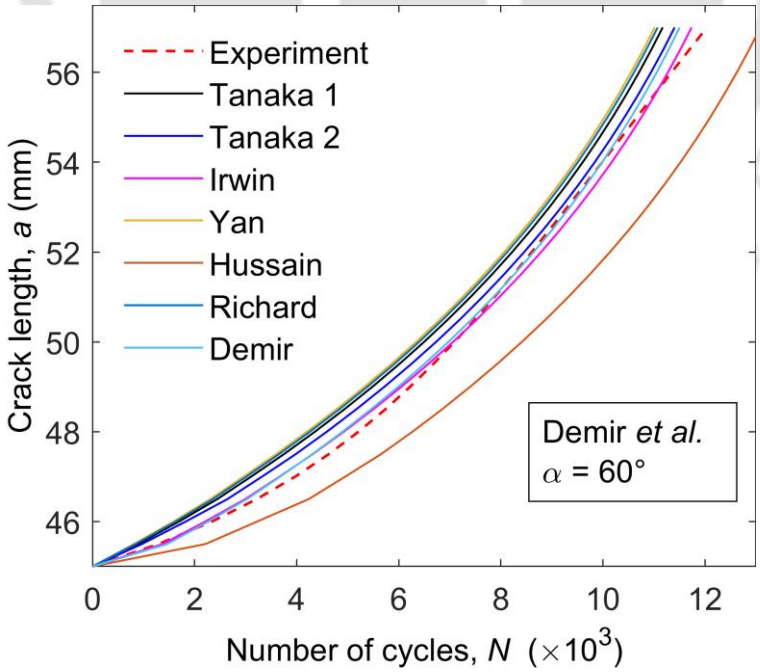

Figure 9.17 Comparison of the crack length versus the number of loading cycles (Demir et al., 2018) **(60°)**

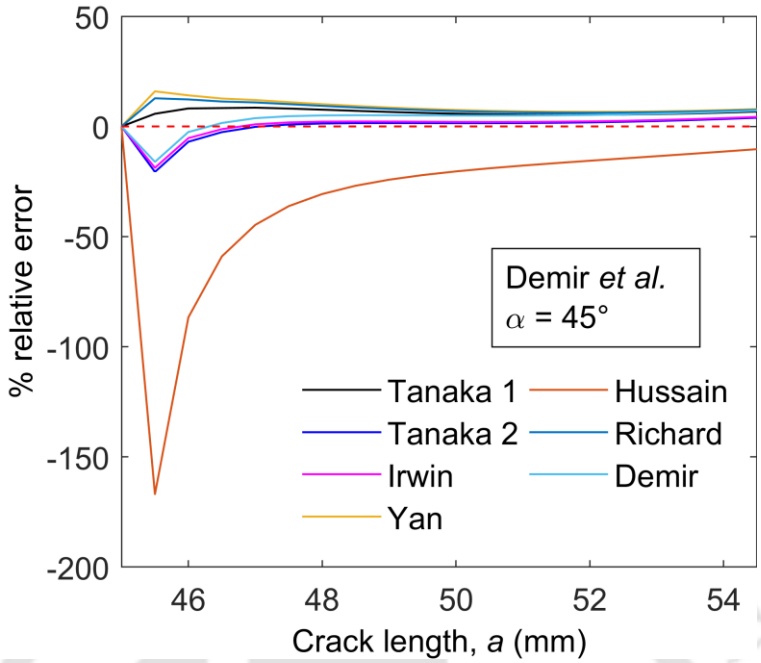

Figure 9.18 Percentage relative error in the fatigue life prediction (Demir et al., 2018) **(45°)**

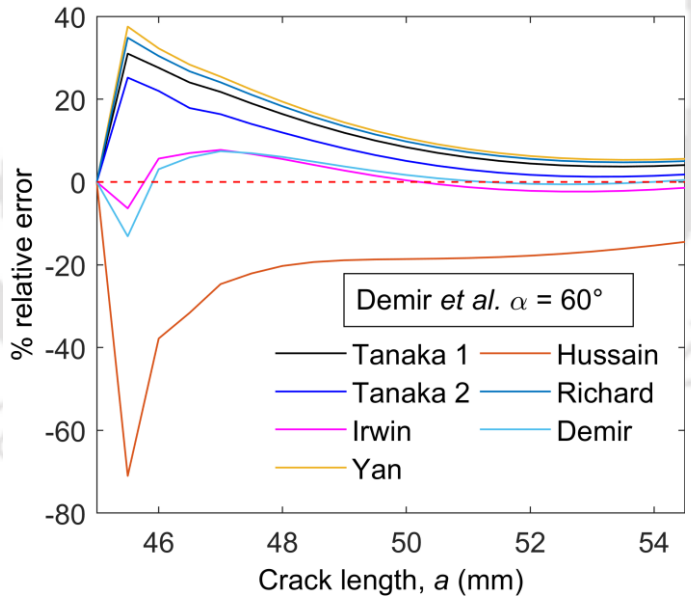

Figure 9.19 Percentage relative error in the fatigue life prediction (Demir et al., 2018) **(60°)**

It can be noted from Figs. 9.18 and 9.19 that all models exhibit relatively more error at the initial stages of the crack growth, and later the error decreases. Considering the overall performance of the models (as depicted in Figs. 9.16-9.19 and Table 9.9), it can be noticed that Irwin's ΔK_{eq} model again predicts the mixed mode (I/II) fatigue life close to the experimental value for both the loading angles considered in this study. Similarly, the predictions using

Tanaka 2 model are also very accurate for the lower loading angles (i.e., for 30°), whereas predictions using the Demir model are accurate for the higher loading angles (i.e., for 60°). It can also be seen from Figs. 9.16-9.19 and Table 9.9 that the models proposed by Yan and Richard are consistently providing conservative life predictions as is done in all the previous simulations. Similar results are also noted in studies presented in chapters 7 and 8.

Table 9.9 RMS error and the L_2 norm in estimated fatigue life for $\alpha =$ 45° and 60° (Demir et al., 2018)

α	Error	ΔK_{eq} model						
		Tanaka 1	Tanaka 2	Irwin	Yan	Hussain	Richard	Demir
45°	RMS	478	203	234	602	1554	563	450
	L_2	6.1	2.6	3.0	7.6	19.7	7.1	5.7
60°	RMS	618	414	187	763	1295	709	218
	L_2	7.5	5.0	2.3	9.3	15.8	8.6	2.7

9.4 Summary

In the present chapter, an attempt has been made to study the predictability of the selected ΔK_{eq} models for the numerical prediction of the mixed mode (I/II) fatigue life using already published experimental data by other investigators. The primary objective is to see whether or not the conclusions made in Chapters 7 and 8 on the predictability of the selected models will be repeated for the experimental data obtained by other investigators. Very interestingly, in this special investigation, also, once again, Irwin's ΔK_{eq} model consistently provided predictions close to the experimental data, as observed in Chapters 7 and 8. Further, the Demir's model is again proved to be useful for the higher loading angles or high mode mixity conditions. Even more, interestingly, the Richard's and Yan's models remain consistent in conservative predictions in all these investigations. This work in this chapter also shows that one of the two Tanaka's models (Tanaka 2) is also found to be a promising model for the predictions close to the experimental data for the lower mode mixities.

Chapter 10

Conclusions and scope of future work

10.1 Summary

In the present investigation, a mixed mode (I/II) fatigue life predictability assessment analysis of various ΔK_{eq} models has been carried out using both the experimental and finite element studies. These assessment studies have been carried out using the modified Paris law. To aid the present analysis, a new mixed mode (I/II) SIF extraction method and a new best-fit curve model for the scattered mixed mode experimental fatigue data have also been proposed. Mixed mode (I/II) fatigue crack growth experiments have been conducted using SS 316 and Al 6016 T6 materials. Richards' CTS specimen and its associated loading device have been employed in the mixed mode experiments. Finite element mixed mode (I/II) fatigue crack growth simulation studies of the above experimental specimens have been conducted to determine the fatigue life using the modified Paris law and selected ΔK_{eq} models. The predicted life obtained from these models has been compared with the experimental results to assess the nature of the predictive capabilities of the selected models. Apart from these experimental studies, finite element simulations have also been conducted on the specimens (having different configurations and made of different materials) for which published experimental fatigue life data (presented by various researchers) is available. Here also, the predicted life obtained from the selected models has been compared with the published life data. The results of the present study provide conclusive recommendations regarding the selection of ΔK_{eq} models for numerical prediction of the mixed mode (I/II) fatigue life of engineering components. Fractographic and error analysis has also been carried out to aid in understanding the results obtained in the present investigation. The salient conclusions from the present study are summarized under two sections viz., (a) general conclusions and (b) specific conclusions which are as follows

10.2 Conclusions

10.2.1 Conclusions from the mode I and mixed mode (I/II) FCG experiments

1. Mode I fatigue crack growth experiments on SS 316, and Al 6016-T6 materials provide $a-N$ data and material dependent Paris' constants (C and m), as expected.
2. Nearly the same values of C and m are observed from repeated mode I fatigue crack growth tests.
3. All the mode I fatigue crack growth experiments show a flat and elastic fracture along the crack axis, which indicates the correctness of the present experimental program and specimens' design and fabrication.
4. All the mode I fractographic studies clearly show increasing spacing between the striations, and these are formed perpendicular to the direction of the crack growth, indicating the Paris' regime and correctness of the experiments.
5. In all the mixed mode fatigue crack growth experiments (i.e., 30, 45 and 60 loading angles) on both the materials (i.e., SS 316 and Al 6061-T6) as expected, the cracks have grown in a curvilinear manner (non-self-similar) indicating the presence of mixed mode (I/II) loading at the crack tip.
6. In all the mixed mode fatigue crack growth experiments on both the materials, the crack kink angle increases with an increase in mode mixity angle or loading angle.
7. The fatigue crack growth rate decreased for both the materials with the increasing mode mixity.
8. In all the mixed mode experimental specimens made of both the materials, almost flat fracture has been observed in the fatigue fracture region, indicating SSY conditions due to high cycle fatigue.
9. Fractographic studies of the CTS specimens made of both the materials indicated that the mechanism of crack growth in both the materials is the ductile striations, which further empathizes the crack growth in the Paris regime. Also, the spacing between striations decreases as the mode mixity angle increases owing to the reduction in the crack growth rate.
10. Fractographic studies of the CTS specimens showed a rough fractured surface at the beginning, and afterward a smooth surface of the fatigue crack growth indicating the

presence of mode II at the beginning stages and domination of the mode I with a negligible amount of mode II loading respectively.

11. The proposed three parameter double exponential model is found to represent the experimental fatigue crack growth data accurately, and the goodness of fit is highest for the proposed model compared to other existing curve fitting models for the examples considered in this study. The proposed model can be used for both the mode I and mixed mode (I/II) FCG studies.
12. The proposed best-fit model contains only three constants and produces a smooth curve without any inflection points.

10.2.2 Conclusions from finite element simulations of the mixed mode (I/II) FCG

1. The proposed displacement based SIF extraction method is found capable of estimating the accurate mixed mode SIFs along with their signs. The proposed method shows the convergence of the solutions with the mesh refinement.
2. The proposed SIF extraction method is found easy to implement in any existing codes and equally accurate as of that of displacement extrapolation and path independent integral techniques available in commercial finite element software ANSYS®.
3. The MTS theory predicts accurate crack kink angles and the crack path for both the materials (SS 316 and Al 6061 T6) and various loading angles considered in this study.
4. The MTS theory also found to predict accurate crack kink angles and crack path for the various specimen configurations made of different materials on which the experimental results were already published by other researchers.
5. The numerical simulation results indicate that mode II stress intensity factor (K_{II}) is vanishing after the first step of crack growth simulations, and the contribution of K_{II} in ΔK_{eq} is nearly zero in the subsequent numerical simulation increments.
6. The fatigue life prediction by the selected ΔK_{eq} models differs in the first step of crack propagation. After the first step, the stepwise fatigue life predicted by these models is almost the same.

10.2.3 Conclusions from the comparison of the numerical results with the experimental data

1. Comparison of the present experimental mixed mode (I/II) fatigue life data (obtained using the CTS specimens made of SS 316 and Al 6061 T6 materials) with their finite element prediction of the mixed mode (I/II) fatigue life indicate that irrespective of material and mode mixity (loading angle) (a) amongst the models selected, the Irwin's ΔK_{eq} model consistently predicted the fatigue life close to the experimental data and (b) the Richard's and Yan's ΔK_{eq} models showed consistently conservative predictions of the fatigue life compared to the present experimental data.
2. Further, it is also observed that the Tanaka 2 and Demir's ΔK_{eq} models are promising models for accurate estimation of the mixed mode fatigue life at low and high mode mixity angles, respectively.
3. Comparison of the finite element estimation of the mixed mode (I/II) fatigue life of various specimens appeared in the published literature with their available experimental data shows that irrespective of the specimen configuration, material and loading angle, (a) amongst the models selected, once again Irwin's ΔK_{eq} model consistently predicted the fatigue life close to the published experimental data as compared to the other selected models and (b) interestingly once again the Richard's and Yan's ΔK_{eq} models showed consistently conservative predictions of the fatigue life compared to the published experimental data.
4. Further, in this study, it is also observed that the Tanaka 2 ΔK_{eq} model is a promising model for accurate estimation of the mixed mode fatigue life.
5. It is observed that at very initial stages of crack propagation, a considerable amount of error in life prediction is observed in all the selected models when a crack increment size of 0.5 mm is used. The analysis shows that these initial errors can be greatly reduced using very small crack increments such as 0.1 mm. Thus a very small crack increment may be useful at the beginning of the numerical simulations and can be increased after a few steps of numerical simulations.

10.3 Specific conclusions

1. The results of different analysis of the present investigation clearly indicate that irrespective of the specimen configuration, material, and loading angle Irwin's ΔK_{eq} model is useful in consistently predicting using the numerical methods the mixed mode (I/II) fatigue life close to the experimental data of the engineering components
2. Again irrespective of the specimen configuration, material, and loading angle the Richard's and Yan's ΔK_{eq} models are useful for consistently conservative numerical estimation of the mixed mode (I/II) fatigue life of the engineering components.
3. The proposed three parameter double exponential best-fit model provides smooth fits without inflection points for both the mode I and mixed mode (I/II) experimental fatigue life data.
4. The proposed displacement based SIF extraction method provides highly accurate mixed mode (I/II) SIFs comparable to that of path independent integrals for the given mesh refinement.

10.4 Scope of future work

1. The modified Paris law can be extended to include load ratio along with the ΔK_{eq} models. Even if we consider extension of the simplest possible Walker's (Walker) model to the mixed mode fatigue loading using the modified Paris' law, to incorporate the effect of the stress or load ratio, again the basic question i.e., which of the available ΔK_{eq} need to be considered for acceptable explanation of the effect of stress ratio R needs to be addressed first. As the present work involves large number of experimental and numerical substantiations for answering the above question, a similar extensive amount of work is needed to investigate the effect of the load ratio on the mixed mode fatigue crack growth as a standalone topic.
2. The present study can be extended to the mixed mode loading conditions where all three modes, i.e., mode I, mode II, and mode III, are present simultaneously.
3. Richard's CTS specimen is the most widely used in mixed mode (I/II) fatigue crack growth studies. There is a need to develop ΔK_{eq} solutions for different crack lengths so that the fatigue life can be estimated without performing the finite element FCG analysis.

4. The CTS specimen requires additional complex loading devices, and even small misalignment in the loading changes creates inaccurate solutions. Moreover, the specimen, along with the loading devices, becomes considerably heavy, and therefore a new simple specimen needs to be developed for mixed mode (I/II) fatigue crack growth studies compatible with the axial tensile testing machines.
5. Most of the testing machines apply uniaxial tensile/compressive loads only. Thus they cannot directly apply mode III loading on to the mixed mode (I/II) specimens. Therefore, there is a need to develop additional loading fixtures such that they can apply mode III loading along with mode I and mode II load on the (a) standard Richard's CTS specimen (as it is widely used) and (b) a new simple specimen (as mentioned in 5) using the uniaxial UTM machine.
6. Three dimensional numerical simulations of mixed mode fatigue crack growth is needed as it can show the adequacy of plane stress conditions employed in the present investigation.

References

Albert, W.A.J., 1838. Über Treibseile am Harz. *Archiv für Mineralogie Geognosie Bergbau und Hüttenkunde* 10, 215–234.

Albuquerque, C., Silva, A.L.L., de Jesus, A.M.P., Calçada, R., 2015. An efficient methodology for fatigue damage assessment of bridge details using modal superposition of stress intensity factors. *International Journal of Fatigue* 81, 61–77.

Allen, R.J., Booth, G.S., Jutla, T., 1988. A review of fatigue crack growth characterization by linear elastic fracture mechanics (LEFM). Part I—Principles and methods of data generation. *Fatigue & Fracture of Engineering Materials and Structures* 11, 45–69.

Anderson, T.L. (Ted L.., 2005. Fracture mechanics : fundamentals and applications. Taylor & Francis.

ANSYS, 2007. ANSYS Theory reference manual.

Ayatollahi, M.R., Razavi, S.M.J., Chamani, H.R., 2014. Fatigue life extension by crack repair using stop-hole technique under pure mode-I and pure mode-II loading conditions. *Procedia Engineering* 74, 18–21.

Ayatollahi, M.R., Razavi, S.M.J., Yahya, M.Y., 2015. Mixed mode fatigue crack initiation and growth in a CT specimen repaired by stop hole technique. *Engineering Fracture Mechanics* 145, 115–127.

Ayatollahi, M.R., Sedighiani, K., 2012. A T-stress controlled specimen for mixed mode fracture experiments on brittle materials. *European Journal of Mechanics - A/Solids* 36, 83–93.

Banks-Sills, L., Arcan, M., Bortman, Y., 1984. A mixed mode fracture specimen for mode II dominant deformation. *Engineering Fracture Mechanics* 20, 145–157.

Banks-Sills, L., Sherman, D., 1986. Comparison of methods for calculating stress intensity factors with quarter-point elements 32, 127–140.

Barsoum, R.S., 1977. Triangular quarter-point elements as elastic and perfectly-plastic crack tip elements. *International Journal for Numerical Methods in Engineering* 11, 85–98.

Barsoum, R.S., 1976. On the use of isoparametric finite elements in linear fracture mechanics. *International Journal for Numerical Methods in Engineering* 10, 25–37.

Bauschinger, J., 1886. Über die Veränderung der Elasticitätsgrenze und Festigkeit des Eisen und Stahls durch Strecken und Quetschen, durch Erwarmen und Abkühlen und durch oftmal wiederholte Beanspruchung. *Mitteilungen Aus Dem Mechanisch-Technischen Laboratorium Der K Polytechnischen Schule* 1836–1877.

Benthem, J.P., Koiter, W.T., 1973. Asymptotic approximations to crack problems, in: Methods of Analysis and Solutions of Crack Problems. Springer Netherlands, Dordrecht, pp. 131–178.

Bilby, B.A., Cottrell, A.H., Swinden, K.H., 1963. The spread of plastic yield from a notch. *Proceedings of the Royal Society of London. Series A. Mathematical and Physical Sciences* 272, 304–314.

Biner, S.B., 2001. Fatigue crack growth studies under mixed-mode loading. *International Journal of Fatigue* 23, 259–263.

Blažić, M., Maksimović, S., Petrović, Z., Vasović, I., Turnić, D., 2014. Determination of fatigue crack growth trajectory and residual life under mixed modes. *Strojniški vestnik – Journal of Mechanical Engineering* 60, 250–254.

Boljanović, S., Maksimović, S., 2014. Mixed mode crack growth simulation with/without overloads. *International Journal of Fatigue* 67, 183–190.

Boljanović, S., Maksimović, S., 2011. Analysis of the crack growth propagation process under mixed-mode loading. *Engineering Fracture Mechanics* 78, 1565–1576.

Borrego, L.P., Antunes, F.V., Costa, J.M., Ferreira, J.M., 2006. Mixed-mode fatigue crack growth behaviour in aluminium alloy. *International Journal of Fatigue* 28, 618–626.

Braithwaite, F., 1854. On the fatigue and consequent fracture of metals. *Minutes of the Proceedings of the Institution of Civil Engineers* 13, 463–467.

Broek, D., 1991. The civil damage tolerance requirements in theory and practice. pp. 73–86.

Broek, D., 1989. The practical use of fracture mechanics. Springer Netherlands, Dordrecht.

Broszeit, E., Preussler, T., Wagner, M., Zwirlein, O., 1986. Stress hypotheses and material stresses in hertzian contacts. *Materialwissenschaft und Werkstofftechnik* 17, 238–246.

Cao, J., Li, F., Ma, X., Sun, Z., 2018. Study of anisotropic crack growth behavior for aluminum alloy 7050-T7451. *Engineering Fracture Mechanics* 196, 98–112.

Chan, S.K., Tuba, I.S., Wilson, W.K., 1970. On the finite element method in linear fracture mechanics. *Engineering Fracture Mechanics* 2, 1–17.

Chen, C.H., Wang, C.L., 2008. Stress intensity factors and T-stresses for offset double edge-cracked plates under mixed-mode loadings. *International Journal of Fracture* 152, 149–162.

Chen, W.R.R., Keer, L.M., 1991. Fatigue crack growth in mixed mode loading. *Journal of Engineering Materials and Technology* 113, 222.

Chow, C.L., Lu, T.J., 1991. Cyclic J-integral in relation to fatigue crack initiation and propagation. *Engineering Fracture Mechanics* 39, 1–20.

Chowdhury, P., Sehitoglu, H., 2016. Mechanisms of fatigue crack growth - a critical digest of theoretical developments. *Fatigue & Fracture of Engineering Materials & Structures* 39, 652–674.

Dally, J.W., Sanford, R.J., 1987. Strain-gage methods for measuring the opening-mode stress-intensity factor,K I. *Experimental Mechanics* 27, 381–388.

Davies, K.B., Feddersen, C.E., 1973. Evaluation of fatigue crack growth rates by polynomial curve fitting. *International Journal of Fracture* 9, 2–4.

Demir, O., Ayhan, A.O., İriç, S., 2017. A new specimen for mixed mode I/II fracture tests: Modeling, experiments and criteria development. *Engineering Fracture Mechanics* 178, 457–476.

Demir, O., Ayhan, A.O., Iric, S., Lekesiz, H., 2018. Evaluation of mixed mode I/II criteria for fatigue crack propagation using experiments and modeling. *Chinese Journal of Aeronautics* 31, 1525–1534.

Dirik, H., Yalçinkaya, T., 2018. Crack path and life prediction under mixed mode cyclic variable amplitude loading through XFEM. *International Journal of Fatigue* 114, 34–50.

Dover, W.D., Boutle, N.F., 1978. The influence of mean stress and thickness on the fatigue crack

growth behaviour of the aluminium alloy BS2L71. *The Journal of Strain Analysis for Engineering Design* 13, 129–139.

Duchaczek, A., Mańko, Z., 2016. The influence of a cracking mode on fatigue crack propagation in steel girders in military bridges. *European Journal of Environmental and Civil Engineering* 20, 1–18.

Erdogan, F., Sih, G.C., 1963. On the crack extension in plates under plane loading and transverse shear. *Journal of Fluids Engineering, Transactions of the ASME* 85, 519–525.

Ewing, J.A., Rosenhain, W., 1900. The crystalline structure of metals (second paper). *Philosophical Transactions of the Royal Society A: Mathematical, Physical and Engineering Sciences* 195, 279–301.

Farjoo, M., Pal, S., Daniel, W., Meehan, P.A., 2012. Stress intensity factors around a 3D squat form crack and prediction of crack growth direction considering water entrapment and elastic foundation. *Engineering Fracture Mechanics* 94, 37–55.

Fatemi, A., Socie, D.F., 1988. A critical plane approach to multiaxial fatigue damage including out of phase loading. *Fatigue & Fracture of Engineering Materials and Structures* 11, 149–165.

Fayed, E.A.S.M., 2002. Mixed mode crack tip deformation due to multi-axial cyclic loading. Al-Azhar University.

Findlay, S.J., Harrison, N.D., 2002. Why aircraft fail. *Materials Today* 5, 18–25.

Forman, R.G., Kearney, V.E., Engle, R.M., 1967. Numerical analysis of crack propagation in cyclic-loaded structures. *Journal of Basic Engineering* 89, 459.

Forman, R.G., Mettu, S.R., 1990. Behavior of Surface and Corner Cracks Subjected to Tensile and Bending Loads in Ti-6A1-4V Alloy. Houston, TX.

Forth, S.C., Keat, W.D., Favrow, L.H., 2002. Experimental and computational investigation of three-dimensional mixed-mode fatigue. *Fatigue and Fracture of Engineering Materials and Structures* 25, 3–15.

Gao, M., Chen, S., Wei, R.P., 1992. Crack paths, microstructure, and fatigue crack growth in annealed and cold-rolled AISI 304 stainless steels. *Metallurgical Transactions A* 23, 355–371.

Gao, M., Wei, R.P., 1992. Morphology of corrosion fatigue cracks produced in 3.5% NaCl solution and in hydrogen for a high purity metastable austenitic (Fe18Cr12Ni) steel. *Scripta Metallurgica et Materialia* 26, 1175–1180.

Ghaffari, M.A., Pahl, E., Xiao, S., 2015. Three dimensional fatigue crack initiation and propagation analysis of a gear tooth under various load conditions and fatigue life extension with boron/epoxy patches. *Engineering Fracture Mechanics* 135, 126–146.

Ghosh, A., Mallik, A.K., 2010. Manufacturing science, 2nd ed. Ellis Horwood.

Grbović, A., Kastratović, G., Sedmak, A., Balać, I., Popović, M.D., 2019a. Fatigue crack paths in light aircraft wing spars. *International Journal of Fatigue* 123, 96–104.

Grbović, A., Kastratović, G., Sedmak, A., Eldweib, K., Kirin, S., 2019b. Determination of optimum wing spar cross section for maximum fatigue life. *International Journal of Fatigue* 127, 305–311.

Griffith, A.A., 1921. The phenomena of rupture and flow in solids. *Philos. Trans. R. Soc. A*, 221, 163–198.

Guinea, G. V., Planas, J., Elices, M., 2000. KI evaluation by the displacement extrapolation technique. *Engineering Fracture Mechanics* 66, 243–255.

Hallbäck, N., 1997. The influence of finite geometry and material properties on mixed mode I/II fracture of aluminum. *International Journal of Fracture* 87, 151–188.

He, W., Liu, J., Xie, D., 2015. Probabilistic life assessment on fatigue crack growth in mixed-mode by coupling of Kriging model and finite element analysis. *Engineering Fracture Mechanics* 139, 56–77.

He, W., Liu, J., Xie, D., 2014. Numerical study on fatigue crack growth at a web stiffener of ship structural details by an objected oriented approach in conjunction with ABAQUS. *Marine Structures* 35, 45–69.

Heirani, H., Farhangdoost, K., 2018. Effect of compressive mode I on the mixed mode I/II fatigue crack growth rate of 42CrMo4. *Journal of Materials Engineering and Performance* 27, 138–146.

Hellen, T.K., 1975. On the method of virtual crack extensions. *International Journal for Numerical Methods in Engineering* 9, 187–207.

Hello, G., 2018. Derivation of complete crack-tip stress expansions from Westergaard–Sanford solutions. *International Journal of Solids and Structures* 144–145, 265–275.

Hello, G., Ben Tahar, M., Roelandt, J.-M., 2012. Analytical determination of coefficients in crack-tip stress expansions for a finite crack in an infinite plane medium. *International Journal of Solids and Structures* 49, 556–566.

Henn, K., Richard, H.A., Linning, W., 1988. Fatigue crack Growth under mixed mode and mode II cyclic loading, Proceedings of European Conference on Fracture (ECF7).

Henshell, R.D., Shaw, K.G., 1975. Crack tip finite elements are unnecessary. *International Journal for Numerical Methods in Engineering* 9, 495–507.

Horas, C.S., Alencar, G., De Jesus, A.M.P., Calçada, R., 2018. Development of an efficient approach for fatigue crack initiation and propagation analysis of bridge critical details using the modal superposition technique. *Engineering Failure Analysis* 89, 118–137.

Hoshide, T., Socie, D.F., 1987. Mechanics of mixed mode small fatigue crack growth. *Engineering Fracture Mechanics* 26, 841–850.

Hosseini, S., Choupani, N., Gharabaghi, A., 2008. Experimental estimation of mixed mode fracture properties of steel weld. *International Journal of Civil and Environmental Engineering* 2, 86–91.

Hua, G., Alagok, N., Brown, M., Miller, K., 1985. Growth of Fatigue Cracks Under Combined Mode I and Mode II Loads, in: Multiaxial Fatigue. ASTM International, 100 Barr Harbor Drive, PO Box C700, West Conshohocken, PA 19428-2959, pp. 184-184–19.

Hussain, M., Pu, S., Underwood, J., 1974. Strain energy release rate for a crack under combined mode I and mode II. *Fracture Analysis, ASTM STP 560* 2–28.

Iida, S., Kobayashi, A.S., 1969. Crack propagation rate in 7075-T6 plates under cyclic tensile and transverse shear loadings. *Journal of Basic Engineering* 91, 764–769.

Inglis, C.E., 1913. Stresses in a plate due to the presence of cracks and sharp corners. *Transactions of the Royal Institute of Naval Architectes* 55, 219–241.

Ingraffea, A., Blandford, G., Liggett, J., 1983. Automatic modelling of mixed-mode fatigue and quasi-static crack propagation using the boundary element method, in: Fracture Mechanics: Fourteenth Symposium—Volume I: Theory and Analysis. ASTM International, 100 Barr Harbor Drive, PO Box C700, West Conshohocken, PA 19428-

2959, pp. 407–407.

Irwin, G.., 1957. Analysis of stresses and strains near the end of a crack transversing a plate. *Journal of applied mechanics* 24, 361–370.

Irwin GR, 1957. Analysis of stresses and strains near the end of a crack traversing a plate. *J Appl Mech* 24, 361–364.

Isida, M., 1971. Effect of width and length on stress intensity factors of internally cracked plates under various boundary conditions. *International Journal of Fracture Mechanics* 7, 301–316.

Jameel, A., Harmain, G.A., 2016. Modeling and numerical simulation of fatigue crack growth in cracked specimens containing material discontinuities. *Strength of Materials* 48, 294–307.

Jogdand, P.V., Murthy, K.S.R.K., 2010. A finite element based interior collocation method for the computation of stress intensity factors and T-stresses. *Engineering Fracture Mechanics* 77, 1116–1127.

Jogi, B.F., Brahmankar, P.K., Nanda, V.S., Prasad, R.C., 2008. Some studies on fatigue crack growth rate of aluminum alloy 6061. *Journal of Materials Processing Technology* 201, 380–384.

Kaushik, B., Murthy, K., Robi, P., 2008. Determination of strain gage locations for the accurate measurement of opening mode stress intensity factors. *Journal of Mechanics of Materials and Structures* 3, 1757–1771.

Khan, S.M.A., Khraisheh, M.K., 2000. Analysis of mixed mode crack initiation angles under various loading conditions. *Engineering Fracture Mechanics* 67, 397–419.

Kim, J.K., Kim, C.S., 2002. Fatigue crack growth behavior of rail steel under mode I and mixed mode loadings. *Materials Science and Engineering: A* 338, 191–201.

Kim, K.S., Lee, H.S., 2007. An incremental formulation for the prediction of two dimensional fatigue crack growth with curved paths. *International Journal for Numerical Methods in Engineering* 72, 697–721.

Kim, T.Y.Y., Kim, H.K.K., 2013. Mixed mode fatigue crack growth behavior of fully lower bainite steel. *Materials Science and Engineering A* 580, 322–329.

Kirthan, L.J., Hegde, R., Girisha, V.A., Kumar, R.G., 2016. Evaluation of mode 1 stress intensity factor for edge crack using displacement extrapolation method. *International Journal of Materials and Structural Integrity* 10, 11.

Kong, X.M., Schlüter, N., Dahl, W., 1995. Effect of triaxial stress on mixed-mode fracture. *Engineering Fracture Mechanics* 52, 379–388.

Kumar, S., Singh, I.V., Mishra, B.K., Rabczuk, T., 2015. Modeling and simulation of kinked cracks by virtual node XFEM. *Computer Methods in Applied Mechanics and Engineering* 283, 1425–1466.

Laham, S. Al, 1998. Stress intensity factor and limit load handbook. British Energy Generation Ltd, Gloucester.

Lardner, R.W., 1968. A dislocation model for fatigue crack growth in metals. *Philosophical Magazine* 17, 71–82.

Leite, P.G.P., Gomes, G., 2019. Numerical simulation of fatigue crack propagation in mixed mode (I+II) using the program BemCracker2D. *International Journal of Structural Integrity* 10, 497–514.

Leonel, E.D., Venturini, W.S., 2011. Multiple random crack propagation using a boundary element formulation. *Engineering Fracture Mechanics* 78, 1077–1090.

Lesiuk, G., Correia, J.A.F.O., Smolnicki, M., De Jesus, A.M.P., Duda, M., Montenegro, P.A., Calcada, R.A.B., Lesiuk, G., Correia, J.A.F.O., Smolnicki, M., De Jesus, A.M.P., Duda, M., Montenegro, P.A., Calcada, R.A.B., 2019. Fatigue crack growth rate of the long term operated puddle iron from the Eiffel bridge. *Metals* 9, 53.

Lesiuk, G., Kucharski, P., Correia, J.A.F.O., De Jesus, A.M.P., Rebelo, C., da Silva, L.S., 2016. Mixed mode (I + II) fatigue crack growth of long term operating bridge steel. *Procedia Engineering* 160, 262–269.

Lesiuk, G., Kucharski, P., Correia, J.A.F.O., De Jesus, A.M.P., Rebelo, C., Simões da Silva, L., 2017. Mixed mode (I+II) fatigue crack growth in puddle iron. *Engineering Fracture Mechanics* 185, 175–192.

Li, C.Q., Fu, G., Yang, W., 2016. Stress intensity factors for inclined external surface cracks in pressurised pipes. *Engineering Fracture Mechanics* 165, 72–86.

Li, H., Yuan, H., Li, X., 2015. Assessment of low cycle fatigue crack growth under mixed-mode

loading conditions by using a cohesive zone model. *International Journal of Fatigue* 75, 39–50.

Lim, I.L., Johnston, I.W., Choi, S.K., 1992a. Comparison between various displacement-based stress intensity factor computation techniques 58, 193–210.

Lim, I.L., Johnston, I.W., Choi, S.K., 1992b. On stress intensity factor computation from the quarter point element displacements. *Communications in Applied Numerical Methods* 8, 291–300.

Lo, K.W., Gong, Y.B., Tamilselvan, T., Lai, M.O., 2003. A proposed specimen for KIIC testing. *International Journal of Fracture* 124, 127–137.

Lo, K.W., Tamilselvan, T., Chua, K.H., Zhao, M.M., 1996. A unified model for fracture mechanics. *Engineering Fracture Mechanics* 54, 189–210.

Ma, S., Zhang, X.B., Recho, N., Li, J., 2006. The mixed mode investigation of the fatigue crack in CTS metallic specimen. *International Journal of Fatigue* 28, 1780–1790.

Madia, M., Beretta, S., Schödel, M., Zerbst, U., Luke, M., Varfolomeev, I., 2011. Stress intensity factor solutions for cracks in railway axles. *Engineering Fracture Mechanics* 78, 764–792.

Mahanty, D.K., Maiti, S.K., 1990. Experimental and finite element studies on mode I and mixed mode (I and II) stable crack growth-I. Experimental. *Engineering Fracture Mechanics* 37, 1237–1250.

Maiti, S.K., Mahanty, D.K., 1990. Experimental and finite element studies on mode I and mixed mode (I and II) stable crack growth—II. finite element analysis. *Engineering Fracture Mechanics* 37, 1251–1275.

Maiti, S.K., Smith, R.A., 1983a. Comparison of the criteria for mixed mode brittle fracture based on the preinstability stress-strain field Part I: Slit and elliptical cracks under uniaxial tensile loading. *International Journal of Fracture* 23, 281–295.

Maiti, S.K., Smith, R.A., 1983b. Theoretical and experimental studies on the extension of cracks subjected to concentrated loading near their faces to compare the criteria for mixed mode brittle fracture. *Journal of the Mechanics and Physics of Solids* 31, 389–403.

Martins, R.F., Ferreira, L., Reis, L., Chambel, P., 2016. Fatigue crack growth under cyclic torsional loading. *Theoretical and Applied Fracture Mechanics* 85, 56–66.

Miao, X.T., Yu, Q., Zhou, C.Y., Li, J., Wang, Y.Z., He, X.H., 2018. Experimental and numerical investigation on fracture behavior of CTS specimen under I-II mixed mode loading. *European Journal of Mechanics - A/Solids* 72, 235–244.

Mills, K., American Society for Metals., ASM Handbook Committee., 1987. Fractography. ASM International.

Miranda, A., Meggiolaro, M., Castro, J., Martha, L., Bittencourt, T., 2002. Fatigue crack propagation under complex loading in arbitrary 2D geometries, in: Applications of Automation Technology in Fatigue and Fracture Testing and Analysis: Fourth Volume. ASTM International, 100 Barr Harbor Drive, PO Box C700, West Conshohocken, PA 19428-2959, pp. 120–126.

Miranda, A.C. de O., Meggiolaro, M.A., Castro, J.T.P. de, Martha, L.F., 2003. Fatigue life prediction of complex 2D components under mixed-mode variable amplitude loading. *International Journal of Fatigue* 25, 1157–1167.

Miranda, A.C.O., Meggiolaro, M.A., Castro, J.T.P., Martha, L.F., 2007. Path and life predictions under mixed mode I-Mode II complex loading. *Mechanics of solids in Brazil* 421–432.

Miranda, A.C.O., Meggiolaro, M.A., Castro, J.T.P., Martha, L.F., Bittencourt, T.N., 2003. Fatigue life and crack path predictions in generic 2D structural components. *Engineering Fracture Mechanics* 70, 1259–1279.

Mohanty, J.R., Verma, B.B., Ray, P.K., 2009. Prediction of fatigue crack growth and residual life using an exponential model: Part I (constant amplitude loading). *International Journal of Fatigue* 31, 418–424.

Mohanty, J.R., Verma, B.B., Ray, P.K., 2008. Evaluation of overload-induced fatigue crack growth retardation parameters using an exponential model. *Engineering Fracture Mechanics* 75, 3941–3951.

Mróz, K.P., Mróz, Z., 2010. On crack path evolution rules. *Engineering Fracture Mechanics* 77, 1781–1807.

Mukherjee, B., 1972. A note on the analysis of fatigue crack growth data. *International Journal of Fracture Mechanics* 8, 449–452.

Mukhopadhyay, N.K., Maiti, S.K., Kakodkar, A., 2000. A review of SIF evaluation and modelling of singularities in BEM.

Munro, H.G., 1973. The determination of fatigue crack growth rates by a data smoothing technique. *International Journal of Fracture* 9, 366–368.

Murthy, K.S.R.K., Mukhopadhyay, M., 2001. Unification of stress intensity factor (SIF) extraction methods with an h-adaptive finite element scheme 17, 509–520.

Musuva, J.K., Radon, J.C., 1979. The effect of stress ratio and frequency on fatigue crack growth. *Fatigue & Fracture of Engineering Materials and Structures* 1, 457–470.

Muzvidziwa, M., Okazaki, M., Suzuki, K., Hirano, S., 2016. Role of microstructure on the fatigue crack propagation behavior of a friction stir welded Ti–6Al–4V. *Materials Science and Engineering: A* 652, 59–68.

Nakamura, T., 1991. Three dimensional stress fields of elastic interface cracks. *Journal of Applied Mechanics* 58, 939–346.

Nasri, K., Zenasni, M., 2017. Fatigue crack growth simulation in coated materials using X-FEM. *Comptes Rendus Mécanique* 345, 271–280.

Newman, J., 2009. A crack closure model for predicting fatigue crack growth under aircraft spectrum loading, in: Methods and Models for Predicting Fatigue Crack Growth Under Random Loading: ASTM STP. ASTM International, 100 Barr Harbor Drive, PO Box C700, West Conshohocken, PA 19428-2959, pp. 53-53–32.

Newman, J.C., 1984. A crack opening stress equation for fatigue crack growth. *International Journal of Fracture* 24, 131–135.

Paris, P.C., 2014. A brief history of the crack tip stress intensity factor and its application. *Meccanica* 49, 759–764.

Paris, P.C., Gomez, M.P., Anderson, W.E., 1961. A rational analytic theory of fatigue. *The Trends in Engineering* 13, 9–14.

Parks, D.M., 1974. A stiffness derivative finite element technique for determination of crack tip stress intensity factors. *International Journal of Fracture* 10, 487–502.

Patel, A.B., Pandey, R.K., 1981. Fatigue crack growth under mixed mode loading. *Fatigue & Fracture of Engineering Materials and Structures* 4, 65–77.

Peixoto, D.F.C., de Castro, P.M.S.T., 2017. Fatigue crack growth of a railway wheel. *Engineering Failure Analysis* 82, 420–434.

Polak, J., Knesl, Z., 1975. On the fatigue crack growth rate evaluation from experimental data. *International Journal of Fracture* 11, 693–696.

Pook, L.P., Frost, N.E., 1973. A fatigue crack growth theory. *International Journal of Fracture* 9, 53–61.

Portela, A., Aliabadi, M.H., Rooke, D.P., 1993. Dual boundary element incremental analysis of crack propagation. *Computers & Structures* 46, 237–247.

Pustejovsky, M.A., 1979a. Fatigue crack propagation in titanium under general in-plane loading—I: Experiments. *Engineering Fracture Mechanics* 11, 9–15.

Pustejovsky, M.A., 1979b. Fatigue crack propagation in titanium under general in-plane loading—II: Analysis. *Engineering Fracture Mechanics* 11, 17–31.

Qi, S., Cai, L.X., Bao, C., Chen, H., Shi, K.K., Wu, H.L., 2019. Analytical theory for fatigue crack propagation rates of mixed mode I–II cracks and its application. *International Journal of Fatigue* 119, 150–159.

Qian, G., González, Albuixech, V.F., Niffenegger, M., Giner, E., 2016. Comparison of KI calculation methods 156, 52–67.

Qian, J., Fatemi, A., 1996a. Mixed mode fatigue crack growth: A literature survey. *Engineering Fracture Mechanics* 55, 969–990.

Qian, J., Fatemi, A., 1996b. Fatigue crack growth under mixed mode I and II loading. *Fatigue & Fracture of Engineering Materials and Structures* 19, 1277–1284.

Rahulkumar, P., Saigal, S., Yunus, S., 1997. Singular p-version finite elements for stress intensity factor computations. *International Journal for Numerical Methods in Engineering* 40, 1091–1114.

Raju, I.S., Newman, J.C., 1977. Three-dimensional finite element analysis of finite thickness fracture specimens. Hampton.

Ramamurthy, T.S., Krishnamurthy, T., Narayana, K.B., Vijayakumar, K., Dattaguru, B., 1986. Modified crack closure integral method with quarter point elements. *Mechanics Research Communications* 13, 179–186.

Ramesh, K., Gupta, S., Srivastava, A.K., 1996. Equivalence of multi-parameter stress field equations in fracture mechanics. *International Journal of Fracture* 79, R37–R41.

Rankine, W.J.M., 1843. On the causes of the unexpected breakage of the journals of railway axles; and on the mean of preventing such accidents by observing the law of continuity in their construction. *Journal of the Franklin Institute* 36, 178–180.

Ravi-Chandar, K., 2008. Fracture mechanics, in: Springer Handbook of Experimental Solid Mechanics. Springer US, Boston, MA, pp. 125–158.

Reddy, S., Fatemi, A., 1992. Small crack growth in multiaxial fatigue, in: Advances in Fatigue Lifetime Predictive Techniques. ASTM International, 100 Barr Harbor Drive, PO Box C700, West Conshohocken, PA 19428-2959, pp. 276-276–23.

Reimers, P., 1991. Simulation of mixed mode fatigue crack growth. *Computers & Structures* 40, 339–346.

Rice, J.R., 1968. A path independent integral and the approximate analysis of strain concentration by notches and cracks. *Journal of Applied Mechanics* 35, 379–386.

Richard, H.A., 1981. A new compact shear specimen. *International Journal of Fracture* 17, R105–R107.

Richard, H.A., Benitz, K., 1983. A loading device for the creation of mixed mode in fracture mechanics. *International Journal of Fracture* 22, 55–58.

Richard, H.A., Buchholz, F.G., Kullmer, G., Schöllmann, M., 2003. 2D and 3D mixed mode fracture criteria. *Key Engineering Materials* 251–252, 251–260.

Richard, H.A., Fulland, M., Sander, M., 2005. Theoretical crack path prediction. *Fatigue and Fracture of Engineering Materials and Structures* 28, 3–12.

Richard, H.A., Linnig, W., Henn, K., 1991. Fatigue crack propagation under combined loading. *Forensic engineering* 3, 99–109.

Richard, H.A., Schramm, B., Schirmeisen, N.H., 2014. Cracks on mixed mode loading - Theories, experiments, simulations. *International Journal of Fatigue* 62, 93–103.

Roberts, R., Kibler, J.J., 1971. Mode II fatigue crack propagation. *Journal of Basic Engineering* 93, 671.

Rosenhain, W., Humfrey, J.C.W., 1910. The crystalline structure of iron at high temperatures. *Proceedings of the Royal Society A: Mathematical, Physical and Engineering Sciences* 83, 200–209.

Rozumek, D., 2014. Survey of formulas used to describe the fatigue crack growth rate. *Materials Science* 49, 723–733.

Rozumek, D., Macha, E., 2009. A survey of failure criteria and parameters in mixed-mode fatigue crack growth. *Materials Science* 45, 190–210.

Rozumek, D., Marciniak, Z., Lesiuk, G., Correia, J.A., de Jesus, A.M.P., 2018. Experimental and numerical investigation of mixed mode I + II and I + III fatigue crack growth in S355J0 steel. *International Journal of Fatigue* 113, 160–170.

Rybicki, E.F., Kanninen, M.F., 1977. A finite element calculation of stress intensity factors by a modified crack closure integral. *Engineering Fracture Mechanics* 9, 931–938.

Sadeghirad, A., Chopp, D.L., Ren, X., Fang, E., Lua, J., 2016. A novel hybrid approach for level set characterization and tracking of non planar 3D cracks in the extended finite element method. *Engineering Fracture Mechanics* 160, 1–14.

Sajjadi, S.H., Ostad Ahmad Ghorabi, M.J., Salimi-Majd, D., 2015. A novel mixed-mode brittle fracture criterion for crack growth path prediction under static and fatigue loading. *Fatigue & Fracture of Engineering Materials & Structures* 38, 1372–1382.

Sander, M., Richard, H.A., 2006. Experimental and numerical investigations on the influence of the loading direction on the fatigue crack growth. *International Journal of Fatigue* 28, 583–591.

Sander, M., Richard, H.A., 2005. Finite element analysis of fatigue crack growth with interspersed mode I and mixed mode overloads. *International Journal of Fatigue* 27, 905–913.

Sanford, R.J., 2003. Principles of fracture mechanics. Prentice Hall.

Sanford, R.J., 1979. A critical re-examination of the westergaard method for solving opening-mode crack problems. *Mechanics Research Communications* 6, 289–294.

Sarangi, H., Murthy, K.S.R.K., Chakraborty, D., 2012. Optimum strain gage locations for accurate determination of the mixed mode stress intensity factors. *Engineering Fracture Mechanics* 88, 63–78.

Sarangi, H., Murthy, K.S.R.K., Chakraborty, D., 2010. Radial locations of strain gages for accurate measurement of mode I stress intensity factor. *Materials & Design* 31, 2840–2850.

Schijve, J., 2009. Fatigue of structures and materials, 2nd ed. Springer Netherlands.

Schijve, J., 2003. Fatigue of structures and materials in the 20th century and the state of the art. *International Journal of Fatigue* 25, 679–702.

Schütz, W., 1996. A history of fatigue. *Engineering Fracture Mechanics* 54, 263–300.

Seifi, R., Eshraghi, M., 2013. Effects of mixed-mode overloading on the mixed-mode I+II fatigue crack growth. *Archive of Applied Mechanics* 83, 987–1000.

Seo, K.J., Choi, B.H., Lee, J.M., Shin, S.M., 2010. Investigation of the mixed mode fatigue crack growth of a hot rolled steel plate with a circular microdefect. *International Journal of Fatigue* 32, 1190–1199.

Sethuraman, R., Maiti, S.K., 1988. Finite element based computation of strain energy release rate by modified crack closure integral. *Engineering Fracture Mechanics* 30, 227–231.

Shi, J., Chopp, D., Lua, J., Sukumar, N., Belytschko, T., 2010. Abaqus implementation of extended finite element method using a level set representation for three dimensional fatigue crack growth and life predictions. *Engineering Fracture Mechanics* 77, 2840–2863.

Shih, C.F., Delorenzi, H.G., German, M.D., 1976. Crack extension modeling with singular quadratic isoparametric elements. *International Journal of Fracture* 12, 647–651.

Shih, C.F., Moran, B., Nakamura, T., 1986. Energy release rate along a three-dimensional crack front in a thermally stressed body. *International Journal of Fracture* 30, 79–102.

Shivakumar, K.N., Tan, P.W., Newman, J.C., 1988. A virtual crack closure technique for calculating stress intensity factors for cracked three dimensional bodies. *International Journal of Fracture* 36, 43–50.

Sih, G.C., 1974. Strain energy density factor applied to mixed mode crack problems. *International Journal of Fracture* 10, 305–321.

Sih, G.C. (Ed.), 1973. Methods of analysis and solutions of crack problems. Springer Netherlands, Dordrecht.

Sih, G.C., Barthelemy, B.M., 1980. Mixed mode fatigue crack growth predictions. *Engineering Fracture Mechanics* 13, 439–451.

Smith, R.A., 1973. The determination of fatigue crack growth rates from experimental data.

International Journal of Fracture 9, 352–355.

Socie, D.F., Hua, C.T., Worthem, D.W., 1987. Mixed mode small crack growth. *Fatigue & Fracture of Engineering Materials and Structures* 10, 1–16.

Srilakshmi, R., Ramji, M., Chinthapenta, V., 2015. Fatigue crack growth study of CFRP patch repaired Al 2014-T6 panel having an inclined center crack using FEA and DIC. *Engineering Fracture Mechanics* 134, 182–201.

Srinivas, V., Vasudevan, P., 1993a. Studies of mixed mode crack propagation in D16AT aluminium alloy. *Engineering Fracture Mechanics* 45, 415–430.

Srinivas, V., Vasudevan, P., 1993b. Experimental observations on mixed mode fatigue crack propagation. *International Journal of Pressure Vessels and Piping* 56, 319–329.

Srinivas, V., Vasudevan, P., 1993c. Study of the influence of mixed mode overload on mode I fatigue crack propagation. *International Journal of Pressure Vessels and Piping* 56, 409–417.

Srivastava, Y.P., Garg, S.B.L., 1988. Study on modified J-integral range and its correlation with fatigue crack growth. *Engineering Fracture Mechanics* 30, 119–133.

Strifors, H.C., 1974. A generalized force measure of conditions at crack tips. *International Journal of Solids and Structures* 10, 1389–1404.

Suresh, S., 1998. Fatigue of materials, 2nd ed. Cambridge University Press, Cambridge.

Swamy, S., Srikanth, M., Murthy, K., Robi, P., 2008. Determination of mode I stress intensity factors of complex configurations using strain gages. *Journal of Mechanics of Materials and Structures* 3, 1239–1255.

Tada, H., Paris, P.C., Irwin, G.R., 2000. The stress analysis of cracks handbook, 3rd ed. ASME, Three Park Avenue New York, NY 10016-5990.

Tamilselvan, T., Lo, K., Gong, Y., Zhao, M., 2005. A model for mixed mode fatigue. *Journal of Testing and Evaluation* 33, 188–196.

Tanaka, K., 1974. Fatigue crack propagation from a crack inclined to the cyclic tensile axis. *Engineering Fracture Mechanics* 6, 493–507.

Tavares, S.M.O., de Castro, P.M.S.T., 2017. An overview of fatigue in aircraft structures. *Fatigue & Fracture of Engineering Materials & Structures* 40, 1510–1529.

Tavares, S.M.O., Reis, L., de Freitas, M., de Castro, P.M.S.T., 2019. Mixed mode fatigue and fracture in planar geometries: Observations on Keq and crack path modelling. *Fatigue and Fracture of Engineering Materials and Structures* 42, 2441–2456.

Theocaris, P.S., Andrianopoulos, N.P., 1982. The T-criterion applied to ductile fracture. *International Journal of Fracture* 20, R125–R130.

Tracey, D.M., 1977. Discussion of 'on the use of isoparametric finite elements in linear fracture mechanics' by R. S. Barsoum. *International Journal for Numerical Methods in Engineering* 11, 401–402.

Treifi, M., Olutunde Oyadiji, S., Tsang, D.K.L., 2008. Computations of modes I and II stress intensity factors of sharp notched plates under in-plane shear and bending loading by the fractal-like finite element method. *International Journal of Solids and Structures* 45, 6468–6484.

Varfolomeev, I., Burdack, M., Moroz, S., Siegele, D., Kadau, K., 2014. Fatigue crack growth rates and paths in two planar specimens under mixed mode loading. *International Journal of Fatigue* 58, 12–19.

Virkler, D.A., Hilberry, B.M., Goel, P.K., 1979. The statistical nature of fatigue crack propagation. *J. Eng. Mater. Technol.* 101, 148–153.

Vormwald, M., Hos, Y., Freire, J.L.F., Gonzáles, G.L.G., Díaz, J.G., 2018. Crack tip displacement fields measured by digital image correlation for evaluating variable mode-mixity during fatigue crack growth. *International Journal of Fatigue* 115, 53–66.

Walker, K., 1970. The effect of stress ratio during crack propagation and fatigue for 2024-T3 and 7075-T6 aluminum, in: Effects of Environment and Complex Load History on Fatigue Life. ASTM International, 100 Barr Harbor Drive, PO Box C700, West Conshohocken, PA 19428-2959, pp. 1-1–14.

Wang, Q., Liu, X., Wang, W., Yang, C., Xiong, X., Fang, H., 2017. Mixed mode fatigue crack growth behavior of Ni-Cr-Mo-V high strength steel weldments. *International Journal of Fatigue* 102, 79–91.

Wawrzynek, P., Ingraffea, A., 1994. FRANC2D: A two-dimensional crack propagation simulator. Version 2.7: User's guide.

Weertman, J., 1966. Rate of growth of fatigue cracks calculated from the theory of infinitesimal

dislocations distributed on a plane. *International Journal of Fracture Mechanics* 2, 460–467.

Westergaard, H.M.W., 1939. Bearing pressures and cracks. *Journal of Applied Mechanics* 6, 49–53.

Williams, M.L., 1957. On the stress distribution at the base of a stationary crack. *Journal of Applied Mechanics* 24, 109–114.

Wilson, W.K., 1969. Combined mode fracture mechanics. University of Pittsburgh, California.

Wőhler, A., 1860. Versuche zur Ermittlung der auf die Eisenbahnwagenachsen einwirkenden Kräfte und die Widerstandsfahigkeit der Wagen-Achsen. *Zeitschrift für Bauwesen* Vol. 10, 583–616.

Yan, A.M., Nguyen-Dang, H., 1995. Multiple cracked fatigue crack growth by BEM. *Computational Mechanics* 16, 273–280.

Yan, X., 2007. Automated simulation of fatigue crack propagation for two dimensional linear elastic fracture mechanics problems by boundary element method. *Engineering Fracture Mechanics* 74, 2225–2246.

Yan, X., Du, S., Zhang, Z., 1992. Mixed mode fatigue crack growth prediction in biaxially stretched sheets. *Engineering Fracture Mechanics* 43, 471–475.

Yan, X., Liu, B., Hu, Z., 2010. SIFs of rectangular tensile sheets with symmetric double edge defects. *Journal of Mechanics of Materials and Structures* 5, 795–803.

Yang, Y., Vormwald, M., 2017. Fatigue crack growth simulation under cyclic non-proportional mixed mode loading. *International Journal of Fatigue* 102, 37–47.

Yukitaka Murakami, 1987. Stress intensity factors handbook. Pergamon.

Zarrinzadeh, H., Kabir, M.Z., Deylami, A., 2017. Experimental and numerical fatigue crack growth of an aluminium pipe repaired by composite patch. *Engineering Structures* 133, 24–32.

Zerbst, U., Beretta, S., 2011. Failure and damage tolerance aspects of railway components. *Engineering Failure Analysis* 18, 534–542.

Zerbst, U., Schödel, M., Beier, H.T., 2011. Parameters affecting the damage tolerance behaviour of railway axles. *Engineering Fracture Mechanics* 78, 793–809.

Zhang, H.H., Li, L.X., An, X.M., Ma, G.W., 2010. Numerical analysis of 2D crack propagation problems using the numerical manifold method. *Engineering Analysis with Boundary Elements* 34, 41–50.

Zhang, X.B., Ma, S., Recho, N., Li, J., 2006. Bifurcation and propagation of a mixed-mode crack in a ductile material. *Engineering Fracture Mechanics* 73, 1925–1939.

Zheng, J., Powell, B.E., 1999. Effect of stress ratio and test methods on fatigue crack growth rate for nickel based superalloy Udimet720. *International Journal of Fatigue* 21, 507–513.

Zheng, J., Powell, B.E., 1997. A method to reduce the scatter in fatigue crack growth data. *Fatigue and Fracture of Engineering Materials and Structures* 20, 1341–1350.

Zhu, W.X., Smith, D.J., 1995. On the use of displacement extrapolation to obtain crack tip singular stresses and stress intensity factors. *Engineering Fracture Mechanics* 51, 391–400.

List of publications from this thesis

International Journals

1. **S Sajith**, KSRK Murthy, PS Robi (2020). Experimental and numerical investigation of mixed mode fatigue crack growth models in Aluminum 6061-T6, *International Journal of Fatigue* 130:105285

2. **S Sajith**, SS Shukla, KSRK Murthy, PS Robi (2020). Mixed mode fatigue crack growth studies in AISI 316 stainless steel, *European Journal of Mechanics: A-Solids* 80:103898

3. **S Sajith**, KSRK Murthy, PS Robi (2019). Prediction of accurate mixed mode fatigue crack growth curves using the Paris' law, *Journal of The Institution of Engineers (India): Series C*, 100(1):165-174

4. **S Sajith**, KSRK Murthy, PS Robi (2018). A simple technique for estimation of mixed mode (I/II) stress intensity factors, *Journal of Mechanics of Materials and Structures*: 13(2):141–54

5. **S Sajith**, KSRK Murthy, PS Robi. A three-parameter double exponential model for curve fitting of mixed mode fatigue crack growth data (To be communicated)

Book Chapters

1. **S Sajith**, KSRK Murthy, PS Robi (2020). Accurate Estimation of Mixed-Mode Stress Intensity Factors Using Crack Flank Displacements. In L. Li, D. Pratihar, S. Chakrabarty, & P. Mishra (Eds.), *Advances in Materials and Manufacturing Engineering.* Springer Nature Singapore, 1:503–509

International conferences

1 . **S Sajith**, KSRK Murthy, PS Robi (2020). Estimation of stress intensity factors from crack flank displacements, *Materials Today Proceedings* 24(2), 887-894

2 . **S Sajith**, KSRK Murthy, PS Robi (2019). Mixed mode fatigue crack growth studies of crack emanating from circular hole. *AIP Conference Proceedings*, 2200(1), 020041

3 . **S Sajith**, KSRK Murthy, PS Robi (2018). Fatigue crack growth and life prediction under mixed-mode loading. In G. C. M. Kumar (Ed.), *AIP Conference Proceedings*, 1943, 020068.

4 . **S Sajith**, KSRK Murthy, PS Robi (2018). Fatigue life prediction under mixed-mode loading using equivalent stress intensity factor models. In V. Jayakumar, S. Ranganathan, D. Devika, & S. Sridevi (Eds.), *MATEC Web of Conferences*, 172, 03005

5 . **S Sajith**, KSRK Murthy, PS Robi (2014). A Novel Method for Computation of Mixed Mode Stress Intensity Factors of 2D Cracked Configurations. *Proceedings of the 5th International Congress on Computational Mechanics and Simulation*, 840–847

About the author

Mr. Sajith S is born to Mr. V Soman and Ms. Sudharma Kumari in the year 1985. He completed the Class X from the Kerala State Education Board, securing first division in the examinations. He secured the three-year engineering diploma from Carmel Polytechnic, Alappuzha, Kerala, which is affiliated to the State Board of Technical Education, Kerala. He completed the Bachelor's degree (A.M.I.E.) in Mechanical Engineering from The Institution of Engineers (India), Kolkata in the year 2007, securing first division. He worked as a lecturer at VIET, Kottayam, Kerala, during the period 2007-2009. He completed the Master of Technology (M.Tech.) in Machine Design from the Department of Mechanical Engineering of the Indian Institute of Technology Guwahati (IIT Guwahati) during 2009-2011 and secured first division. He joined the Mechanical Engineering Department, Indian Institute of Technology Guwahati (IIT Guwahati), as a regular research scholar in the year 2011. His areas of research are experimental and numerical fatigue crack growth studies, failure analysis, fracture mechanics, and finite element methods.